Recyclable Electrical Machine Designs with 3D Flux and Non-Traditional Materials

Gonzalez, Adolfo Garcia

Publication date:
2019

Document Version
Publisher's PDF, also known as Version of record

RECYCLABLE ELECTRICAL MACHINE DESIGNS WITH 3D FLUX AND NON-TRADITIONAL MATERIALS

BY
ADOLFO GARCIA GONZALEZ

DISSERTATION SUBMITTED 2019

AALBORG UNIVERSITY
DENMARK

Recyclable Electrical Machine Designs with 3D Flux and Non-Traditional Materials

Ph.D. Dissertation

Adolfo Garcia Gonzalez

Dissertation submitted September, 2019

Dissertation submitted: September, 2019

PhD supervisor: Associate Professor Peter Omand Rasmussen
Aalborg University

Assistant PhD supervisor: Assistant Professor Dong Wang
Aalborg University

PhD committee: Associate Professor Lasse Schmidt (chairman)
Aalborg University

Professor Bogi Bech Jensen
Glasir – Torshavn College

Professor Yujing Liu
Chalmers University of Technology

PhD Series: Faculty of Engineering and Science, Aalborg University

Department: Department of Energy Technology

ISSN (online): 2446-1636
ISBN (online): 978-87-7210-510-9

Published by:
Aalborg University Press
Langagervej 2
DK – 9220 Aalborg Ø
Phone: +45 99407140
aauf@forlag.aau.dk
forlag.aau.dk

Printed in Denmark by Rosendahls, 2019

Contents

List of Figures v

List of Tables ix

Abstract xi

Resume xiii

Acknowledgement xv

1 Introduction 1
- 1.1 Background . . . 1
- 1.2 Introduction to the State of the Art . . . 4
  - 1.2.1 Review of Electrical Machines in (H)EVs . . . 4
  - 1.2.2 Transverse Flux Machine (TFM) . . . 6
  - 1.2.3 Axial Flux Machine (AFM) . . . 7
  - 1.2.4 The Hybrid Stepper Motor (HSM) . . . 9
- 1.3 Magnetic Materials in Electrical Machines . . . 11
- 1.4 Proposed Structure of a 3D-Flux Machine . . . 16
- 1.5 Objectives and Limitations of the Project . . . 19
  - 1.5.1 Objectives . . . 19
  - 1.5.2 Limitations . . . 19
- 1.6 Motivation . . . 20
- 1.7 Outline of the Thesis . . . 20
  - 1.7.1 Publications . . . 21

2 A Surface Mounted 3D-Flux PM Machine 23
- 2.1 Analytical Approach and Working Principle . . . 23
  - 2.1.1 Construction of the Reluctance Network . . . 23
  - 2.1.2 Description of the Working Principle . . . 26
- 2.2 Dimensioning of the SM3D Machine . . . 28
- 2.3 2D-FEM Modelling . . . 31
  - 2.3.1 Comparison Between Analytical and 2D-FEM Models . . . 33
- 2.4 3D-FEM Modelling . . . 34
  - 2.4.1 Evaluation of the PM Coverage . . . 35
  - 2.4.2 Evaluation of the PM Thickness . . . 37

2.4.3 Evaluation of the Selection of Stator Modules and Rotor Poles . . . 42
2.5 Study of the Surface Mounted 3D-Flux Permanent Magnet Machine . . . 45
2.5.1 No-Load Back-EMF . . . 45
2.5.2 Production of Torque . . . 46
2.5.3 Inductance Profile vs. Current Density . . . 47
2.5.4 Calculation of the Iron Losses . . . 48
2.5.5 Magnet Losses of the Surface Mounted 3D-Flux Machine 49
2.5.6 Main Parameters of the SM 3D-Flux Machine . . . 51
2.6 A Surface Mounted PM 3D-Flux Demonstrator . . . 52
2.6.1 Characterization of Iron Losses in Amorphous C-Shaped Cores . . . 53
2.6.2 Validation of FEM Calculations with Test Measurements 54
2.6.3 Comparison of Measured and Calculated Rotational Losses 61
2.6.4 Estimation of the Torque . . . 61
2.7 Summary . . . 62

3 Hybrid Rotor 3D-Flux Machine 65
3.1 Description of the Working Principle . . . 65
3.1.1 Production of PM Flux . . . 65
3.1.2 Variation of the Tooth Width . . . 69
3.1.3 Study of the Variation of the PM Thickness . . . 72
3.1.4 Study of the Variation of the PM Width . . . 75
3.2 Preliminary Calculation of the Hybrid Rotor 3D-Flux Machine 79
3.3 Increment of Torque Production . . . 81
3.3.1 PM Losses of the Hybrid Rotor 3D-Flux Machine . . . 85
3.4 A Hybrid Rotor 3D-Flux Prototype . . . 86
3.4.1 Assembly of the Prototype . . . 88
3.5 Testing of the HM3D Machine . . . 93
3.5.1 No-Load Back-EMF . . . 93
3.5.2 Torque Measurement . . . 96
3.5.3 Inductance Measurement . . . 99
3.5.4 Thermal Test of the HM3D Machine . . . 101
3.5.5 Rotational Losses . . . 103
3.5.6 Summary of the Main Dimensions of the HM3D Machine 105
3.6 Summary . . . 106

4 Recyclability Evaluation of Permanent Magnets in Electrical Machines 109
4.1 Recyclability Evaluation Definition . . . 109
4.1.1 Evaluation of the Assembly and Disassembly Processes 110
4.1.2 Evaluation of the Energy Consumption . . . 113

4.2 Energy Evaluation of the HM3D Machine 119
4.2.1 Efficiency Map of the HM3D Machine 119
4.2.2 Drive Cycle and Vehicle Modelling 120
4.2.3 Energy Consumption Investigation 121
4.3 Summary 123

5 Conclusion **125**
5.1 Summary 125
5.2 Main Contributions 127
5.3 Future Work 128

Bibliography **131**

Appendix A **141**

Appendix B **149**

Appendix C **157**

Appendix D **165**

Appendix E **173**

List of Figures

1.1 Three recycling loops for REEs of PMs in (H)EVs. 2
1.2 Dismantled rotor container. 4
1.3 Claw-pole TFM SMC machine. 4
1.4 Rotor of a claw pole machine, conceived for reuse of PMs. . . . 4
1.5 Machine topologies found in (H)EVs, (a) synchronous, (b) induction, and (c) interior permanent magnet [27]. 5
1.6 Basic topologies of a TFM, (a) single sided SMTFM, (b) double sided SMTFM. 7
1.7 Main topologies of AFMs, (a) Single sided slotted, (b) double sided slot-less, (c) double sided slotted, (d) double sided coreless, (e) double sided external salient pole stator and internal rotor, (f) double sided internal salient pole stator and external twin rotor. 8
1.8 Rotor of a HSM. 10
1.9 Flux paths in the HSM, (a) flux produced by the PM in the rotor, (b) flux produced by the currents in the stator. 10
1.10 Rise in magnetic loss with frequency. 11
1.11 Niche applications of soft magnetic materials. 12
1.12 Amorphous metals, (a) melt-spinning diagram for the production, (b) final product: ribbon, (c) final C-shaped cores. 13
1.13 BH curves of electrical sheet and amorphous materials. 13
1.14 Stator made of amorphous laminations. 14
1.15 Modular teeth stator structure. 14
1.16 Stator made of amorphous laminations. 15
1.17 Segmented stator made of amorphous laminations. 15
1.18 AFM rotor structure; (a) uncut, (b) cut. 15
1.19 AFM with wounded amorphous stator cores. 16
1.20 Modular stator pieces of a claw-pole TFM. 16
1.22 Hybrid rotor topology. 17
1.21 Proposed machine geometry, (a) section of an AFM, (b) stator core stretched, (c) stator core bended, (d) C-shaped stator core and (e) C-shaped stator final approximation. 18

2.1 Simplified SM3D geometry. 24
2.2 Simplified reluctance network of the SM3D. 24
2.3 Simplified equivalent circuit of the SM topology. 24

2.4 Main PM dimensions. 25
2.5 Reluctance network for the calculation of the inductance. . . . 25
2.6 Simplified circuit of the SM3D. 25
2.8 PM flux linkage distribution of the SM3D machine. 28
2.13 SM3D 2D simplified geometry. 32
2.14 SM3D 2D symmetry. 32
2.15 Torque comparison for various rotor poles and stator module combinations. 33
2.16 Calculated torque with analytical and 2D-FEM models. 34
2.18 Ψ_m vs. PM coverage. 36
2.19 Torque per PM mass vs. PM_{cov}. 37
2.20 Ψ_m vs. PM thickness. 38
2.21 Torque vs. PM thickness. 39
2.22 Inductance vs. PM thickness. 40
2.23 Power factor vs. PM thickness. 40
2.25 Magnetic flux density vs. PM thickness. 41
2.26 SM3D geometry yz-plane. 42
2.28 Torque production vs. current density. 47
2.29 Magnetic flux density distribution at 13 A/mm^2. 47
2.30 Static torque of the 12 stator modules 16 rotor poles. 48
2.31 Inductance vs. current density. 49
2.32 Iron losses vs. speed. 49
2.33 Calculated PM losses vs. speed. 50
2.34 PM current density distribution @ 3000 rpm, (a) isometric view, (b) yz-plane view. 51
2.35 Demonstrator assembly. 53
2.36 Set-up for testing of the demonstrator. 53
2.37 Test coil for characterization of the iron losses. 53
2.38 Specific losses comparison between amorphous iron and SiFe laminations. 54
2.39 Main dimensions of the SM demonstrator. 56
2.40 SM demonstrator 3D-FEM model geometry. 56
2.41 Back-EMF measured and calculated with 3D-FEM @ 100 rpm. 56
2.42 Back-EMF measured and calculated with 3D-FEM at various speeds. 57
2.43 Inductance measured at various frequencies. 57
2.44 No-load losses measured at various speeds. 58
2.45 Measured mechanical losses at various speeds. 59
2.46 Resistivity of PM material vs. temperature. 60
2.47 PM current density distribution at 500 rpm and t=6 ms, (a) isometric view, (b) zoomed view. 60
2.48 Stator iron, PM and rotor back losses vs. speed. 61
2.49 Measured and calculated rotational losses. 62

2.50 Torque production. 62

3.1 3D-FEM model of the 27/18 HM3D machine. 66
3.2 Magnetic flux density distribution of the 27/18 HM3D machine . 66
3.4 Permanent magnet flux distribution of the HM3D machine. . . 68
3.5 PM flux linkage Ψ_m variation with angular position, HM3D 27 stator modules and 18 rotor teeth. 68
3.6 Harmonic spectrum of Ψ_m, 27 stator modules 18 rotor teeth. . 68
3.8 Variation of Ψ_m with rotor tooth width. 70
3.9 Variation of torque with rotor tooth width. 71
3.10 Rotor tooth dimensions. 72
3.11 Variation of inductance with rotor tooth width. 73
3.12 Variation of power factor with rotor tooth width. 73
3.13 PM ring on the rotor structure. 74
3.14 Variation of Ψ_m with PM thickness l_m. 74
3.15 Variation of torque with PM thickness l_m. 75
3.16 PM equivalent air-gap. 76
3.17 Variation of inductance with PM thickness l_m. 76
3.18 Variation of power factor with PM thickness l_m. 77
3.19 Variation of Ψ_m with PM width w_m. 77
3.20 Variation of torque with PM width w_m. 78
3.21 Inductance vs. PM width. 78
3.22 Power factor vs. PM thickness. 79
3.23 3D-FEM calculated torque HM3D machine. 80
3.24 PM flux linkage vs. mechanical angle. 81
3.25 Demonstration of Vernier's principle, (a) conventional machine, (b) multiple teeth per pole topology. 82
3.26 Magnetic flux density distribution of the HM3D machine at no-load; (a) original geometry, (b) n_{seg}=2, (c) n_{seg}=4, and (d) n_{seg}=8. 84
3.27 Detail of the air-gap of the HM3D machine with 6 stator and 8 teeth; (a) original geometry, and (b) n_{seg}=8. 84
3.28 Current density in the PM ring at 2300 rpm, n_{seg}=4. t=685 μs. 85
3.29 PM losses of the HM3D machine with n_{seg}= 4. 86
3.30 CAD model of the HM3D machine; (a) exploded view, and (b) section view. 87
3.31 Stator modules in electrical sheet; (a) general view, and (b) zoomed view of the stack. 89
3.32 Assembly of modules and coils. 89
3.33 Completed assembly of the stator. 90
3.34 Assembly of the PM blocks in one of the rotor stacks. 91
3.35 Rotor assembly on a lathe; (a) stack assembly, and (b) shaft assembly. 91

3.36 Rotor stack zoomed view. 92
3.37 Rotor assembly general view. 92
3.38 Complete assembly. 92
3.39 Test set-up of the HM3D machine as generator. 93
3.40 Measured back-EMF vs. time at 500 rpm. 94
3.41 Back-EMF vs. time at 500 rpm. 94
3.42 Stator modules; (a) welds in the middle region, (b) "short circuited" coils modelled in 3D-FEM. 95
3.43 Back-EMF vs. time @ 500 rpm. 95
3.44 Measured back-EMF vs. speed. 96
3.45 Set-up for measuring torque with a load machine. 97
3.46 Measured and calculated steady state torque at 500 rpm. . . . 97
3.47 Efficiency vs. current density at various speeds. 98
3.48 Set-up for measurement of torque with a DC power source. . . 99
3.49 Circuit for measuring torque with a DC power source. 99
3.50 Measured torque with DC current. 99
3.51 Measured inductance vs. frequency. 100
3.52 Equivalent circuit for thermal measurement of the HM3D fed with a DC current. 101
3.53 Placement of the thermocouples for temperature measurement; (a) general view, (b) zoomed view. 101
3.54 Temperature evolution with time. 102
3.55 Evolution of the rotational losses with speed, measured and calculated. 104
3.56 Calculated rotational losses at various current densities. 105
3.57 Measured rotational losses in motor mode. 105

4.1 Motor used for recyclability evaluation definition. 110
4.2 Disassembly process, (a) machine mounted on a lathe for rotor extraction, (b) disassembled rotor and (c) disassembled stator. 111
4.3 Flow chart of the calculation of the energy consumption. 114
4.4 Set-up used for measurements. 114
4.5 Geometry modelled in FEM, magnetic flux density distribution. 115
4.6 Efficiency map of the outer rotor PM motor. 116
4.7 NEDC driving cycle. 117
4.8 WLTP driving cycle. 117
4.9 Efficiency map of HM3D machine with amorphous stator modules and virgin PMs. 119
4.10 Efficiency map of HM3D machine with amorphous stator modules and recycled PMs. 120
4.11 Torque vs. speed envelope for a small city car under WLTP driving cycle. 121

List of Tables

1.1 Summary of AFM topologies. 9
1.2 Summary of research on amorphous materials in electrical machines. 17

2.1 Calculated PM flux of the SM3D machine. 26
2.2 Flux linkage generated by the MMF in the winding. 29
2.3 Specification for the design of the SM3D machine. 30
2.4 Air-gap diameters of various combinations of stator modules and rotor poles. 31
2.5 Main dimensions of a SM3D machine with 15 stator modules and 20 poles. 36
2.7 C-shaped core main dimensions. 43
2.9 Torque and radius per combination of poles and stator modules. 43
2.10 Selection of SM3D machines. 44
2.11 Main dimensions of a SM3D machine with 12 stator modules and 16 poles. 45
2.12 Main parameters of the SM3D machine. 52
2.13 Main dimensions of the demonstrator. 55
2.14 Measured and calculated values of inductance. 58

3.1 Main dimensions of a HM3D machine with 27 stator modules and 18 rotor teeth. 69
3.2 Main dimensions of a HM3D machine with 12 stator modules and 8 teeth. 80
3.3 Main parameters of a HM3D machine with 6 stator modues and 8 teeth, and n_{seg}=2, 4, and 8. 83
3.4 Main dimensions of the HM3D prototype. 87
3.6 Inductance and DC resistance of the HM3D machine. 100
3.7 Main measured parameters of the SM3D machine. 106

4.1 CO_2 equivalent emissions in production of REOs. 118
4.2 Main vehicle parameters. 121
4.3 Energy evaluation of the HM3D machine with virgin and recycled PM material. 122

ABSTRACT

Permanent Magnet (PM) machines are important in the electrification of transportation for the reduction of CO_2 emissions and reducing global warming. In order to maintain the increasing demand for Hybrid and Electrical Vehicles ((H)EVs) a stable supply of Rare Earth Elements (REEs) used in the production of PMs is required. Nowadays, some REEs (e.g. Neodymium and Dysprosium) are classified as critical raw materials by the European Commission, due to the high risk in their supply. Such a risk was demonstrated in 2011 when the REE crisis reached its peak with the dramatic increase of the prices of REEs, specially Dysprosium, when export quotas were introduced from the main producing country, China.

With the current economic and political scenarios at global level, the probability of having a similar crisis as in 2011 remains high. Hence, securing the supply of REEs is still of major relevance and have increased awareness in recent years. Despite of being a subject of extensive research, recycling of PMs remains a challenging task. Some of the existing technologies either have poor efficiency or are highly polluting. Consequently, the European Training Network for the Design and Recycling of Rare-Earth Permanent Magnet Motors and Generators in Hybrid and Full Electric Vehicles (DEMETER) project was created. DEMETER project works toward the evaluation an improvement of the recycling routes of REEs in (H)EVs. Additionally, it intends to develop innovative techniques for the production of PMs, and both life-cycle assessment and life-cycle costing of PMs with recycled REEs.

Regardless of the recycling method, separation and classification of PM material are important steps in order to start a recycling process. Therefore, the improvement of the recycling methods would be insufficient unless the electrical machines are designed so that the access to the PMs is facilitated once the End of Life of the machine is reached and the motor is scrapped. Hence, this thesis work proposes an alternative machine topology. Such machine consists of a hybrid rotor structure in conjunction with a modular stator.

The Finite Element Method (FEM) has been used to create a design that has subsequently been validated with measurements from a manufactured prototype. Although the performance of the prototype was substantially lower in comparison to a Synchronous Permanent Magnet Surface Mounted (SPMSM)

machine, from the recyclability perspective it is considered that the proposed structure has a potential as glue is not required for the assembly of PMs on the rotor. In addition, the 3D nature of the flux in the magnetic system allows the use of non-traditional materials (e.g. iron based amorphous laminations, SMC, grain oriented electrical sheet, etc.). Finally, a recyclability index has been developed to provide a quantitative evaluation of the recyclability of PM electrical machines in the context of e-mobility.

RESUME

Elmotorer med permanente magneter (PM) er vigtige mht. at elektrificere transport sektoren, hvorved CO_2 udledningerne og den globale opvarmning kan begrænses. For at bibeholde den øgede efterspørgelse på el- og hybrid-biler (HEV) kræves en stabil forsyningssikkerhed af de sjældne jordarter (REE), der anvendes i produktionen af de permanente magneter. I dag klassificeres nogle REE'er (f.eks. Neodymium og Dysprosium) som kritiske råvarer af EU-Kommissionen da der er en hvis risiko i forsyningskæden. En sådan risiko blev demonstreret i 2011, da REE-krisen nåede sit højdepunkt med en dramatisk stigning i priserne på REE'er, specielt Dysprosium, da der blev indført eksportkvoter fra det vigtigste producerende land, Kina.

Med de nuværende økonomiske og politiske scenarier på globalt plan er sandsynligheden for en lignende krise, som i 2011, fortsat høj. Derfor er det stadig vigtigt at sikre udbuddet af REE'er og bibeholde den øgede opmærksomhed. På trods af at genanvendelse har været genstand for omfattende forskning, er denne måde at bibeholde forsyningen på stadig en udfordrende opgave. Nogle af de udviklede genanvendelses teknologier har enten en dårlig effektivitet eller er meget forurenende. Som følge heraf blev det europæiske træningsnetværk til design og genanvendelse af sjældne jordarter fra motorer og generatorer i hybride og fulde elektriske køretøjer (DEMETER-projektet) oprettet. Formålet med DEMETER-projekt er at kunne evaluere og forbedre af genvindingsveje for REEs i hybrid og fuld elektrisk (H)EV køretøjer. Derudover har det til hensigt at udvikle innovative teknikker til produktion af PM'er og give livscyklusvurderinger og livscyklusudgifter for PM'er med genanvendte REE'er.

Uafhængig af genvindingsmetoden er adskillelse og klassificering af PM-materiale et vigtigt trin for at starte en genvindingsproces. Derfor vil fremskridtene med forbedring af genanvendelsesmetoderne være utilstrækkelige, hvis ikke de elektriske maskiner er konstrueret således, at der er nem adgang til magneterne når motor skrottes. I denne afhandling foreslås der derfor en alternativ motor teknologi der efterfølgende evalueres. Motor teknologien består af en hybrid rotor konstruktion og en modulær stator.

3D Finite Element Metoden (FEM) er blevet brugt til at lave et design der efterfølgende er blevet valideret med målinger fra en fremstillet prototype. Selvom ydelsen af den fremstillede prototype var væsentligt lavere i sammen-

ligning med en Synkron Permanent Magnet maskine med overflade magneter (SPMSM), betragtes det fra genanvendelighedsperspektiv, at den foreslåede struktur har et potentiale, da der ikke skal bruges lim til samlingen af magneterne på rotoren. Derudover tillader fluksens 3D-natur i det magnetiske system brugen af ikke-traditionelle materialer (f.eks. Amorf stål lamineringer, SMC, kornorienteret elektrisk blik osv.). Endelig er der udviklet et energiindeks for at give en kvantitativ evaluering af genanvendeligheden af elektriske maskiner med permanente magneter i forbindelse med e-mobilitet.

ACKNOWLEDGEMENT

I would like to express my gratitude to DEMETER project, for the financial support that allowed the completion of this Ph.D. work. In addition, I would like to thank the DEMETER project team; general coordinator, management support team, researchers, supervisors, and partners for the good work and fun moments. Specially Professor Afef Lebouc, Jean-Marc Dubus, and Early Stage Researchers 9, 11 and 12.

These past years in Denmark have been a fantastic experience, and I am grateful and proud of being part of Aalborg University. Furthermore, I would like to express my appreciation to my supervisors, Professor Peter Omand Rasmussen and Professor Dong Wang for their guidance, support and patience. I am also grateful to Professor Ewen Ritchie, who worked at the beginning of this project before his retirement. In addition, I would like to thank my colleagues at the Energy Technology Department, and the staff, for allowing a smooth, friendly, and peaceful work environment.

Lastly, I would like to thank my family for their support and care.

Denmark, September 2019.

Chapter 1 INTRODUCTION

1.1 BACKGROUND

The development and production of Hybrid and Electrical Vehicles ((H)EVs) have gained significant relevance due to the reduction of the environmental impact related to CO_2 emissions with source in transportation. Part of the successful implementation of (H)EVs is related to the type of electric motor implemented for their propulsion. Permanent Magnet Synchronous Machines (PMSMs) are widely used given their high efficiency, torque and power densities, when compared with other types of machines [1], [2]. The application of PMSMs in (H)EVs is based on two main technological advances:

- The application of Rare Earth Elements (REEs) in the production of Permanent Magnets (PMs) with high energy product (i.e., Samarium Cobalt (SmCo) and Neodymium Iron Boron (NdFeB)).
- The development and implementation of power electronics and motor control techniques.

According to reports on critical raw materials, carried out by the European Commission, REEs are considered to be the most problematic due to the high rate of supply risk [3], [4]. The criticality of REEs was demonstrated in 2011 with the REEs crisis; in that occasion the prices of REEs reached a historical maximum, due to the imposition of exporting quotas by the main producers. Despite the falling prices since 2011, REEs remain listed as critical materials [5]. Moreover, during the REEs crisis of 2011, alternative solutions were evaluated:

- Exploring mines in new locations.
- Developing REE free PMs, with similar energy product as either SmCo, or NdFeB PMs.
- Increasing the recovery of REEs by recycling.

Although deposits of REEs have been explored in Europe, it might take several years before such deposits become operational [6]. On the other hand, car manufacturers have started working toward the reduction of the content of REEs in their PMs [7]. Nevertheless, REEs are still required in order to obtain PMs with a large energy product. Consequently, the recovery of REEs through recycling emerged as a valuable option in order to guarantee the supply of such

materials. Currently, methods applied for recycling REEs (i.e. hydrometallurgical and pyrometallurgical) have both low efficiency and large environmental impact [8], [9]. Hence, it is required to re-think the recycling of PMs in electrical machines, by bringing it to the dimensioning and design stages. Although work has been carried out in the evaluation of the use of recycled PM material in electrical machines [10], the recycling of these materials at a larger scale remains a challenge from both economical and ecological perspectives [11]. The recycling of REEs in PMs have been addressed with two approaches:

- Developing and improving recycling techniques of REEs, making them more efficient and less hazardous for both population and environment.
- Investigating and developing alternative machine topologies which facilitate an efficient recycling of the PMs.

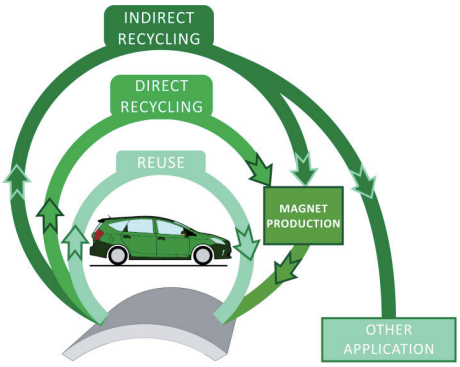

Figure 1.1. Three recycling loops for REEs of PMs in (H)EVs.

Figure 1.1 describes the various recycling loops of PM materials in (H)EVs [3]. These loops may be summarized as follows for a machine which has reached its End of Life (EoL):

- Reuse: The PMs extracted are used directly in a new machine.
- Direct Recycling: The PMs extracted are processed as raw material and manufactured as new PMs to be used in electrical machines for (H)EVs.
- Indirect Recycling: The PMs extracted are processed as raw material and transformed to their basic elements.

The thesis work presented in this report belongs to Work Package 3 (WP3): "Design for Reuse of SmCo and NdFeB Magnet Motors in (H)EVs", part of the European Training Network for the Design and Recycling of Rare-Earth Permanent Magnet Motors and Generators in Hybrid and Full Electric Vehicles (DEMETER) [3].

A large percentage of the market share of NdFeB PMs belongs to motors and generators according to the review presented in [9] and [12]. Therefore, the recycling of REEs requires to be addressed due to the increasing demand of electric vehicles. Such increment on the demand of zero emission vehicles is linked to the environmental policies which main goals are to reduce the emissions of green house gases by making the transition to zero emission vehicles by 2050 in Europe [13].

The recyclability of REEs has been addressed in various reports. For example, in [14], a forecast of the recyclable available material is carried out, showing the potential and the importance of recycling in the development of (H)EVs. In [15] a methodology is developed for the recovery of PMs in electrical machines that have reached the EoL. In [16] and [17] hydrogen is used to separate and recycle NdFeB PMs used in hard disk drives, showing a good efficiency, but at a small scale. New rotor structures are proposed in [18] and [19], in which the PM material is encapsulated in the rotor, facilitating the recovery at the EoL of the machine. However, one disadvantage of the recycling process is that the handling of the PM material should be under a protective atmosphere in order to avoid the oxidation of the recycled powder, thus, increasing the complexity of the overall process. Figure 1.2 illustrates the dismantled rotor used where the PM powder is encapsulated in a metallic container. Additionally, the reuse of the PMs is evaluated in a wind power generator study case, in which the poles are formed with PMs of smaller size in a "LEGO" like structure [20]. However, such approach might not result convenient due to the large amount of air-gaps between PMs which might affect the resulting air-gap remanence and posing difficulties if very accurate tolerances are required. Additionally, the reuse of PMs might not be convenient since both the magnetic and mechanical properties of the PMs after their use, might be subjected to degradation (i.e. demagnetization, corrosion, etc.). Regarding the specific case of recyclable electrical machines in (H)EVs, in [21] a claw-pole TFM topology is proposed. Using Soft Magnetic Composites (SMC) in both the stator and rotor structures and a SmCo PM ring, such structure was expected to facilitate the recovery of the PM material at the EoL. Figure 1.3 depicts the geometry of the machine structure. Finally, and most recently, a claw-pole machine is proposed in which the PMs are inserted in the structure of the rotor. The structure have been conceived in such fashion that the direct reuse would be possible [22]. The structure proposed is illustrated in Figure 1.4.

Figure 1.2. Dismantled rotor container [18].

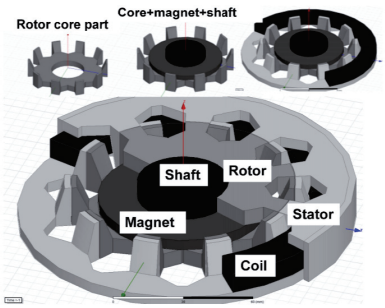

Figure 1.3. Claw-pole TFM SMC machine [21].

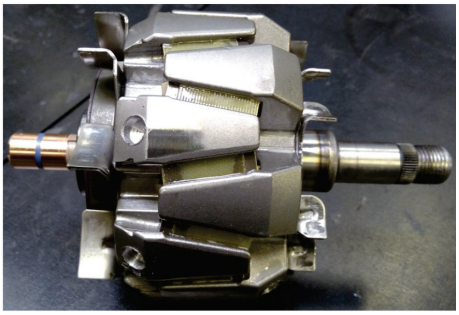

Figure 1.4. Rotor of a claw pole machine, conceived for reuse of PMs [22].

1.2 INTRODUCTION TO THE STATE OF THE ART

1.2.1 REVIEW OF ELECTRICAL MACHINES IN (H)EVS

Machines designed for traction applications, shall fulfil the following main design and performance characteristics [23], [24]:

- High torque and power densities.
- High torque at starting, low speed and climbing. High power for high-speed cruising.
- Wide speed range with a constant power speed range of around 3 to 4 times the base speed. A good ratio between the peak torque and the nominal power supplied by the inverter (i.e. power factor).

- High efficiency over both the speed and torque ranges including low torque operations.
- High instantaneous overload capacity. Generally, 200%.
- High reliability and robustness appropriate to the vehicle environment.
- Acceptable costs.

In addition to the aforementioned characteristics, and according to what is proposed in this thesis, the PMs used in the machine should be easily recyclable at the EoL. Figure 1.5 shows the three main types of machine found predominantly in the market of (H)EVs [25], [26]:

- Induction Machine.
- Interior Permanent Magnet machine.
- Synchronous machine (i.e. rotor wounded).

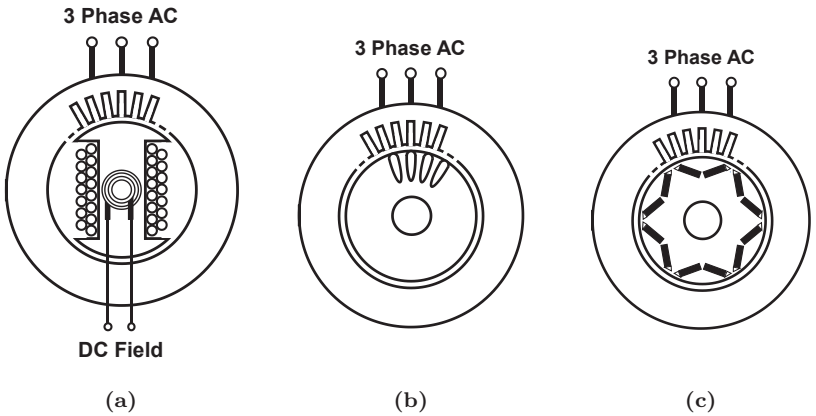

Figure 1.5. Machine topologies found in (H)EVs, (a) synchronous, (b) induction, and (c) interior permanent magnet [27].

The advantages of each machine over another have been subject of extensive investigation and may be found in the literature proposed in this work [23], [2], [28]. Furthermore, synchronous, induction, and interior permanent magnet machines are out of the scope of this thesis, the main reasons:

- All of the three types of machines are of radial field operation principle.
- PM material is not required by both induction, and synchronous machines.
- Interior permanent magnet machines are not ideal for recycling, since the PMs are "buried" in the rotor, restraining their recovery at the EoL.

Therefore, further description of the advantages and disadvantages, and working principles, of each type of machine are not included in this document. The fact that electrical machines with 3D-flux paths are not widespread in (H)EVs is consequence of technical challenges. Further discussion on machines with 3D-flux paths will be presented in coming sections, since it is considered that there is potential for their study in the context of (H)EVs.

1.2.2 TRANSVERSE FLUX MACHINE (TFM)

This type of machine was first proposed in the 80's [29]. Though different variants have been developed, all of them work under the same principle: a toroidal shaped coil producing a Magneto Motive Force (MMF) in the air-gap. This MMF is modulated by a combination of stator poles interacting with PMs placed on the rotor. The number of stator poles is usually half of the number of rotor poles, and it is much higher than conventional PM machines.

Such topology allows the increment of the number of poles without reducing the MMF distribution per pole. In this regard, the TFM is similar to claw-pole topologies, having up to three times higher torque density than conventional PM machines [30]. Therefore, TFMs are excellent candidates for applications that require low speed and high torque (e.g. wind turbines, ship propulsion systems, etc.). Additionally, applications where there are limitations of size and space. Although many variants of the TFM have been proposed, there is no report of commercial production. Furthermore, TFM have disadvantages to overcome. Some of them are listed as follows:

- High complex construction.
- Requires in most of the cases a true 3D-flux structure, only possible to achieve with SMC materials [31].
- Low power factor, due to a high amount of leakage which is basically translated to an oversized converter [32], [33].

Variations of the TFM topologies include the Surface Mounted Transverse Flux Machine (SMTFM), Flux Concentrated Surface Mounted Transverse Flux Machine (FCSMTFM). In addition, TFMs might not include PMs in the rotor, in which case the Transverse Flux Reluctance Machine (TFRM) have similar features as a Switched Reluctance Machine (SRM) [34].
Regarding the construction of the stator, it might have a single or double sided construction as it is shown in Figures 1.6a and 1.6b. In the case of a TFM with permanent magnets the rotor may be of surface mounted topology or with buried PMs. In either of the cases, TFMs shall have two or more phases form-

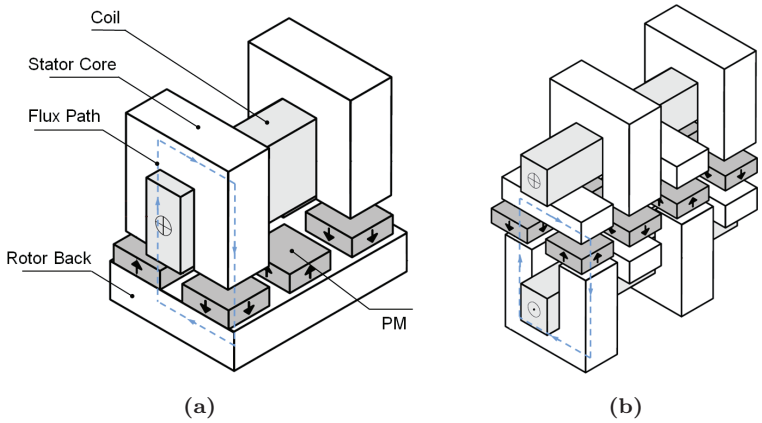

Figure 1.6. Basic topologies of a TFM, (a) single sided SMTFM, (b) double sided SMTFM [35].

ing a stacked structure in order to produce a starting torque. Consequently, increasing their complexity during the manufacturing process.

1.2.3 AXIAL FLUX MACHINE (AFM)

The earliest AFMs were reported in the 19th century. In theory, any conventional radial flux machine should have its counterpart in an axial version [36]. Generally, AFMs may be divided into two major groups: single-sided and double sided, and the stator may have several variants as well as the topology of the rotor. In [37] and [38] extensive reviews of this type of machines are carried out. However, the description done in [36] is fair enough for an introduction to what is intended in this work. When compared with conventional radial flux PM machines, some advantages may be identified as:

- The air-gap of AFMs is planar and adjustable to some extent.
- Higher power density design capabilities with savings in core materials [39].
- AFMs are ideal for designing in a modular approach.

In Table 1.1 some of the topologies of AFMs are summarized. Additionally, in Figure 1.7 each topology is described. Special attention shall be paid to AFM topologies, since the work presented in this document is based on the structure illustrated in Figure 1.7f. The principle of operation will be described in coming sections.

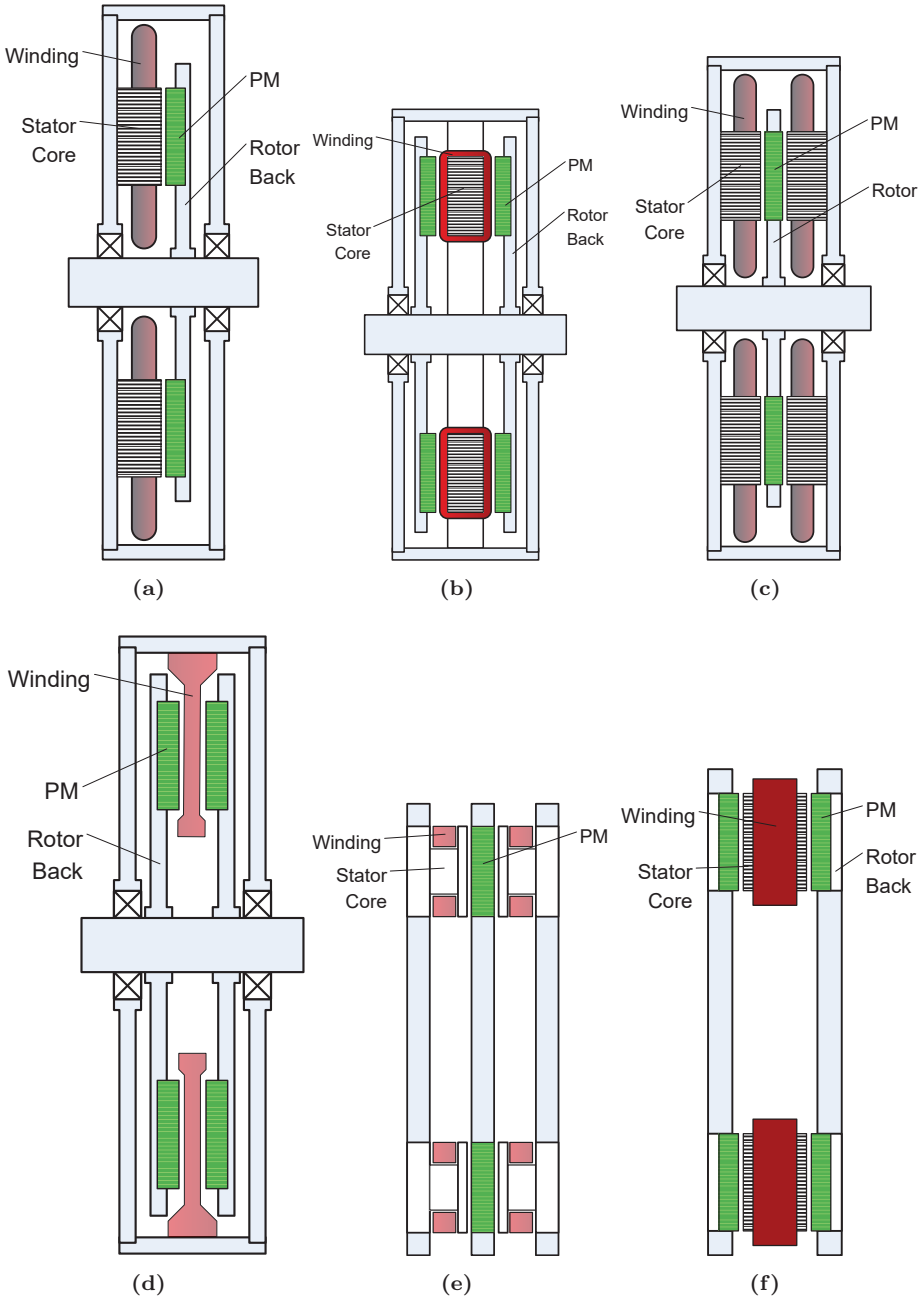

Figure 1.7. Main topologies of AFMs, (a) Single sided slotted, (b) double sided slot-less, (c) double sided slotted, (d) double sided core-less, (e) double sided external salient pole stator and internal rotor, (f) double sided internal salient pole stator and external twin rotor.

Topology	Variant	Sub-variant
Single-sided		Slotted stator
		Slot-less stator
		Salient-pole stator
Double-sided	Internal stator	Slotted stator
		Slot-less stator
		Iron core stator
		Core-less stator
		No rotor/stator cores
		Salient-pole stator
	Internal rotor	Slotted stator
		Slot-less stator
		Salient-pole stator

Table 1.1. Summary of AFM topologies.

Although the widespread of this type of machines have been slow [37], [40], in recent years, there has been an increment in the production of this type of machines for traction applications. Some examples of companies specialized on the production of AFMs are: YASA e-motors [41], MAGNAX yokeless AFMs [42] and EMRAX innovative e-motors [43].

1.2.4 THE HYBRID STEPPER MOTOR (HSM)

The term hybrid given to this type of stepper motor is the result of the working principle which combines both PM and variable reluctance machines. Hence, the rotor structure is composed by an axially magnetized ring or disk and a toothed structure which resembles a variable reluctance machine. The PM is placed in the rotor, between two laminated stacks, which are generally made of electrical sheet as shown in Figure 1.8. Although two and four phases are the most widely spread configurations for this type of machine, the three and five phases structures are also used. In any case, the constructive structure of the rotor has basically no difference independent of the number of phases.

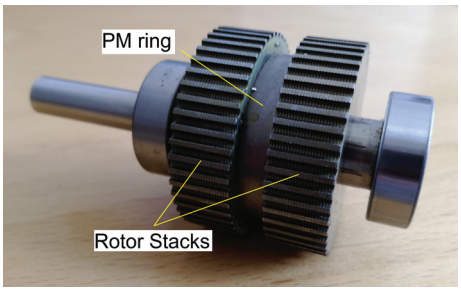

Figure 1.8. Rotor of a HSM.

As it is observed in Figure 1.9a, there is an axial direction of the flux produced in the rotor, which makes the HSM a machine with 3D-flux paths, although the flux in the stator is still of radial nature. The working principle of the HSM is as follows; if phase X in figure 1.9b is energized, the coils X and X' will generate south and north polarity respectively. Consequently, the north polarized stack will rotate for aligning with coil X, and the south polarized rotor stack will rotate for aligning with coil X'. Once the alignment is achieved, the torque produced by the current applied to phase X will be zero, and then it will be necessary to energize the remaining phases of the machine. A complete rotation is then achieved by energizing both phases X and Y in the required sequence.

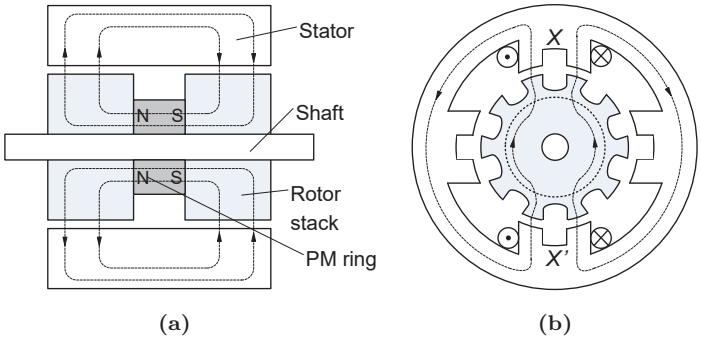

Figure 1.9. Magnetic paths in the HSM, (a) flux produced by the PM in the rotor, (b) flux produced by the currents in the stator [44].

1.3 MAGNETIC MATERIALS IN ELECTRICAL MACHINES

Magnetic losses may be divided into two main components: hysteresis losses and eddy current losses. The former are due to the movement of the ferromagnetic domains when these align with the time changing flux. The latter, are generated by the changing flux circulating in the material. Eddy currents are the main reason for using laminations in the magnetic systems of most electrical machines (e.g., transformers, motors, actuators, etc.). Figure 1.10 shows the behaviour of both hysteresis and eddy current losses with frequency. It shows, that hysteresis losses vary linearly with the frequency, whereas eddy current losses vary approximately with the frequency squared. Consequently, magnetic losses might get to be dominant at high frequencies.

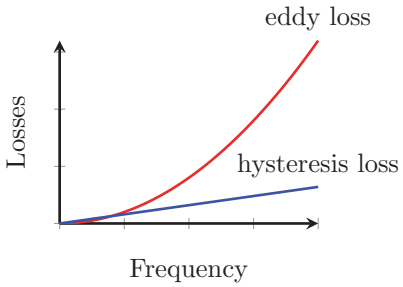

Figure 1.10. Rise in magnetic loss with frequency.

In order to reduce the losses due to eddy currents, the laminations are required either to be as thin as possible, to have a large resistivity or both. In electrical machines there are various materials for the design of the magnetic systems. Figure 1.11 describes some of them. From the conventional Silicon Iron (SiFe) electrical sheets with Oriented and Non-Oriented Grains (GO and NO). The list continues with Nickel Irons (NiFe), Cobalt Irons (CoFe), composite materials, microcrystalline alloys and amorphous metals.

Amorphous Metals

In addition to the reduction of the losses as a goal in the design of electrical machines, the increment of the permeability is of interest. Given that permeability indicates the magnetization level in any material. A large value of permeability is achieved by the increment of the perfect crystal orientation and the purity of the metals used. In addition, when a metallic alloy is cooled at a rate of millions of degrees Celsius per second, the material becomes solid without the presence of crystallization. Hence, energy minimization associated with regular crystal formation in the atoms does not take place. The resulting structure

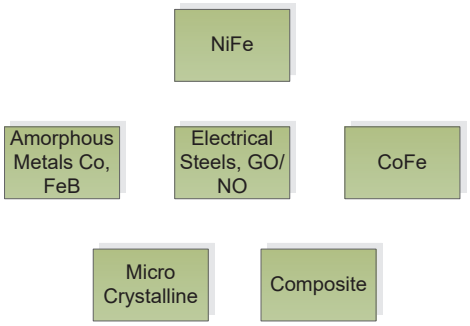

Figure 1.11. Niche applications of soft magnetic materials [45].

may be compared with ordinary glass which is an unstable structure able to form crystals under appropriate conditions. In addition, due to the rapid cooling of the material, the formation of the nucleation centres is avoided. From a macroscopic point of view, the material is isotropic, which means that the material may be magnetized in any direction. Figures 1.12a, 1.12b and 1.12c describe both the process of manufacturing amorphous materials and the final products, respectively. Amorphous materials for applications in electrical machines are alloys composed mainly by Iron, with the addition of materials such as Silicon, Boron, Manganese and Carbon.

The superior properties of amorphous metal arise from the thinness (e.g. 25 μm) and high electrical resistivity of the alloy (e.g. over 100 $\mu\Omega$·cm), which restrains eddy currents [46]. Additionally, domain walls can move freely through the random atomic structure. The rapid cooling results in a strip which is highly stressed and requires a stress-relief anneal. A low temperature of approximately 250 degrees Celsius, must be used to avoid destructive crystallization of the metal. Magnetic losses in amorphous alloys are around 1/3 of those for grain-oriented electrical sheet. However, the cost of production and the problems of handling it and avoiding compressive stress, limit its widespread use for large machines. Figure 1.13 shows the comparison of the BH curves for both standard electrical sheet and amorphous metals. Note that a logarithmic scale was necessary in order to evaluate its behaviour at low values of H. It is important to highlight that the saturation value of amorphous materials is lower in comparison to the electrical sheet. Which yields a reduction on the performance of the machine, as it will be shown in coming sections of this thesis report.

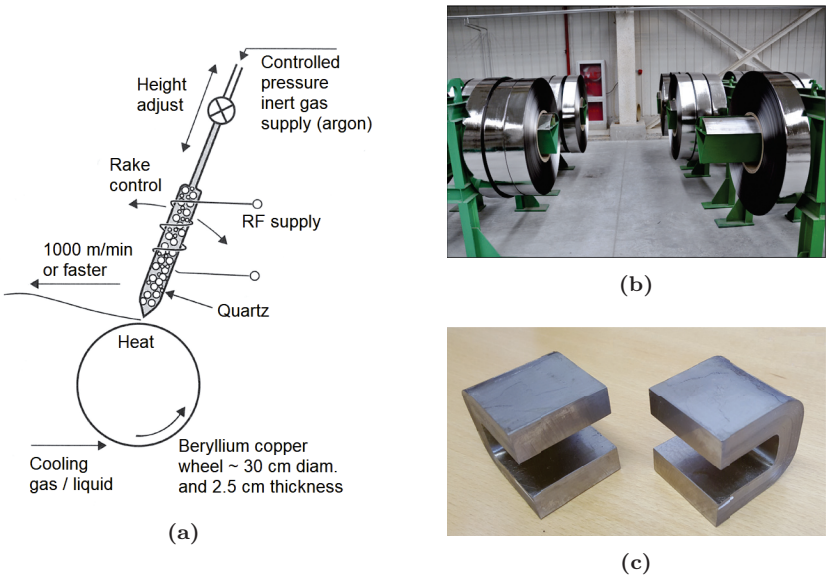

Figure 1.12. Amorphous metals, (a) melt-spinning diagram for the production [46], (b) final product: ribbon [47], (c) final C-shaped cores.

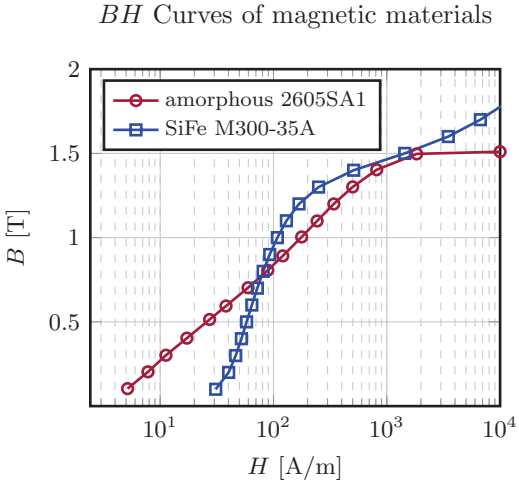

Figure 1.13. BH curves of electrical sheet and amorphous materials.

Review of the Implementation of Amorphous Materials in Electrical Machines

Although the use of amorphous metals in electrical machines is not widespread, various studies of machines implementing such material have been found in the literature. For example, a prototype of an induction motor was developed in [48]. The stator was build with amorphous laminations as it is shown in Figure 1.14. A comparison of the no-load losses is performed with standard electrical sheet. Additionally, in [49] an experimental evaluation of an IPM prototype is performed. Such prototype implements amorphous laminations in a segmented stator, as it is illustrated in Figure 1.15. Similarly, a comparison of the iron losses between standard and amorphous laminations is performed in [50] on a prototype of an IPM machine, the stator built with laminated amorphous material is shown in 1.16. Finally, in [51] a Surface Permanent Magnet Synchronous Motor (SPMSM) was built. The evaluation of the iron losses in three different materials, including amorphous alloys, is performed in a machine with a modular teeth structure. Figure 1.17 shows the stator structure used in this type of machine.

Figure 1.14. Stator made of amorphous laminations [48].

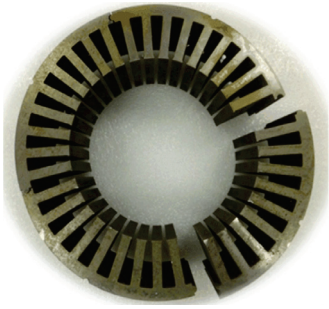

Figure 1.15. Modular teeth stator structure [49].

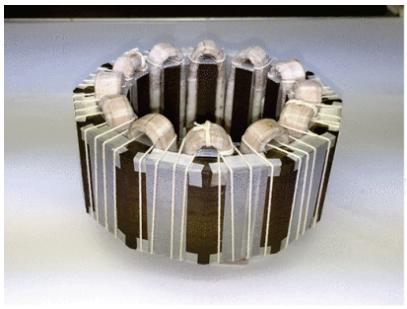

Figure 1.16. Stator made of amorphous laminations [50].

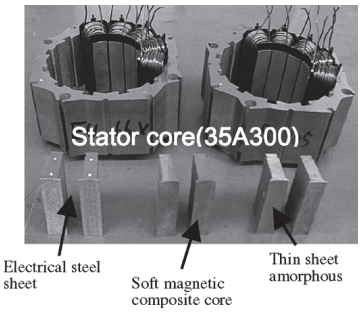

Figure 1.17. Segmented stator made of amorphous laminations [51].

Amorphous laminated materials have been also evaluated in machines with 3D-flux paths. In [52] an AFM was constructed and tested. In addition to the evaluation of the iron losses implementing amorphous materials, a new approach in the manufacturing of the rotor is proposed by using water-jet cutting. Figure 1.18 shows the structure of the stator, uncut 1.18a and after the cutting process 1.18b. An additional approach, with AFMs is proposed in [53]. The prototype tested is built with wounded amorphous modules, as shown in Figure 1.19. Finally, a segment of a claw-pole TFM rotor structure was developed and studied in [54]. Such machine implements C-shaped cores made of laminated amorphous material in conjunction with SMC in order to complete the claw structure. A comparison between standard electrical sheet and amorphous laminations is carried out. The measurement of the no-load losses was performed to one pole pair in the stator, which is shown in Figure 1.20.

(a) **(b)**

Figure 1.18. AFM rotor structure; (a) uncut, (b) cut [52].

Figure 1.19. AFM with wounded amorphous stator cores [53].

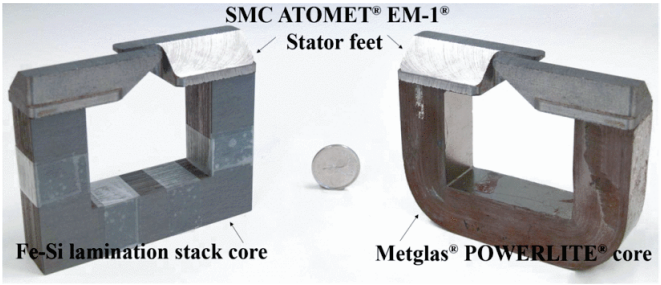

Figure 1.20. Modular stator pieces of a claw-pole TFM [54].

The review on electrical machines developed, confirms that there has been relevant work on the evaluation of amorphous materials in electrical machines. Furthermore, its beneficial low level of iron losses have been demonstrated with experimental results in most of the publications described above and summarized in Table 1.2. In contrast, it is shown that its implementation is challenging from the manufacturing and assembling perspectives (i.e. cutting, punching, annealing). Therefore, there is still work to be carried out in finding alternatives in order to deal with the mechanical challenges that amorphous laminations have.

1.4 PROPOSED STRUCTURE OF A 3D-FLUX MACHINE

The machine proposed in this thesis may be summarized with the following analysis: if one coil of the AFM machine in Figure 1.7f is taken, the section in Figure 1.21a is obtained. Then, if the iron core is stretched as in Figure 1.21b, it will be long enough to be bended as in Figure 1.21c. Then the axial air-gap has been changed to a radial air-gap as in Figure 1.21d. The result is a stator

Reference	Type of Machine	Power [kW]	Results
[48]	IM	0.88	Max. reduction by a factor of 6.8 compared to electrical sheet.
[49]	IPM	20	Max. reduction by a factor of 1.8 compared to electrical sheet.
[50]	IPM	Not specified	Max. reduction by a factor of 2 compared to electrical sheet.
[51]	SPMSM	0.4	Max. reduction by a factor of 2 compared with electrical steel.
[52]	AFM	1.5	-
[53]	AFM	0.2	-
[54]	TFM	-	Max. reduction by a factor of 11, compared with electrical steel.

Table 1.2. Summary of research on amorphous materials in electrical machines.

with a convenient C shape. Thus, allowing the implementation of a modular stator, and the use of C-shaped cores. The geometry may be further extended for using two C-shaped cores as in Figure 1.21e obtaining a stator structure similar to the E-core TFM [34] [55]. Additionally, the SM rotor structure may be modified as in Figure 1.22 to obtain a rotor structure which resembles the HSM rotor.

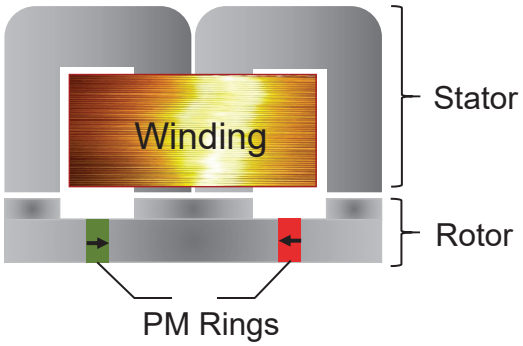

Figure 1.22. Hybrid rotor topology.

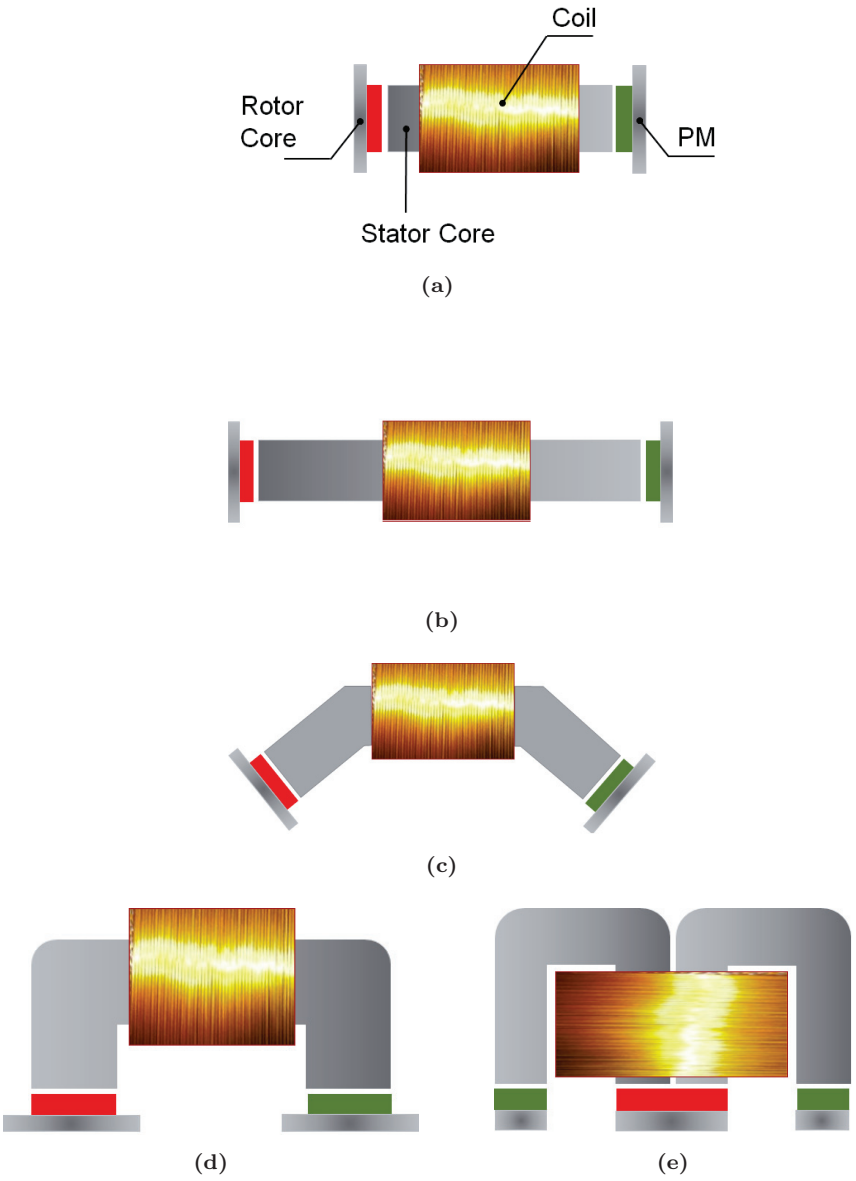

Figure 1.21. Proposed machine geometry, (a) section of an AFM, (b) stator core stretched, (c) stator core bended, (d) C-shaped stator core and (e) C-shaped stator final approximation.

The recyclability of PMs is expected to be improved by adopting a stator with a modular structure. The development of stator with modular structures have been investigated in [56], [55], [57]. On the other hand, the use of amorphous laminations will allow to have a machine with a high pole count, which is ideal in order to improve the torque production. The use of laminated amorphous C-shaped cores have been investigated in a simulation study of a linear machine in [58] and the experimental evaluation of a claw-pole TFM in [54]. This thesis will focus on the topologies presented in Figures 1.21e and 1.22, exploring their main advantages and disadvantages. In addition, the definition of two demonstrators for prototyping will be carried out in coming chapters.

1.5 OBJECTIVES AND LIMITATIONS OF THE PROJECT

The main objectives and limitations are presented in this section. The work has been carried out around the definition of a PM machine with 3D-flux paths which allows both the efficient extraction of the PMs and the use of non-traditional materials. In addition, validations of the models developed with the Finite Element Method (FEM) are performed with the experimental evaluation of a prototype. Finally, the definition of a methodology for evaluation of recyclability of PMs in electrical machines has been developed.

1.5.1 OBJECTIVES

The main objectives of this thesis may be summarized as follows:

1. Studying the advantages of using non-traditional materials, in electrical machines for use in (H)EVs.
2. Evaluating the possibility of using non-traditional materials in conjunction with the recyclability of the PMs.
3. Designing electrical machines for (H)EVs, allowing recyclability of the PMs and using non-traditional materials.
4. Defining, manufacturing and testing of a machine prototype.

1.5.2 LIMITATIONS

This project is limited to the definition and study of an alternative machine with 3D-flux paths based on existing topologies (i.e. AFMs, TFMs and HSMs). Such machine is required to comply with recyclability feasibility and shall account for the use of non-traditional materials. The recyclability feasibility is

evaluated by developing a recycling index which allows to quantify the recyclability of PMs in electrical machines for (H)EVs. In addition, the term "non-traditional materials" might cover a wide range of materials. Initially, two non-traditional materials were considered as possible candidates: SMC and iron based laminated amorphous material. SMC materials were discarded at early stages of this work due to previous un-successful attempts of using them. Initially, in 2004 in a TFM [59] and in 2016 in a motor integrated magnetic gear [60]. In both projects, poor mechanical properties were identified. Hence, an electrical machine with a modular stator made of C-shaped cores of laminated amorphous material is proposed.

1.6 MOTIVATION

The successful electrification of the transportation in order to reduce CO_2 emissions depends largely on the production of electric vehicles and consequently, the production of electrical machines. Therefore, in order to secure the supply of critical materials such as REEs for the production of PMs, it is required to explore the existing recycling technologies. However, as it was explained in the introduction, it is not enough with the development of large scale recycling processes. It is also required to facilitate the access to PMs in electrical machines once the vehicle has reached its EoL. That is, the development of innovative electrical machine topologies which make recyclability an efficient process.

1.7 OUTLINE OF THE THESIS

The remainder of the thesis report presented here has the following outline:

Chapter 1: Introduction

In this first Chapter a brief review of the recycling of PMs in electrical machines was presented. In addition, an initial introduction to various types of machines with 3D-flux paths was included. Furthermore, a description of the properties of amorphous alloys was carried out along with a review of the use of amorphous materials in electrical machines. Finally, an alternative of a 3D-flux machine was proposed, based on the TFM, AFM and HSM topologies. The main objectives and motivation were also introduced.

Chapter 2: A Surface Mounted 3D-Flux PM Machine

In this chapter the study of a SPMSM machine with 3D-flux paths is performed. A preliminary dimensioning and definition is carried out through sensitivity

analyses. Both 2D and 3D-FEM models are developed in order to evaluate various parameters. In addition, a characterization of the iron losses in amorphous laminated materials is performed. Afterwards, a demonstrator was built and measurements of various parameters such as back-EMF, iron losses, no-load losses, PM losses, etc., are investigated. Finally, the models developed are validated with measurements.

Chapter 3: Hybrid Rotor 3D-Flux PM Machine

After the work on the surface mounted rotor was developed, an alternative rotor is defined and investigated. Similarly to Chapter 2, sensitivity analyses and calculations with FEM are carried out. The main dimensions of a hybrid rotor 3D-flux machine are proposed for manufacturing a final prototype. This chapter includes both the measurements and the calculated values with the models developed throughout this project.

Chapter 4: Recyclability Evaluation of PMs in Electrical Machines

The definition of a methodology for evaluation of the recyclability of PMs in electrical machines, is proposed and discussed in this chapter. Such definition was required in order to perform a quantitative evaluation of the recyclability potential of the machines designed within WP3 of DEMETER project. The recyclability of PMs in electrical machines was addressed from two perspectives; an assembly and disassembly approach and an energy consumption approach. The former, was based on the Failure Mode and Effect Analysis (FMEA). The latter, based on the evaluation of the energy consumption of the machine through its life time. The energy consumption investigation was performed on the hybrid rotor 3D-flux machine developed in Chapter 3.

Chapter 5: Conclusion

Lastly, the results obtained are discussed in this chapter. Additionally, conclusions are drawn and future work is proposed.

1.7.1 PUBLICATIONS

Dissemination of the findings of this research work was carried out through oral presentations and poster sessions in international conferences. Both publications as first author and co-author are listed in chronological order.

P1 A. G. Gonzalez, J. Millinger and J. Soulard. "Magnet losses in inverter-fed two-pole PM machines". In: *2016 XXII International Conference on Electrical Machines (ICEM)*. Sept. 2016, p.p. 1854-1860.

P2 A. G. Gonzalez, A. K. Jha, Z. Li, P. Upadhayay and P. Rasmussen. "Validation of Efficiency Maps of an Outer Rotor Surface Mounted Permanent Magnet Machine for Evaluation of Recyclability of Magnets". In: *2018 IEEE International Magnetic Conference (INTERMAG)*. April 2018.

P3 A. K. Jha, Z. Li, A. Garcia, P. Upadhayay, P. O. Rasmussen, A. Kedous-Lebouc and L. Garbuio. "Weighted Index of Recycling and Energy (WIRE) Cost for Motors in Electric Vehicles". In: *2018 International Symposium on Power Electronics, Electrical Drives, Automation and Motion (SPEEDAM)*. June 2018. p.p. 407-412.

P4 P. Upadhayay, A. G. Garcia, Z. Li, A. K. Jha, P. O. Rasmussen, A. Kedous-Lebouc and J. Mipo. "Evaluation of Energy Cost Index for an Electric Vehicle Motor Over a Particular Drive Cycle with Recycled Magnet Concept". In: *2018 XIII International Conference on Electrical Machines (ICEM)*. Sept. 2018. p.p. 738-744.

P5 A. G. Gonzalez, W. Dong and P. O. Rasmussen. "Investigation of a Surface Mounted PM Machine Concept with 3D-Flux Paths, Modular Stator and Amorphous Material". In: *2019 International Electric Machines and Drives Conference (IEMDC)*. May. 2019.

P6 A. G. Gonzalez, W. Dong, J. M. Dubus, and P. O. Rasmussen. "Design and Experimental Investigation of a Machine with 3D Flux Paths, Accounting for Recyclability of Permanent Magnets". Paper to be submitted to IEEE access.

Chapter 2 A SURFACE MOUNTED 3D-FLUX PM MACHINE

In this chapter an initial approach to the dimensioning of a Surface Mounted 3D-Flux machine (SM3D) is carried out. In order to obtain the initial dimensions, analytical calculations were performed with models available in the literature. Afterwards, both 2D and 3D models of the machine were built and FEM calculations were carried out in order to estimate values of torque, inductance, permanent magnet flux, among others. Additionally, sensitivity analyses were performed in order to evaluate the performance of the machine with variation of some key dimensions. At the end a demonstrator was built and some parameters were measured allowing the validation of the models developed.

2.1 ANALYTICAL APPROACH AND WORKING PRINCIPLE

2.1.1 CONSTRUCTION OF THE RELUCTANCE NETWORK

A simplified reluctance network of the SM3D machine is described in the following. The importance of this step is that it allows preliminary calculations of parameters such as PM flux and inductance. Initially, the geometry corresponding to a single module and a portion of the rotor are depicted in Figure 2.1. Such geometry differs from the geometry described in Section 1.4 in that the rotor is composed by a solid cylinder, allowing a returning path for the PMs flux. A simplified reluctance network for the calculation of the PM flux is shown in Figure 2.2. As it might be noticed, some components of the reluctance network are neglected. For example, the reluctance path followed by the PM leakage between PMs and between PMs and the rotor back.
Generally, the material of both the rotor back and the stator modules have a large value of relative permeability. In addition, such materials have a nonlinear characteristic. Therefore, in order to facilitate an analytical approximation for the calculation on the PM flux, the reluctances corresponding to these regions might be neglected (i.e. $\mathcal{R}_{rot1}$, $\mathcal{R}_{rot2}$, $\mathcal{R}_{rot3}$, $\mathcal{R}_{leg1}$, $\mathcal{R}_{leg2}$, $\mathcal{R}_{back1}$ and $\mathcal{R}_{lkg}$). Consequently, the reluctance network shown in Figure 2.2, might be further simplified to the magnetic circuit in Figure 2.3. Hence, the calculation of the PM flux Ψ_m is reduced to the following expression:

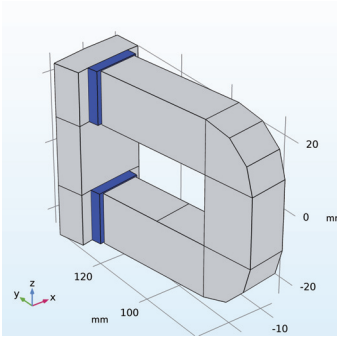

Figure 2.1. Simplified SM3D geometry.

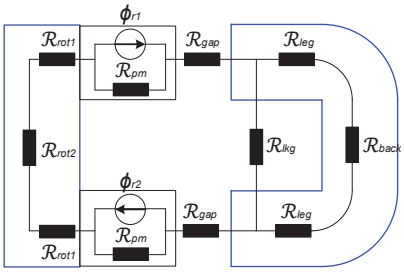

Figure 2.2. Simplified reluctance network of the SM3D.

$$\Psi_m = \frac{\phi_r \mathcal{R}_{PM}}{\mathcal{R}_{PM} + \mathcal{R}_{gap}} \tag{2.1}$$

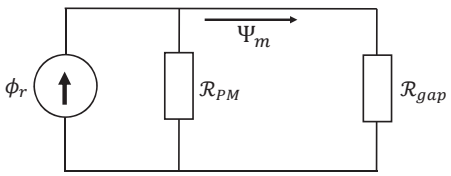

Figure 2.3. Simplified equivalent circuit of the SM topology.

Where ϕ_r, $\mathcal{R}_{PM}$ and $\mathcal{R}_{gap}$ are given by:

$$\phi_r = B_r A_m, \quad \mathcal{R}_{PM} = \frac{l_m}{\mu_{PM}\mu_0 A_m} \quad \text{and} \quad \mathcal{R}_{gap} = \frac{l_g}{\mu_0 A_g} \tag{2.2}$$

With B_r as the remanence of the PMs, $A_m = w_m h_m$ is the surface area of the PM and l_m is the PM thickness. In Figure 2.4, the PM dimensions are shown, with the PM geometry simplified as a rectangular solid.
The reluctance network for the calculation of the inductance is shown in Figure 2.5. The contribution of the PM flux is neglected, consequently ϕ_r has been extracted from the magnetic circuit in Figure 2.2. On the other hand, the contribution of the MMF of the coils in inserted in the circuit.
The self inductance is given by the ratio of the flux linked by the coil and the current that is producing it, that is:

$$L = \frac{\lambda}{I} \tag{2.3}$$

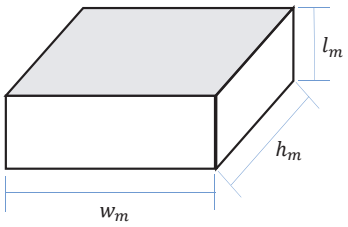

Figure 2.4. Main PM dimensions.

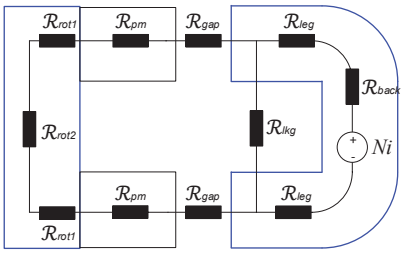

Figure 2.5. Reluctance network for the calculation of the inductance.

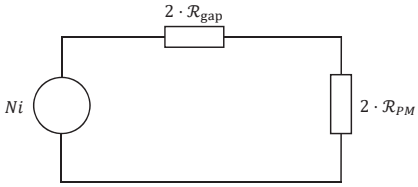

Figure 2.6. Simplified circuit of the SM3D.

Where $\lambda = N\phi$, with N the number of turns in the winding. Since $\phi = NI/\mathcal{R}$, then (2.3) becomes:

$$L = \frac{N^2}{\mathcal{R}} \tag{2.4}$$

The approaches presented so far allow a rough estimation of the PM flux linkage and inductance. Both approximations are assuming lineal materials with a high permeability, that is, the non-linearity of the magnetic materials in both the stator and rotor are disregarded. Consequently, in order to account for the non-linearity of the materials and to perform an accurate calculation of such parameters FEM models are required. Nonetheless, a comparison between the analytical models developed so far with 2D-FEM calculations is performed in 2.3.1.

2.1.2 DESCRIPTION OF THE WORKING PRINCIPLE

In order to give an overview on the working principle of the SM3D machine, a preliminary 3D-FEM model was built. It consists of a single module as it is shown in Figure 2.7. When the PMs of the rotor are aligned with the stator module, as in Figure 2.7a a maximum PM flux Ψ_m is reached. If the rotor is moving clockwise, the position described in Figure 2.7b is reached, and there is virtually no PM flux linking flowing throw the stator module, hence Ψ_m is zero. If the rotor continues moving in the same direction, the position described in Figure 2.7c is obtained. Hence Ψ_m has a minimum value. The behaviour of Ψ_m is depicted in Figure 2.8. Thus, the SM3D machine may be driven simply as any PM machine with sinusoidal flux linkage/back-EMF.

The working principle is extended to a 3-phase topology. Therefore, the model of a machine with 21 stator modules and 28 poles is presented in Figures 2.9 and 2.10. Although the rotor configuration is different in both cases, the behaviour of the PM flux is similar. Furthermore, an initial calculation of the values of PM flux Ψ_m showed a deviation of approximately 1.6%. The results are included in Table 2.1. Where the geometry described in Figures 2.9 and 2.10 have been defined as solid and divided rotor back respectively.

Similarly to the working principle for a single module, the PM flux paths are estimated in the 3-phase configuration. As it is observed, the flux main paths are concentrated in the top and bottom regions of the rotor, where the PMs are located, and the flux linking from the PMs of the top and the bottom regions is minimum. Which explain the low deviation between the values calculated in Table 2.1.

Geometry	Value [mWb]
Solid rotor back	4.50
Divided rotor back	4.57

Table 2.1. Calculated PM flux of the SM3D machine.

The study is extended to investigate the flux linked by the MMF generated by the current in the windings. A current is applied to the winding in the middle module or phase *b*. Additionally, the permanent magnet remanence was set as zero. The results for both geometries are depicted in Figures 2.11 and 2.12. As it is observed, the flux generated by the MMF of the winding describes a different path when contrasted to the PM flux. In order to quantify the difference between the two geometries, the flux linked by the coils λ_a, λ_b,

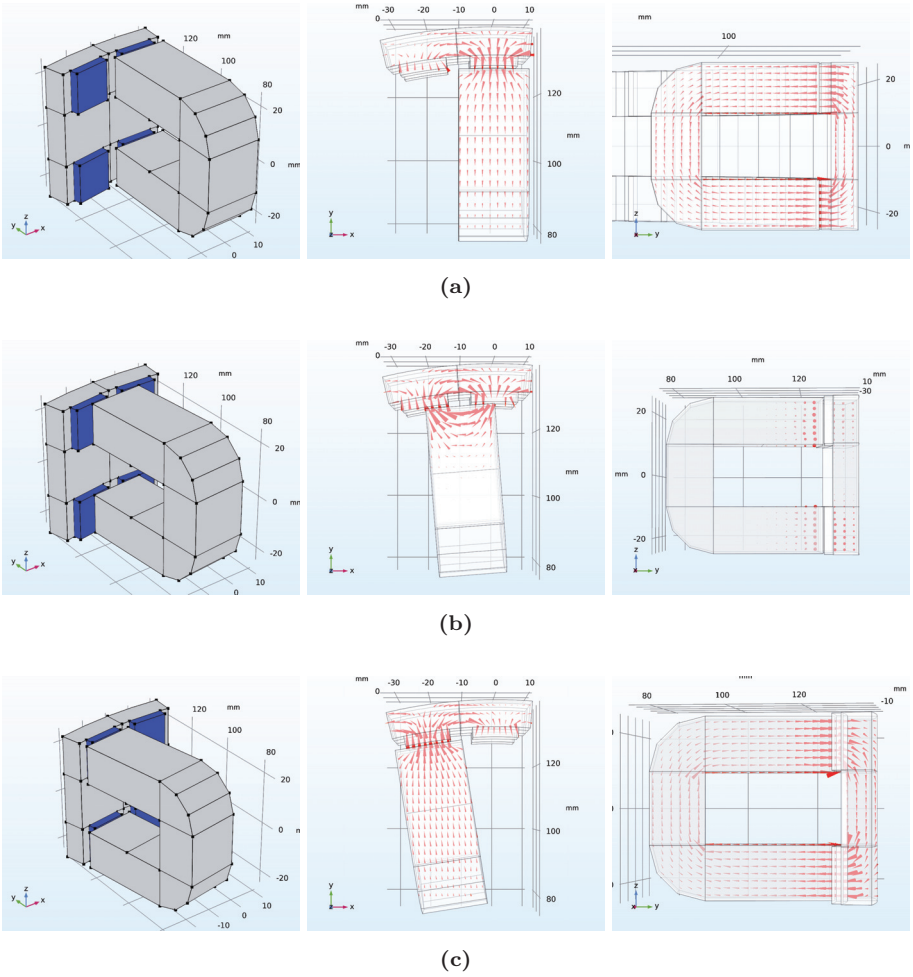

Figure 2.7. SM3D machine principle, isometric view, xy-plane view and yz-plane, (a) at maximum, (b) zero, and (c) minimum positions.

and λ_c was calculated. The results are presented in Table 2.2. The largest difference is present in the adjacent phases a and c. Which is clear since with the modification the axial path of the flux in the rotor in Figure 2.11a is eliminated, therefore, the flux finds its way of circulating through the remaining phases, which in turn represents an increment in the mutual inductance of the system. At this preliminary stage, the machine with the divided rotor back is selected. It will be demonstrated that the division of the rotor back into two regions allows the simplification of the magnetic system to a 2D model.

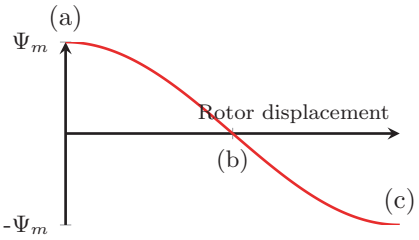

Figure 2.8. PM flux linkage distribution of the SM3D machine.

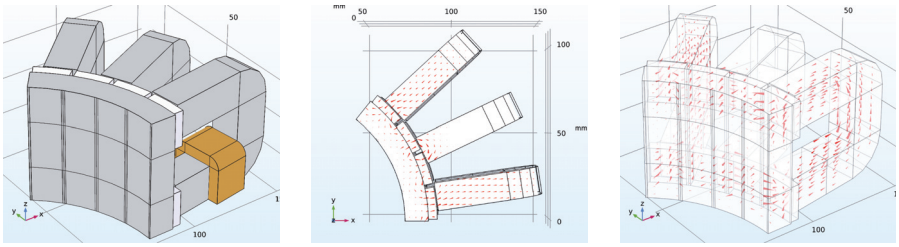

(a) (b) (c)

Figure 2.9. SM3D machine with 21 stator modules and 28 poles, solid rotor back.

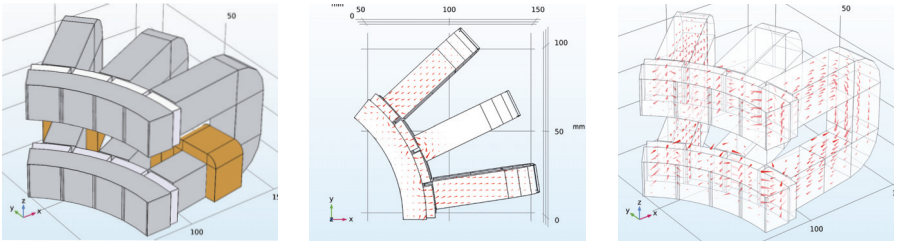

(a) (b) (c)

Figure 2.10. SM3D machine with 21 stator modules and 28 poles, divided rotor back.

2.2 DIMENSIONING OF THE SM3D MACHINE

As a start, the specification of a machine for application on (H)EVs was followed. Some of the requirements are listed in Table 2.3.

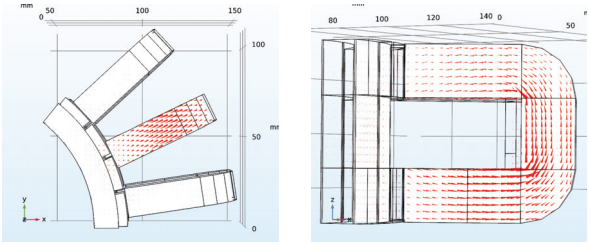

(a) **(b)**

Figure 2.11. SM3D machine with 21 stator modules and 28 poles, solid rotor back MMF flux distribution.

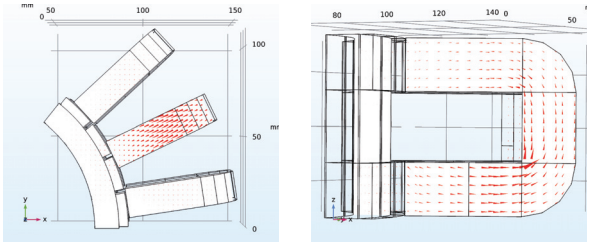

(a) **(b)**

Figure 2.12. SM3D machine with 21 stator modules and 28 poles, divided solid rotor back MMF flux distribution.

Geometry	λ_a [mWb]	λ_b [mWb]	λ_c [mWb]
Solid rotor back	-0.11	0.64	-0.11
Divided rotor back	-0.15	0.60	-0.15

Table 2.2. Flux linkage generated by the MMF in the winding.

As it was discussed in Chapter 1, the low value of specific losses that amorphous materials have, might allow the operation of the machine at higher frequencies when compared with electrical sheet. Consequently, having a higher pole counting is of interest for enhancing the performance of the machine [61], [62]. The limitation is then set by the converter used and the fundamental frequency. In addition, the modular structure of the stator is ideal for the manufacturing of a non-overlapping concentrated winding as it was suggested in Section 1.4. In

Parameter	Value
Nominal speed [rpm]	1000
Continuous torque [Nm]	100
Maximum torque [Nm]	200
Rated speed at maximum torque [rpm]	2300
Nominal power [kW]	24
Nominal rms current density J_{rms} [A/mm^2]	6.5

Table 2.3. Specification for the design of the SM3D machine.

theory, having one coil per module would facilitate the manufacturing of the winding, for example, by using coil bobbins. Therefore, the manufacturing of the coils might be automated, facilitating the assembly process.

Hence, combinations of stator modules and rotor pole combinations yielding a slot per pole per phase q lower than 1 are of interest. A study of the winding factor in machines with non-overlapping concentrated windings was developed in [63], where the combinations yielding the higher winding factors are recommended. However, as it is highlighted in [62], some combinations with $0.25 < q < 0.5$ might have issues of noise and vibration. Following such principles, combinations with a large value of symmetry were selected for studying in this chapter. As an initial approach, and following the procedure proposed in [64], the aspect ratio of a synchronous machine χ is the ratio of the stack length L_{stack} over the air-gap diameter D_g:

$$\chi = \frac{L_{stack}}{D_g} \tag{2.5}$$

An initial estimate of χ may be obtained as:

$$\chi = \frac{\pi\sqrt{p}}{4 \cdot p} \tag{2.6}$$

Where p is the number of poles. Then it is possible to approximate the value of L_{stack} if the value of torque T is known with the expression:

$$T = \sigma_{Ftan} \frac{\pi D_g^2}{2} L_{stack} \tag{2.7}$$

Where σ_{Ftan} is the tangential stress of the machine, with typical values between 21 to 48 kPa for surface mounted PM machines. Table 2.4 summarizes the results for various machines with different number of poles.

Rotor poles	Stator modules	D_g [mm]	χ [%]	L_{stack} [mm]
8	6	198	39.3	78
12	9	212	32.1	68
16	12	222	27.8	62
20	15	230	24.8	57
24	18	237	22.7	54
28	21	244	20.1	51
32	24	249	19.6	49
36	27	254	18.5	47

Table 2.4. Air-gap diameters of various combinations of stator modules and rotor poles.

2.3 2D-FEM MODELLING

A 2D-FEM model was built in order to evaluate the performance of the SM3D machine. The division of the rotor into two sections as described in Section 2.1.2, allows the simplification of the SM3D as shown in Figure 2.13. That is, the inner and outer rotors, represent the top and the bottom sections of the rotor in the model described in Figure 2.10. In an additional step, the geometry described previously may be reduced by using symmetries. In addition, the boundary conditions in the external edge of the modules is set as the field is normal (Neumann boundary condition) in Figure 2.14. Hence, only one air-gap is required to be modelled.
At this stage some of the dimensions of the C-shaped cores are not required. That is, only the width of the stator modules (i.e. dimension D) needs to be defined. The torque, calculated in Nm per unit length is required to be multiplied by the dimension A of the module in Table 2.5. Furthermore, D was set as a parameter, varying with the air-gap diameter of the machine. An analysis with the complete set of dimensions is required when building the 3D-FEM model, which will be investigated in coming sections of the report. Some assumptions are required in order to start the calculations of torque with various combinations of stator modules and poles:

- The rotor outer radius r_{ro} was varied in increments of 4 mm. In addition, the outer diameter of the machine was kept fixed. Consequently, the winding height h_{win} is reducing with the increased r_{ro}. On the other hand, the winding width w_{win} is increasing with the perimeter of the

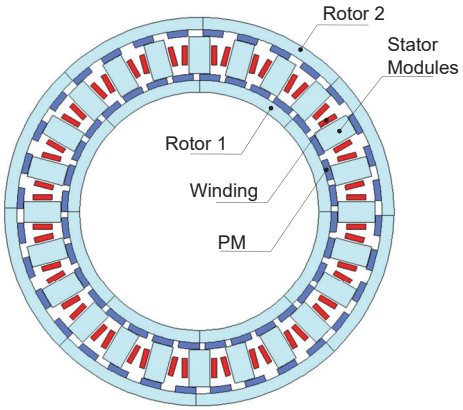

Figure 2.13. SM3D 2D simplified geometry.

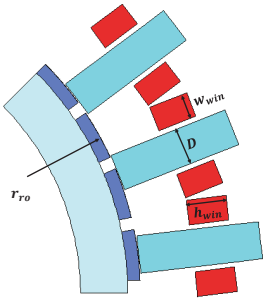

Figure 2.14. SM3D 2D symmetry.

air-gap.

- The PM coverage PM_{cov} is assumed to be 70%. In addition, the dimension D of the module is equal to the PM pitch and is kept constant.
- The air-gap length l_g is kept at a constant value of 0.5 mm. Consequently, the thickness of the permanent magnet l_m is kept constant at a value of 5 mm in all cases.
- The current density was assumed to be 6.5 A/mm^2 rms.

The values of the calculated torque with 2D-FEM model are illustrated in Figure 2.15, where it may be observed that for each stator modules and rotor combinations there is a rotor radius r_{ro} and a copper area which yields a maximum value of torque. Therefore, reducing the air-gap radius for allowing a larger copper area results in a reduction of the produced torque (left region of the plots from the maximum torque in Figure 2.15). Similar situation is present if the diameter is increased. Then the area available for copper is reduced. Thus, the torque production is reduced as it is observed in the right points from the maximum torque points in Figure 2.15. According to the specifications presented in Table 2.3, there is one machine which delivers the torque required with the lowest rotor radius. The machine with 15 stator modules and 20 rotor teeth delivers its maximum torque of approximately 100 Nm with r_{ro}= 0.1 m of air-gap radius. Therefore, this combination was selected for further calculations with 3D-FEM.

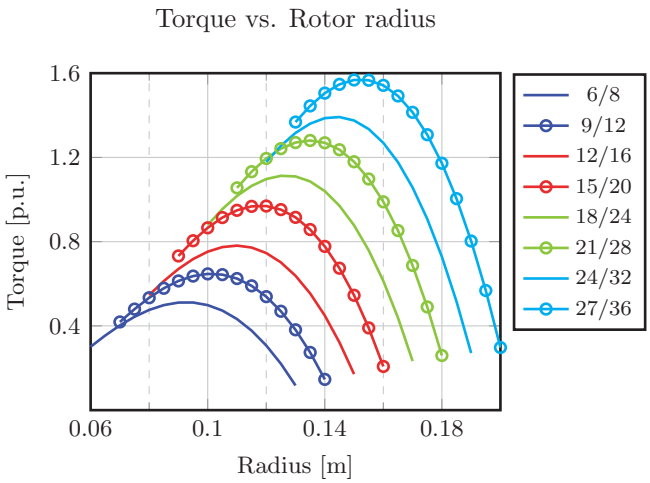

Figure 2.15. Torque comparison for various rotor poles and stator module combinations.

2.3.1 COMPARISON BETWEEN ANALYTICAL AND 2D-FEM MODELS

The comparison between the analytical model developed in 2.1.1 and the 2D-FEM approach is shown in Figure 2.16. The values of maximum torque and radius in Figure 2.15 were selected for performing analytical calculations. As it may be observed, the analytical values follow a similar trend when compared with 2D-FEM simulations. However, the deviations vary from 20 to 34%. Despite such deviations, the analytical calculations might serve as an initial approach in order to perform the dimensioning of the SM3D machine. The values of torque calculated analytically, are obtained with the expression:

$$T = \frac{3}{2}\hat{\Psi}_m \cdot \hat{I}_q \cdot 2p \tag{2.8}$$

Where Ψ_m is obtained with (2.1) and $\hat{I}_q$ is the peak q-axis current obtained with:

$$\hat{I}_q = \sqrt{2} J_{rms} h_{win} w_{win} k_{fill} \tag{2.9}$$

With k_{fill} as the slot fill factor.

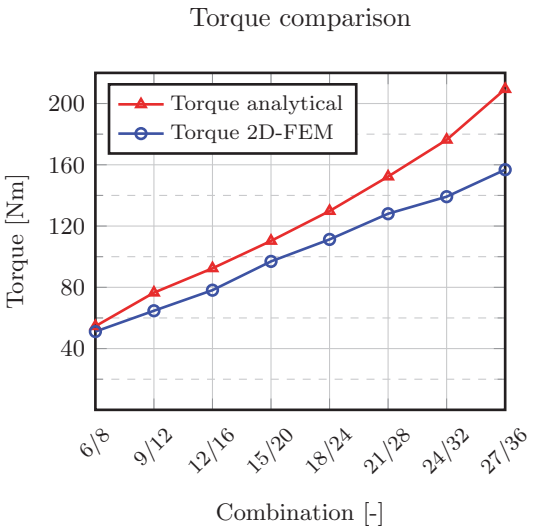

Figure 2.16. Calculated torque with analytical and 2D-FEM models.

2.4 3D-FEM MODELLING

Although the simplification of the machine was possible and both analytical and 2D-FEM models were developed, there are certain phenomena that shall be accounted for with a full 3D model. Therefore, parameters such as permanent magnet flux, torque production, inductance, power factor, among others, are evaluated through sensitivity analyses in order to investigate the behaviour of the SM3D machine. Initially, a geometry is selected, and the effect of the magnet coverage, and PM thickness is investigated. Finally, a definition of the number of stator modules and rotor poles is carried out. At the end of this section, a combination of stator modules and rotor poles is selected and analysed in depth. An SM3D machine with 15 stator modules and 20 rotor poles was selected. In Figure 2.17a 1/5 of the geometry and half the axial length is illustrated. The main parameters described in Figure 2.17b for starting of the study are summarized in Table 2.5, along with a description of the main dimensions of the C-shaped modules. Note that the dimension D is estimated with the outer radius of the rotor r_{ro} with the expression:

$$D = \frac{2\pi \cdot r_{ro} \cdot 0.7}{p} \tag{2.10}$$

Where the factor 0.7 accounts for the space available for the end windings between modules.

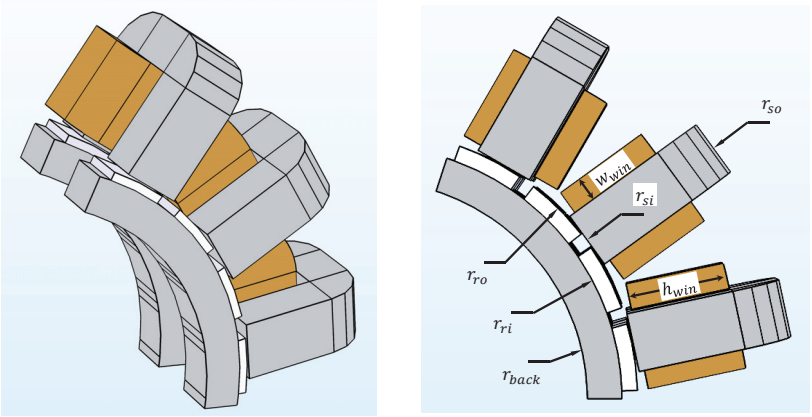

(a) (b)

Figure 2.17. Geometry defined for sensitivity analysis, (a) isometric view, (b) definition of the main dimensions.

2.4.1 EVALUATION OF THE PM COVERAGE

The impact of the variation of PM coverage PM_{cov} on the production of PM flux Ψ_m is of interest since this parameter is directly related with torque production. Additionally, when addressing the recycling issue, it is also important to optimize the amount of PM material that is being used. Hence, the PM_{cov} is evaluated from 50% to 100% the pole pitch. The results are shown in Figure 2.18.

As observed in Figure 2.18, the increment of the permanent magnet flux slows down as the value of PM_{cov} reaches unity. An increment of 40% of PM volume (i.e. $PM_{cov} = 70\%$), results in an increment of approximately 29% of Ψ_m. In contrast, an increment of 60% (i.e $PM_{cov} = 80\%$), results in an increment of approximately 39% of Ψ_m. Finally, an increment of 100% of PM volume (i.e $PM_{cov} = 100\%$) yields an increment of approximately 46% of Ψ_m. Hence, the increment of Ψ_m does not follow the increment of PM material introduced with the variation of PM_{cov} due to the presence of leakage between PMs, which starts to be significant as PM_{cov} reaches unity.

Parameter	Value [mm]
Rotor outer radius r_{ro}	100
Rotor inner radius r_{ri}	97
Rotor back radius r_{back}	84
Stator outer radius r_{so}	152.5
Stator inner radius r_{si}	101.5
Winding width w_{win}	10
Winding height h_{win}	39.5
Module dimension A	19
Module dimension B	25
Module dimension C	41.5
Module dimension D	22
PM thickness l_m	3
Air-gap length l_g	0.5

Table 2.5. Main dimensions of a SM3D machine with 15 stator modules and 20 poles.

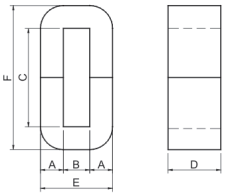

Main dimensions of the amorphous C-shaped cores.

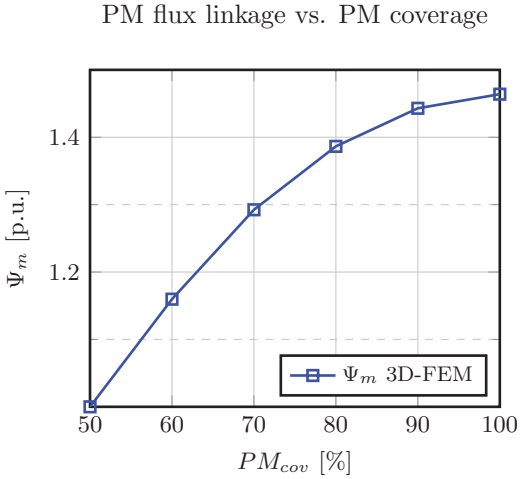

Figure 2.18. Ψ_m vs. PM coverage.

Additionally, values of torque were estimated in order to quantify the impact

of the PM leakage. Once the torque was estimated, the torque per mass of PM was obtained. As it is shown in Figure 2.19, this parameter reduces as 100% coverage is reached. Which is a result of the large leakage due to the presence of large air spaces among modules due to the modular topology of the stator. The PM mass was calculated assuming a density of 7500 kg/m^3 for sintered PMs. In order to continue with the study of the SM3D machine, a PM coverage of 80% was selected. Additional parameters such as inductance and power factor are not evaluated, since the permeability of the PM is close to unity. Hence, variations of inductance with PM coverage would not be expected.

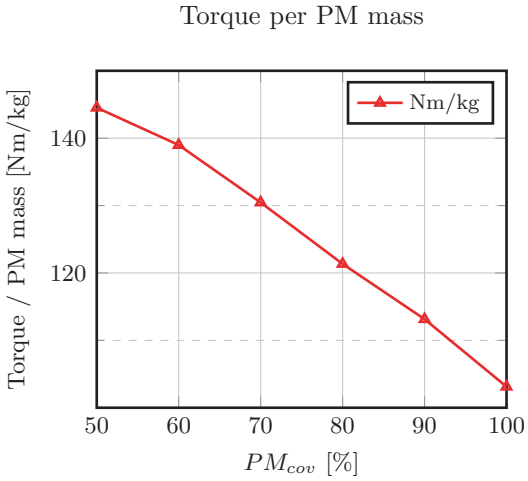

Figure 2.19. Torque per PM mass vs. PM_{cov}.

2.4.2 EVALUATION OF THE PM THICKNESS

The PM thickness l_m was varied from 3 to 8 mm and values of PM flux, inductance, torque and power factor were calculated. Parameters such as the rotor inner radius r_{ri}, rotor back radius r_{back}, winding width and w_{win} and height h_{win}, and the module dimensions A, B and C were kept fixed. The parameters stator inner and outer radius r_{si} and r_{so} varied with the thickness of the permanent magnet l_m. As l_m is varying, r_{ro} is also varying, consequently D is varying according to (2.10).

Permanent Magnet Flux

An increment of maximum 13% in the production of PM flux linkage was obtained when increasing the PM thickness by 166%. Hence, increasing the PM thickness further, did not show a significant increment of the production of Ψ_m, as it is observed in Figure 2.20. On the contrary, the increment of the PM thickness would result in the sub-utilisation of the material. Nevertheless, it is required to evaluate the effect of the increment of the PM thickness in additional parameters such as torque, inductance and power factor.

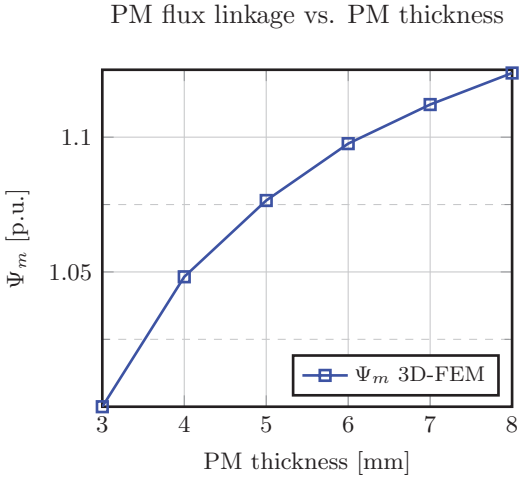

Figure 2.20. Ψ_m vs. PM thickness.

Torque

The torque production was evaluated with the increment of the PM thickness. A current density J_{rms}= 6.5 A/mm^2 was applied to the windings. The results are presented in Figure 2.21. Since the production of torque is proportional to Ψ_m as in (2.8), a similar trend in the production of torque is expected as for the case of the PM flux Ψ_m.

Inductance

The synchronous inductance and power factor are also evaluated in this section of the report. The results are presented in Figure 2.22. The synchronous inductance corresponds to the value of flux linkage calculated when a current is applied to the q-axis. Then, the contribution of the PM flux is subtracted,

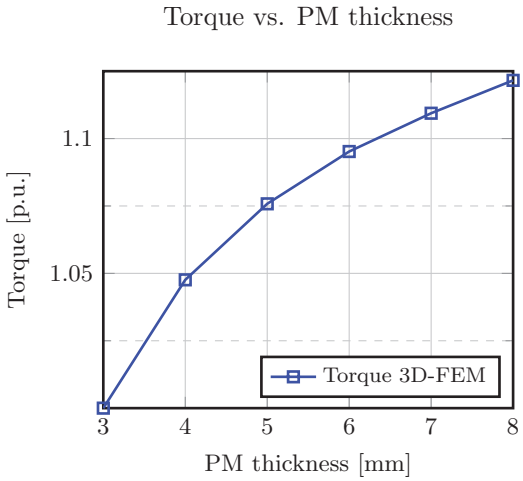

Figure 2.21. Torque vs. PM thickness.

and the result is divided by the applied current I_a, as in the expression:

$$L_a = \frac{\Psi_a - \Psi_m}{I_a} \tag{2.11}$$

As the dimension l_m increases, the PM reluctance $\mathcal{R}_{PM}$ (see Figure 2.5) increases. Since the inductance L is inversely proportional to the reluctance, the result is the decreasing of the value of L. The trend showed in Figure 2.22 is consistent with this description.

Power Factor

The power factor of the machine was estimated with the values of PM flux Ψ_m, inductance L_a and applied current I_a with the expression [59]:

$$\cos\varphi = \arctan\left(\frac{L_a I_a}{\Psi_{m(1)}}\right) \tag{2.12}$$

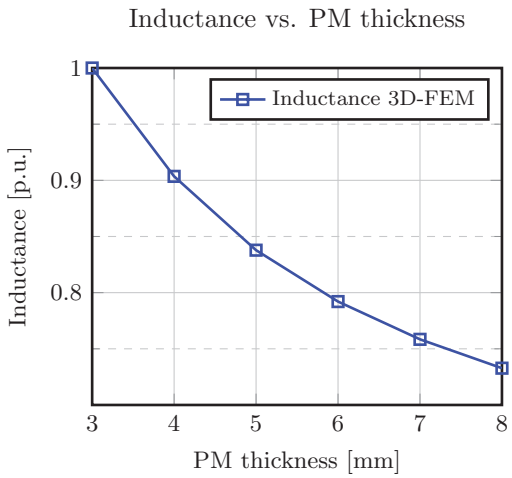

Figure 2.22. Inductance vs. PM thickness.

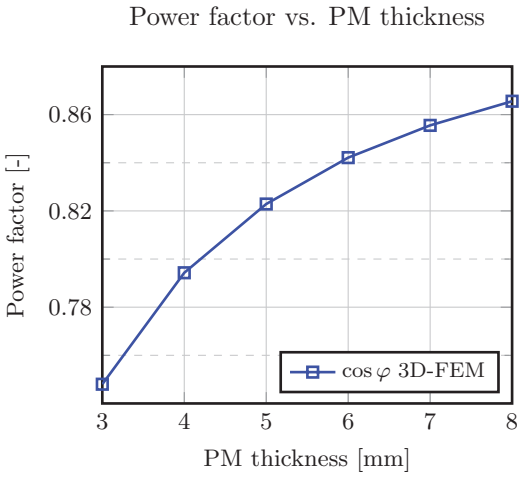

Figure 2.23. Power factor vs. PM thickness.

As discussed previously, the increment of the PM thickness, did not yield a significant increment of the production of permanent magnet flux and consequently torque production. However, it shows a significant impact in the calculated values of inductance and power factor. Therefore, the selection of the PM thickness should account for these two parameters. As an additional step, the distribution of magnetic flux density in the stator modules was verified

in order to evaluate the saturation levels. Three points in the stator modules were selected for the calculation of the magnetic flux density. Figure 2.24, shows the definition of such points. The results are shown in Figure 2.25.

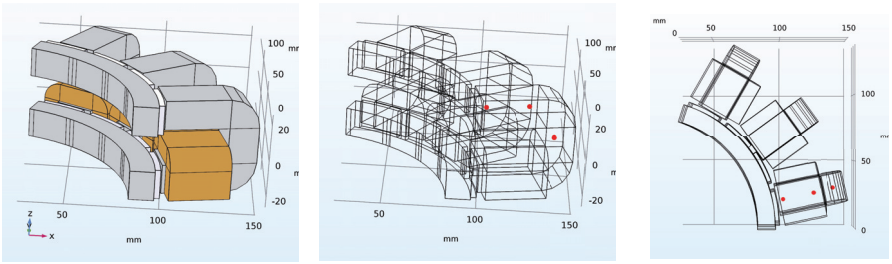

(a) **(b)** **(c)**

Figure 2.24. Definition of points for plotting the magnetic flux density, (a) isometric view, (b) isometric view, and (c) *xy*-view.

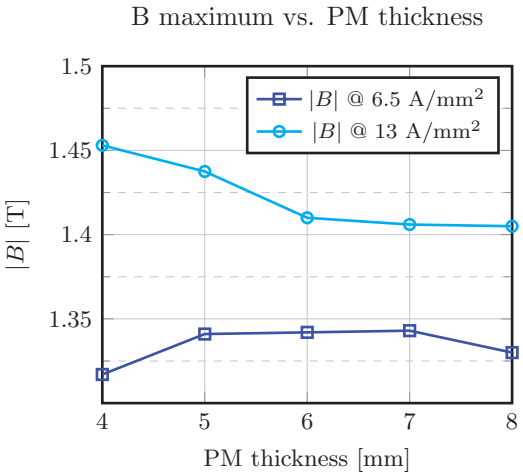

Figure 2.25. Magnetic flux density vs. PM thickness.

At load, the levels of magnetic flux density in the stator modules have a low value bearing in mind that the knee point in the BH plot is approximately 1.5 T for electrical sheet. On the other hand, for amorphous laminated material, the saturation knee point is reached at approximately 1.4 T, as shown in Figure 1.13. Which results in a reduction of the performance of the machine with amorphous laminated material. In addition, the optimization process of the

SM3D machine is limited to the fixed dimensions of the modules available [65], [47], [66]. Moreover, the winding width w_{win} is much lower than the dimension B of the module as it is shown in Figure 2.26, resulting in the under-utilisation of the available window of the module.

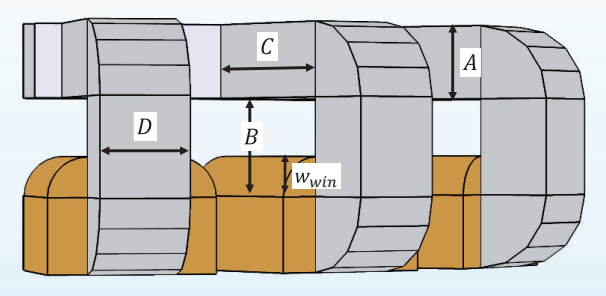

Figure 2.26. SM3D geometry yz-plane.

Generally, the optimization process of the machine is performed by varying the air-gap diameter, the slot dimensions and the length of the machine. However, in the case of the SM3D, most of the dimensions are fixed. Hence the optimization process becomes challenging since all module dimensions A, B, C and D are changing non-uniformly from module to module. Therefore, it was decided to use a different approach in the optimization process which is discussed in the following section.

2.4.3 EVALUATION OF THE SELECTION OF STATOR MODULES AND ROTOR POLES

As it has been described previously, the C-shaped cores are already available at standardized dimensions, which makes the optimization of the stator cores a challenging task. Therefore, a different approach is suggested. According to the window area available ($B \times C/2$), there will be a minimum diameter at which such window area is fully utilised. Initially, the modules dimensions in Table 2.7 are selected.

Core dimensions [mm]				
A	*B*	*C/2*	*D*	*F*
13	15	28	25	82
16	20	35	25	102
19	25	41.5	35	121

Table 2.7. C-shaped core main dimensions.

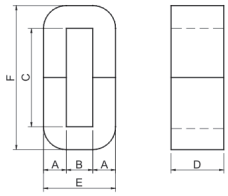

Main dimensions of the amorphous C-shaped cores.

According to the stator topology described in Figure 2.26, the copper area is maximum when the winding width w_{win} is equal to the dimension B of the module. Hence, with the dimension D of the module and the number of stator modules, it is possible to determine the air-gap radius r_{gap} as described in (2.13), and consequently to calculate the torque production of such combination. The calculated air-gap radius r_{gap} and the values of torque are shown in Table 2.9. The values of air-gap radius are calculated with the expression:

$$r_{gap} = \frac{(2B + D)N_{mod}}{2\pi} \tag{2.13}$$

Where N_{mod} is the number of stator modules. The calculations of torque, were performed with the 2D-FEM approximation. Therefore, the results of torque per unit length were multiplied by the dimension A of each module. In addition, the air-gap length was kept constant with l_g= 0.5 mm, as well as, the PM thickness which was kept as l_m= 5 mm.

Modules	Poles	*A*= 19 [mm]		*A*= 16 [mm]		*A*= 13 [mm]	
		air-gap radius [mm]	Torque [Nm]	air-gap radius [mm]	Torque [Nm]	air-gap radius [mm]	Torque [Nm]
6	8	71.6	67.7	62.1	35.2	52.5	15.18
9	12	(107.4	157.2)	93.1	82	78.8	35.5
12	16	143.2	283.7	(124.1	148.2)	105	64.3
15	20	179.0	447.5	155.2	236.1	131.3	101.4
18	24	214.9	640.3	186.2	335.5	(157.6	145.9)
21	28	250.7	874.9	217.2	458.7	183.8	199.7

Table 2.9. Torque and radius per combination of poles and stator modules.

The combinations in brackets, are of interest for an optimization process given the values of torque and air-gap radius. Various criteria were evaluated for each one of the three machines. The first criterion is the torque density T_{den}. Torque density is defined as the ratio of the torque produced by a machine and its active volume. Therefore, it can be evaluated with the expression:

$$T_{den} = \frac{T}{\pi r_{so}^2 L_{stack}} \tag{2.14}$$

The second criterion is the stator surface current density of the machine A_{load}. It is defined as the ratio of the total current rms in the stator windings and the perimeter described by the rotor radius [67]. For the SM3D machine it might be estimated with the expression:

$$A_{load} = \frac{J_{rms} C B k_{fill}}{2\pi r_{gap}} \tag{2.15}$$

Where k_{fill} is assumed to be 0.5, and the current density was assumed to be 6.5 A/mm^2 rms. The third criterion was the machine constant K_T which is the ratio between the torque produced and the square root of the copper losses [68]:

$$K_T = \frac{T}{\sqrt{p_{cu}}} \tag{2.16}$$

Parameter	Combination		
	9/12	12/16	18/24
Torque density [Nm/L]	11.6	12.2	11.8
Current load (rms) [kA/m]	45	35	24.8
Copper losses [W]	581	412	310
Machine constant K_T [Nm $\cdot$ W$^{-0.5}$]	6.5	7.3	8.3

Table 2.10. Selection of SM3D machines.

All these three parameters were evaluated on the three machines selected. The results are summarized in Table 2.10. As it is observed, the combination of 12 stator modules and 16 poles yielded the higher value of torque density. On the other hand, in terms of size, the machine with 9 stator modules and 12 poles would be a suitable choice. However, the higher level of copper losses might not be convenient. Hence, the combination of 12 stator modules and 16 poles was selected.

2.5 STUDY OF THE SURFACE MOUNTED 3D-FLUX PERMANENT MAGNET MACHINE

The dimensions of the machine with a combination of 12 stator modules and 16 poles are summarized in Table 2.11.

Parameter	Value [mm]
Rotor outer radius r_{ro}	115
Rotor inner radius r_{ri}	106
Rotor back radius r_{back}	88
Stator outer radius r_{so}	166.5
Stator inner radius r_{si}	115.5
Window width w_{win}	20
Window height h_{win}	30
Module dimension A	16
Module dimension B	20
Module dimension C	35
Module dimension D	24
PM thickness l_m	9
PM coverage cov [%]	90
Air-gap length l_g	0.5

Table 2.11. Main dimensions of a SM3D machine with 12 stator modules and 16 poles.

2.5.1 NO-LOAD BACK-EMF

The no-load back-EMF of the SM3D machine is shown in Figure 2.27, evaluated with both electrical sheet and amorphous material. As it is observed, at no-load the deviation of the values of both materials is negligible.

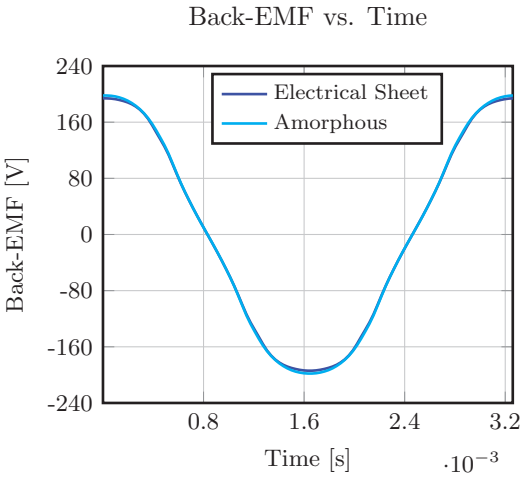

Figure 2.27. Back-EMF at 2300 rpm.

2.5.2 PRODUCTION OF TORQUE

The torque was estimated at various values of current density. Static, non-linear simulations were run, and the values obtained are shown in Figure 2.28. The requirement is that the machine delivers a maximum torque of 200 Nm. In addition, a comparison between both electrical sheet and amorphous materials was performed. The materials in 3D-FEM were modelled with the BH curves in Figure 1.13. The torque production with amorphous material, shows a lower value when compared with electrical sheet. Due partially to the lower saturation point that amorphous material have. In addition, the stacking factor of amorphous material, is much lower than for the electrical sheet. That is, for amorphous laminations it is approximately 82%, whereas for electrical sheet, it is larger than 90% depending on the thickness of the lamination. However, as it is observed in the results, the linear behaviour of the torque shows that the knee of the BH plot of the material is not reached. The magnetic flux distribution in both stator and rotor is shown in Figure 2.29 with electrical sheet. Large variations of the magnetic flux density in the PMs may be identified. Such variations are due to the permeance variation seen by the PMs with the transition from air to iron. Additionally, Figure 2.30 shows the torque of the SM3D machine at 6.5 A/mm^2 with amorphous C-shaped cores. The torque ripple of the machine is estimated in 11.6%.

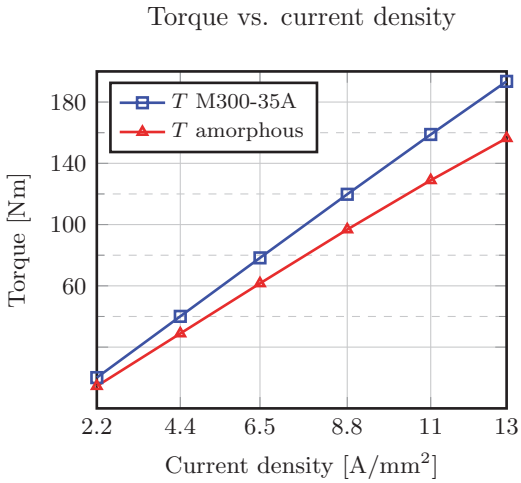

Figure 2.28. Torque production vs. current density.

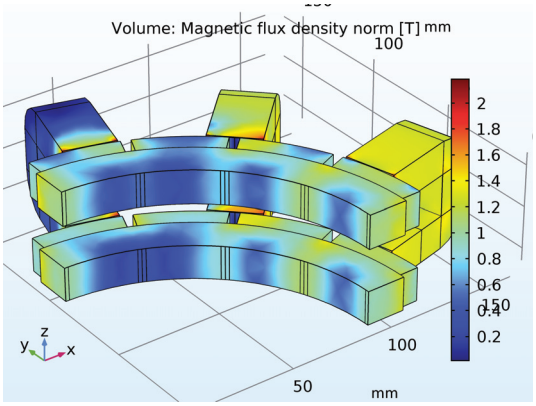

Figure 2.29. Magnetic flux density distribution at 13 A/mm^2.

2.5.3 INDUCTANCE PROFILE VS. CURRENT DENSITY

An additional step in the calculation of the SM3D machine calculation is the variation of the inductance with the increment of the current. These calculations were performed with both electrical sheet and amorphous material. Figure 2.31 shows the results of the calculations. The results are for a single

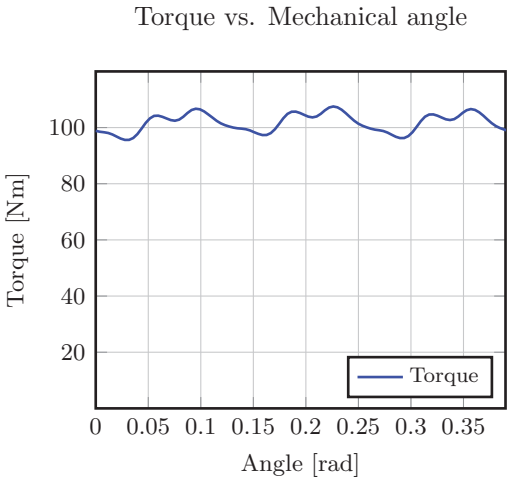

Figure 2.30. Static torque of the 12 stator modules 16 rotor poles.

turn. That is, the values are required to be scaled by the final number of turns, which are annexed in Table 2.12.
As it is observed, the inductance calculated in the machine with amorphous laminations, presents a larger reduction, which is an indication that the lamination is closer to the saturation point.

2.5.4 CALCULATION OF THE IRON LOSSES

For the estimation of the iron losses the model described in [69] is followed. Therefore, the magnetic flux density in the radial $\hat{b}_r$, tangential $\hat{b}_t$ and axial $\hat{b}_z$ directions, at each finite element was calculated in both stator and rotor regions. Afterwards, a Fourier transformation was applied and the losses were estimated for each harmonic component. The results are shown in Figure 2.32, for both SiFe and amorphous material. The iron losses were estimated in 3 cases of current density, and a quadratic fit was performed in order to approximate them in the whole speed range up to 2300 rpm. As it is observed, the standard laminations show the largest losses. In contrast, lower losses are obtained with amorphous laminations. Moreover, the iron losses with amorphous materials show a linear trend which might be due to the reduced eddy current loss component. The impact of the MMF of the windings is negligible as it is observed.

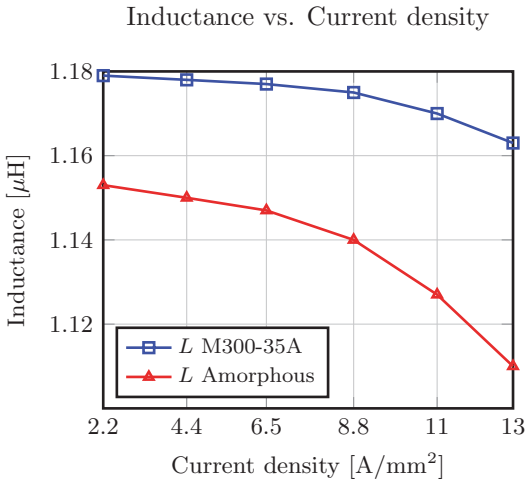

Figure 2.31. Inductance vs. current density.

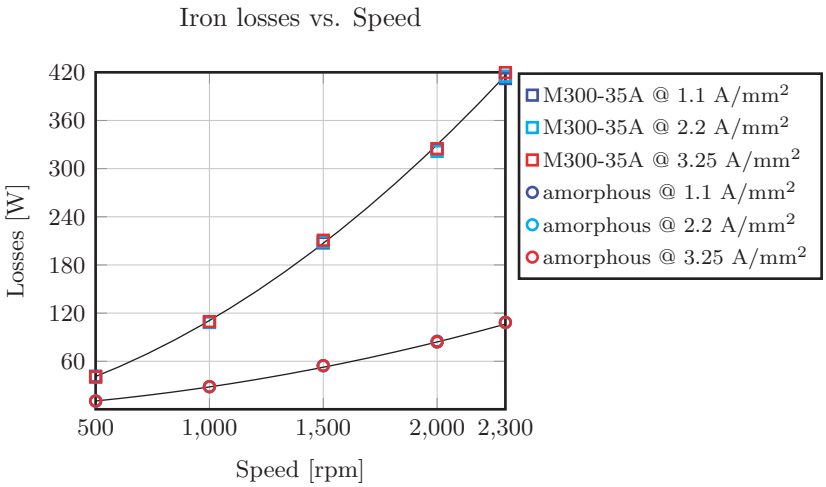

Figure 2.32. Iron losses vs. speed.

2.5.5 MAGNET LOSSES OF THE SURFACE MOUNTED 3D-FLUX MACHINE

An important aspect of the SM3D machine, is the variation of the permeance in the air-gap. Given that the stator is built in a modular fashion, such vari-

ation is large and the permanent magnets located on the surface of the rotor, are exposed to such variations. In general, for radial flux machines the calculation of this type of magnet losses is not interesting, since the slot openings are small. Therefore, in most calculations the effect of these losses is disregarded. As described in Figure 2.29 previously, the variation of the magnetic flux density inside the PMs showed to be large in the SM3D machine. In [70] and [71] analytical models are proposed for the calculation of these type of losses. However, as it was demonstrated in [72] and [73], both analytical and 2D-FEM approaches are valid under the assumption of a permanent magnet length much larger than its thickness $h_m >> l_m$. Therefore, in order to calculate the PM losses due to slotting effect, transient simulations were performed to the 3D-FEM model, at three speeds: 1000, 2000 and 3000 rpm. The results are shown in Figure 2.33. The calculations were performed with the machine modelled at no-load. Hence, the model does not account for losses due to time and space harmonics (i.e. the effect of the harmonics due to the PWM modulation and the winding distribution). Additionally, the conductivity of the PMs was selected as 1.25 MS/m.

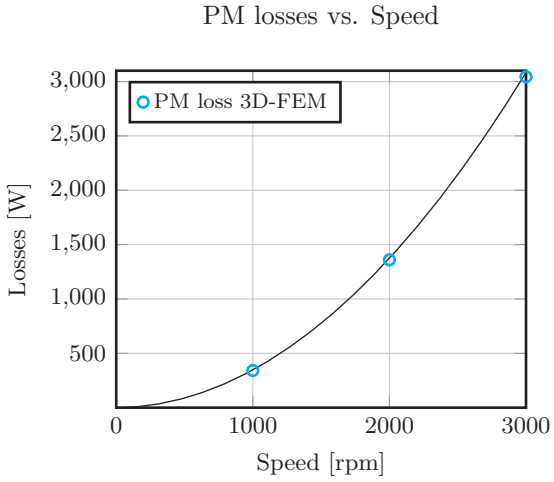

Figure 2.33. Calculated PM losses vs. speed.

Note that the calculation was performed at 3 speeds, and the curve is a quadratic fitting of the losses. In addition to the calculated values of PM losses, the distribution of the current density J_{mag} inside the magnets is shown in Figures 2.34a and 2.34b. It shows both the direction and the magnitude. It is observed, the fashion in which eddy currents are produced in the boundaries where there is a transition from iron to air and vice-versa, showing a pronounced slotting effect. In addition, these losses show a rather high value,

which might represent a risk of demagnetization, due to the high temperatures generated by having such large values of losses in a small volume.

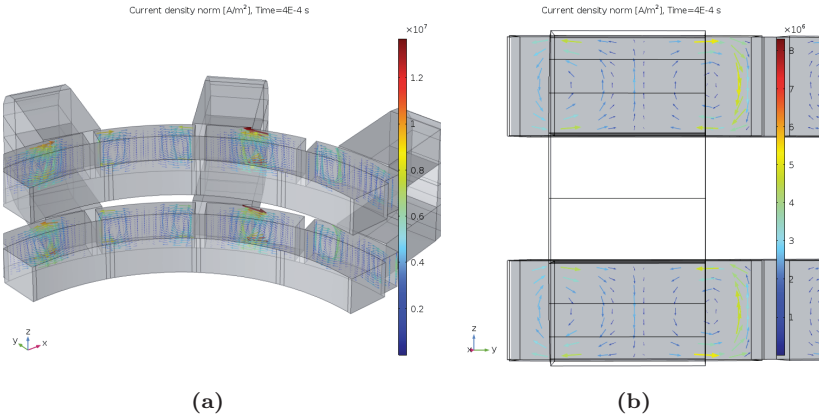

(a) **(b)**

Figure 2.34. PM current density distribution @ 3000 rpm, (a) isometric view, (b) yz-plane view.

2.5.6 MAIN PARAMETERS OF THE SM 3D-FLUX MACHINE

The analysis of the SM3D machine ends with the description of the main parameters. The values summarized in Table 2.12 are implementing amorphous C-shaped stator cores.

Parameter	Value
Torque density [Nm/L] @ 6.5 A/mm^2	11.2
PM mass [kg]	2.7
Rotor iron mass [kg]	5.4
Stator iron mass [kg]	7
Copper mass [kg]	5.8
Torque per active weight [Nm/kg] @ 6.5 A/mm^2	4.9
Volume [m^3]	9.1×10^{-3}
Number of turns per phase [-]	104
Back-EMF constant [Wb/rad]	0.093
Iron losses [W] @ 2300 rpm	108.3
Copper losses [W] @ 80^o	632
Synchronous inductance [mH]	0.71
Phase Resistance [mΩ] @ 20^o	29.6
Line voltage [V]	400
PM losses @ 2300 rpm [W]	1816
Power factor [-]	0.8
Rated torque @ 6.5 A/mm^2 [Nm]	100

Table 2.12. Main parameters of the SM3D machine.

2.6 A SURFACE MOUNTED PM 3D-FLUX DEMONSTRATOR

In order to validate the models developed in the calculation of the SM3D machine, a demonstrator was built. Such demonstrator is shown in Figure 2.35. It consists of a single phase machine with two C-shaped modules made of amorphous laminated material and 40 rotor poles. In order to simplify the manufacturing process, some of the components of an outer rotor machine were used [74]. That is, shaft, end-shields and rotor back. New permanent magnets were used and it was necessary to manufacture a new stator structure for keeping the modules and coils in place. Various parameters were evaluated. The test set-up is shown in Figure 2.36 and the results of the study of this machine were reported in [75].

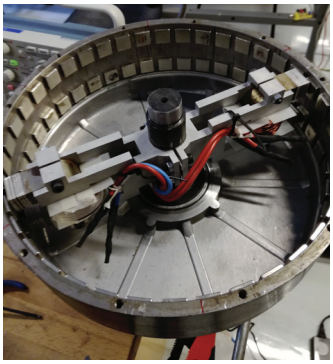

Figure 2.35. Demonstrator assembly [75].

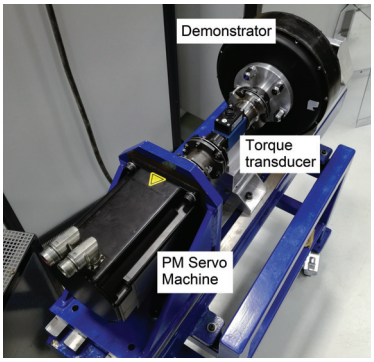

Figure 2.36. Set-up for testing of the demonstrator [75].

2.6.1 CHARACTERIZATION OF IRON LOSSES IN AMORPHOUS C-SHAPED CORES

Initially, the potential loss reduction of amorphous laminated materials was evaluated. Samples of C-shaped cores made with iron based amorphous alloy, as in Figure 1.12c were obtained and a test coil was manufactured. The C-shaped cores corresponded to the quality 2605SA1, specified by the supplier [65]. The specimen for the characterization of the iron losses is shown in Figure 2.37. The iron losses in the C-shaped laminated amorphous modules were determined as the difference between the total measured losses and the copper losses.

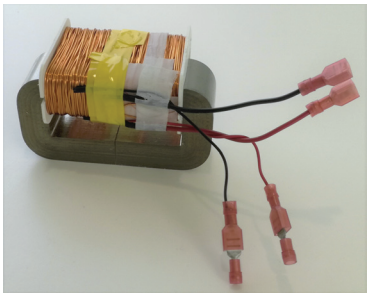

Figure 2.37. Test coil for characterization of the iron losses.

Figure 2.38 shows the superior performance of the amorphous laminations in terms of specific losses. It shows that the reduction of iron losses might get

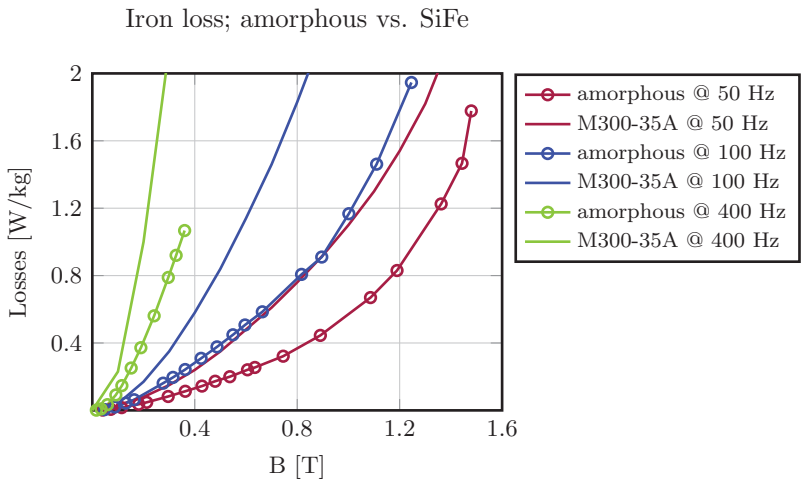

Figure 2.38. Specific losses comparison between amorphous iron and SiFe laminations.

to reach 68% when compared with standard electrical sheet. Furthermore, the reduction of losses is more noticeable as the frequency increases. Meaning that having a large pole count machine and/or higher frequency are possible by using amorphous laminated materials. The values of specific losses of M300-35A laminations are taken from data-sheet of the manufacturer [76].

2.6.2 VALIDATION OF FEM CALCULATIONS WITH TEST MEASUREMENTS

Various parameters were measured with the test set-up presented in Figure 2.36. A FEM model was built with the main dimensions presented in Table 2.13 and Figure 2.39. Figure 2.40 shows the model built in 3D-FEM.

Measurement of Back-EMF

The measurement of back-EMF was performed at a range of speeds from 100 to 500 rpm. Figure 2.41 illustrates the waveform of the back-EMF at 100 rpm, of both measured and calculated with 3D-FEM simulations. The results shows that the waveforms have a similar trend. In addition, the rms values of back-EMF at speeds of 200, 300, 400 and 500 rpm, are illustrated in Figure 2.42.
As it may be observed, the trend of the calculations follows the values measured

Dimension	Value
Rotor outer radius r_{ro} [mm]	139
Rotor inner radius r_{ri} [mm]	128
Stator outer radius r_{so} [mm]	127.5
Stack Length [mm]	52
Air-gap length [mm]	0.5
PM thickness l_m [mm]	3
PM width w_m [mm]	15
PM length h_m [mm]	15
PM remanence B_r [T]	1.37
Number of turns per coil	150
Pole pairs $2p$	20

Table 2.13. Main dimensions of the demonstrator [75].

at different speeds. However, these might be subjected to deviations. That is, in the FEM model the air-gap length has a constant value. However, in the prototype the PMs are of rectangular shape. In addition, the value of air-gap during the assembly could have changed. The deviation between measurements and 3D-FEM was of approximately 12%.

Measurement of Inductance

The measurement of the inductance was performed using a Precision Magnetics Analyser© equipment. The values were obtained at various frequencies within a range from 50 to 500 Hz. Figure 2.43, shows the results of measurements. Similarly, the inductance was calculated with the model developed in 3D-FEM, the results are included in Table 2.14. As the frequency reached 500 Hz, a reduction of the inductance value was identified as 17% of the initial value at 50 Hz. The calculation of the inductance with the 3D-FEM model, was performed applying a current density of 5 A/mm^2 to the windings, removing the contribution of the PMs (i.e. the PMs were modelled as air). Since it is a single phase machine, the inductance L_a was obtained as:

$$L_a = \frac{\Psi_a}{I_a} \tag{2.17}$$

The results of the calculations show a good agreement with the measurements, with a deviation of approximately 9%.

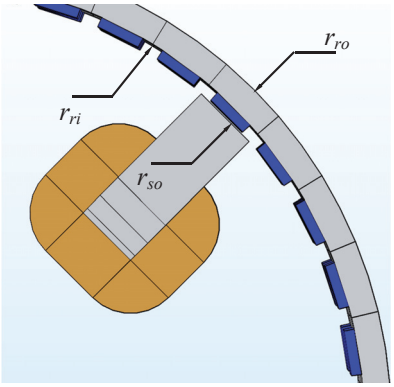

Figure 2.39. Main dimensions of the SM demonstrator.

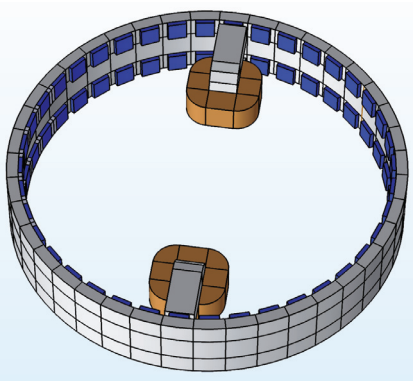

Figure 2.40. SM demonstrator 3D-FEM model geometry.

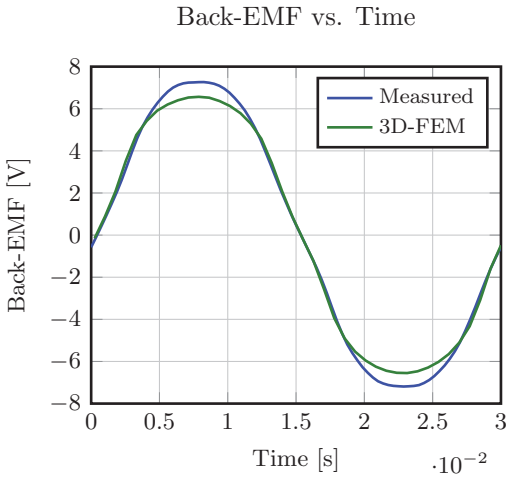

Figure 2.41. Back-EMF measured and calculated with 3D-FEM @ 100 rpm [75].

Measurement of Rotational Losses

Two approaches were used for measuring the total rotational losses:

- *Case 1:* The torque was read from the torque transducer, with the machine running without any load connected to its terminals, the rotational losses are $p_0 = T_0 \cdot \omega_{mech}$.
- *Case 2:* A decay test was performed on the machine. The rotor was pulled to rotate, and the decaying waveform of the back-emf was recorded. The losses are estimated by quadratic fitting.

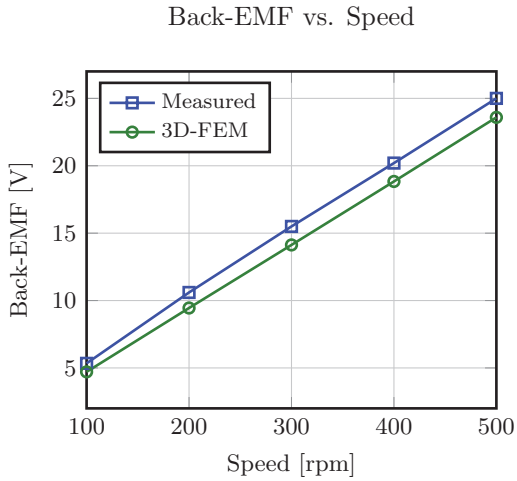

Figure 2.42. Back-EMF measured and calculated with 3D-FEM at various speeds [75].

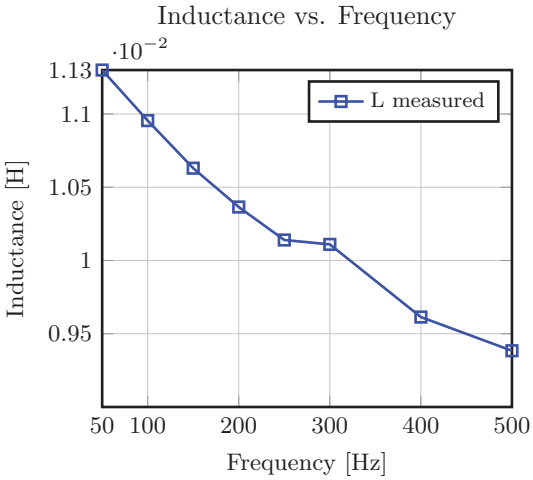

Figure 2.43. Inductance measured at various frequencies.

In both approaches, the effect of the MMF of the windings is neglected. However, as it was shown in 2.5.4, such effect is negligible. The results are presented in Figure 2.44. There is a maximum deviation of 19% between the losses measured with the approach described in *Case 1* and *Case 2*. Such deviation might be explained by the fact that a mathematical approximation is used in the *Case*

Measured [mH]	3D FEM [mH]
11.3	10.3

Table 2.14. Measured and calculated values of inductance.

2 approach. In addition, for calculating the losses with the decay test it is necessary to know the inertia of the rotor of the machine, which estimation might add to the deviation of the calculations.

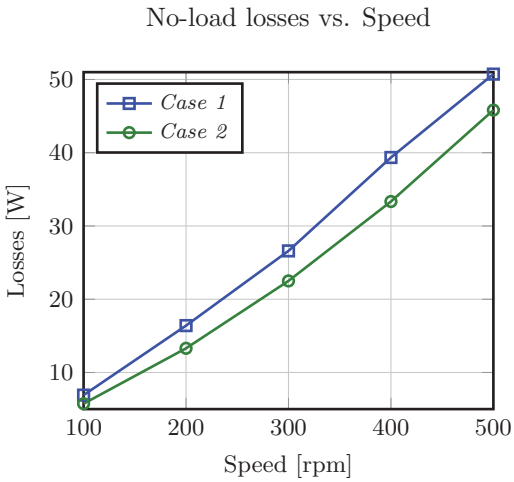

Figure 2.44. No-load losses measured at various speeds [75].

Measurement of Mechanical Losses

The study of the losses continued with the measurement of the mechanical losses (i.e. bearing losses). Such measurement was performed extracting the stator components of the demonstrator. Thus, eliminating iron, rotor and PM losses. In addition, the contribution of the PM forces to the bearing losses is neglected with this approach. The measured torque of the machine running under these conditions, corresponds to the bearing losses, which are estimated indirectly as the product of torque and speed $p_{mech} = T_0 \cdot \omega_{mech}$. The results are shown in Figure 2.45.

The measured losses show a linear behaviour, which corresponds to the characteristics expected for bearing losses [77]. The measurement of these losses is crucial in order to contrast the measured and calculated values of rotational

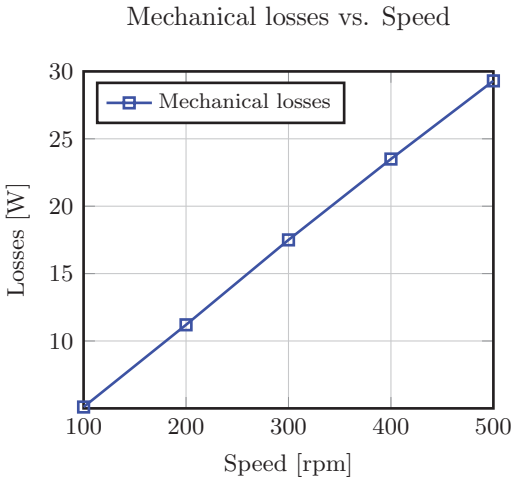

Figure 2.45. Measured mechanical losses at various speeds [75].

losses p_0. That is, the calculated rotational losses will correspond to the summation of the bearing losses, measured previously and the calculated PM, rotor back and stator iron losses. Such values are estimated in the coming section of this report.

Calculation of Rotational Losses

PM Losses

In order to estimate PM losses, transient simulations were carried out at no-load. PM losses were evaluated at 100, 200, 300, 400 and 500 rpm. A crucial parameter in the calculation of the PM losses, is the conductivity of the material. In the investigation performed on an outer rotor PM machine (Chapter 4) a characterization of the conductivity of sintered NdFeB PMs was carried out. Such measurement was performed with the Physical Property Measurement System (PPMS) from Quantum Design ®, at CRISMAT laboratory in ENSICAEN, France. At 80 °C the conductivity was of approximately 1.25 MS/m according to Figure 2.46.
The current density distribution is shown in Figure 2.47. It is shown the way the current density is generated in the PMs at the vicinity of the stator modules. The results at various speed are included in Figure 2.48.

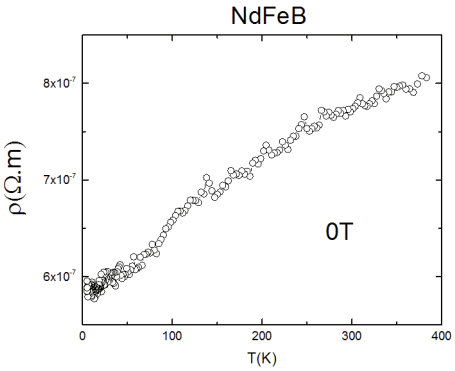

Figure 2.46. Resistivity of PM material vs. temperature [75].

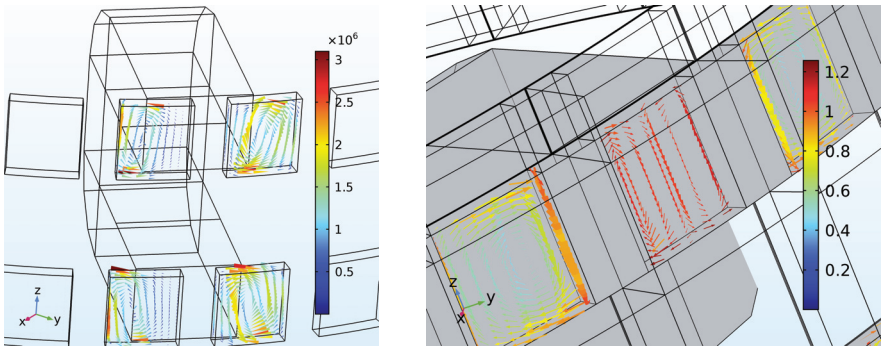

(a) **(b)**

Figure 2.47. PM current density distribution at 500 rpm and t=6 ms, (a) isometric view, (b) zoomed view.

Rotor Back Losses

The rotor back is a solid piece of steel, therefore, the calculation of the losses in this component followed a similar procedure as in the calculation of the PM losses. In the FEM model, the region corresponding to the rotor was modelled with a value of conductivity of 10.3 MS/m. The results are shown in Figure 2.48 along with the calculated PM losses and stator iron losses.

Stator Iron Losses

The calculation of the iron losses was performed following the method proposed

in [69]. Hence, similar approach was used as in Section 2.5.4. The results are illustrated in Figure 2.48.

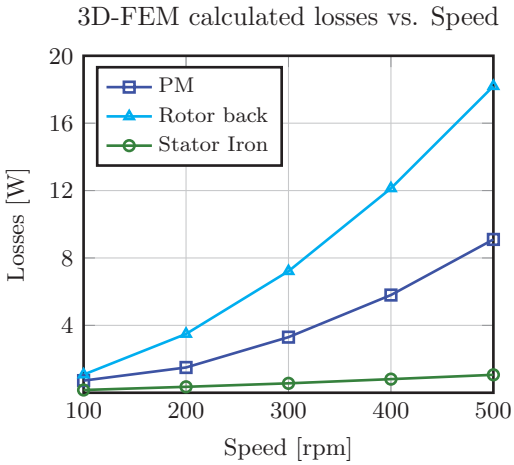

Figure 2.48. Stator iron, PM and rotor back losses vs. speed [75].

2.6.3 COMPARISON OF MEASURED AND CALCULATED ROTATIONAL LOSSES

Once the three components of the no-load losses were calculated (i.e. stator iron, rotor back and PM losses), it was possible to contrast them with the measured values. The no-load losses may be expressed as the summation of the bearing, PM, rotor back iron and stator iron losses. The measured values and the calculated values are contrasted in Figure 2.49. Which illustrates that the calculations with 3D-FEM are over-estimating the measured values. With a largest deviation of 11% at the highest speed.

2.6.4 ESTIMATION OF THE TORQUE

For closing the analyses presented in this chapter, the calculation of the torque was performed in order to contrast it with measurements. In order to perform the calculation of torque, the measured current and estimated load angle were applied to the 3D-FEM model [75]. The measured values and the results from simulations, are reported in Figure 2.50.

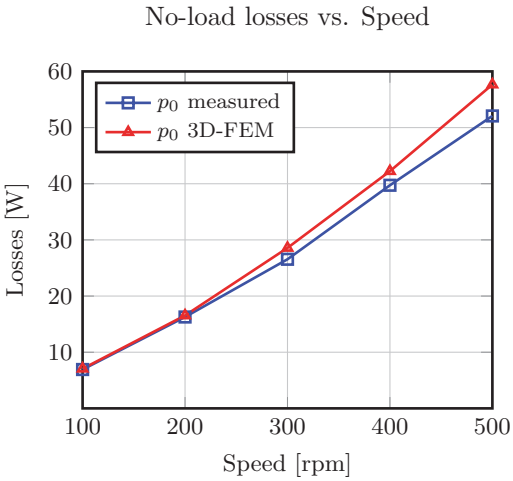

Figure 2.49. Measured and calculated rotational losses [75].

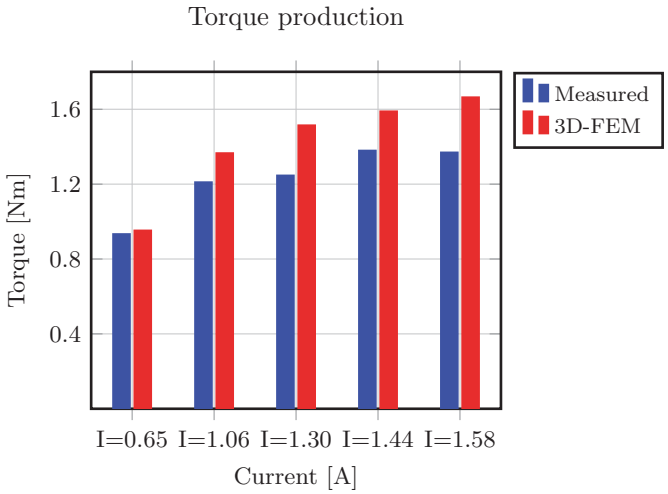

Figure 2.50. Torque production [75].

2.7 SUMMARY

Despite the axial path described by the flux in the stator modules, the working principle of the SM3D machine resembles any SPMSM machine. Consequently, it was possible to simplify the SM3D machine with a two dimensional model.

Moreover, a preliminary dimensioning of the SM3D with both analytical and 2D-FEM models was carried out. An investigation of the torque production with the variation of the air-gap diameter was performed for various combinations of stator modules and rotor poles. Additionally, the initial dimensioning of the SM3D was complemented with the development of a 3D-FEM model, in order to investigate additional parameters such as inductance, PM flux and torque, accounting for the additional phenomena present in a 3D structure such as the one found in the SM3D machine.

As the dimensions of the C-shaped cores were already fixed, an alternative for optimizing the machine dimensions was proposed. Such approach was evaluated on various combinations of stator modules and rotor poles. An SM3D machine for investigating additional parameters such as iron and PM losses was selected. The performance of such machine was investigated with both electrical sheet and amorphous laminated material. The SM3D machine with electrical sheet showed to have a better performance due to both the higher saturation level of the material and a higher stacking factor. However, the iron losses with electrical steel showed to be 3.5 times higher than the iron losses with amorphous material. Furthermore, such difference is expected to increase at higher frequencies, according to the loss characterization performed in Section 2.6.1.

Additionally, a study of the PM losses due to slotting effect was carried out. It showed that the losses generated in the PMs due to the variations of permeance with the transition from air to iron in the air-gap region, are significantly large. Furthermore, such losses increase with the square of the frequency. Therefore, as the speed increases these reaches values in order of kW and demagnetization of the PMs might occur. Hence, a topology with a surface mounted rotor and a modular stator might not be convenient. Although segmentation of the PMs is a solution for the reduction of the PM losses, that option is not explored in this work. Moreover, it might contradict the recyclability principle, in which having a large number of PM pieces in the rotor in conjunction with the use of glue, might difficult the assembly and disassembly processes, and consequently the recovery of the PMs at the EoL of the machine.

In order to validate some of the models proposed in this chapter, the manufacturing of a demonstrator was carried out. The values calculated with simulations were validated with measurements, showing a fair agreement. It was possible to evaluate the losses in the rotor (i.e. PM losses, rotor back losses), and the behaviour of these with speed showed a similar trend as in simulations. It was found that the rotor back losses were the larger component in the no-load losses, since the rotor back of the machine used is composed by a solid iron cylinder. In addition, the bearing losses were large in comparison to

the overall power of the demonstrator. Hence, the efficiency had a low value, estimated approximately in 30%, which could be improved by adding more modules to the stator structure. Finally, the modularity of the stator, showed also an advantage in terms of assembly and disassembly, which is one of the goals when addressing recyclability. Part of the work performed in this chapter was published [75].

Chapter 3 HYBRID ROTOR 3D-FLUX MACHINE

The large values of PM losses due to slotting effect exhibited by the SM3D machine, required the exploration of alternatives to the surface mounted SM3D machine. Therefore, an introduction to the 3D-Flux Hybrid Rotor (HM3D) machine is carried out in this chapter. The study of such structure is based on the results obtained with the SM3D machine. As described in Chapter 1, the rotor of the machine is based on the HSM. A modular stator as in the SM3D machine is selected. As a start, the working principle of the machine is described, a 3D-FEM model is built in order to perform various sensitivity analyses. At the end, the dimensions of a machine for manufacturing of a prototype are defined.

3.1 DESCRIPTION OF THE WORKING PRINCIPLE

3.1.1 PRODUCTION OF PM FLUX

In order to illustrate the behaviour of the PM flux linkage of the HM3D machine, a preliminary geometry of a HM3D machine with 27 stator modules and 18 rotor (27/18) teeth was built. Figure 3.1 shows the complete geometry modelled in FEM. In addition, the solution of the magnetic flux density is illustrated in Figure 3.2.

A preliminary simulation at no-load was carried out. The analysis presented here will focus on the stator module labelled as "1" in Figure 3.3a. Then, a similar analysis as for the SM3D machine might be carried out. When rotor tooth is aligned with a stator module as in Figure 3.3a, a maximum value of Ψ_m is reached. If the rotor continues moving counter-clockwise, Ψ_m starts reducing, and an intermediate position is reached as in Figure 3.3d. This is important, since the point reached represents the "q-axis" of the HM3D machine. If the rotor continues moving in the same direction, the unaligned position is reached with a minimum value of Ψ_m, represented in Figure 3.3e. The magnetic flux density arrows represents both the direction of the flux and its magnitude. As it is observed in Figures 3.3b, 3.3d, and 3.3f the direction of the flux does not

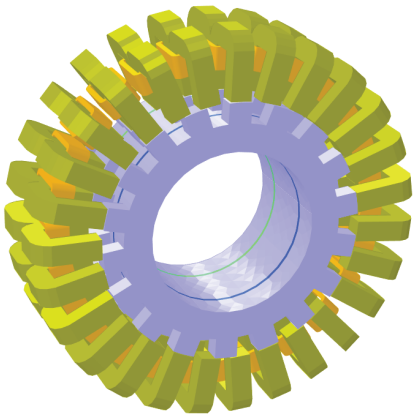

Figure 3.1. 3D-FEM model of the 27/18 HM3D machine.

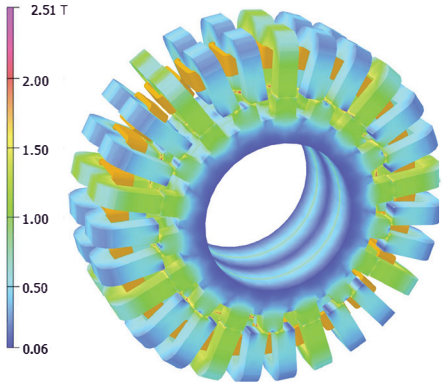

Figure 3.2. Magnetic flux density distribution of the 27/18 HM3D machine .

vary. In addition, the color of the arrows indicates the reduction of the PM flux in the transition from aligned, to unaligned.

The behaviour of Ψ_m in the HM3D machine is illustrated in Figure 3.4. As it was shown in Figure 3.3, the direction of the flux remained constant, consequently, Ψ_m shows a homo-polar trend. However, the behaviour of Ψ_m is still of sinusoidal nature, with an offset value. The introduction to the flux principle in the HM3D machine is complemented with the calculation of the PM flux linkage Ψ_m in phase 1 (Figure 3.3a). Figure 3.5 shows the evolution of Ψ_m with angular position. In addition, a Fourier analysis is performed to the waveform in order to determine its harmonic spectrum. The results are illustrated in Figure 3.6.

As discussed previously, the maximum value of Ψ_m in Figure 3.5 corresponds to the aligned position. In contrast, the minimum value of Ψ_m in Figure 3.5 corresponds to the unaligned position. As it was anticipated, the value of Ψ_m does not reach zero. Furthermore, the PM flux linkage Ψ_m has a large offset component $\Psi_{m(0)}$, as it is described by Figure 3.6. Furthermore, such value is larger than the fundamental $\Psi_{m(1)}$. Some preliminary conclusions may be drawn at this stage regarding these two facts:

- At unaligned position, there is permanent magnet flux flowing through the coils in the stator, which reduces the amplitude of the fundamental of Ψ_m.
- The saturation of the stator core will be increased, due to the offset of the waveform of the air-gap magnetic flux distribution.

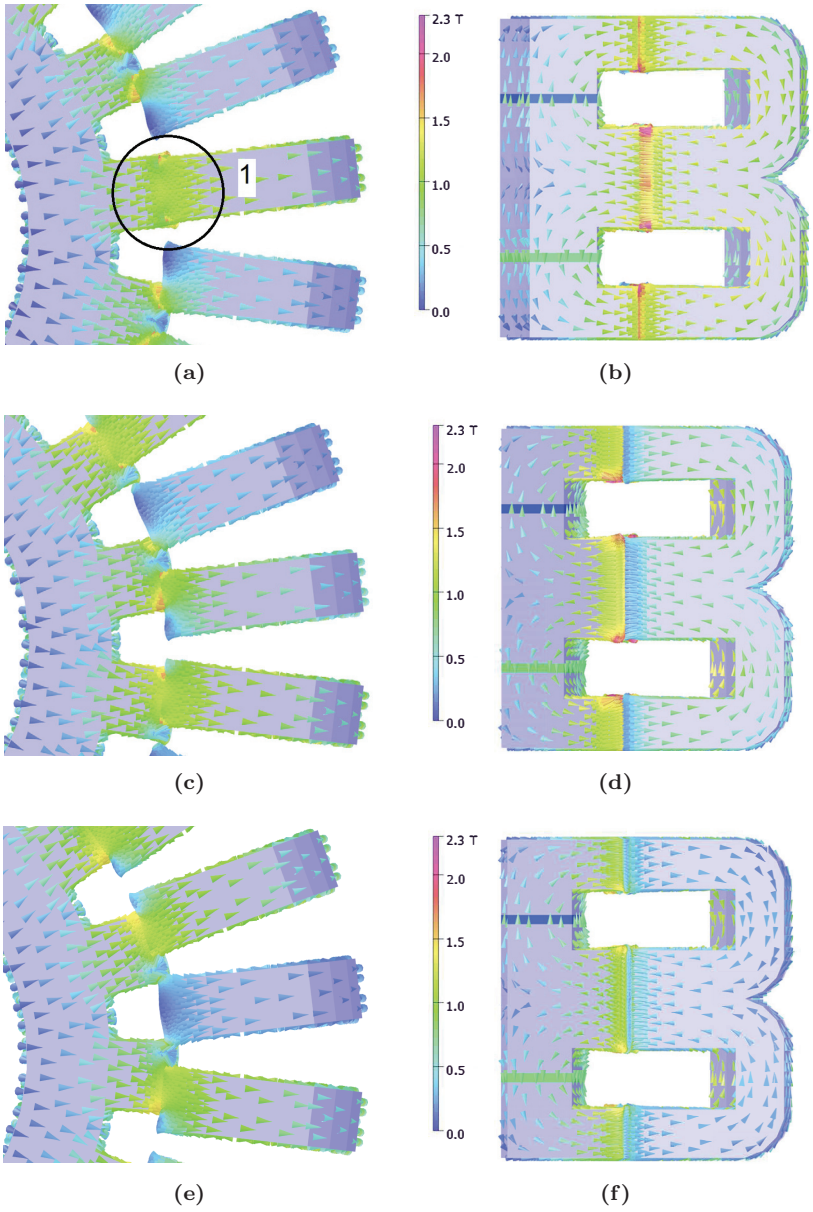

Figure 3.3. HM3D machine principle, *xy* and *yz*-plane views, (a) at aligned, (b) intermediate, and (c) unaligned, positions.

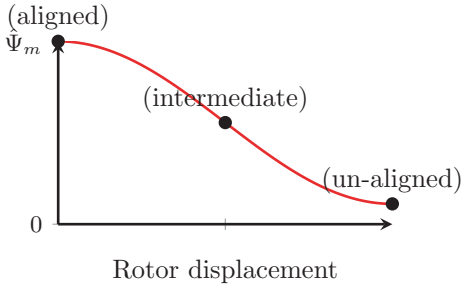

Figure 3.4. Permanent magnet flux distribution of the HM3D machine.

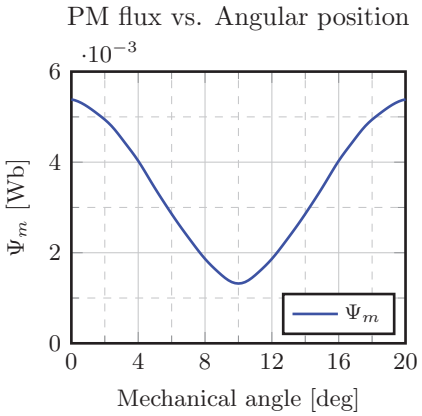

Figure 3.5. PM flux linkage Ψ_m variation with angular position, HM3D 27 stator modules and 18 rotor teeth.

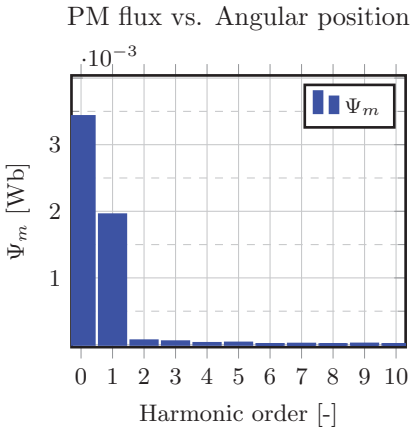

Figure 3.6. Harmonic spectrum of Ψ_m, 27 stator modules 18 rotor teeth.

- Due to the homo-polar nature of the waveform, the amplitude of $\Psi_{m(0)}$ will be equal or larger than the amplitude of the fundamental $\Psi_{m(1)}$.

In the following, several sensitivity analyses are performed in order to evaluate parameters such as permanent magnet flux, torque, inductance, power factor, etc. At first, the effect of the tooth width on the production of torque is evaluated. Secondly, the effect of the variation of the permanent magnet dimensions (i.e., thickness and width) is studied.

3.1.2 VARIATION OF THE TOOTH WIDTH

Figure 3.7 shows the geometry and the main parameters of an HM3D machine with a combination of 27 stator modules and 18 rotor teeth. Note that only 1/9 of the machine was modelled. The main dimensions of the selected HM3D machine are presented in Table 3.1.

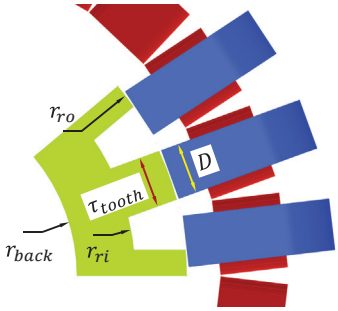

Figure 3.7. Description of the main dimensions HM3D machine 27/18.

Parameter	Value [mm]
Rotor outer radius r_{ro}	102
Rotor inner radius r_{ri}	84
Rotor back radius r_{back}	64
Stator outer radius r_{so}	153.5
Stator inner radius r_{si}	102.5
Window width win_w	20
Window height win_h	30
Module dimension A	16
Module dimension B	20
Module dimension C	35
Module dimension D	24
PM thickness l_m	3
Air-gap length l_g	0.5

Table 3.1. Main dimensions of a HM3D machine with 27 stator modules and 18 rotor teeth.

Permanent Magnet Flux

As it has been reported in [78] and [44], the variation of the tooth width has a major impact in the production of torque in the case of HSMs. Therefore, an evaluation of this dimension was carried out. The rotor tooth width was changed from 70% to 110% of the dimension D of the stator modules. Here, the term duty cycle $\%duty$ is introduced and follows the ratio:

$$\%duty = \frac{\tau_{tooth}}{D} \tag{3.1}$$

Where τ_{tooth} is the rotor tooth width and D is the thickness of the stator modules (Figure 3.7). Both the fundamental of the PM flux $\Psi_{m(1)}$ and the offset $\Psi_{m(0)}$ were estimated through 3D-FEM static simulations. The results are presented in Figure 3.8.

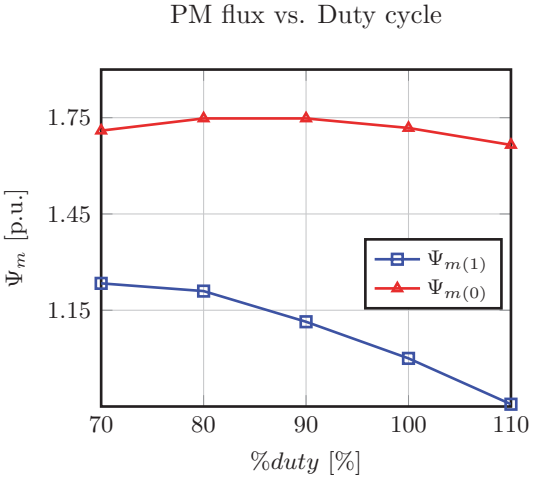

Figure 3.8. Variation of Ψ_m with rotor tooth width.

The base value selected for plotting of the results in Figure 3.8 corresponds to the value of permanent magnet flux at 100% of tooth width (i.e. the tooth width is equal to the dimension D of the stator module). The maximum value was found when the tooth width was of 70% with an increment of approximately 23%. Regarding the value of $\Psi_{m(0)}$, its behaviour is approximately constant, remaining at a value much larger than the fundamental $\Psi_{m(1)}$.

Torque

The production of torque with the variation of tooth width is also evaluated. A current density of 6.5 A/mm^2 was applied to the windings. As it was shown previously, the reduction of the tooth width yielded an increment of $\Psi_{m(1)}$.

However, the torque increases up to a $\%duty$=80%. As the effective area of the tooth is reduced, if a similar current is applied, saturation effect will start being significant, and the value of torque would not increase further. That may be observed in the behaviour of the torque, illustrated in Figure 3.9.

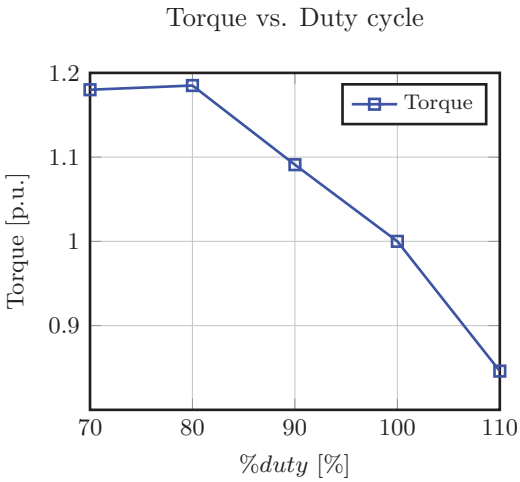

Figure 3.9. Variation of torque with rotor tooth width.

Inductance

The variation of the inductance with rotor teeth width was also investigated. The values are illustrated in Figure 3.11. It might be observed that the inductance L is reducing with the duty cycle $\%duty$, as a result of the decreasing teeth section. As it is shown in 3.10, the section of the tooth is changing with the variation of τ_{tooth}. Therefore, the equivalent area $A \times \tau_{tooth}$ changes. If such area reduces, the equivalent reluctance $\mathcal{R}_{gap}$ increases, and consequently, the inductance reduces. Note that the calculation of inductance with FEM was performed with (2.11).

Power Factor

The calculation of the power factor was performed with (2.12). Hence, both the reduction of inductance and increment of $\Psi_{m(1)}$ yield an improvement on the value of power factor as the tooth width is reduced.
As a conclusion of this preliminary study, the reduction of the duty cycle yielded an improvement of PM flux production of approximately 20% when compared to the initial $\%duty$= 100%. In addition, as described in Figure 3.9, a maximum value of torque is reached when the rotor teeth width is 80% of the dimension

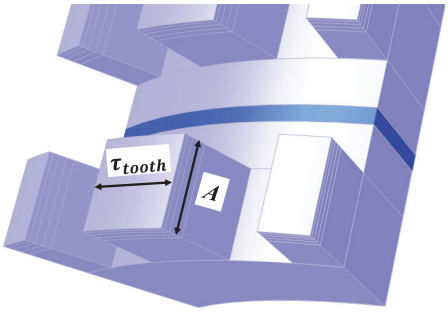

Figure 3.10. Rotor tooth dimensions.

D of the module. So that, an increment on torque production of approximately 18% was achieved. The power factor is also improved with the reduction of the tooth width, showing a maximum value when the tooth width is 70%. Finally, since the maximum torque was obtained with a tooth width of 80% this value was selected for the coming analyses.

3.1.3 STUDY OF THE VARIATION OF THE PM THICKNESS

In the following analyses, both PM thickness l_m and width w_m are varied in order to evaluate the effect in various parameters. Figure 3.13 illustrates these two dimensions. The dimensions of the machine described in Table 3.1 were kept, and a $\%duty$= 80% was selected.

Permanent Magnet Flux

The impact of the variation of the PM ring thickness l_m was investigated by increasing its value from 3 to 7 mm. Similarly to the study on the variation of the rotor tooth width, both $\Psi_{m(0)}$ and $\Psi_{m(1)}$ were calculated.
Figure 3.14 shows that the increment of $\Psi_{m(1)}$ reaches approximately 20%, when increasing l_m from an initial value of 3 mm to 7 mm. It is important to note that for a larger value of PM thickness the increment of $\Psi_{m(1)}$ is not significant, due to the PM leakage. Such behaviour is reflected in the value of $\Psi_{m(0)}$ which is much larger when contrasted to $\Psi_{m(1)}$. Therefore, selecting a low value of PM thickness l_m might result convenient.

Torque

The torque was estimated for similar values of PM thickness. A current density of 6.5 A/mm^2 was applied to the windings. The results are shown in Figure

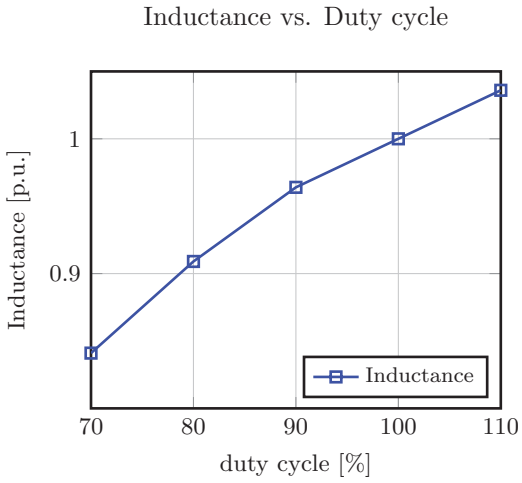

Figure 3.11. Variation of inductance with rotor tooth width.

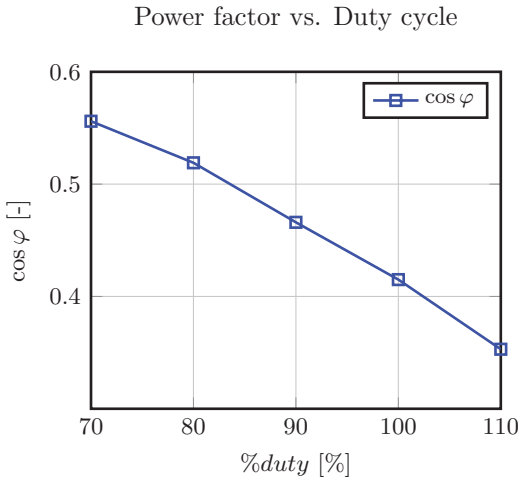

Figure 3.12. Variation of power factor with rotor tooth width.

3.15. An increment of torque of approximately 11% is reached with a PM ring thickness l_m of 7 mm. In addition, increasing the PM volume to almost twice only yields an increment of 10% in torque production, which is not efficient in terms of PM utilization.

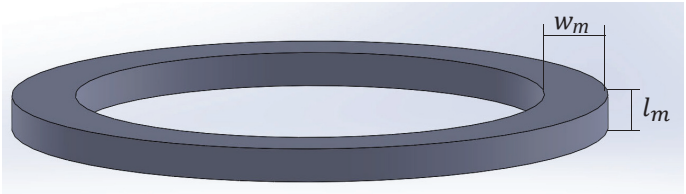

Figure 3.13. PM ring on the rotor structure.

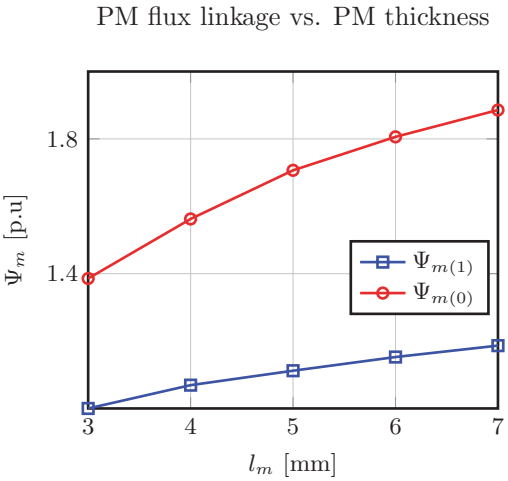

Figure 3.14. Variation of Ψ_m with PM thickness l_m.

Inductance

Continuing the analysis of the HM3D machine at load, the calculation of the inductance for every case of PM thickness was performed. The results are reported in Figure 3.17. As it is observed, the inductance starts reducing as the PM thickness is increased. As the only dimension varying is the PM thickness, such variation is directly related with the reluctance of the PM ring air-gap PM_{gap}, as it is show in 3.16. The reduction of the inductance reaches a minimum of approximately 79%.

Power Factor

As it was shown previously, the inductance is varying with the thickness of the PM l_m. This section of the report is intended to show the effect of this behaviour in the power factor. The results of power factor are illustrated in Figure 3.18. As it is expected, the power factor is increasing with the increment

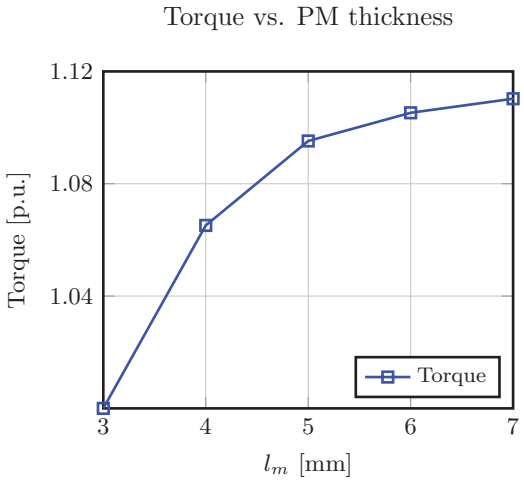

Figure 3.15. Variation of torque with PM thickness l_m.

of PM thickness.
Some preliminary conclusions might be drawn from the study performed in previous sections. It was found that a reduction of the tooth width by 20%, yielded an increment of torque of approximately 18%. In addition, it was found that varying the PM thickness l_m did not yield substantial increment. Furthermore, it yielded an increment of the PM leakage, reflected in the increase value of $\Psi_{m(0)}$. For the coming analysis a PM thickness l_m= 4mm was selected.

3.1.4 STUDY OF THE VARIATION OF THE PM WIDTH

The PM width w_m (Figure 3.13) was varied at 3 mm intervals. In order to keep the most dimensions of the HM3D machine fixed, the inner diameter of the ring was varied along with the inner rotor back radius r_{back}. Similar dimensions of the machine analysed in 3.1.3 were adopted. However, a PM thickness of l_m=4 mm was selected. The PM width w_m was varied from 10 to 25 mm.

Permanent Magnet Flux

Figure 3.19 shows the behaviour of the PM flux linkage Ψ_m with the increment of w_m.
Both $\Psi_{m(0)}$ and $\Psi_{m(1)}$ follow a similar trend, with a constant deviation of approximately 40%. In addition, the overall increment of Ψ_m is of approximately 40%. Which shows that increasing the PM ring width w_m has a much more

Figure 3.16. PM equivalent air-gap.

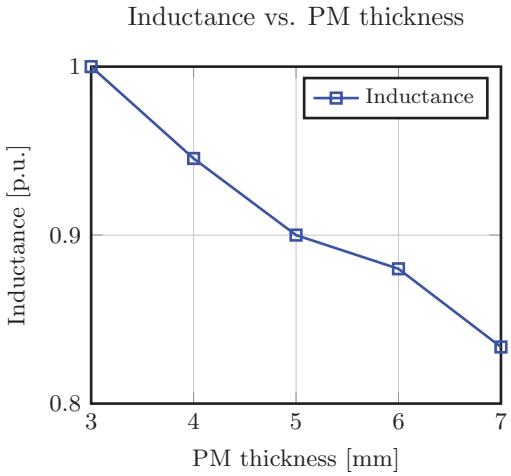

Figure 3.17. Variation of inductance with PM thickness l_m.

significant effect in the production of PM flux linkage when contrasted with the increments obtained varying the PM thickness l_m in 3.1.3.

Torque

Similarly to the calculation of Ψ_m, the increment of the torque is of approximately 40% with the variation of w_m. Which confirms that the variation of w_m might be more convenient in an optimization process of the HM3D machine. The results with an increment of approximately 40% of torque are shown in Figure 3.20.

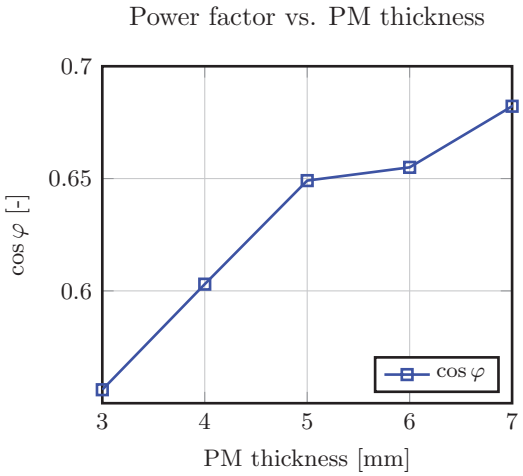

Figure 3.18. Variation of power factor with PM thickness l_m.

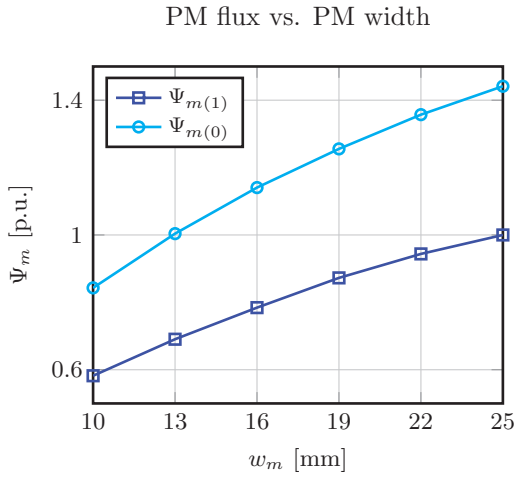

Figure 3.19. Variation of Ψ_m with PM width w_m.

Inductance

The calculation of the inductance shows a decreasing behaviour with the increment of w_m. As the only parameter varying is the PM width, and the PM flux linkage is increased significantly, the reduction of the inductance, might be the result of saturation of the stator. However, such reduction is of approximately 4%, which is low if it is compared to the reduction of inductance when

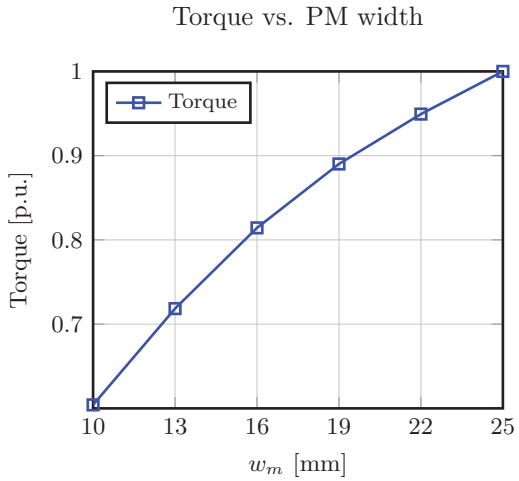

Figure 3.20. Variation of torque with PM width w_m.

increasing the PM thickness l_m (approx. 17%).

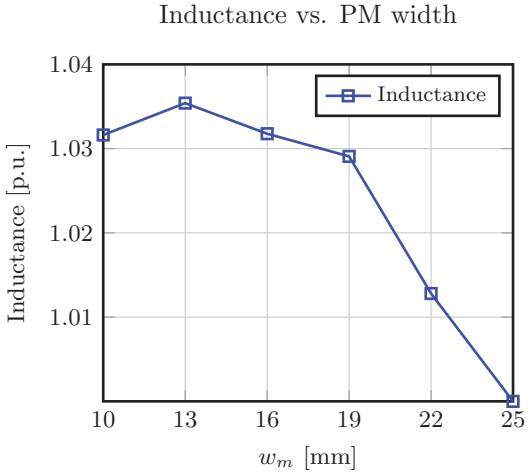

Figure 3.21. Inductance vs. PM width.

Power Factor

As Ψ_m is increasing, and the inductance is reducing with the increment of w_m, the result is the increment of the power factor, which is illustrated in Figure

3.22.

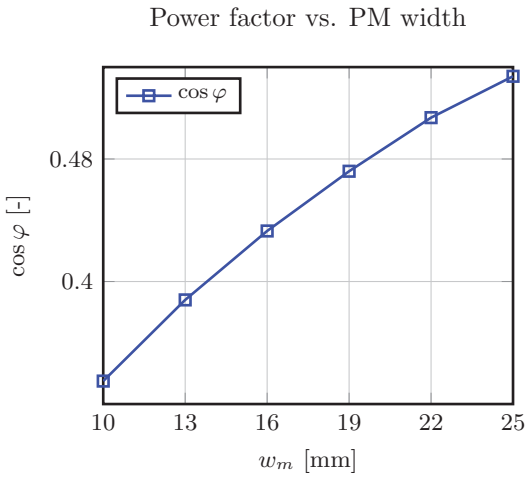

Figure 3.22. Power factor vs. PM thickness.

3.2 PRELIMINARY CALCULATION OF THE HYBRID ROTOR 3D-FLUX MACHINE

Following the results obtained in the previous analyses, a preliminary HM3D machine was selected. Furthermore, in order to perform a comparison, similar stator dimensions as for the SM3D studied in Chapter 2 were selected. In addition, a rotor with 8 teeth, a PM ring with l_m= 4 mm and w_m= 25 mm was selected. Initial calculations of torque were performed. The remaining dimensions of the HM3D machine selected are summarized in Table 3.2.
The calculated values of torque with various values of current density are shown in Figure 3.23.

Parameter	Value [mm]
Rotor outer radius r_{ro}	115
Rotor inner radius r_{ri}	89
Rotor back radius r_{back}	64
Stator outer radius r_{so}	166.5
Stator inner radius r_{si}	115.5
Module dimension A	16
Module dimension B	20
Module dimension C	35
Module dimension D	24
PM thickness l_m	4
Air-gap length l_g	0.5

Table 3.2. Main dimensions of a HM3D machine with 12 stator modules and 8 teeth.

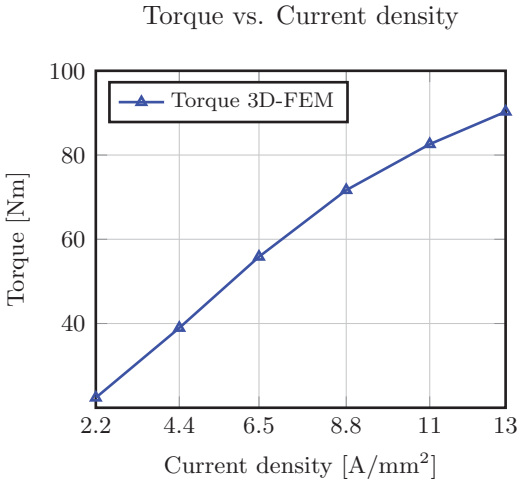

Figure 3.23. 3D-FEM calculated torque HM3D machine.

As it may be observed, the torque of the HM3D machine is significantly lower than the torque of the SM3D machine in Figure 2.28 of Chapter 2. Hence, a comparison between the PM flux linkage of the SM3D and the HM3D machines is presented in Figure 3.24. Hence, it is demonstrated that the lower value of

torque is a result of the lower value of the fundamental of the PM flux linkage $\Psi_{m(1)}$ of the HM3D machine.

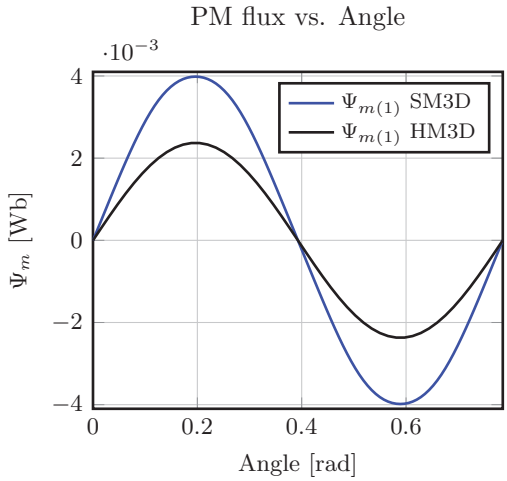

Figure 3.24. PM flux linkage vs. mechanical angle.

3.3 INCREMENT OF TORQUE PRODUCTION

The low value of the fundamental of the PM flux linkage $\Psi_{m(1)}$, poses a different scenario. It was required to investigate alternatives in order to improve the torque production of the HM3D machine. Hence, it was decided to evaluate the Vernier's, or magnetic gear principle. Such principle is illustrated in Figure 3.25 for a surface mounted PM machine [59].
Although the geometry in Figure 3.25 corresponds to a linear machine, the same principle may be applied to a rotating electrical machine. Consequently, the force in a machine like the one in Figure 3.25a is given by the ratio of the product of the flux linked by the PMs $\Delta\Psi$, the current in the windings Ni and the dimension D travelled by the PMs on the rotor. In the case of the machine in Figure 3.25a:

$$F_{av} = \frac{\Delta\Psi \cdot Ni}{D} \tag{3.2}$$

Then, if the dimension D is equally sub-divided in a given number of segments n_{seg}, the machine in Figure 3.25b is obtained. Hence, the resulting force F_{av} is increased by n_{seg}, that is:

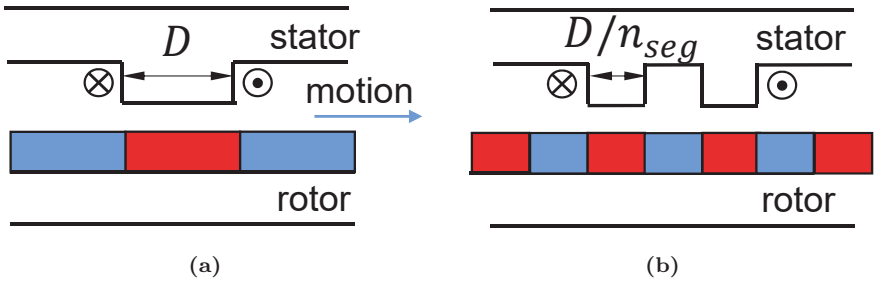

Figure 3.25. Demonstration of Vernier's principle, (a) conventional machine, (b) multiple teeth per pole topology.

$$F_{av} = \frac{\Delta\Psi \cdot Ni}{D} n_{seg} \tag{3.3}$$

Given that the variation of both PM flux $\Delta\Psi$ and MMF of the windings Ni remain constant, the increment of the force would be proportional to the factor n_{seg}. Nevertheless, (3.3) neglects phenomena such as leakage, and fringing fluxes. Hence, in order to investigate the increment of the torque, with the increment of the factor n_{seg}, an HM3D machine with 6 stator modules and 8 rotor teeth was selected. The selection of such combination is based on two main constrains:

- The fundamental frequency.
- Manufacturing complexity.

The former, is related to the limitations of the converter required for feeding the machine. The latter, is related to the fact that having a large amount of stator modules would make the assembly of the stator a complex task. Furthermore, for a fixed air-gap radius, the increment of the number of modules per coil will yield a reduction of the dimension D of the stator modules. Consequently, requiring a narrow cut of the modules, putting under risk their integrity. Considering these two constrains, four models were built in FEM for the calculation of torque, among other parameters.

The geometries of the original machine and machines with sub-division of the stator modules and rotor teeth by factors n_{seg} of 2, 4 and 8 are illustrated in Figures 3.26a, 3.26b, 3.26c, and 3.26d, respectively. Note that only half of the machine is described. The calculations were performed with the dimensions of A, B, and C of the modules, as well as, air-gap length l_g as described in Tables 3.1 and 3.2. In addition, some changes to the dimensions were introduced:

- The air-gap radius r_{ro} was selected as 91 mm.
- A value of PM thickness l_m=4 mm was adopted.
- With the selected dimensions of l_g, A, and C, the outer stator radius r_{so} was 142.5 mm.
- The calculation of the number of turns was performed for a nominal voltage of 230 V rms, line to neutral.

Such changes were performed in an attempt to reduce the dimensions of the HM3D machine. Thus, increasing the torque density. Table 3.3 summarizes key dimensions of the machines selected along with the results of 3D-FEM calculations. Note that the calculated values of inductance and PM flux linkage are given for one turn. That is, they are required to be scaled by the number of turns. Additionally, the iron losses were estimated with electrical sheet.

Parameter	original	n_{seg}=2	n_{seg}=4	n_{seg}=8
Rotor inner radius r_{ri} [mm]	62.2	76.6	83.8	87.4
Rotor back radius r_{back} [mm]	38.4	58.9	68	72.4
Dimension D of the module [mm]	36	18	9	4.5
Synchronous Inductance [μH]	0.84	1.11	1.30	1.43
Power factor [-]	0.34	0.26	0.17	0.08
PM flux (fundamental) [mWb]	0.98	0.95	0.71	0.37
Torque @ 6.5 A/mm^2 [Nm]	17	31	44	46.5
Iron losses @ 1000 rpm [W]	91.3	152.2	368.5	1085.5
PM mass [kg]	0.45	0.45	0.45	0.45
Number of turns [-]	68	29	13	6

Table 3.3. Main parameters of a HM3D machine with 6 stator modues and 8 teeth, and n_{seg}=2, 4, and 8.

An increment of PM flux leakage is observed in the increasing magnetic flux density in the stator modules at unaligned position in Figures 3.26a to 3.26d. Such increment is the result of the variation of the equivalent air-gap length. Since the surface of the stator modules facing the air-gap is flat, the equivalent air-gap length is reducing as the dimension D of the modules is reducing for a fixed value of rotor diameter. Figure 3.27 is intended for giving a better explanation of the variation of the air-gap with the increment of the factor n_{seg}.

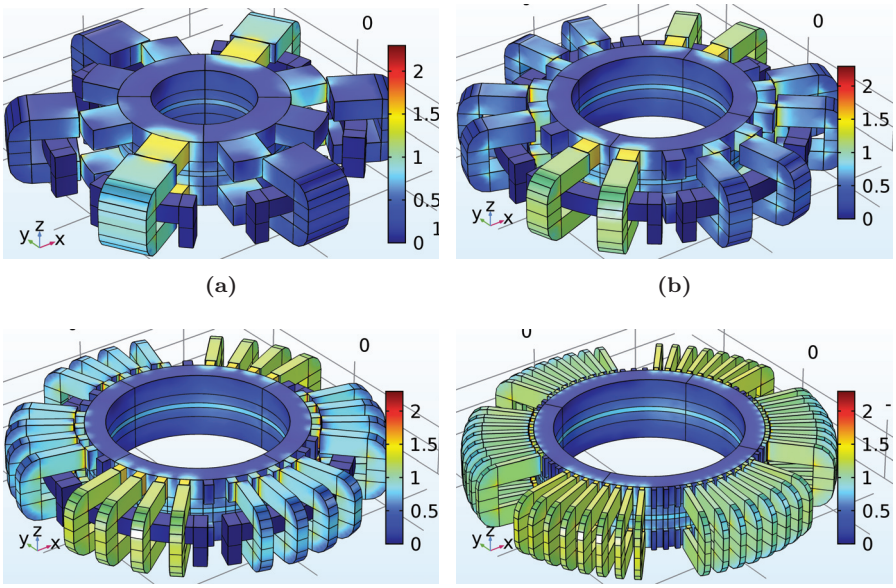

Figure 3.26. Magnetic flux density distribution of the HM3D machine at no-load; (a) original geometry, (b) n_{seg}=2, (c) n_{seg}=4, and (d) n_{seg}=8.

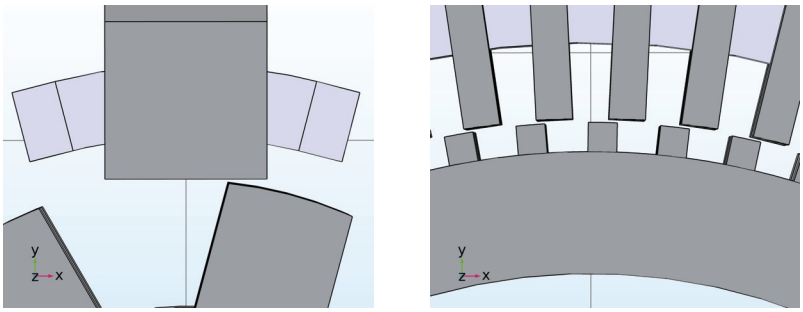

Figure 3.27. Detail of the air-gap of the HM3D machine with 6 stator and 8 teeth; (a) original geometry, and (b) n_{seg}=8.

Some preliminary conclusions may be drawn from the results in Table 3.3.

- Increasing the number of sub-divisions further than n_{seg}=4, would not yield substantial increment on the production of torque.

- The increment of n_{seg} yielded an increment of the fundamental frequency, which in turn, increases the iron losses of the machine.
- Increasing n_{seg} results in the variation of the equivalent air-gap length. Which in turn, increases both the flux leakage in unaligned position and the inductance. Consequently, as n_{seg} increases, the power factor reduces drastically.

At this point, the main goal was to maximize the torque density of the HM3D machine. As it was demonstrated with the results of the analysis performed in this section, the machine with n_{seg}=4 showed the larger increment of torque. In addition, with the use of amorphous material, the consequent increment of fundamental frequency was not a concern regarding iron losses. Therefore, the HM3D machine with 6 stator modules, 8 rotor teeth and 4 subdivisions (Figure 3.26a) was selected for manufacturing of a prototype.

3.3.1 PM LOSSES OF THE HYBRID ROTOR 3D-FLUX MACHINE

One of the main hypothesis was the possible reduction of PM losses by placing the PM between stacks in the rotor. In order to estimate the PM losses, transient simulations were run at no-load. In addition, similar conductivity was set to the PM region in the rotor as in the SM3D machine case (i.e. 1.25 MS/m). The distribution of the current density inside the PM region is shown in Figure 3.28.

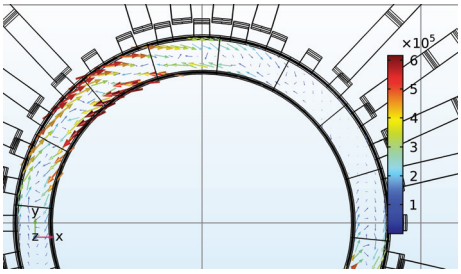

Figure 3.28. Current density in the PM ring at 2300 rpm, n_{seg}=4. t=685 μs.

Finally, the PM loss waveform during one electrical period is shown in Figure 3.29, where it is observed the oscillation of the losses over one electrical period. In addition, the average value of the PM losses was estimated in approximately 6 W, which is significant lower in comparison to the SM3D machine which reached approximately 1.8 kW.

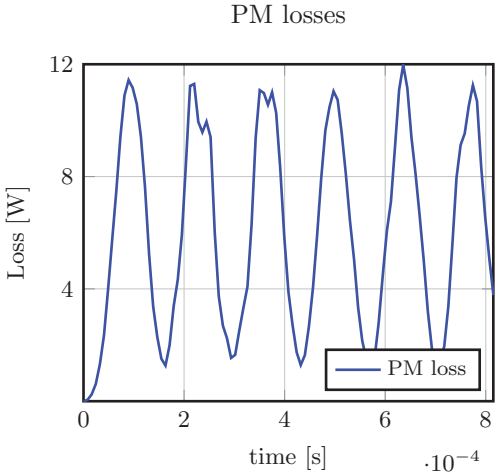

Figure 3.29. PM losses of the HM3D machine with n_{seg}= 4.

3.4 A HYBRID ROTOR 3D-FLUX PROTOTYPE

In this section a description of the assembly process of the HM3D is carried out. In addition, the test results of the manufactured prototype are presented along with the simulation results in order to validate the models developed throughout this thesis work. The CAD model of the HM3D machine is shown in Figure 3.30. Both Figures 3.30a and 3.30b give an insight of the main components and the sequence to be followed in the assembly of the HM3D machine. Note that the windings are not included in the CAD model. Special emphasis is put on the description of the assembly process, given the modular configuration of the stator aimed at recycling the PMs. In addition, the main dimensions of the demonstrator are summarized in Table 3.4.

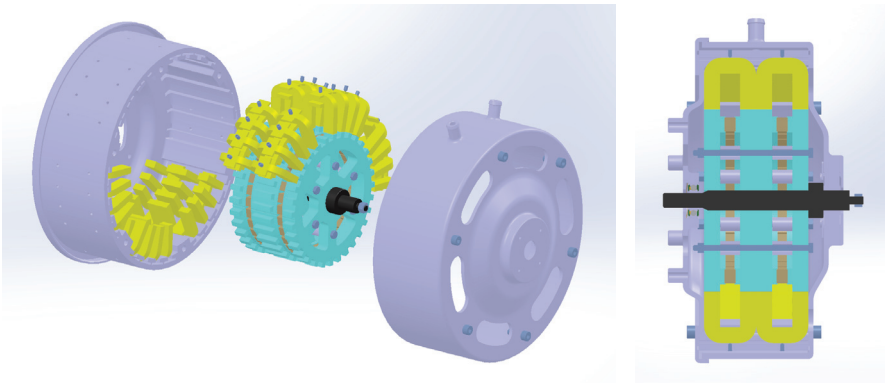

(a) (b)

Figure 3.30. CAD model of the HM3D machine; (a) exploded view, and (b) section view.

Parameter	Value [mm]
Rotor outer radius r_{ro}	91
Rotor inner radius r_{ri}	84
Rotor back radius r_{back}	68
Stator outer radius r_{so}	142.5
Stator inner radius r_{si}	91.5
Module dimension A	16
Module dimension B	20
Module dimension C	35
Module dimension D	9
PM thickness l_m	4
Air-gap length l_g	0.5
Stack length L_{stack}	104

Table 3.4. Main dimensions of the HM3D prototype.

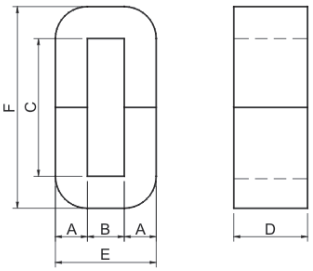

Main dimensions of the amorphous C-shaped cores.

VALEO Electrical Systems was in charge of the mechanical design and manufacturing of the components of the HM3D machine. During the definition of

the mechanical design of the prototype of the HM3D machine, changes were required because of various issues. For example, the lead time of some of the components, the materials and dimensions available at the moment of the definition, the standard parts used by the manufacturer, etc. Therefore, it is worth to highlight the main changes of the final prototype in comparison to the models proposed from the beginning of the project:

- The rotor PM rings defined in the models were changed to PM blocks. The dimensions of the PM blocks, according to Figure 2.4 in Chapter 2 are: l_m=11 mm, w_m=13.8 mm, and h_m=12.1 mm.
- The material of the stator, was changed to standard electrical sheet.
- The manufacturing of the windings was carried out at Aalborg University.

3.4.1 ASSEMBLY OF THE PROTOTYPE

Stator Assembly

The stator bracket was defined with a slotted structure for accommodating the modules, which are fixed by screws. Such concept requires the stator modules to have a defined shape, which the suppliers of amorphous C-shaped cores could not provide. Therefore, the material selected for the stator modules was electrical sheet, specifically M300-35A laminations. In addition, the C-shaped cores were replaced by E-shaped cores. The stator modules supplied are described in Figure 3.31. With a general view in Figure 3.31a, and a detailed view of the stacking in the middle region in Figure 3.31b. Nevertheless, having the laminations stacked as in the original amorphous C-shaped cores (Figure 1.12c) would have been beneficial. That is, having the laminations stacked perpendicular to the direction described in Figure 3.31 facilitates the use of alternative laminations, such as Grain Oriented electrical sheet. Consequently, having reduced iron losses and improved performance due to the higher saturation level, when compared with Non-Oriented Grain electrical sheet.

The use of E-cores, as the ones illustrated in Figure 3.31, results in the increment of eddy current losses in the middle region of the core. In addition, the weld on the surfaces facing the air-gap, might result in the increment of losses and in a reduction of the performance of the machine. The effect of the welds on the performance of the machine has not been accounted for in the models developed so far. However, a investigation of the impact of the welds in the stator modules is carried out in the measurement sections of the report.

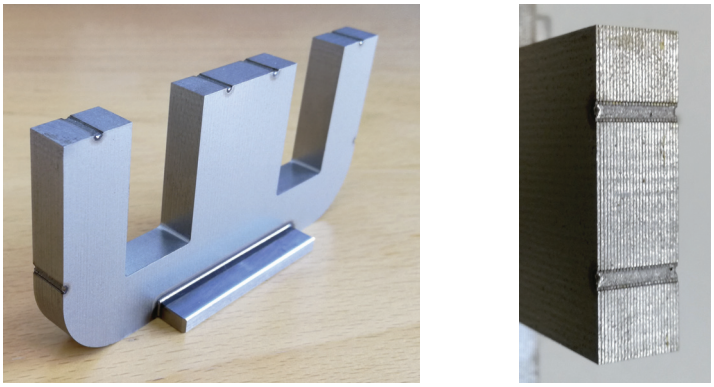

(a) (b)

Figure 3.31. Stator modules in electrical sheet; (a) general view, and (b) zoomed view of the stack.

The assembly process started with the manufacturing of the coils. After the modules corresponding to one coil were placed on the stator bracket, the coils were inserted manually and held in place with fibreglass wedges. That is, standard materials were used for the assembly of the coils to the stator frame, which is convenient when considering the recyclability of the machine. The assembly of the initial two coils are shown in Figure 3.32. The manufacturing of the winding was carried out at Aalborg Universities facilities, and the manufacturing was performed by hand. Hence, the slot fill factor of 0.5 defined in the models was not achieved.

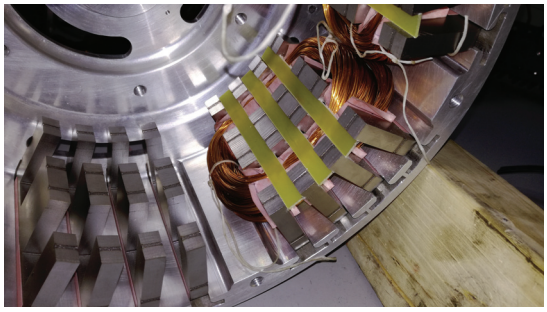

Figure 3.32. Assembly of modules and coils.

Once the windings were completed and the connections made, the stator did not required further assembly process, showing a fair degree of simplicity. Figure 3.33 shows the stator completely assembled.

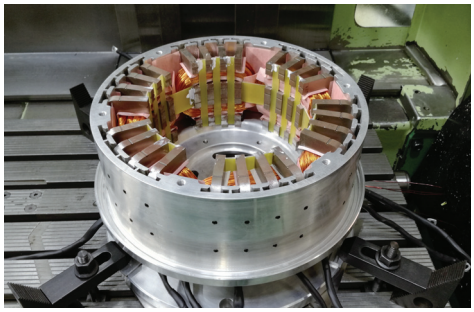

Figure 3.33. Completed assembly of the stator.

Rotor Assembly

Although the PMs of the rotor were conceived as rings at modelling stages, difficulties with the supply were the main reason for using PM blocks. Despite of the simplicity on the assembly of the PM blocks on the rotor stacks, it was necessary to verify a correct alignment between rotor stacks. For example, if a PM ring was used, it would be expected that the time of assembly was reduced. In addition, using a ring would be more convenient since at the EoL of the machine it would be simpler to manipulate a single component. That is, having least PM pieces when addressing the recyclability of PM material could be beneficial. However, having simple shapes, like PM blocks could reduce the complexity in their definition and manufacturing.

The PM blocks supplied are made of sintered NdFeB material protected by a sprayed layer of epoxy. The grade of the PM blocks corresponds to F40SH, with a remanence B_r of 1.31 T, as it is stated in the manufacturers catalogue [79]. Having a layer of epoxy facilitates the recyclability of the PMs since the removal of coating materials might pose a disadvantage when processing the PM material at the recycling stages.

Similarly to the stator assembly, the assembly of the PM blocks on the rotor stacks was performed manually. Part of the assembly is shown in Figure 3.34. In contrast, for completing the assembly of the rotor, the use of a lathe was required due to the forces generated when placing two rotor stacks together. The process of the assembly of the rotor is shown in Figures 3.35a and 3.35b. Noting that for fixing the PMs no glue was required, which is crucial when focusing on recycling.

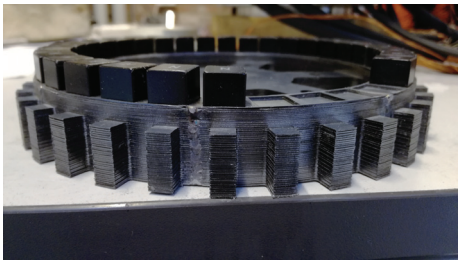

Figure 3.34. Assembly of the PM blocks in one of the rotor stacks.

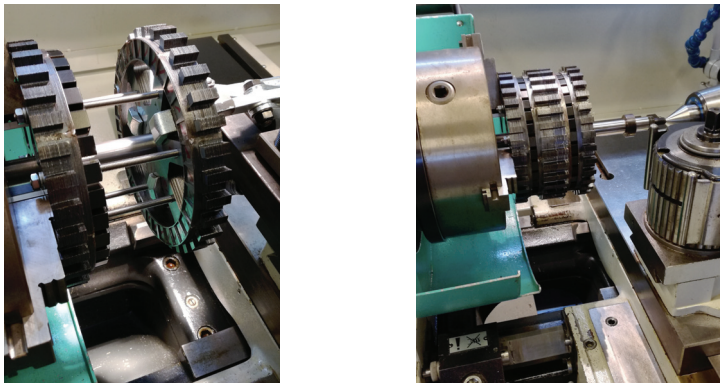

(a) **(b)**

Figure 3.35. Rotor assembly on a lathe; (a) stack assembly, and (b) shaft assembly.

Quality issues were identified in the rotor stacks which cutting, stacking and alignment among laminations and rotor stacks might not guarantee a constant surface on the area facing the air-gap region. In addition, the welds create a path for eddy currents which are not accounted for in the models developed.

Complete Assembly

The assembly of the complete machine was carried out on a milling machine in order to guarantee the correct alignment of both the rotor and stator components. The process is shown in Figure 3.38.

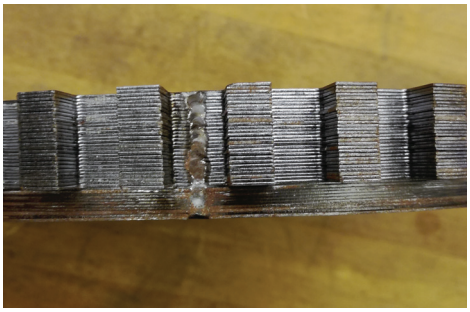

Figure 3.36. Rotor stack zoomed view.

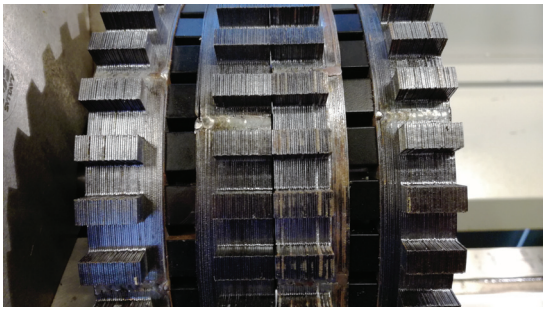

Figure 3.37. Rotor assembly general view.

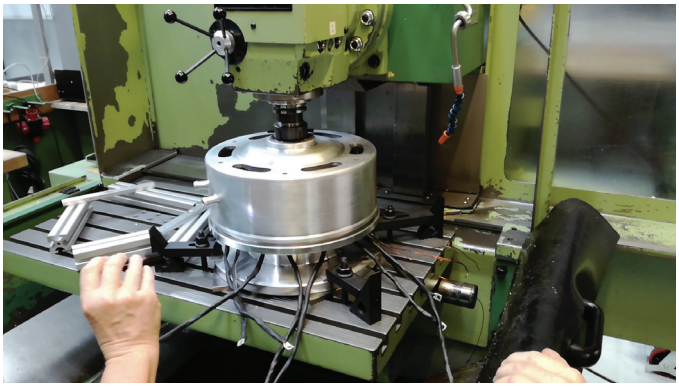

Figure 3.38. Complete assembly.

3.5 TESTING OF THE HM3D MACHINE

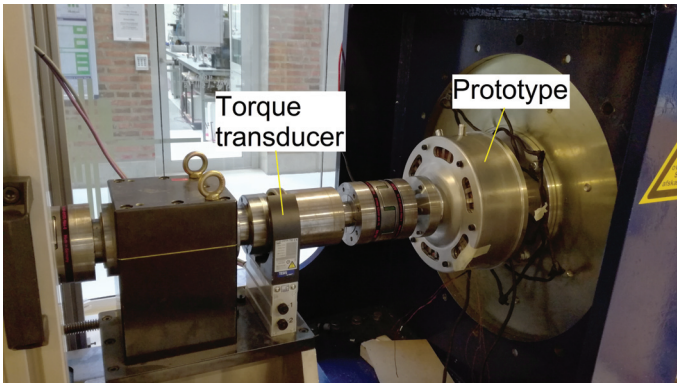

Figure 3.39. Test set-up of the HM3D machine as generator.

3.5.1 NO-LOAD BACK-EMF

The test set-up is described in Figure 3.39. The no-load back-EMF test was performed coupling the prototype to a servo-motor, and measuring the back-EMF in the three phases. At a speed of 500 rpm, the voltages obtained are illustrated in Figure 3.40. Note, that the values correspond to phase voltages (i.e. line to neutral). A deviation of the amplitude in each phase was estimated at 4%. Such deviation, might be the result of an eccentricity of the stator. Given that the stator modules are placed individually, it is likely that the air-gap length is not uniform around the circumference of the stator.

A comparison between the back-EMF calculated with 3D-FEM, and measured is illustrated in Figure 3.41. There are substantial differences between the two waveforms, in both amplitude and shape. Therefore, it was decided to evaluate the impact of the welds on the middle region of the stator modules as it is illustrated in Figure 3.42a. In order to investigate this hypothesis, a modification was performed on the 3D-FEM model. It consisted in the introduction of a "short circuited" coil, represented by a conductive region built around the stator module, as it is illustrated in Figure 3.42b. Given that the direct measurement of the resistance introduced by the welds was not possible, the dimensions of the short circuited coils in the model were approximated with the dimension of the welds in Figure 3.42a. The conductivity of the material of the short-circuited coils was varied until a back-EMF waveform similar to the measured value was obtained. Such conductivity was found to be 1.68 MS/m.

Additionally, the material was modelled with a relative permeability μ_r=4000. Figure 3.43 illustrates the calculated back-EMF with the modification.

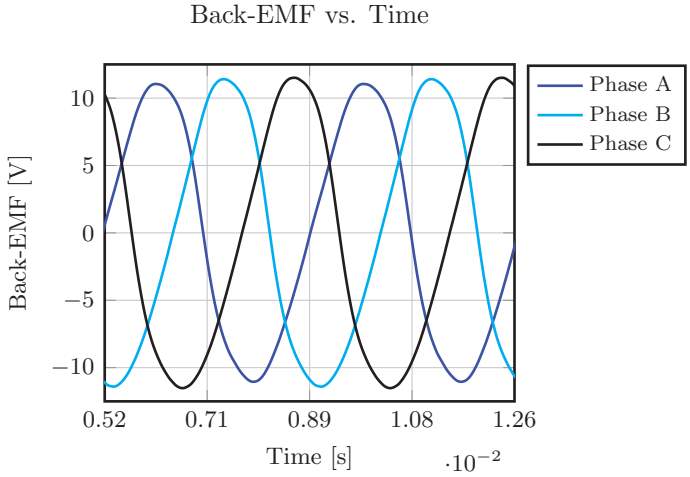

Figure 3.40. Measured back-EMF vs. time at 500 rpm.

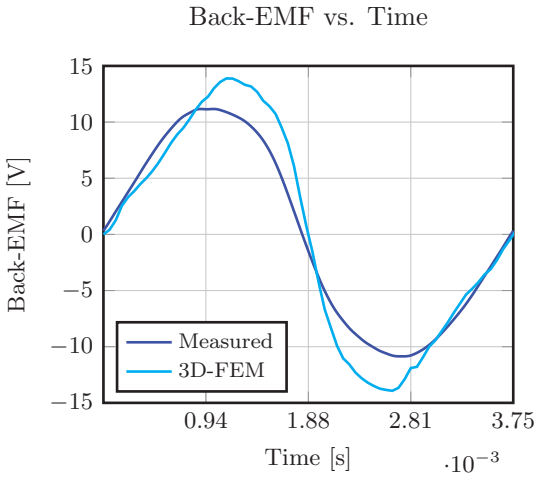

Figure 3.41. Back-EMF vs. time at 500 rpm.

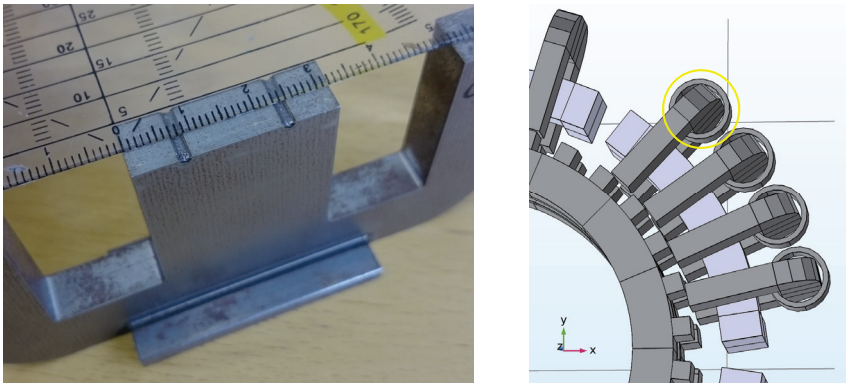

(a) (b)

Figure 3.42. Stator modules; (a) welds in the middle region, (b) "short circuited" coils modelled in 3D-FEM.

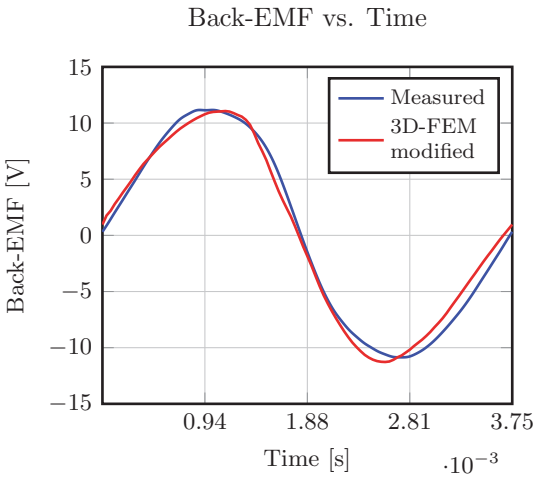

Figure 3.43. Back-EMF vs. time @ 500 rpm.

It is evident the incidence that the welds have on the back-EMF. Hence, the back-EMF was measured at various speeds. The measured rms values of back-EMF are illustrated in Figure 3.44 along with the calculated results, with both original and modified FEM models.

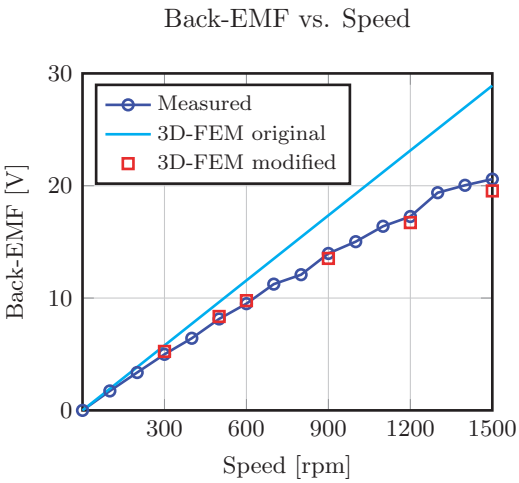

Figure 3.44. Measured back-EMF vs. speed.

Ideally, the back-EMF increment with speed should follow a linear trend as it is observed in the calculated values with the original FEM model in Figure 3.44. However, the welds on the stator modules facilitate a path for the flow of eddy currents. Such currents create a flux which opposes the main PM flux linkage in the module. Hence, the resulting PM flux linkage is reduced, and consequently, the back-EMF is reduced. As the speed increases, eddy currents are larger, and the reduction of the back-EMF is larger. In Figure 3.44 the measured back-EMF and the calculated with the modified model follow such behaviour.

3.5.2 TORQUE MEASUREMENT

The set-up used on the measurement of the torque is described in Figure 3.45. The prototype was connected to a VLT® AutomationDrive FC302 from Danfoss. Readings of torque, speed, and input power were registered. In order to perform a comparison between the measured and calculated values, the input current measured was applied to the models developed in FEM. The results of both measured and simulated torque, at 500 rpm are shown in Figure 3.46.

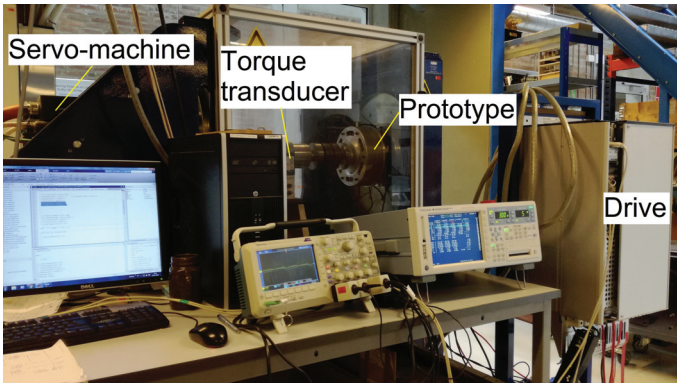

Figure 3.45. Set-up for measuring torque with a load machine.

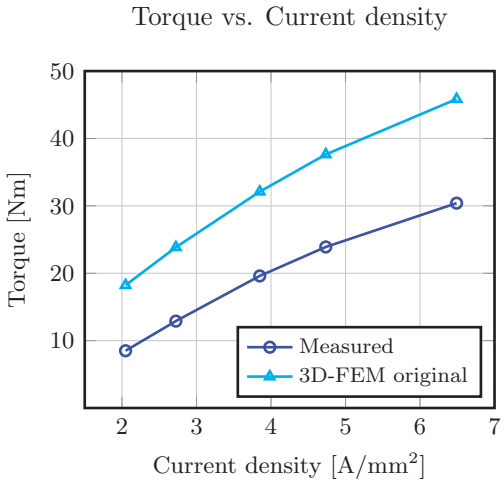

Figure 3.46. Measured and calculated steady state torque at 500 rpm.

As it is observed, the calculated value of torque follow a similar trend with the measurements. However, the deviation is large. The absolute error varies from approximately 5 to 15 Nm. It is worth mentioning that only iron losses were calculated with FEM. Hence, the mechanical losses and the additional losses induced by the PWM modulation are not included in the calculation of the torque. In addition, the effect of the welds on the torque production, was not evaluated. Despite the deviations obtained in the calculation of torque, the efficiency was measured at various working points of torque and speed. Figure 3.47 shows the efficiency measured.

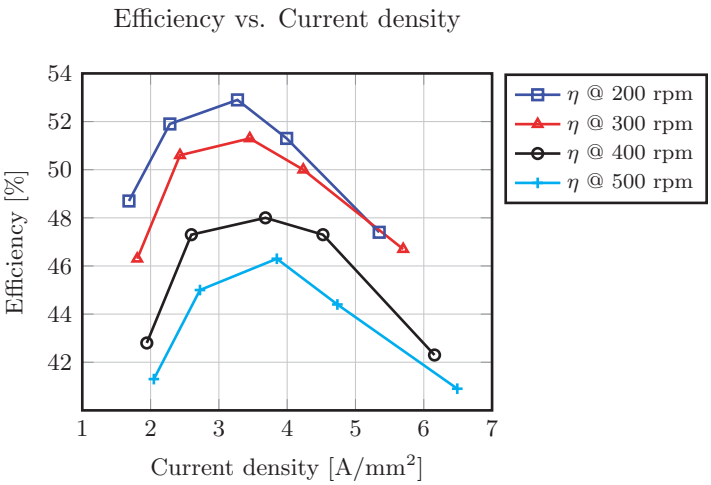

Figure 3.47. Efficiency vs. current density at various speeds.

Due to the high level of rotational losses, it was not possible to reach higher speeds and higher torque-speed points without tripping the over-current protections of the driver. In addition, the power factor obtained varied from approximately 0.9 to 1.9. The large level of losses and low value of torque are reflected in poor efficiency as it is illustrated in Figure 3.47. In order to isolate the incidence of both the PWM modulation and the welds in the stator modules on the measurement of the torque, a DC torque test was performed. Such test consisted in attaching a metallic arm to the shaft, in order to rotate it manually, while the windings were connected to a DC power source. Figure 3.48 illustrates the set-up used during the test. The peak value of torque was registered at various levels of DC current. The connection used during the test is illustrated in the circuit diagram in Figure 3.49.

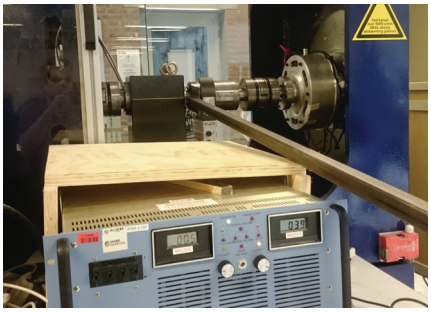

Figure 3.48. Set-up for measurement of torque with a DC power source.

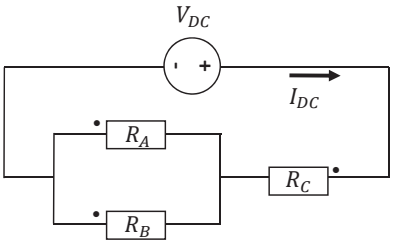

Figure 3.49. Circuit for measuring torque with a DC power source.

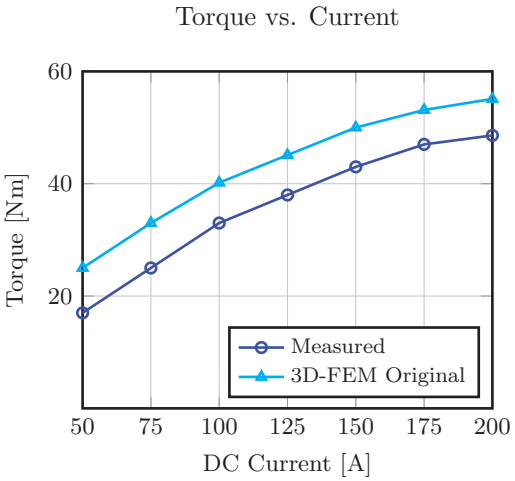

Figure 3.50. Measured torque with DC current.

Figure 3.50 describes both measured and calculated torque when applying a DC current. Although a lower deviation was expected, the torque difference remain approximately constant at a value of 7 Nm. Tolerances on the prototype that were not accounted for in the FEM models might be attributed as cause of such deviations.

3.5.3 INDUCTANCE MEASUREMENT

The inductance of the machine was measured with a Precision Magnetics Analyser. The measurement was performed at various frequencies and the results

of the measurement per phase are illustrated in Figure 3.51. As it is observed increasing the frequency up to 1 kHz led to a decreasing of the inductance value of approximately 31%. Such behaviour demonstrates the incidence of the welds on the stator modules on the increment of eddy currents.

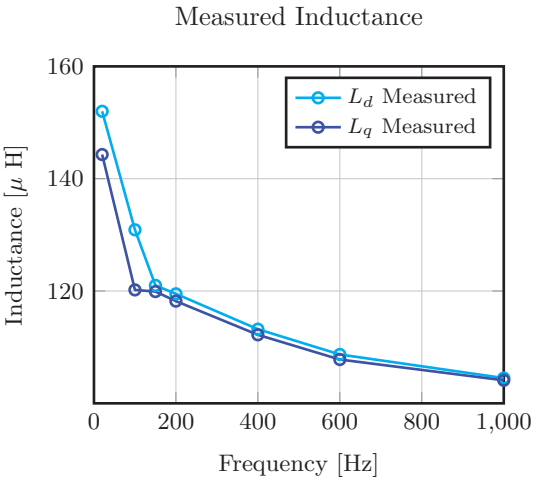

Figure 3.51. Measured inductance vs. frequency.

A comparison between the measured values of both inductance and DC resistance is presented in Table 3.6. As it is observed, the deviation between measured and calculated values of inductance is 12%. On the other hand, the deviation between the measured and calculated values of DC resistance is approximately 3%.

Parameter	Calculated	Measured
d-axis inductance L_d [μH]	170	152
q-axis inductance L_q [μH]	153	144
Phase Resistance [mΩ] @ 20^o	7.8	7.6

Table 3.6. Inductance and DC resistance of the HM3D machine.

The calculation of the inductances L_d and L_q in Table 3.6 was performed at a current density of 6.5 A/mm^2. In addition, both inductances were estimated with (2.11) applying -I_d to the d-axis and I_q in q-axis. According to measured values, the deviation between L_q and L_d is of approximately 5%, which means that the saliency of the HM3D is low, despite of being a double salient structure.

3.5.4 THERMAL TEST OF THE HM3D MACHINE

The thermal evaluation of the prototype was performed by connecting the windings to a DC power source. A constant DC current of I_{DC}=100 A was applied during the test, which corresponds to a current density of 6.4 A/mm^2, close to the rated current of the prototype. The diagram in Figure 3.52 describes the connection used for performing the test, which was extended for few hours until the temperature in various parts of the machine was stable. Three T-type thermocouples were placed on the windings, stator modules and the stator bracket as it is illustrated in Figure 3.53.

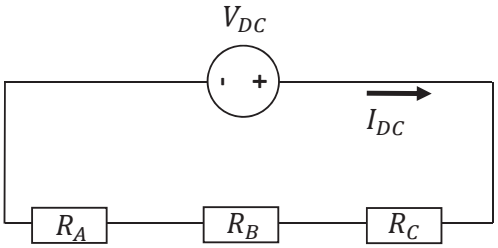

Figure 3.52. Equivalent circuit for thermal measurement of the HM3D fed with a DC current.

(a) **(b)**

Figure 3.53. Placement of the thermocouples for temperature measurement; (a) general view, (b) zoomed view.

The temperature stabilised after 14700 seconds, as it is illustrated in Figure

3.54. The highest temperature, corresponds to the windings, which maximum value reached 116 °C. In contrast, the temperatures in both the stator modules and stator bracket reached a value of 70 °C. That is, the temperature difference between winding and stator frame is of 46 K. Noting that the room temperature during the test remained at 25.5 °C.

In order to evaluate the thermal capability of the machine, the equivalent convection coefficient h_{eq} is introduced. Such coefficient is determined with the expression:

$$h_{eq} = \frac{1}{R_{th} A_{he}} \tag{3.4}$$

Where, A_{he} is the area of the heat exchange surface, and R_{th} is the equivalent thermal resistance, given by $R_{th} = \Delta T / p_{cu}$. With ΔT and p_{cu} as the measured temperature difference and copper losses, respectively. With the dimensions of the HM3D prototype, the estimated h_{eq} is of approximately 190 W/(m^2·°C), which according to the literature, would correspond to a machine with air forced convection [80]. Although the mechanical design of the HM3D machine was conceived for water cooling, such option was not tested. However, the thermal behaviour of the HM3D would be improved by enabling this feature.

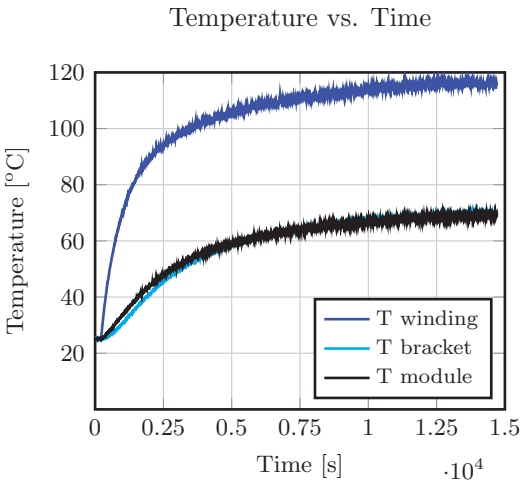

Figure 3.54. Temperature evolution with time.

3.5.5 ROTATIONAL LOSSES

Three approaches were used in order to measure the rotational losses of the HM3D machine:

1. A decay test. Such test consisted in rotating the shaft of the prototype by an external device, in this case, a drill. The decaying waveform of the back-EMF was registered and the iron losses were obtained with the inertia J_m of the prototype.

2. Running the prototype as a generator with a servo-motor and registering the values of torque and speed. The rotational losses were obtained as the product of the mechanical speed and the torque measured at no-load.

3. Running the prototype as a motor, fed with a converter and registering the torque output and the power input in order to obtain the rotational losses.

Figure 3.55 illustrates the results of both the simulated and measured values of rotational losses. The calculated values with 3D-FEM simulations with electrical sheet and amorphous material are also included in the figure. It is worth noting that the losses calculated with the 3D-FEM model, does not account for the mechanical losses in the HM3D prototype. Preliminary conclusions might be drawn from the results:

- The losses estimated with amorphous laminated material are half of the losses calculated with electrical sheet. Such low reduction is the reflection of the larger loss component of the rotor, which material is electrical sheet. In addition, the calculated losses in Figure 3.55, do not account for the effect of the welds on the stator modules.

- The deviation between the rotational losses estimated with the decay test and the losses measured in generator mode, might be caused by uncertainties in the calculations. For example, during the decay test, it was not possible to reach the nominal speed, which might affect the quadratic fit performed to obtain the losses.

- The deviation between the losses measured in motor mode and in generator mode are due to the effect of both the modulation of the PWM of the drive and the MMF of the windings.

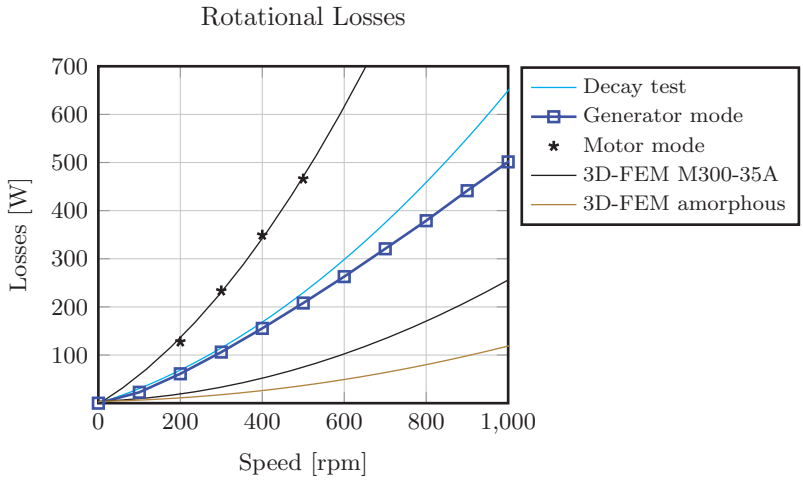

Figure 3.55. Evolution of the rotational losses with speed, measured and calculated.

In order to evaluate the incidence of the MMF of the windings on the rotational losses, these were estimated at various levels of current. Figure 3.56 illustrates the behaviour of the calculated rotational losses with increasing current density. As it is observed, at half the rated current density, the rotational losses are increased approximately 1.5 times. At rated current density, the rotational losses are increased approximately 2.7 times. The study of the rotational losses is finished with the comparison of the measured losses at various current densities. The rotational losses p_0 were obtained as the difference of the input and output power, and the copper losses, that is:

$$p_0 = P_{in} - P_{out} - p_{cu} \tag{3.5}$$

Where, P_{in} is the input electrical power measured with the power analyser, and P_{out} is the output power measured in the shaft. The rotational losses measured accounting for both the harmonics induced by the PWM modulation and the MMF of the windings are illustrated in 3.57. It is observed that the losses are increasing with the current density. The increment of the rotational losses with the current density is of approximately 2.3 when increasing the current density from 3.25 to 6.5 A/mm^2.

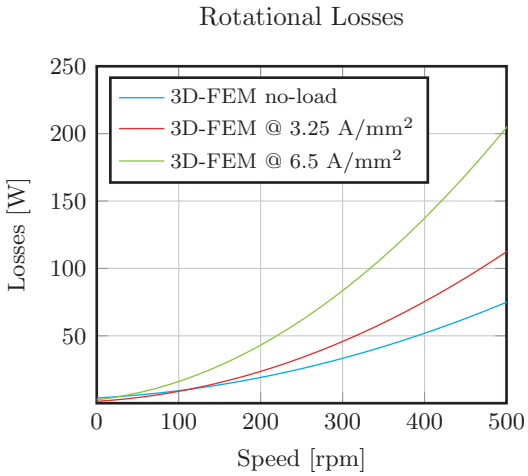

Figure 3.56. Calculated rotational losses at various current densities.

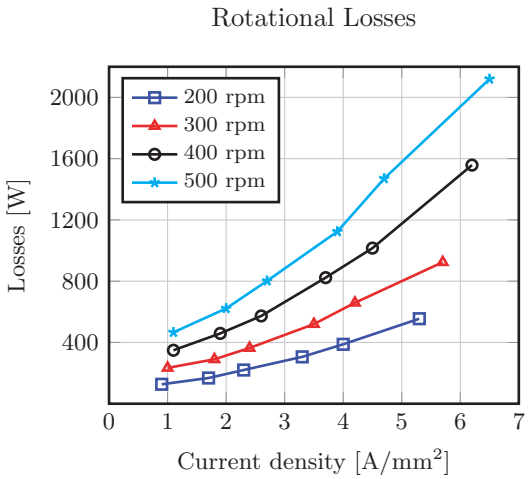

Figure 3.57. Measured rotational losses in motor mode.

3.5.6 SUMMARY OF THE MAIN DIMENSIONS OF THE HM3D MACHINE

Table 3.7 summarizes key figures of the HM3D machine.

Parameter	Value
Torque density [Nm/L] @ 5.9 A/mm^2	4.6
PM mass [kg]	0.9
Rotor iron mass [kg]	8.9
Stator iron mass [kg]	7.3
Copper mass [kg]	3.9
Torque/PM mass [Nm/kg]	33.7
Torque per active weight [Nm/kg] @ 5.9 A/mm^2	1.4
Volume [m^3]	6.6×10^{-3}
Number of turns per phase	22
Back-EMF constant @ 1000 rpm [mWb/rad]	6.3
Iron losses [W] @ 500 rpm, 5.9 A/mm^2	2120
Copper losses [W] @ 80°C, 5.9 A/mm^2	247
d-axis inductance [μH]	152
Phase Resistance [mΩ] @ 20^o	7.6
Power Factor [-]	0.15
Nominal voltage (line to neutral) [V]	230

Table 3.7. Main measured parameters of the SM3D machine.

3.6 SUMMARY

A hybrid rotor machine with 3D-flux paths was defined and investigated. Initially, the working principle was explained, and sensitivity analyses were carried out in order to evaluate the effect of the variation of the PM dimensions on various parameters. Additionally, it was found that the performance of the HM3D machine was inferior in contrast to the SM3D version.

Hence, the Vernier's principle was studied, as an alternative for increasing the torque capability. The sub-division of the magnetic system was evaluated as a solution in order to increase the torque density. Despite of the improvement of the torque production, the level of complexity for manufacturing was increased, and parameters such as power factor and iron losses were negative affected with the increment of sub-divisions. Nevertheless, a machine with 6 stator modules, 8 rotor teeth and 4 sub-divisions was selected for prototyping. In addition,

it was demonstrated that the PM losses were significantly reduced by using a hybrid rotor. Finally, the elimination of the use of glue for assembly of the PMs on the rotor may be highlighted as one important advantage when addressing recycling.

Unfortunately, there were three main setbacks during the manufacturing of the machine components. The first one, was the change of the PM ring to PM blocks. The second, it was not possible to find a winding supplier. Hence, the coils had to be manufactured at Aalborg University. Consequently, the slot fill factor was significantly reduced. Finally, and the most important, there were difficulties in the supply of the stator modules manufactured with amorphous material. Hence, it was agreed that the stator modules would be manufactured in standard electrical sheet. As it was shown, the solution provided had issues, which affected the performance of the machine (i.e. welds in the stator modules). In addition, quality issues were spotted on the rotor structure. However, it provided an opportunity to study additional phenomena.

The temperature rise exhibited by the HM3D machine confirmed that the modular structure of the stator might have issues regarding its thermal efficiency. However, as the slot fill factor may be improved and the winding resistance reduced, it is expected that the temperature reduces.

Chapter 4 RECYCLABILITY EVALUATION OF PMs IN ELECTRICAL MACHINES

The Weighted Index of Recycling and Energy Cost (WIRE) is introduced in this chapter. As described in Chapter 1, the main objective of DEMETER project is the study, development and improvement of recycling technologies of REEs used in PMs for electrical machines in (H)EVs. In addition, the design for recycling plays a crucial role in the recyclability of PM material at the EoL of this type of machines. Hence, it is required to give a quantitative evaluation of the recyclability criterion. For this purpose, two methodologies are proposed:

- Evaluation of the assembly and disassembly processes.
- Evaluation of the energy consumption of the machine.

The former, is intended to grade the feasibility of the machine based in both the manufacturing processes and the materials used. The latter, is based on the evaluation of the energy consumption of the machine during its lifetime. Eventually, contrasting both the total energy consumption cost and the initial cost of PM material. That is, evaluating the use of PMs of recycled material from an economic perspective. For such analyses, a machine was disassembled and a test set-up was built in order to perform measurements at various working points of torque and speed.

4.1 RECYCLABILITY EVALUATION DEFINITION

The proposed WIRE methodology was investigated and validated on a commercially available machine as in Figure 4.1. Such machine is used in electrical scooters and small city cars.
In order to define the recyclability evaluation the disassembly of the machine under investigation was performed. For extracting the non-drive end-shield and the rotor, it was necessary to mount the specimen on a lathe. Figure 4.2a shows the machine without the end-shield. Once the end-shield was extracted, it was possible to extract the rotor, which is the most challenging part due to the forces that are present due to the magnetization of the PMs. Figures 4.2b and 4.2c describe the rotor and the stator once the disassembly was completed.

Figure 4.1. Motor used for recyclability evaluation definition [74].

After the disassembly process, a complete dismantling of the remaining parts was carried out, with a complete registration of the main dimensions, materials and weights. Additionally, a characterization of the permanent magnets used in this machine was carried out in order to built the FEM models.

4.1.1 EVALUATION OF THE ASSEMBLY AND DISASSEMBLY PROCESSES

The methodology proposed for the evaluation of both the assembly and disassembly processes is based on the Failure Mode and Effect Analysis (FMEA) [81]. Ideally, for performing an FMEA analysis, specialists with diverse backgrounds within the design of electrical machines would be required (i.e. mechanical, electrical, etc.). Nevertheless, this exercise was performed within the ESRs participating in WP3. As in FMEA analyses, the main goal is to provide a quantitative evaluation of the assembly and disassembly processes of any given PM machine. Thus, it would be possible to determine at an early stage of the design the degree of recyclability of the machine under investigation.

Furthermore, one of the objectives of the method is to serve as a tool for helping designers in deciding the type of machine that might be advantageous from a recycling perspective by evaluating the assembly and disassembly processes, and the materials used for manufacturing. Therefore, the method is by no means analysing the performance of the machine. The methodology is evaluated on two main aspects: "Standard" and "Cost".

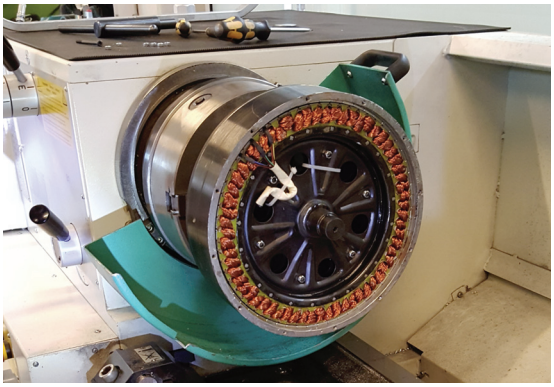

(a)

(b)

(c)

Figure 4.2. Disassembly process, (a) machine mounted on a lathe for rotor extraction, (b) disassembled rotor and (c) disassembled stator.

Standard

The main goal of this section is to evaluate the processes and materials in terms of their standardization. That is, the availability of both the processes and the materials at the time of manufacturing the machine. Thus, three main fields are considered:

- Material.
- Assembly.
- Disassembly.

In these three fields, two values are required in order to perform the evaluation. The first is the Score S depending on its relative scale in its corresponding section. The second is the Importance I, which is graded according to its criticality with regards to the recyclability of the material. In the case of the factor I, its value needs to be agreed and fixed from a start. The final grade is the product of S and I. Following the methodology, the use of standard materials will have higher S than materials that are not usual in the manufacturing of machines. For example, a machine which is designed to be manufactured with round, copper wire will have a higher S, than a machine which implements the use of, for example, Litz wire. Similar comparison might be made regarding the assembly and disassembly perspectives. If a completely new method that requires highly qualified personnel and costly tools shall be used for assembling or disassembling the machine, then S will have a low value. In contrast, if standard tools are sufficient for the assembly or disassembly of the machine S will be high. Such way to evaluate represents a challenge, since an innovative design with unconventional materials will inherently have a low S. Thus punishing innovation in design and manufacturing of electrical machines, which might be identified as a weakness of this approach.

Cost

A similar procedure is followed for evaluation of the assembly and disassembly processes. That is, the higher the cost, the lower S in terms of recyclability. However, a different approach was adopted for the calculation of the importance I, regarding the cost of the materials. The principle is that a machine with a large amount of certain material encourages its recycling. Therefore, the importance I of that material will have a high value. Following that principle, the assignment of the importance I of the remaining materials is carried out proportionally with respect to the material with the larger mass. For example, a machine has a given mass of copper W_c and a mass of electrical sheet W_s. If it is assumed that the highest mass corresponds to the electrical sheet, the factor I of the copper will be given by the ratio of the copper and the electrical sheet masses times the highest score, as follows:

$$I(W_c) = \frac{W_c \cdot 5}{W_s} \tag{4.1}$$

Where 5 is the maximum achievable score.

Final Scoring of WIRE Sheet

The final scoring R_w is obtained with the summation of all the products $S \times I$ divided by the total sum of the factor I as in (4.2). The grading of both factors S and I have a range from 1 to 5. In the specific case of factor S in the "Standard" Section, 5 corresponds to a machine where all processes and materials are standard. In the case of the factor I, 5 indicates that the assembly or disassembly processes are highly crucial in order to achieve recyclability. On the other hand, same principle applies in the fields Assembly and Disassembly of the "Cost" Section. However, in the field Material the higher Importance I is given to the material with the larger mass. The Score factor S determines its cost, assigning a 5 to the more costly material.

$$R_w = \frac{\sum_{i=1}^{n} S_n I_n}{\sum_{i=1}^{n} I_n} \tag{4.2}$$

At the end, this methodology was applied to the machines within WP3. The results, and a detailed description of the methodology are reported in [82].

4.1.2 EVALUATION OF THE ENERGY CONSUMPTION

The energy evaluation is the second approach of the WIRE methodology. Figure 4.3 describes the various steps required in order to obtain the energy consumption of the electrical machine. In the following, a brief description of each step is carried out.

FE Analysis of Machine and Efficiency Map

Measurements of torque and speed were performed to the outer rotor PM machine (Figure 4.1). The test set-up is described in Figure 4.4. An FEM model was built with the main dimensions of the disassembled machine. In addition, the measured values of current were used as inputs in the FEM models and the results contrasted with the measured values, showing a fair agreement. Thus, it was possible to determine the losses at any working point of the machine. Consequently, facilitating the elaboration of the efficiency map. Figure 4.5 shows the FEM geometry and the distribution of the magnetic flux density.

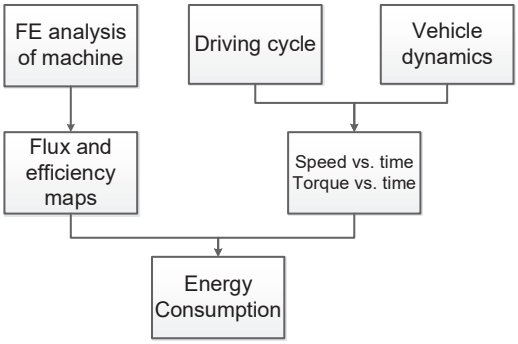

Figure 4.3. Flow chart of the calculation of the energy consumption [83].

The FEM modelling of the machine was not straightforward, since the calculations required certain inputs that were unknown. For example, it was necessary to perform a characterization of the PMs of the test machine, in order to determine their remanence. Hence, samples of the PMs were processed and sent to the Laboratory of Cristallography and Material Sciences CRISMAT at ENSICAEN. In the case of the laminations of the stator, their quality was assumed to be of a standard electrical sheet, specifically M400-50. The efficiency map of the machine under analysis is illustrated in Figure 4.6.
In order to evaluate recyclability with the energy consumption approach, a study case was performed in which the PMs were assumed to be recycled. Therefore, their remanence was set as 20% lower, than the remanence of virgin PMs. Such reduction in remanence was selected based on the results presented in [84]. The methodology followed up to this point, and the efficiency comparison between virgin PMs and recycled PMs was published in [85].

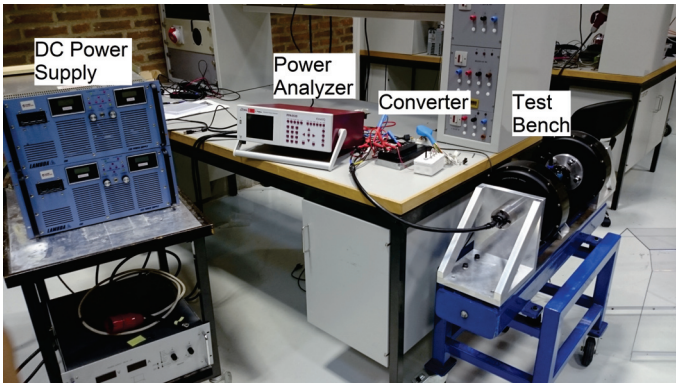

Figure 4.4. Set-up used for measurements [85].

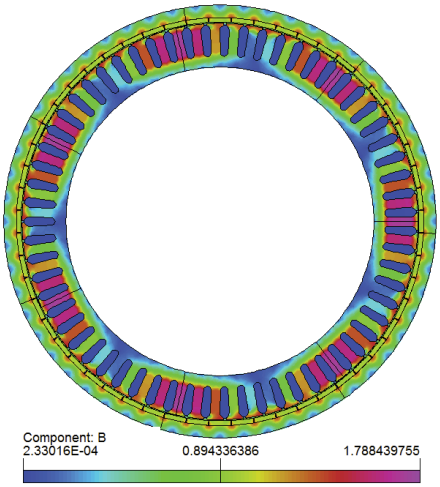

Figure 4.5. Geometry modelled in FEM, magnetic flux density distribution [85].

Driving Cycle and Vehicle Dynamics

Driving cycles are designed for emulating real driving conditions under a controlled environment, for the measurement of road vehicle emissions. The conditions of the tests may vary according to the type of vehicle under study. There exists, however, various types of driving cycles and there has been discussion about the accuracy they have in representing real driving conditions. Since 2017, the European Union have replaced the outdated NEDC [86] with the newest Worldwide Harmonised Light Vehicle Test Procedure (WLTP) [87]. Although there are not driving cycles specifically defined for (H)EVs, it is possible to utilise a driving cycle for the estimation of the energy consumption of the machine, given that the vehicle dynamics are identical. As a matter of comparison, both NEDC and WLTP driving cycles are described in Figures 4.7 and 4.8.
For the estimation of the energy consumption, a model of the vehicle is required. The model will allow the calculation of the forces to accelerate the vehicle at the various intervals of the driving cycle. Consequently, there are dimensions that are required to be determined in order to perform the calculation [88], [89]:

1) *Rolling resistance force:* This parameter is directly related with the friction produced by the vehicle on the road. Hence, the parameter is related with the mass of the car m and the acceleration of gravity g. And it is described by the expression:

$$F_{rr} = \mu_{rr} m g \tag{4.3}$$

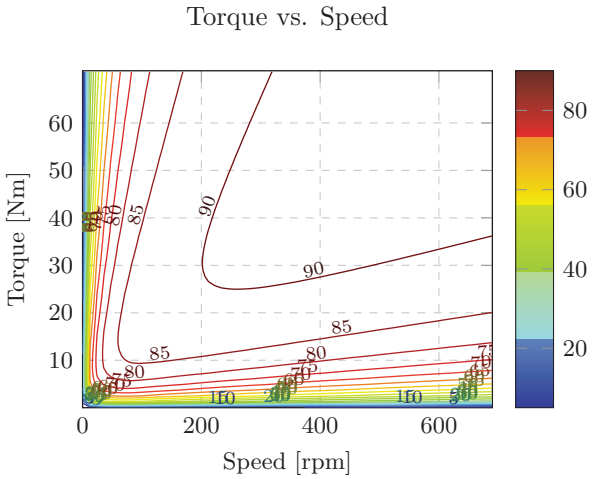

Figure 4.6. Efficiency map of the outer rotor PM motor [85].

The rolling resistance coefficient μ_{rr} may be expressed in terms of the speed as $\mu_{rr} = 0.01(1 + v/44.4)$.

2) *Aerodynamic drag:* This parameter is related to the friction of the vehicle as it moves through air. Therefore, it is highly dependent on the geometry of the car. This parameter may be estimated as:

$$F_{ad} = \frac{1}{2}\rho A_f C_d v^2 \tag{4.4}$$

Where ρ is the density of the air, C_d is the drag coefficient, A_f and v are the frontal area and speed of the vehicle, respectively.

3) *Acceleration force:* Given that the speed of the vehicle is continuously changing, it is required to provide the force that will allow such acceleration. Therefore, for the estimation of this force the Newtonian equation suffices:

$$F_a = ma \tag{4.5}$$

The total tractive effort corresponds to the summation of all the components described previously.

Energy Consumption

Finally, the calculation of the energy consumption is performed with the efficiency map, the driving cycle and the dynamics of the vehicle. The process for calculating the energy consumption is summarized as follows:

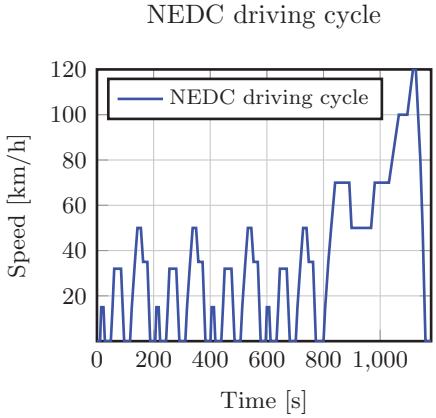

Figure 4.7. NEDC driving cycle.

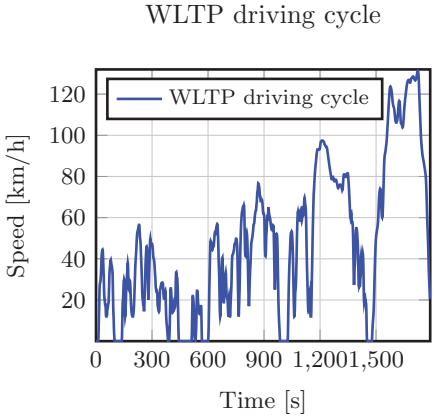

Figure 4.8. WLTP driving cycle.

- The speed vs. time characteristic of the driving cycle (Figure 4.8) should be converted to acceleration vs. time.
- Once the acceleration vs. time is obtained, the tractive force is calculated with the parameters of the vehicle.
- The torque vs. speed characteristic for a specific vehicle is obtained.
- The power consumed by the machine is determined at each point by interpolation of the losses from the efficiency map.
- Finally the energy consumption is computed as the integral of the power at a defined time interval, which is, in this case the life span of the vehicle.

The study is finalized by performing an economic evaluation of the cost of the energy consumed by the machine during the entire life of the vehicle, with virgin PMs, and the energy consumed when using recycled PMs. For such purpose, the energy cost index EC_i is presented and it is evaluated as the ratio:

$$EC_i = \left(\frac{E_c(j)}{E_c(b)} \right) \tag{4.6}$$

Where $E_c(b)$ corresponds to the initial cost of the energy consumed by the machine with virgin PMs, and $E_C(j)$, corresponds to the energy consumed by the machine using recycled PMs. In [83], the recyclability of the PMs was involved, by multiplying EC_i by the ratio $Mag_c(j)/Mag_c(b)$, where $Mag_c(b)$ represents the cost of virgin PMs, and $Mag_c(j)$ is the cost of recycled PMs. However, such approach might become misleading, since the cost of the PMs might represent only a fraction of the energy consumed by a vehicle. Hence, a modification is proposed in this work. In order to account for the recyclability of the PMs, the energy cost index EC_i should be given by the following expression:

$$EC_i = \left(\frac{E_c(j) + Mag_c(j)}{E_c(b) + Mag_c(b)} \right) \tag{4.7}$$

Where all four variables are weighted evenly. The evaluation of the energy index as proposed in [83] is not complete. That is, the reduction on the environmental impact of recycling shall be accounted for in the evaluation. Therefore, it is proposed to evaluate the CO_2 emissions during the processing of REEs at the mining location. Various publications have reported the estimation of the environmental impact of mining. For example, in [90] the impact on global warming of the use of energy and resources in the production or Rare Earth Oxides (REO) is carried out. Both mass-based and price-based allocations approaches are included in the report. In addition, the investigation is focused on the production of the mine Bayan Obo in China. In [91], the production of REOs in Bayan Obo mine is compared in a study case with the mine Norra Kärr in Sweden. In addition, the allocation method used is a combination of the mass of produced REEs and their prices on the market. A broader investigation is reported in [92]. In addition to Bayan Obo mine, the study of the environmental impact of the production of REOs is extended to Sichuan and seven southern provinces in China. The findings regarding the emissions of CO_2 in the production of REOs are reported in Table 4.1.

REO	CO_2 [eq./kg]
Nd [90]	66
Dy [90]	739
Nd [91]	289
Dy [91]	709
Not specified [92]	2040

Table 4.1. CO_2 equivalent emissions in production of REOs.

Note that in this evaluation only Dysprosium and Neodymium are investigated due to their criticality. In order to estimate the footprint of the virgin PMs used, the amount of both Dysprosium and Neodymium in NdFeB PMs is required. However, the percentage of both REEs depends on the grade of PM used, and it might vary widely. According to [93], [94], the percentages of both Neodymium and Dysprosium might vary from 23 to 26%, and 3.5 to 5%, respectively.

4.2 ENERGY EVALUATION OF THE HM3D MACHINE

4.2.1 EFFICIENCY MAP OF THE HM3D MACHINE

The energy consumption evaluation is applied to the HM3D machine. As it was described in Chapter 4, the performance of the machine with stator modules of electrical sheet was poor. Hence, for this study, it is assumed that the stator modules are built with amorphous laminated material, and the efficiency maps are obtained from calculations with FEM. In addition, a study case is performed, in which similarly to [85] and [83] PMs manufactured with recycled material are evaluated. That is, the remanence of the PMs manufactured with recycled materials is assumed to be B_r =1.08 T. The efficiency map of the machine with virgin PMs and in motor mode is shown in Figure 4.9. Similarly, the efficiency map of the machine with PMs manufactured with recycled material is shown in Figure 4.10.

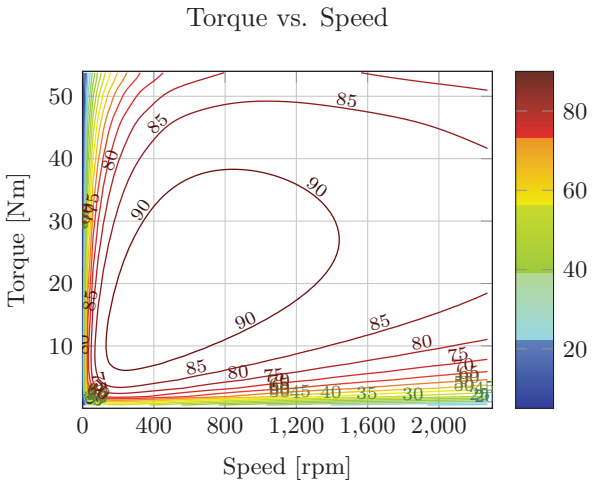

Figure 4.9. Efficiency map of HM3D machine with amorphous stator modules and virgin PMs.

The reduction of B_r as a result of the use of recycled material, resulted in a reduction of torque production in a range that varies from 5.5 to 8.7%. Hence, in order to compensate such reduction, keeping similar dimensions of the machine, with similar stator current, two approaches were available. The first, increasing the PM thickness l_m. Increasing the PM thickness did not yield significant increment of torque, even when increasing the PM thickness from 11 mm to 20 mm. Hence, increasing the dimension h_m of the PM blocks (Figure

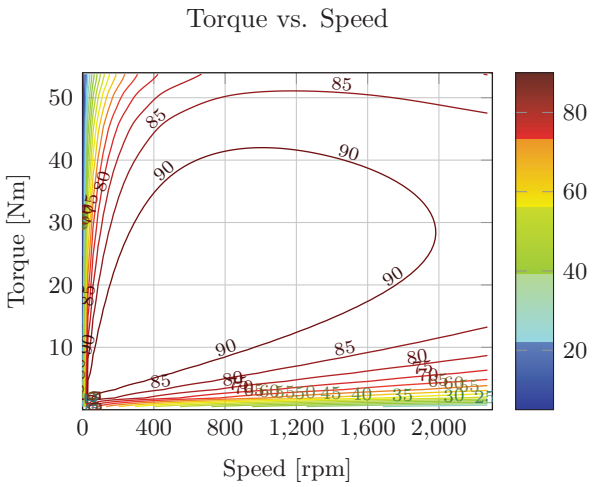

Figure 4.10. Efficiency map of HM3D machine with amorphous stator modules and recycled PMs.

2.4 in Chapter 2) was verified, obtaining an increment of the required torque, increasing h_m by approximately 22%. In addition, there is an improvement of the efficiency by reducing the remanence of the PMs, as it is observed when comparing both 4.9 and 4.10. The reduction of the iron losses, results in the improvement of the electromagnetic torque, which is the difference between the simulated torque, and the equivalent torque of the iron losses.

4.2.2 DRIVE CYCLE AND VEHICLE MODELLING

A small city car with the parameters presented in Table 4.2 and under the WLTP driving cycle (Figure 4.8), has the torque-speed envelope presented in Figure 4.11. Once the operating points of torque and speed are calculated, it is possible to estimate the energy consumed during a defined period of time [83].

Parameter	Value
Vehicle Mass [kg]	500
Air density [kg/m^3]	1.225
Frontal area [m^2]	1.85
Drag coefficient [-]	0.4
Tyre radius [m]	0.273

Table 4.2. Main vehicle parameters [88]

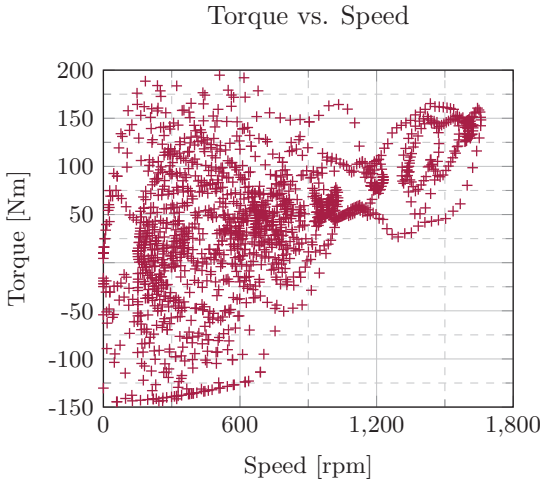

Figure 4.11. Torque vs. speed envelope for a small city car under WLTP driving cycle.

4.2.3 ENERGY CONSUMPTION INVESTIGATION

Both motoring and generating modes of the HM3D machine are considered in the calculation of the energy consumption. In addition, as it is shown in Figure 4.11 the maximum torque requirement is of 200 Nm. Hence, a number of 4 HM3D machines would be required. Thus, the results summarized in Table 4.3 is given by machine unit. Various assumptions are required:

- It is assumed that the life time of the vehicle is 10 years, and that is driven two hours in a daily basis.

- The price of the electricity corresponds to 0.21 €/kWh, the average in Europe at the end of 2018 [95].
- The price of virgin PMs is 55.91 €/kg, the actual cost of the PMs supplied by VALEO.
- Finally, according to [96], the CO_2 emitted per kWh of electricity was of 296 g/kWh in 2016.

Parameter	HM3D virgin PM	HM3D recycled PM
Total energy consumption [kWh]	7495	7388
Total energy re-generated [kWh]	-643	-664
Total energy cost [€]	1439	1412
Total mass of PM material [kg]	0.9	1.2
Price of PMs [€/kg]	55.91	27.96
Total PM cost [€]	50.4	33.5
CO_2 usage [kg]	2028	1990
CO_2 mining [kg]	175	-

Table 4.3. Energy evaluation of the HM3D machine with virgin and recycled PM material.

As it was discussed in 4.2.1, the efficiency of the machine with recycled PMs is higher. Hence, it has a lower energy consumption. Unfortunately, there is not certainty about the price of PMs with recycled materials, but as exercise it is assumed that the price would be half of the price of virgin PMs. The field CO_2 usage in Table 4.3 corresponds to the equivalent emissions of the electricity consumed during the life time of the vehicle. Hence its calculation is straightforward. On the other hand, the field CO_2 mining corresponding to the emissions from mining activities, requires further steps. As described in 4.1.2, two parameters are required: the equivalent CO_2 emissions from mining and the amount of Neodymium and Dysprosium in the virgin PMs. Hence, for this evaluation, the values presented in [90], [93] are adopted. That is 26% Neodymium and 5% Dysprosium. In contrast, the value of CO_2 emissions corresponding to the recycled PMs is assumed to be zero. Nevertheless, there will be emissions during the recycling processes, and they will depend on the type of method used for recycling. Hence, their estimation require further study as this is a topic that is subject of ongoing research, therefore the discussion is open.

As a conclusion, the HM3D machine with recycled PMs showed to have lower

energy consumption. In addition, with the assumptions adopted, it also showed to be economically and environmentally beneficial. However, further investigation is required with regard to the cost of PMs with recycled material and the CO_2 emissions from the recycling processes.

4.3 SUMMARY

In this chapter a methodology for evaluation of recyclability was defined and applied in a study case to an outer rotor PM machine. A first approach was adopted from the perspective of both assembly and disassembly processes and the cost of the materials used for manufacturing. A preliminary comparison among the machines in WP3 was carried out, and the results were reported in [82]. As it was discussed above, the machine proposed in this project had the lowest score, due mainly to the unusual topology, which is not a standard nowadays.

The second approach accounted for the energy consumption of the machine during the life time of the vehicle. Such approach required as inputs, the efficiency of the machine and a model of a car under a given driving cycle. As a final step, an energy consumption index was determined in which an electrical machine with recycled PMs may be contrasted with a machine with virgin PMs. The method was validated with an outer rotor PM machine [85], and the study over various scenarios were reported in [83]. In addition, suggestions that are believed might improve the evaluation of such index were formulated.

An evaluation of the energy consumption was carried out on the HM3D machine. The efficiency maps were estimated assuming the use of stator modules with amorphous material. Additionally, it was necessary to assume the use of several motor units to match the requirement of the vehicle under analysis. Afterwards, a study case was selected in which the remanence of the PMs manufactured with recycled material was assumed to be 20% less than the remanence of the virgin PMs. In order to compensate the torque production with PMs of lower remanence, it was necessary to increase the PM mass by 22%. It was found that the energy consumption was not drastically affected when using PMs with lower remanence. In addition, in order to account for recyclability, the evaluation of the PM prices was carried out assuming the price of recycled material to be half of the virgin PMs. Hence, using recycled materials showed to be beneficial. Nevertheless it is necessary to perform the evaluation with the real cost of the recycled PMs.

Finally, the energy consumption index was complemented with an evaluation

of the CO_2 emissions in order to account for the environmental impact of using either virgin or recycled PMs. Nevertheless, more investigation is required in order to estimate the emissions associated with the recycling methods.

Chapter 5 CONCLUSION

The work carried out during this Ph.D. project is summarized in this chapter. In addition, the main contributions are highlighted, conclusions are drawn, and future work is proposed.

5.1 SUMMARY

The motivation of this thesis project along with the main objectives were presented in Chapter 1. In addition, a literature review was provided, covering the following topics:

- Recyclable electrical machines.
- Electrical machines with 3D-Flux paths.
- Laminated amorphous metals in electrical machines.

The literature review was complemented with the description of an alternative machine topology based on existent technologies, along with the objectives and limitations of the project. The remainder of the thesis was focused on the research objectives, that were described in Chapter 1 as:

Studying the advantages of using non-traditional materials, in electrical machines for use in (H)EVs.

The use of non-traditional materials was investigated in Chapter 2. Both simulations and experimental work were carried out in order to evaluate non-traditional materials on the proposed topology. Specifically, amorphous laminated material was investigated and contrasted to electrical sheet. FEM simulations showed a superior torque production when using electrical sheet. In contrast, a reduction of iron losses was achieved with amorphous laminated material. In addition, it was found that the PM losses on the SM3D machine had a large value due to slotting effect.

Chapter 2 was finished with the definition of a single phase outer rotor surface mounted demonstrator. The stator consisted of two C-shaped laminated amorphous cores. Hence, the advantage of such material on the reduction of

the iron losses was validated. Furthermore, a loss characterization of the amorphous C-shaped cores was carried out. Finally, a study on the rotational losses was performed in order to validate the calculation of PM losses.

Evaluating the possibility of using non-traditional materials in conjunction with the recyclability of the PMs.

Chapter 3 was focused on the definition of a hybrid rotor 3D-flux machine (HM3D). The evaluation of an alternative to the SM3D machine was required, due to the high levels of PM losses that the SM3D machine yielded. An identical stator structure was chosen combined with a hybrid rotor. FEM simulations were carried out and the performance of the HM3D machine was inferior when compared with the SM3D machine.

A HM3D prototype was built. However, due to issues with lead time of suppliers, the experimental validation of the HM3D machine with amorphous laminated alloys was not possible. Instead, electrical sheet was used. Nevertheless, it is believed that the modular structure of the stator, conceived for the use of C-shaped amorphous laminated material, allows the use of alternatives such as SMC, oriented grain electrical sheet, etc. Finally, the recycling of the PMs was addressed by removing the requirement of glue for assembling the PMs on the rotor structure.

Designing electrical machines for (H)EVs, allowing recyclability of the PMs and using non-traditional materials.

Given that the dimensions of the amorphous C-shaped cores available in the market are already defined, an alternative approach for dimensioning an SM3D machine was proposed on Chapter 2. Furthermore, an SM3D machine topology was defined and studied in depth with FEM. Finally, extra steps were defined for the increment of the torque of the HM3D machine by applying Vernier's principle.

Defining, manufacturing and testing of a machine prototype.

As mentioned above, two demonstrators were manufactured during this project: a proof of concept of an SM3D machine, and a final prototype of the HM3D machine. The SM3D demonstrator was developed and investigated in Chapter 2. A final prototype was defined and built in Chapter 3. The testing was performed in the drives traction lab at Aalborg University. Due to the combination of changes of the design and quality issues of the supplied parts, the values of torque and efficiency obtained during tests, were significantly low. Hence, the

poor power factor and the low value of torque achieved raise questions about the HM3D topology.

5.2 MAIN CONTRIBUTIONS

Few work focused on electrical machines designs focused on recycling was found in the literature. On the other hand, the use of non-traditional materials, specifically, laminated amorphous alloys, have been investigated on prototypes of various machines topologies. Hence, the believed main contributions of this thesis work covers three main aspects:

- The definition of a machine structure intended to facilitate the extraction of the PMs, and consequently the recycling of REEs.
- The investigation of alternative materials in electrical machines. Specifically, iron based laminated amorphous alloys.
- The definition of an methodology, in order to quantify the recyclability of PMs in electrical machines.

Hence, based on the aforementioned aspects, the main contributions of this thesis work, are believed to be the following:

- A machine with a modular stator intended to facilitate the recycling process of PMs is proposed. The 3D flux working principle of the machine allows the use of non-traditional materials. Moreover, the investigation focused on iron based amorphous laminated alloys and non-oriented grain electrical sheet. Nevertheless, it is expected that such structure allows the use of alternative materials such as SMC, grain oriented electrical sheet, etc.
- A relevant study of the PM losses was performed. It was demonstrated that the combination of a machine with a modular stator and a rotor with surface mounted PMs might not be a convenient approach. The large variations of the air-gap permeance resulted in a large level of eddy currents induced in the PMs due to slotting effect.
- In connection with the previous item, a rotor with hybrid structure is proposed. The implementation of such structure showed to solve the issue of large PM losses of the surface mounted topology. In addition, it allowed the assembly of the PMs without requiring the use of glue. Therefore, facilitating the extraction of the PMs for a recycling process.
- A methodology was developed in order to quantify and evaluate the recycling potential of PM machines. Such methodology evaluates the recycling from two perspectives; assembly and disassembly, and energy consumption. Additionally, the methodology is intended to be used at design

stages in order to help designers to identify electrical machine topologies that allow an efficient recycling.

5.3 FUTURE WORK

Activities related with the investigation carried out in this thesis project are proposed as future work:

- Unfortunately, lead time did not allow the manufacturing of the stator in the final prototype with amorphous material. Hence, improvements on the mechanical design for fixing the modules to the stator are proposed as future work.
- During the mechanical design stage, it was decided to use PM blocks instead of a PM ring. It is considered that having a single PM ring will improve the recyclability potential since less PM pieces would be required. Thus, reducing the assembly and disassembly times. Hence, the manufacturing of a prototype with a PM ring is set as future work in order to verify the feasibility of such approach.
- In addition, the modular structure showed to have poor thermal performance. Such issue might be improved by casting the stator coils with a thermal epoxy in order to improve the thermal conductivity between coils and stator bracket. Additionally, increasing the slot fill factor is set as future work. Furthermore, there is potential for automating the manufacturing of the coils, in order to improve the assembly and disassembly processes.
- As it was discussed in Chapter 3, the quality of the supplied components, specifically the rotor, along with the welds on the stator modules had a negative impact on the performance of the HM3D machine. Hence, a better cutting and stacking technique shall be adopted in the manufacturing of the rotor. In addition, the use of welds should be avoided.
- Additional mechanical aspects, such as noise and vibration on the final prototype were not investigated in this work. However, they are stated as future work, in order to have a complete picture on the performance of the HM3D machine.
- The calculation of the PM losses did not accounted for neither time nor space harmonics. It is required to perform the corresponding calculations in order to have the complete picture of this losses in both the SM3D and the HM3D machine.
- Regarding the definition of the methodology for evaluating recycling. The energy consumption evaluation, requires information that is either unavailable or uncertain. For example, the cost of recycled PMs, as well

as, the CO_2 emissions during the recycling process. These two topics required to be addressed in order to have the complete picture of the recyclability in electrical machines.

Bibliography

[1] M. Yilmaz, "Limitations/capabilities of electric machine technologies and modeling approaches for electric motor design and analysis in plug-in electric vehicle applications," *Renewable and Sustainable Energy Reviews*, vol. 52, pp. 80 – 99, 2015.

[2] A. M. El-Refaie, "Motors/generators for traction/propulsion applications: A review," *IEEE Vehicular Technology Magazine*, vol. 8, pp. 90–99, March 2013.

[3] DEMETER, "European training network for the design and recycling of rare-earth permanent magnet." [Online]. Available: `https://etn-demeter.eu/project`. [Accessed: Dec. 04, 2018].

[4] European Commission, "Tackling the challenges in commodity markets and on raw materials." [Online]. Available: `https://eur-lex.europa.eu/legal-content/en/TXT/?uri=CELEX%3A52011DC0025`, February 2010. [Accessed: Mar. 28, 2019].

[5] European Commission, "On the review of the list of critical raw materials for the eu and the implementation of the raw materials initiative." [Online]. Available: `https://eur-lex.europa.eu/legal-content/EN/TXT/?uri=CELEX:52014DC0297`, May 2014. [Accessed: Mar. 28, 2019].

[6] NERC ©, "EURare Project." [Online]. Available: `http://www.eurare.eu/about.html`. [Accessed: Sept. 22, 2018].

[7] S. Hope, "Toyota's long-term vision on electrified vehicles: Sustainability throughout the product life cycle." Presentation - DEMETER Concluding Symposium, February 2019. Leuven, Belgium.

[8] K. Binnemans, P. T. Jones, B. Blanpain, T. V. Gerven, Y. Yang, A. Walton, and M. Buchert, "Recycling of rare earths: a critical review," *Journal of Cleaner Production*, vol. 51, pp. 1 – 22, 2013.

[9] Y. Yang, A. Walton, R. Sheridan, K. Güth, R. Gauß, O. Gutfleisch, M. Buchert, B.-M. Steenari, T. Van Gerven, P. T. Jones, and K. Binnemans, "Ree recovery from end-of-life NdFeB permanent magnet scrap: A critical review," *Journal of Sustainable Metallurgy*, vol. 3, pp. 122–149, Mar 2017.

[10] M. Kimiabeigi, R. S. Sheridan, J. D. Widmer, A. Walton, M. Farr, B. Scholes, and I. R. Harris, "Production and application of hpms recycled bonded permanent magnets for a traction motor application," *IEEE Transactions on Industrial Electronics*, vol. 65, pp. 3795–3804, May 2018.

[11] T. Elwert, D. Goldmann, F. Roemer, and S. Schwarz, "Recycling of NdFeB magnets from electric drive motors of (hybrid) electric vehicles," *Journal of Sustainable Metallurgy*, vol. 3, pp. 108–121, Mar 2017.

[12] T. M. Letcher and J. L. Scott, eds., *Materials for a Sustainable Future*. The Royal Society of Chemistry, 2012.

[13] EAFO.eu, "The transition to a zero emission vehicles fleet for cars in the eu by 2050." [Online]. Available: `http://www.eafo.eu/sites/default/files/The%20transition%20to%20a%20ZEV%20fleet%20for%20cars%20in%20the%20EU%20by%202050%20EAFO%20study%20November%202017.pdf`, November 2017. [Accessed: Mar. 28, 2019].

[14] H. M. D. Bandara, M. A. Mantell, J. W. Darcy, and M. H. Emmert, "Rare earth recycling: Forecast of recoverable nd from shredder scrap and influence of recycling rates on price volatility," *Journal of Sustainable Metallurgy*, vol. 1, pp. 179–188, Sep 2015.

[15] T. Klier, F. Risch, and J. Franke, "Disassembly strategies for recovering valuable magnet material of electric drives," in *2013 3rd International Electric Drives Production Conference (EDPC)*, pp. 1–3, Oct 2013.

[16] A. Walton, H. Yi, N. Rowson, J. Speight, V. Mann, R. Sheridan, A. Bradshaw, I. Harris, and A. Williams, "The use of hydrogen to separate and recycle neodymium–iron–boron-type magnets from electronic waste," *Journal of Cleaner Production*, vol. 104, pp. 236 – 241, 2015.

[17] A. Williams, I. R. Harris, J. Speight, and A. Walton, "Magnet recycling." Patent, WO/2012/072989, June 2012. `https://patentscope.wipo.int/search/en/detail.jsf?docId=WO2012072989&redirectedID=true`.

[18] S. Höegberg, F. B. Bendixen, N. Mijatovic, B. Bech Jensen, and J. Holbøll, "Influence of demagnetization-temperature on magnetic performance of recycled nd-fe-b magnets," in *2015 IEEE International Electric Machines Drives Conference (IEMDC)*, pp. 1242–1246, May 2015.

[19] P. Kjeldsteen, A. I. Sørensen, and F. B. Bendixen, "A permanent magnet rotor for a machine, a method for manufacturing a permanent magnet rotor and a manufacturing system." Patent, WO/2010/066251, June 2010. `https://patentscope.wipo.int/search/en/detail.jsf?docId=WO2010066251&tab=PCTBIBLIO`.

[20] S. Högberg, T. S. Pedersen, F. B. Bendixen, N. Mijatovic, B. B. Jensen, and J. Holbøll, "Direct reuse of rare earth permanent magnets — wind turbine generator case study," in *2016 XXII International Conference on Electrical Machines (ICEM)*, pp. 1625–1629, Sep. 2016.

[21] M. Alatalo, S. T. Lundmark, and E. A. Grunditz, "Electric machine design for traction applications considering recycling aspects-review and new solution," in *IECON 2011 - 37th Annual Conference of the IEEE Industrial Electronics Society*, pp. 1836–1841, Nov 2011.

[22] P. Upadhayay, *Electrical machine designs based on 3D flux paths with reuse & recycle magnet concepts for automotive applications*. Theses, Université Grenoble Alpes, Dec. 2018.

[23] Z. Q. Zhu and D. Howe, "Electrical machines and drives for electric, hybrid, and fuel cell vehicles," *Proceedings of the IEEE*, vol. 95, pp. 746–765, April 2007.

[24] C. C. Chan, "The state of the art of electric, hybrid, and fuel cell vehicles," *Proceedings of the IEEE*, vol. 95, pp. 704–718, April 2007.

[25] T. Elwert, D. Goldmann, F. Römer, M. Buchert, C. Merz, D. Schueler, and J. Sutter, "Current developments and challenges in the recycling of key components of (hybrid) electric vehicles," *Recycling*, vol. 1, no. 1, pp. 25–60, 2015.

[26] L. Kumar and S. Jain, "Electric propulsion system for electric vehicular technology: A review," *Renewable and Sustainable Energy Reviews*, vol. 29, pp. 924 – 940, 2014.

[27] T. Miller, *Brushless permanent-magnet and reluctance motor drives*. Monographs in electrical and electronic engineering, Clarendon Press, 1989.

[28] D. G. Dorrell, A. M. Knight, M. Popescu, L. Evans, and D. A. Staton, "Comparison of different motor design drives for hybrid electric vehicles," in *2010 IEEE Energy Conversion Congress and Exposition*, pp. 3352–3359, Sept 2010.

[29] G. Hennenberg and J. A. Viorel, *Variable Reluctance Electrical Machines*. Aachen: Shaker Verlag, 2001.

[30] M. R. Harris and B. C. Mecrow, "Variable reluctance permanent magnet motors for high specific output," in *1993 Sixth International Conference on Electrical Machines and Drives (Conf. Publ. No. 376)*, pp. 437–442, Sep. 1993.

[31] J. G. Washington, G. J. Atkinson, N. J. Baker, A. G. Jack, B. C. Mecrow, B. B. Jensen, L. O. Pennander, G. L. Nord, and L. Sjöberg, "Three-phase modulated pole machine topologies utilizing mutual flux paths," *IEEE Transactions on Energy Conversion*, vol. 27, pp. 507–515, June 2012.

[32] W. M. Arshad, T. Backstrom, and C. Sadarangani, "Analytical design and analysis procedure for a transverse flux machine," in *IEMDC 2001. IEEE International Electric Machines and Drives Conference (Cat. No.01EX485)*, pp. 115–121, 2001.

[33] K. Y. Lu, E. Ritchie, P. O. Rasmussem, and P. Sandholdt, "Modeling and power factor analysis of a single phase surface mounted permanent magnet transverse flux machine," in *The Fifth International Conference on Power Electronics and Drive Systems, 2003. PEDS 2003.*, vol. 2, pp. 1609–1613 Vol.2, Nov 2003.

[34] P. O. Rasmussen, G. Runólfsson, T. Thorsdóttir, U. Jakobsen, and A. H. Pedersen, "E-core transverse flux machine with integrated fault detection system," in *2011 International Conference on Electrical Machines and Systems*, pp. 1–6, Aug 2011.

[35] D. Svechkarenko, *On Design and Analysis of a Novel Transverse Flux Generator for Direct-driven Wind Application*. PhD thesis, KTH, Electrical Machines and Power Electronics, 2010. QC 20101109.

[36] J. F. Gieras, R. J. Wang, and M. J. Kamper, *Axial Flux Permanent Magnet Brushless Machines*. Dordrecht: Springer Netherlands, 2008.

[37] S. Kahourzade, A. Mahmoudi, H. W. Ping, and M. N. Uddin, "A comprehensive review of axial-flux permanent-magnet machines," *Canadian Journal of Electrical and Computer Engineering*, vol. 37, pp. 19–33, winter 2014.

[38] M. Aydin, S. Huang, and T. Lipo, "Axial flux permanent magnet disc machines: A review," *Conf. Record of SPEEDAM*, 01 2004.

[39] K. Sitapati and R. Krishnan, "Performance comparisons of radial and axial field, permanent-magnet, brushless machines," *IEEE Transactions on Industry Applications*, vol. 37, pp. 1219–1226, Sep 2001.

[40] Y. J. Cao, Y. K. Huang, and L. Jin, "Research on axial magnetic force and rotor mechanical stress of an air-cored axial-flux permanent magnet machine based on 3d fem," in *Vibration, Structural Engineering and Measurement I*, vol. 105 of *Applied Mechanics and Materials*, pp. 160–163, Trans Tech Publications, 1 2012.

[41] YASA Limited, "YASA p400r series e-motor." [Online]. Available: https://www.yasa.com/wp-content/uploads/2018/01/YASA_P400_Product_Sheet.pdf. [Accessed: Mar. 01, 2019].

[42] MAGNAX, "Magnax yoke-less axial flux permanent magnet machine." [Online]. Available: https://www.magnax.com/product. [Accessed: Mar. 01, 2019].

[43] EMRAX, "Emrax 188 - emrax." [Online]. Available: https://emrax.com/products/emrax-188/. [Accessed: Mar. 01, 2019].

[44] T. Kenjo and A. Sugawara, *Stepping Motors and Their Microprocessor Controls*. Monographs in Electrical and E, Clarendon Press, 1994.

[45] B. Philip, *Electrical Steels for Rotating Machines*, ch. Competing materials, pp. 197–202. Energy Engineering, Institution of Engineering and Technology, 2002.

[46] B. Philip, *Electrical Steels for Rotating Machines*, ch. High-frequency applications, pp. 85–98. Energy Engineering, Institution of Engineering and Technology, 2002.

[47] Advanced Technology & Materials Co., Ltd., "Antaimo amorphous c-cores." [Online]. Available: http://www.atmcn.com/Subsidiary/Metal/Products/3237.shtml. [Accessed: Sept. 22, 2018].

[48] M. Dems and K. Komeza, "Performance characteristics of a high-speed energy-saving induction motor with an amorphous stator core," *IEEE Transactions on Industrial Electronics*, vol. 61, pp. 3046–3055, June 2014.

[49] T. Fan, Q. Li, and X. Wen, "Development of a high power density motor made of amorphous alloy cores," *IEEE Transactions on Industrial Electronics*, vol. 61, pp. 4510–4518, Sep. 2014.

[50] S. Okamoto, N. Denis, Y. Kato, M. Ieki, and K. Fujisaki, "Core loss reduction of an interior permanent-magnet synchronous motor using amorphous stator core," *IEEE Transactions on Industry Applications*, vol. 52, pp. 2261–2268, May 2016.

[51] Y. Enomoto, M. Ito, H. Koharagi, R. Masaki, S. Ohiwa, C. Ishihara, and M. Mita, "Evaluation of experimental permanent-magnet brushless motor utilizing new magnetic material for stator core teeth," *IEEE Transactions on Magnetics*, vol. 41, pp. 4304–4308, Nov 2005.

[52] N. Ertugrul, R. Hasegawa, W. L. Soong, J. Gayler, S. Kloeden, and S. Kahourzade, "A novel tapered rotating electrical machine topology utilizing cut amorphous magnetic material," *IEEE Transactions on Magnetics*, vol. 51, pp. 1–6, July 2015.

[53] Z. Wang, Y. Enomoto, M. Ito, R. Masaki, S. Morinaga, H. Itabashi, and S. Tanigawa, "Development of a permanent magnet motor utilizing amorphous wound cores," *IEEE Transactions on Magnetics*, vol. 46, pp. 570–573, Feb 2010.

[54] N. Dehlinger and M. R. Dubois, "Clawpole transverse flux machines with amorphous stator cores," in *2008 18th International Conference on Electrical Machines*, pp. 1–6, Sept 2008.

[55] P. O. Rasmussen, "Transverse flux machine with stator made of e-shaped laminates." Patent, WO/2002/091547, November 2002. `https://patentscope.wipo.int/search/en/detail.jsf?docId=WO2002091547&tab=PCTBIBLIO&maxRec=1000`.

[56] ePower Technology, "E-core transverse flux machine (ETFM)." [Online]. Available: `http://epower-technology.com/wp-content/uploads/sites/1655/2014/02/ETFM-datasheet-2013-12-06.pdf`. [Accessed: Dec. 2016].

[57] X. Liu, K. Park, and Z. Chen, "A novel excitation assistance switched reluctance wind power generator," *IEEE Transactions on Magnetics*, vol. 50, pp. 1–4, Nov 2014.

[58] J. Ou, Y. Liu, M. Schiefer, and M. Doppelbauer, "A novel pm-free high-speed linear machine with amorphous primary core," *IEEE Transactions on Magnetics*, vol. 53, pp. 1–8, Nov 2017.

[59] K. Lu, *Design Study for Controllable Electric Motor for Three Wheel Drive, In Wheel Mounting on Professional, Electric, Lawn Mower*. PhD thesis, Aalborg University, 2004.

[60] T. Frandsen, *Motor Integrated Permanent Magnet Gear*. PhD thesis, Aalborg University, 2016. Associate Prof. Peter Omand Rasmussen, Aalborg University.

[61] W. L. Soong, "Sizing of electrical machines." [Online]. Available: `http://www.eleceng.adelaide.edu.au/research/power/pebn/pebn009%20sizing\%20of\%20electrical\%20machines.pdf`, September 2008. [Accessed: Mar. 28, 2019].

[62] F. Meier, *Permanent-Magnet Synchronous Machines with Non-Overlapping Concentrated Windings for Low-Speed Direct-Drive Applications*. Stockholm: KTH, 2008.

[63] F. Magnussen and C. Sadarangani, "Winding factors and joule losses of permanent magnet machines with concentrated windings," in *IEEE International Electric Machines and Drives Conference, 2003. IEMDC'03.*, vol. 1, pp. 333–339 vol.1, June 2003.

[64] J. Pyrhonen, T. Jokinen, and V. Hrabovcova, *Design of Rotating Electrical Machines*. Wiley-Blackwell, 2013.

[65] Hitachi Metals America, Ltd., "Amorphous and Nanocrystalline-POWERLITE C-Cores." [Online]. Available: `https://www.hitachimetals.com/materials-products/amorphous-nanocrystalline/powerlite-c-cores.php`. [Accessed: Sept. 22, 2018].

[66] King Magnetics, "High Performance Amorphous and Nanocrystalline Cores." [Online]. Available: `http://www.kingmagnetics.com/wp-content/uploads/kingmagnetics-catalog.pdf`. [Accessed: Sept. 22, 2018].

[67] T. Lipo, *Introduction to AC Machine Design*. IEEE Press Series on Power Engineering, Wiley, 2017.

[68] D. Hanselman, *Brushless Permanent Magnet Motor Design*. Magna Physics Publishing, 2006.

[69] H. Domeki, Y. Ishihara, C. Kaido, Y. Kawase, S. Kitamura, T. Shimomura, N. Takahashi, T. Yamada, and K. Yamazaki, "Investigation of benchmark model for estimating iron loss in rotating machine," *IEEE Transactions on Magnetics*, vol. 40, pp. 794–797, March 2004.

[70] A. Bettayeb, R. Kaczmarek, and J.-C. Vannier, "Analytical estimation of rotor loss due to stator slotting of synchronous pm machines," *World Academy of Science, Engineering and Technology*, vol. 66, 2010.

[71] Z. X. Fang, Z. Q. Zhu, L. J. Wu, and Z. P. Xia, "Simple and accurate analytical estimation of slotting effect on magnet loss in fractional-slot surface-mounted pm machines," in *2012 XXth International Conference on Electrical Machines*, pp. 464–470, Sep. 2012.

[72] A. G. Gonzalez, J. Millinger, and J. Soulard, "Magnet losses in inverter-fed two-pole pm machines," in *2016 XXII International Conference on Electrical Machines (ICEM)*, pp. 1854–1860, Sept 2016.

[73] A. Garcia Gonzalez, "Magnet losses in inverter-fed high-speed pm machines," Master's thesis, KTH, Electrical Energy Conversion, 2015.

[74] "Wuxi lingming electric drive technology co., ltd." [Online]. Available: `http://www.lingmingmotor.com`. [Accessed: Nov. 22, 2017].

[75] A. G. Gonzalez, D. Wang, and P. O. Rasmussen, "Investigation of a surface mounted pm machine concept with 3d-flux paths, modular stator and amorphous material," in *2019 IEEE International Electric Machines Drives Conference (IEMDC)*, pp. 739–744, May 2019.

[76] "Cogent - surahammars bruks ab." [Online]. Available: https://cogent-power.com/cms-data/downloads/m300-35a.pdf. [Accessed: May, 2016].

[77] P. O. Rasmussen, T. V. Frandsen, K. K. Jensen, and K. Jessen, "Experimental evaluation of a motor-integrated permanent-magnet gear," *IEEE Transactions on Industry Applications*, vol. 49, pp. 850–859, March 2013.

[78] A. Rezzoug and Z. M. E., *Non-Conventional Electrical Machines*. Somerset, UNITED STATES: John Wiley and Sons, Incorporated, 2011.

[79] YANTAI SHOUGANG, Inc., "Yantai Shougang Magnetic Materials, Inc. Rare Earth Products." [Online]. Available: https://cdn.website-editor.net/25bdc0ebec054b3caa18a8f05aeaf1bd/files/uploaded/YSM%2520magnetic%2520properites%25202016.pdf. [Accessed: Sept. 22, 2018].

[80] "Thermal design," in *Introduction to AC Machine Design*, ch. 7, pp. 305–357, John Wiley & Sons, Ltd, 2017.

[81] P. C. Kjær, "Design failure-mode effects analysis (d-fmea) for power electronic converters - tutorial." PhD. Course, September 2018. Aalborg, Denmark.

[82] A. K. Jha, Z. Li, A. Garcia, P. Upadhayay, P. O. Rasmussen, A. Kedous-Lebouc, and L. Garbuio, "Weighted index of recycling and energy (wire) cost for motors in electric vehicles," in *2018 International Symposium on Power Electronics, Electrical Drives, Automation and Motion (SPEEDAM)*, pp. 407–412, June 2018.

[83] P. Upadhayay, A. G. Garcia, Z. Li, A. K. Jha, P. O. Rasmussen, A. Kedous-Lebouc, and J. Mipo, "Evaluation of energy cost index for an electric vehicle motor over a particular drive cycle with recycled magnet concept," in *2018 XIII International Conference on Electrical Machines (ICEM)*, pp. 738–744, Sept 2018.

[84] R. Sheridan, A. Williams, I. Harris, and A. Walton, "Improved hddr processing route for production of anisotropic powder from sintered ndfeb type magnets," *Journal of Magnetism and Magnetic Materials*, vol. 350, pp. 114 – 118, 2014.

[85] A. G. Gonzalez, A. K. Jha, Z. Li, P. Upadhayay, and P. Rasmussen, "Validation of efficiency maps of an outer rotor surface mounted permanent magnet machine for evaluation of recyclability of magnets," in *2018 IEEE International Magnetic Conference (INTERMAG)*, pp. 1–6, April 2018.

[86] T. J. Barlow, S. Latham, I. S. McCrae, and P. G. Boulter, "A reference book of driving cycles for use in the measurement of road vehicle emissions: Version 3." [Online]. Available: https://trl.co.uk/reports/PPR354, 2009. [Accessed: Sept. 22, 2018].

[87] WLTPfacts.eu, "From NEDC to WLTP: What will change?." [Online]. Available: http://wltpfacts.eu/from-nedc-to-wltp-change/, March 2019. [Accessed: Mar. 28, 2019].

[88] J. Larminie and J. Lowry, "Electric vehicle modelling," in *Electric Vehicle Technology Explained*, ch. 8, Somerset, GB: John Wiley and Sons, Inc., second ed., 2012.

[89] B. Mashadi, D. A. Crolla, and B. Mashhadi in *Vehicle Powertrain Systems : Integration and Optimization*, New York, UK: John Wiley and Sons, Inc., 2011.

[90] K. P. and T. A., "Life cycle impact of rare earth elements," *ISRN Metallurgy*, vol. 2014, p. 10, May 2014.

[91] A. Schreiber, J. Marx, P. Zapp, J.-F. Hake, D. Voßenkaul, and B. Friedrich, "Environmental impacts of rare earth mining and separation based on eudialyte: A new european way," *Resources*, vol. 5, p. 32, Oct 2016.

[92] J. C. Lee and Z. Wen, "Rare earths from mines to metals: Comparing environmental impacts from china's main production pathways," *Journal of Industrial Ecology*, vol. 21, no. 5, pp. 1277–1290, 2017.

[93] S. Riaño and K. Binnemans, "Extraction and separation of neodymium and dysprosium from used ndfeb magnets: an application of ionic liquids in solvent extraction towards the recycling of magnets," *Green Chem.*, vol. 17, pp. 2931–2942, 2015.

[94] P. Venkatesan, Z. Sun, J. Sietsma, and Y. Yang, "Electrochemical recovery of rare earth elements from magnet scraps: A theoretical analysis," in *Proceedings of the 1st European Rare Earth Resources Conference ERES 2014)* (E. Balomenos, D. Panias, and I. Paspaliaris, eds.), pp. 163–170, Heliotopos Conferences Ltd., 2014.

[95] Eurostat - Statistic Explained, "Electricity price statistics." [Online]. Available: https://ec.europa.eu/eurostat/statistics-explained/index.php/Electricity_price_statistics, May 2019. [Accessed: Sept. 22, 2018].

[96] European Environment Agency, "CO2 Emission Intensity." [Online]. Available: https://www.eea.europa.eu/data-and-maps/daviz/co2-emission-intensity-5#tab-googlechartid_chart_11_filters=

%7B"rowFilters"%3A%7B%7D%3B"columnFilters"%3A%7B"pre_config_ugeo"%3A%5B"European%20Union%20(current%20composition)"%5D%7D%7D, Dec 2018. [Accessed: Sept. 22, 2018.].

Publication P1

Magnet Losses in Inverter-Fed Two-Pole PM Machines

A. Garcia Gonzalez, J. Millinger and J. Soulard, *Member, IEEE*

***Abstract*—This article deals with the estimation of magnet losses in a permanent-magnet motor inserted in a nut-runner. This type of machine has interesting features such as being two-pole, slot-less and running at a high speed (30000 rpm). Two analytical models were chosen from the literature. A numerical estimation of the losses with 2D Finite Element Method was carried out. A detailed investigation of the effect of simulation settings (e.g., mesh size, time-step, remanence flux density in the magnet, superposition of the losses, etc.) was performed. Finally, calculation of losses with 3D-FEM were also run in order to compare the calculated losses with both analytical and 2D-FEM results. The estimation of the losses focuses on a range of frequencies between 10 and 100 kHz.**

***Index Terms*—Eddy currents, 2D-FEM, 3D-FEM, magnet losses, nut-runner, PM motor, slot-less winding.**

I. Introduction

In general, a nut-runner system is composed by an electrical motor fed by a converter via a filter [1]. New emerging technologies like Silicon Carbide (SiC) transistors, allow a higher switching frequency and in consequence a possible reduction of the size of both inverter and filter [2]. However, it is of prime importance to estimate the consequences of a component change in the performance of the motor, for example in terms of losses. Rare-earth elements used in the manufacturing of the magnets used in PM machines are critical due to the elevated prices they have reached in recent years [3]. Hence, it is appropriate to investigate thoroughly how to best design the magnets in the motor.

Many articles about losses in magnets of PM machines have been published recently. However, there are certainly few articles reporting both 3D-FEM simulations and validations through experimental measurements. Furthermore, only [4] and [5] proposed models of machines with similar characteristics to the machine studied in this project (i.e., slot-less with a magnetized ring). However, the results obtained when implementing the models described in these articles were not satisfactory and in consequence other models were investigated. Since these models neglect the end-effects, it is necessary to investigate to which extent they are adequate for calculating the losses in the machine under study, where the length of the magnet is lower than the magnet width ($l < w$).

The main goal of this article is to enhance the interpretation of the losses appearing in the magnets of a PM machine as a result of the harmonics fed by the Pulse Wide Modulation (PWM) in the inverter. Furthermore, different parameters when calculating magnet losses in FEM software are studied for 2D and 3D models. The main dimensions of the machine and the working characteristics are presented in Section II. In order to predict the value of magnet losses, an extensive literature review was performed. Section III is devoted to the description of the analytical models selected to determine the losses in the magnets. The influence on the losses of mesh elements size, time-step and the remanence flux density of magnet material is studied and presented in Section IV. In addition, the evaluation of the principle of superposition, simulations at zero speed of the rotor and 3D-FEM results are included. The analysis of the results obtained by analytical models, 2D and 3D-FEM simulations is presented in Section V. Lastly, conclusions are drawn and future work is proposed.

A. Garcia Gonzalez is with the Department of Energy Technology, Aalborg University, Aalborg 9220, Denmark (e-mail: agg@et.aau.dk)

J. Millinger is with is with the Department of Electric Power and Energy Systems, KTH Royal Institute of Technology, and with Atlas Copco, Stockholm, Sweden (e-mail: jonasmil@kth.se)

J. Soulard is with is with the Department of Electrical Energy Conversion (E2C), KTH Royal Institute of Technology, SE-10044 Stockholm, Sweden (e-mail: soulard@kth.se)

II. Description of the Machine

A. Main dimensions

The main dimensions of the slot-less machine analysed in this study are shown in table I. The analytical calculations and 2D and 3D FEM simulations were performed on a machine with a length equal to a single magnet segment l.

TABLE I: Main machine dimensions.

PARAMETER	VALUE
Active length L_a [mm]	65
Maximum speed n_{max} [rpm]	30000
Air-gap length l_g [mm]	0.5
Number of winding turns per phase N_c	65
Magnet axial length l [mm]	4.5
Magnet thickness h [mm]	5
Magnet radius R_m [mm]	7.5
Shaft diameter R_r [mm]	2.5
Inner stator diameter R_s [mm]	23.2
Outer stator diameter [mm]	31
Number of poles p	2
Peak phase current I [A]	1
Fundamental frequency f_0 [Hz]	500
Winding type: distributed $q = 1$	

B. Working characteristics

The machine analysed in this project is applied to the power drive of a nut-runner. The working cycle of this type of machine (figure 1) is divided in two stages. The first, in

which the machine is running at maximum speed with zero torque for reaching the tightening point. The second, at which the machine reaches nominal speed as the torque is increased to reach the correct value to be applied to the nut. This study was focused on the first operational stage, since it is this region in which the company manufacturing the nut-runner has more interest.

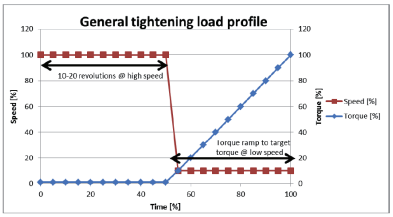

Fig. 1: Typical nut-runner operational characteristic [1].

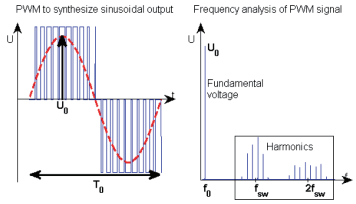

Fig. 2: FFT of PWM voltage [1].

Given the PWM technique implemented in the converter, the running at no-load may involve relatively high losses due to the appearance of harmonics concentrated at 1 time and 2 times the switching frequency f_{sw}. Figure 2 shows the harmonic distribution of the inverter output voltage at no-load. For the coming analyses, it is assumed that the switching frequency f_{sw} is 10 kHz. Additionally, the fundamental frequency f_0 is calculated as $f_0 = n_{max}/60$ where n_{max} is the maximum speed. For this study one harmonic at f_{sw} and one harmonic at $2f_{sw}$ are selected. Thus, the harmonics indexes n_1 and n_2 are given by $n_1 = f_{sw}/f_0$ and $n_2 = 2f_{sw}/f_0$. The harmonic currents applied in the simulations are expressed as:

$$\begin{aligned} I_a &= I\cos(n_1\omega t) + I\cos(n_2\omega t) \\ I_b &= I\cos(n_1(\omega t - 2\pi/3)) + I\cos(n_2(\omega t - 2\pi/3)) \\ I_c &= I\cos(n_1(\omega t - 4\pi/3)) + I\cos(n_2(\omega t - 4\pi/3)) \end{aligned} \quad (1)$$

III. Review of Analytical Models

A. Eddy Currents

The mechanisms governing the eddy currents in a magnet are the same as for the eddy currents in electrical sheets and solid conductors. A time varying magnetic flux density, in this case generated by the mmf of the currents in the stator windings $B_{\delta w}$, penetrates the surface of the magnet. This incident magnetic flux density originates eddy currents as illustrated in figure 3a. It is appropriate to clarify that eddy currents are originated only by time and space harmonics in the stator mmf. That is, the fundamental in space of the mmf at synchronous frequency is seen by the magnets in the rotor as a DC field, consequently, does not create eddy currents. A method to counteract these losses, similar to the lamination technique implemented in a stator core, is the implementation of circumferential and axial segmentations to the magnets [6], [7], [8], [9].

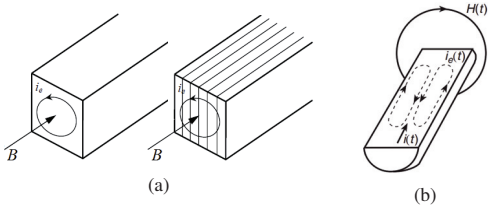

Fig. 3: (a) Eddy currents generation, (b) Skin effect in a long straight round single conductor.

The major consequence of these eddy currents is the heat generated by Joule effect, as the magnets are made of a material with a high conductivity. Additionally, two important phenomena by which the calculation of losses in the magnet can be affected are the reaction field of eddy currents B_{eddy} and the skin effect. The B_{eddy} is generated by the eddy currents themselves, since these are varying in time as well [10]. This B_{eddy} opposes to the external magnetic field $B_{\delta w}$ which is inducing the eddy currents. Consequently, the value of $B_{\delta w}$ is reduced. In addition, $B_{\delta w}$ causes the displacement of the current inside the conductor (figure 3b), being forced to flow close to the conductor's surface. Hence, the effective area is reduced with increasing frequency. This is the definition of skin effect [11].

B. Model neglecting the reaction effect of eddy currents

As described in [12] the calculation of the losses in the magnet when the skin effect is disregarded (low frequencies) is given by the following expression:

$$P_m = \frac{V_m \hat{B}_r^2 \omega_h^2}{16\rho_m} \cdot \frac{w^2 l^2}{l^2 + w^2} \quad (2)$$

Where V_m is the volume of the magnet (assuming that this is of a rectangular section), w is the radial span of the magnet, $\hat{B}_r$ is the peak magnetic flux density in the air-gap due to the mmf of the stator current, ω_h is the electrical angular frequency of the applied harmonic current and ρ_m is the resistivity of the magnet. The assumptions adopted for the calculation of the losses by this model include neglecting skin effect, considering homogeneity of B over the width w of the magnet and neglecting end effects. In addition, this study presents an alternative for the calculation of losses for higher frequencies. Taking [13] as reference, the power losses per area exposed to a field H can be calculated as:

$$P/S = 1/2 \cdot H_{tan}^2 R_s \quad (3)$$

With H_{tan} as the peak tangential incident magnetic field, S being the tangential surface given by $S = 2h(l + w)$, and R_s is the surface impedance $R_s = 1/(\delta_m \sigma_m)$ where δ_m, the skin depth, is given by:

$$\delta_m = \sqrt{\frac{2}{\omega_h \sigma_m \mu_m \mu_0}} \tag{4}$$

With σ_m and μ_m as the conductivity and permeability of the magnet. The criterion for selecting either of the two methods is based on how large the skin depth is in comparison to the magnet dimensions w, h and l. In coming sections of this article these two models are denominated *Huang_a* and *Huang_b*, respectively.

C. Model accounting for the reaction effect of the eddy currents

This model presented in [14] defines the losses in the magnet region as:

$$\begin{aligned} P_{III} = 2\alpha_p \pi L_a R_s^2 \omega_r \mu_0 \mu_m \mu_{sl}^2 \sum_{n=1}^{\infty} \sum_{m=-\infty}^{\infty} \frac{(n+m)}{m} J_{nm}^2 \\ \cdot \mathrm{Re}\left\{ j\frac{C_9}{K} \left[\left(\frac{\tau_m R_r}{m} \mathbf{Y}_{m-1}(\tau_m R_r) - \mathbf{Y}_m(\tau_m R_r) \right) \mathbf{J}_m(\tau_m R_m) \right.\right. \\ \left. - \left(\frac{\tau_m R_r}{m} \mathbf{J}_{m-1}(\tau_m R_r) - \mathbf{J}_m(\tau_m R_r) \right) \mathbf{Y}_m(\tau_m R_m) \right] \\ \cdot \frac{C_9^*}{K^*} \left[\left(\frac{\tau_m R_r}{m} \mathbf{Y}_{m-1}(\tau_m R_r) - \mathbf{Y}_m(\tau_m R_r) \right) \right. \\ \cdot \left(\frac{\tau_m R_m}{m} \mathbf{J}_{m-1}(\tau_m R_m) - \mathbf{J}_m(\tau_m R_m) \right) \\ - \left(\frac{\tau_m R_r}{m} \mathbf{J}_{m-1}(\tau_m R_r) - \mathbf{J}_m(\tau_m R_r) \right) \\ \left.\left. \cdot \left(\frac{\tau_m R_m}{m} \mathbf{Y}_{m-1}(\tau_m R_m) - \mathbf{Y}_m(\tau_m R_m) \right) \right]^* \right\} \end{aligned} \tag{5}$$

Where, the sub-indexes m and n correspond to space and time harmonics, respectively. α_p and ω_r are the pole arc to pole pitch ratio and the rotor angular velocity, respectively. The functions $\mathbf{J}_m$ and $\mathbf{Y}_m$ are Bessel functions of first and second kind of m order, respectively. And the harmonic amplitude of the equivalent current sheet distribution:

$$J_{nm} = \frac{3 N_c I K_{dp\nu} K_{so\nu}}{\pi R_s} \tag{6}$$

Where, $K_{so\nu}$ and $K_{dp\nu}$ the slot opening and winding factors defined in [15]. Other parameters such as C_9, K, τ_m, τ_{sl} and μ_{sl} are described and derived in the reference, as well as, the main assumptions adopted for this model. Therefore, for sake of simplicity and to prevent any misinterpretation, their descriptions are omitted in this article. In coming sections of this document, this model is referred to as *Zhu*.

The analytical models selected were developed for machines with different geometry and characteristics than the slot-less machine under investigation. Therefore, it was required to adapt the expressions to the actual machine. Note that for evaluating the losses with models *Huang_a* and *b*, the magnet ring is assumed to have a rectangular section with a total width of $(R_r + R_m)/2$. On the other hand, for model *Zhu*, the coefficient $K_{so\nu}$ is assumed to be equal to 1, due to the absence of slots in the actual machine. Additionally, the thickness of the retaining sleeve described in the reference is set to zero and the corresponding permeability and conductivity set to 1 and zero, respectively.

IV. FEM Simulations

A. 2D-FEM Simulations

The FEM software selected was FLUX™ v12 from Cedrat. All simulations were performed in the *Transient Magnetic* module. Figure 4 shows the geometry of the 2D model.

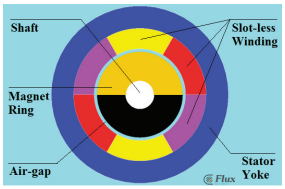

Fig. 4: 2D geometry in FLUX software.

1) Mesh Size Validations: For validating the size mesh required to calculate losses in magnet, three options were adopted. The selection of mesh size was focused on the regions which are believed to be more critical. For all three meshes, the smallest mesh elements are located within the shaft, magnet and air-gap regions. Furthermore, the size of the elements in these regions was selected to be lower than the skin depth of the magnet δ_m at 10 kHz. Additionally, it was decided to link the time-step for each mesh to the size of the elements.

- *Mesh 1: Aided mesh*. For this type of mesh, the aided mesh option was activated. The selection of the time-step in this case, was based on the suggestions from the tutorials of FLUX™. With a number of steps $n_{steps} = 140$ the time-step was selected as $t_{step_1} = T_0/n_{step}$. With T_0 as the period of the fundamental frequency $f_0 = 500$ Hz the time-step was calculated as $t = 14.3\,\mu$s.
- *Mesh 2: Coarse mesh*. This type of mesh is of lower quality when compared with the "aided mesh". Some parameters defining the mesh in the software were set up manually and the aided mesh was disabled. The software offers several options for defining the size of the elements required. Among them, the number of elements that a mesh line should have (*Arithmetic*). A rough calculation of the size of the elements inside the magnet can be done with the perimeter described by the magnet radius R_m and the number of segments n_{seg} defined for this line $size_2 = 2\pi R_m/n_{seg}$. This yields $size_2 = 1.31$ mm which is lower than the skin depth by a factor of 3 approximately. Note that the skin depth for frequencies of 10 and 20 kHz are 5.8 and 4.1 mm respectively (according to equation 4). The definition of the time-step was achieved by introducing $size_2$ in equation 4. An equivalent frequency f_{step2} = 197.11

kHz was obtained. Consequently, the time-step for *Mesh 2* was $t_{step2} = 5.07\,\mu s$.

- *Mesh 3: Fine mesh.* For this mesh type the elements are finer in comparison to those of the "aided mesh". For the calculation of the time-step, similar procedure was followed as for *Mesh 2*. The equivalent frequency for the calculated segment size $size_3$ is f_{step3}= 1404.40 kHz and the time-step $t_{step3} = 0.712\,\mu s$.

The results for each mesh type with its own time-step are shown in figure 5a. The average values of losses for meshes 1, 2 and 3 are; 1.67, 2.67 and 2.81 W, respectively. Showing a highest deviation of 67.95% between *Mesh 3* and *Mesh 1* and the lowest deviation equals to 5.07% between *Mesh 2* and *Mesh 3*.

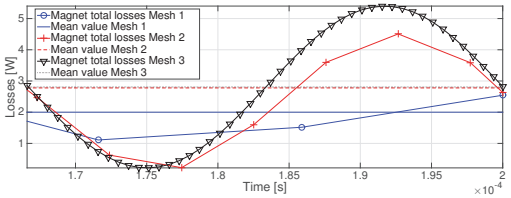

(a)

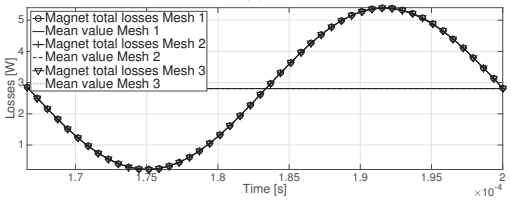

(b)

Fig. 5: Magnet losses for different mesh densities; (a) different time-step, (b) same time-step ($t = 0.712\,\mu s$).

In addition, it was decided to investigate the magnet losses calculated with each mesh type keeping the same time-step (i.e., equals to $t_{step3} = 0.712\,\mu s$). The results are shown in figure 5b. A very good agreement between the three different meshes was obtained with approximately zero deviation. Here an important conclusion may be drawn; the value of the time-step showed to have a stronger effect on the losses than the density of the mesh. In addition, the reduction of both the size of the mesh elements and the value of time-step increased the simulation time. Consequently, it was decided to investigate further the effect of time-step on the calculation of the magnet losses.

2) Time-step validations: As shown in previous sections, the magnet losses were not varying with the size of the mesh elements for the three tested meshes. However, there was a dependence with the time-step, the frequency and the skin depth. Therefore, it was necessary to investigate to what extent the calculation of the losses is affected by changes in the value of the time-step. Thus, the time-step was formulated as a function of the frequency, as $t_{step} = 1/(f_{sw} k_{time})$. Where k_{time} is the number of samples per period. The factor k_{time} was taken from 5 to 50 in steps of 5 and applied to the fine mesh (i.e., *Mesh 3*). The variation of the losses with the number of points per period k_{time} is shown in figure 6. The lower k_{time}, the lower the calculated value of losses and as the number of sampling points increased, the results became more stable converging to a value of 2.64 [W].

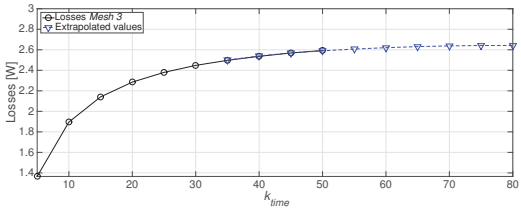

Fig. 6: Magnet losses for different time-step.

The trend is that the deviation in losses between two consecutive values of k_{time} is reducing as the number of samples is increased. Then, it is required to define at which level of deviation is considered that a reliable value has been reached. For example, if it is assumed that the solution is reached when a variation of 1 % is achieved, a number of sampling points $k_{time} = 50$ is required. On the other hand, if a higher level of accuracy is required, the factor k_{time} may increase up to 80. Consequently, the simulation time is increased. Hence, the selection of this factor is a compromise between time and accuracy.

3) Effect of remanence magnetic flux density on losses: These simulations were intended to evaluate the effect that B_r could have in the calculation of the magnet losses. Hence, it was decided to evaluate the losses in two different scenarios:

- *Magnet OFF:* Setting the magnet region as a solid conducting region ($B_r = 0$ T).
- *Magnet ON:* Setting the magnet as a *Linear magnet described by the B_r module*. That is, setting the value of $B_r = 1.12$ T.

In addition to these two scenarios, it was decided to evaluate the effect at a frequency range from 10 to 100 kHz. The losses calculated at 10 kHz are presented in figure 7. The results show a good fit for both cases (magnet ON and OFF). Consequently, the value of the remanence magnetic flux density B_r is not expected to have a significant influence on the losses. Similar results were obtained for a frequency of 100 kHz. In addition, the current density distribution in the magnet is shown in figures 8a and 8b for frequencies 10 and 100 kHz, respectively. Similarly, no influence of B_r in the current density distribution and losses was identified. A symmetrical behaviour of the current density in the magnet was expected. However, an undulating behaviour may be observed in figures 8a and 8b. This is a result of the reaction field of eddy currents B_{eddy}. The skin effect is more pronounced as the frequency increases in figure 8b for a frequency of 100 kHz.

4) Superposition of the losses: It was then verified if the principle of superposition might be applied to the simulations for different harmonic indexes. This was performed keeping

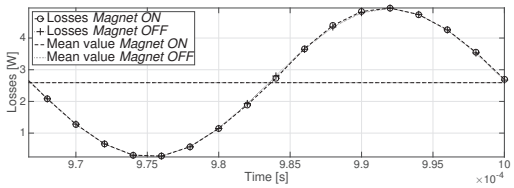

Fig. 7: Magnet losses at 10 kHz magnet on and off.

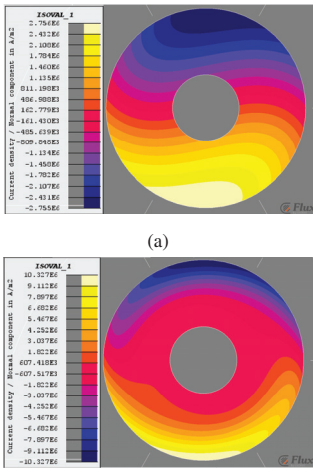

(a)

(b)

Fig. 8: Current density distribution magnet off; (a) 10 kHz, $t = 0.5\,\text{ms}$. (b) 100 kHz, $t = 0.1\,\text{ms}$.

the rotor speed at a value of 30000 rpm, and varying the harmonic indexes n_1 and n_2 accordingly in order to obtain a variation of the switching frequency f_{sw} from 10 to 100 kHz in steps of 1 kHz. Three different cases were studied:

- *Case 1*: Losses only due to the harmonic index n_1 and a phase shift of $\pi/3$.
- *Case 2*: Losses only due to the harmonic index n_2 and a phase shift of $\pi/2$.
- *Case 3*: Total losses due to both n_1 and n_2.

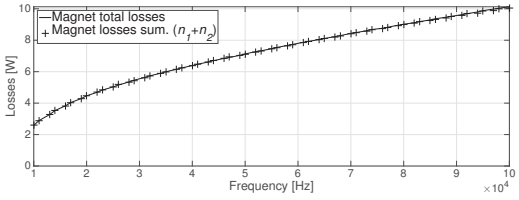

Fig. 9: Magnet losses vs. frequency.

Figure 9 shows that a perfect fit between the two methods was obtained with deviations lower than 1%. This confirms that for this type of machine superposition may be applied and that there will be no interaction between harmonics at f_{sw} and harmonics at $2f_{sw}$.

5) Simulations at zero speed in the rotor: An alternative for running the simulations was setting the speed of the rotor n_{max} as zero. Consequently, the only parameter varying with time would be the applied current. However, it was necessary to determine the direction of rotation of the harmonic indexes n_1 and n_2 in order to define the relative speed of rotation. This condition was evaluated at frequencies of 10 and 100 kHz. Figure 10 shows the results for the losses when the rotor is rotating at a fixed speed and when its speed is set to zero. A similar behaviour was obtained at a frequency of 100 kHz. This machine can be simulated at no speed since the space harmonics from the current loading are negligible. A reduction of the simulation times is expected by using this simulation method. However, in 2D-FEM simulation times were in the same range with both type of simulations.

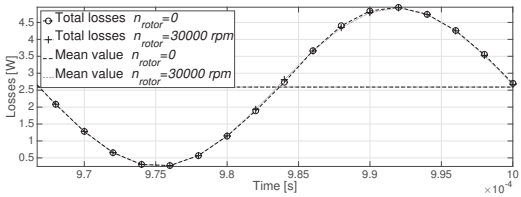

Fig. 10: Losses at 10 kHz.

B. 3D-FEM Simulations

The simulation settings presented in Subsection IV-A apply to the calculation of the losses in 3D-FEM. That is, same time-step factor and a fine mesh were selected in order to guarantee that the values calculated are representative and that a fair comparison can be done with 2D-FEM simulation results. Figure 11a shows the current density distribution over the surface of the magnet at 10 kHz. Yellow colours and large arrows indicate maximum values. At first glance the magnet could be divided into two regions in terms of the eddy current flow indicating the two incident values of $B_{\delta w}$. In addition, some hot-spots of critical regions in which these currents are the highest are identified as the boundaries between the shaft and magnet regions at the top and bottom faces of the magnet. This is due to the curvature described by these regions in which the currents are forced to vary their trajectory.

For performing a better analysis of the behaviour of the eddy currents inside the magnet, a 2D sub-region was defined inside the magnet volume parallel to xz axis. The eddy current plots for grid xz are shown in figure 11b. As predicted in the literature, the eddy currents are forced to flow in the periphery of the magnet finding a common returning path. The plane xy is a transition region in which currents change from the top region to the bottom region, thus closing the loop. The distribution of the losses is shown in figure 12. It follows the behaviour of the eddy currents since the losses are proportional to the square of the current.

The distribution of the losses in the xy plane is shown in figure 13. Here it is shown how the distribution of the current density and consequently the distribution of losses has a more symmetrical behaviour. This indicates that B_{eddy}

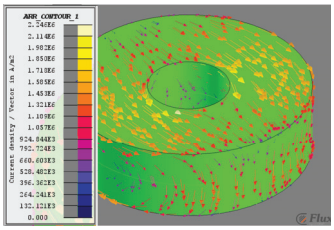

(a)

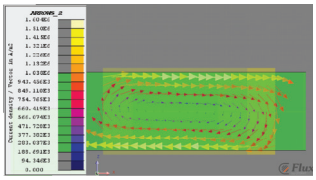

(b)

Fig. 11: Current density distribution at 10 kHz $t = 52\,\mu s$; (a) over the surface, (b) plane *xz*.

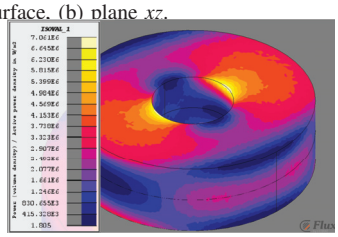

Fig. 12: Magnet loss distribution at 10 kHz; $t = 52\,\mu s$.

in 3D-FEM simulations is less pronounced than for the 2D-FEM simulations.

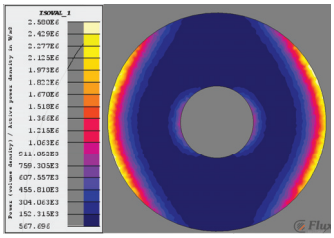

Fig. 13: Magnet loss distribution at 10 kHz; $t = 52\,\mu s$, plane *xy*.

In addition, the superposition principle, the effect of the remanence magnetic flux density of the magnet B_r and simulations of zero speed in the rotor were evaluated for 3D-FEM simulations. There were no significant deviations when calculating the losses with the three cases (*Case 1*, *Case 2* and *Case 3*). The effect of B_r in the magnet losses was negligible. Lastly, the simulations with zero speed of the rotor yielded a reduction of the simulation time of 28%. Same conclusion would be drawn at 100 kHz.

V. Results Analysis and Comparison

Figure 14 summarizes the losses calculated with the selected analytical models and with 2D and 3D-FEM simulations. The calculations of losses in the magnet were performed at frequencies from 10 to 100 kHz. As the frequency increases, model *Huang_a* neglecting the skin effect, shows the highest deviation. In contrast, the model *Huang_b* shows a similar trend when compared with 2D-FEM results but still with a large deviation. Regarding model *Zhu*, the results show not only a similar trend but also the lowest deviation. This allows to confirm that model *Zhu* may be applied to a slotless machine with a diametrically magnetized ring. However, there is a large deviation between the results of 2D and 3D-FEM.

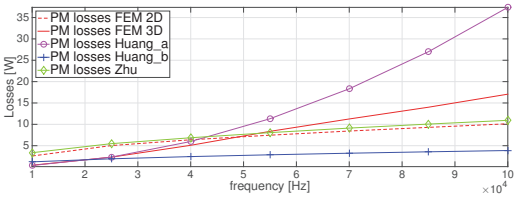

Fig. 14: Losses vs frequency 2D-FEM, 3D-FEM and analytical models.

Table II summarizes the values of losses obtained with both 2D and 3D-FEM calculations with their respective deviations at frequencies of 10, 40, 70 and 100 kHz for a magnet length of *l*. Values of the magnetic flux density in the air-gap $B_{\delta w}$ are also included.

TABLE II: Magnet losses vs. frequency 2D and 3D-FEM.

Freq. [kHz]	Loss magnet length=*l*			$B_{\delta w}$		
	2D FEM [W]	3D FEM [W]	ΔError [%]	2D FEM [mT]	3D FEM [mT]	ΔError [%]
10	2.59	0.44	-83.01	9.83	14.43	46.80
40	6.39	4.99	-21.91	6.51	13.11	101.38
70	8.43	11.16	32.38	5.35	11.99	124.11
100	10.13	16.96	67.42	4.75	10.01	110.74

At 100 kHz, the losses calculated with 3D-FEM are 67.42 % higher than predicted by 2D-FEM. In contrast, the simulation times were of 4419 and 660 seconds, respectively. The explanation to such large deviations at both low and high frequencies is the reaction field of eddy currents B_{eddy}. In 2D-FEM simulations, the end-effects are neglected, the equivalent impedance seen by the current is low and the eddy currents flowing in the magnet are high as a result. As a consequence, the reaction field of eddy currents B_{eddy} is higher and increasing with frequency. The magnetic flux density in the air-gap $B_{\delta w}$ is being reduced, which in return, yields lower losses. This is confirmed in table II where $B_{\delta w}$ for 2D-FEM has a diminution of its value of around 50 %. On the other hand, for 3D-FEM simulations, the eddy currents

described a different flow path, including the end-effects. The impedance seen by the current is much higher and consequently the eddy currents are more limited, resulting in a lower value. This is clarified in table II, where the value of $B_{\delta w}$ is reduced by approximately 30 %.

The investigation was extended to the case in which the magnet length l was affected by a factor of 2. The motivation for this selection, is to show that for a given value of l, the deviation between the losses calculated with both 2D and 3D-FEM should start reducing. The reduction of the deviation between 2D and 3D-FEM simulations is around 27% and 12% at lower and higher frequencies, respectively. In addition, the losses for a magnet length of l and $2l$ are shown in figure 15. The results from 2D-FEM simulations correspond to the values calculated in Subsection IV-A multiplied by 2. In figure 15, two frequencies at which the calculated losses in both 2D and 3D-FEM simulations are equal exist. These frequencies are at around 48 kHz for l and 30 kHz for $2l$. As the length of the magnet increases, the curve representing the losses calculated by 2D-FEM starts approaching to the curve representing 3D-FEM results as expected. This happens when the end-effect of the returning loop for the current in 3D-FEM simulations start to be insignificant (i.e., $l \gg w$).

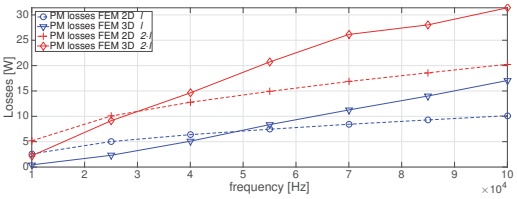

Fig. 15: Magnet losses comparison 2D and 3D-FEM simulations with l and $2l$.

VI. Conclusions

A thorough investigation of FEM simulation settings for calculating magnet losses in a 2-pole PM motor was presented. It was shown that skin and end-effect are not negligible, requiring 3D-FEM simulations. The validity of losses values obtained with models needs to be confirmed. This can only be done through experimental measurements in the actual machine, dealing with the issue of separating the losses in the machine. Additionally, while doing measurements, the machine is fed by harmonic voltage sources. This means that, in another study, the amplitudes of the current harmonics will need to be derived accounting for the variation of the machine impedance with frequency introduced by the eddy currents in the magnets.

References

[1] J. Millinger, "Eddy-current losses in permanent magnets of PM machines due to PWM harmonics," Tech. report - KTH Royal Institute of Technology, June 2015.

[2] K. Shirabe, M. Swamy, J. K. Kang, M. Hisatsune, Y. Wu, D. Kebort, and J. Honea, "Advantages of high frequency pwm in ac motor drive applications," in *Energy Conversion Congress and Exposition (ECCE), 2012 IEEE*, Sept 2012, pp. 2977–2984.

[3] K. Binnemans and P. T. Jones, "Rare earths and the balance problem," *Journal of Sustainable Metallurgy*, vol. 1, no. 1, pp. 29–38, 2015. [Online]. Available: http://dx.doi.org/10.1007/s40831-014-0005-1

[4] M. Markovic and Y. Perriard, "Analytical solution for rotor eddy-current losses in a slotless permanent-magnet motor: The case of current sheet excitation," *Magnetics, IEEE Transactions on*, vol. 44, no. 3, pp. 386–393, March 2008.

[5] A. Qazalbash, S. Sharkh, N. Irenji, R. Wills, and M. Abusara, "Rotor eddy current power loss in permanent magnet synchronous generators feeding uncontrolled rectifier loads," *Magnetics, IEEE Transactions on*, vol. 50, no. 6, pp. 1–9, June 2014.

[6] J. Klotzl, M. Pyc, and D. Gerling, "Permanent magnet loss reduction in pm-machines using analytical and fem calculation," in *Power Electronics Electrical Drives Automation and Motion (SPEEDAM), 2010 International Symposium on*, June 2010, pp. 98–100.

[7] M. Mirzaei, A. Binder, B. Funieru, and M. Susic, "Analytical calculations of induced eddy currents losses in the magnets of surface mounted pm machines with consideration of circumferential and axial segmentation effects," *Magnetics, IEEE Transactions on*, vol. 48, no. 12, pp. 4831–4841, Dec 2012.

[8] J. Wang, K. Atallah, R. Chin, W. Arshad, and H. Lendenmann, "Rotor eddy-current loss in permanent-magnet brushless ac machines," *Magnetics, IEEE Transactions on*, vol. 46, no. 7, pp. 2701–2707, July 2010.

[9] K. Yamazaki and Y. Fukushima, "Effect of eddy-current loss reduction by magnet segmentation in synchronous motors with concentrated windings," *Industry Applications, IEEE Transactions on*, vol. 47, no. 2, pp. 779–788, March 2011.

[10] M. K. Kazimierczuk, "Skin effect," in *High-Frequency Magnetic Components*, 2nd ed. Chichester, UK: John Wiley and Sons, 2013, ch. 3.

[11] C. Carstensen, "Eddy currents in windings of switched reluctance machines." Ph.D. dissertation, RWTH Aachen University, 2007.

[12] W.-Y. Huang, A. Bettayeb, R. Kaczmarek, and J.-C. Vannier, "Optimization of magnet segmentation for reduction of eddy-current losses in permanent magnet synchronous machine," *Energy Conversion, IEEE Transactions on*, vol. 25, no. 2, pp. 381–387, June 2010.

[13] J. R. Brauer, Z. Cendes, B. Beihoff, and K. P. Phillips, "Laminated steel eddy-current loss versus frequency computed using finite elements," *Industry Applications, IEEE Transactions on*, vol. 36, no. 4, pp. 1132–1137, Jul 2000.

[14] Z. Zhu, K. Ng, N. Schofield, and D. Howe, "Improved analytical modelling of rotor eddy current loss in brushless machines equipped with surface-mounted permanent magnets," *Electric Power Applications, IEE Proceedings -*, vol. 151, no. 6, pp. 641–650, Nov 2004.

[15] Z. Zhu and D. Howe, "Instantaneous magnetic field distribution in brushless permanent magnet dc motors. ii. armature-reaction field," *Magnetics, IEEE Transactions on*, vol. 29, no. 1, pp. 136–142, Jan 1993.

VII. Biographies

Adolfo Garcia Gonzalez received his M.Sc. degree in Electrical Engineering from KTH Royal Institute of Technology, Sweden, in 2015. He is currently working toward a Ph.D. degree at the Section of Electrical Machines of the Department of Energy Technology at Aalborg University. His research interests include modelling and design of electrical machines with 3D-Flux and non-traditional materials for traction applications.

Jonas Millinger received his M.Sc. degree in Electrical Engineering from KTH Royal Institute of Technology in 2011. Since 2010, he has been with Atlas Copco Industrial Technique (Stockholm) involved in the design of electrical machines for power tools. He is currently working toward an industrial Ph.D. degree at the Department of Electric Power and Energy Systems, KTH Royal Institute of Technology. His research interests include modelling and design of electrical machines, with a current focus on harmonic loss modelling and motor-drive system optimization.

Juliette Soulard (M'00) received the Ph.D. degree from the University of Paris VI, France, in 1998. She is Associate Professor with the Department of Electric Power and Energy Systems, leading the Electrical Machines and Drives laboratory at KTH Royal Institute of Technology, Stockholm, Sweden. Her research interests include modelling and design of electrical machines, with a current focus on losses and thermal modelling.

Publication P2

Validation of Efficiency Maps of an Outer Rotor Surface Mounted Permanent Magnet Machine for Evaluation of Recyclability of Magnets

Adolfo Garcia Gonzalez[1], Amit Kumar Jha[2], Ziwei Li[3], Pranshu Upadhayay[3], and Peter Rasmussen[1]
[1]Department of Energy Technology, Aalborg University, Aalborg 9220 Denmark
[2]G2Elab Grenoble INP, Grenoble 38031 France
[3]VALEO Electrical Systems, Creteil 94000 France

The goal of this paper is proposing a methodology for the evaluation of the recyclability criterion of permanent magnets (PMs) in electrical machines for Hybrid and Electric Vehicles ((H)EVs). Such methodology was validated with measurements performed to a PM machine of the hub type. In addition, the methodology proposed here is approached in terms of energy consumption. Hence, measurements of torque and speed were taken at various working points. This study comprises the disassembly of one unit in order to determine the main dimensions of the machine for modelling in 2D Finite Element Method (FEM). Additionally, samples of the magnets in the rotor were taken for characterization of their properties. The results of simulations were contrasted with the measurements for the validation of the efficiency maps. Finally, a study case was selected, in which the use of recycled magnet material was simulated and the reduction of efficiency was quantified.

***Index Terms*—Efficiency maps, 2D-FEM, driving cycle, energy consumption, magnet recyclability.**

I. Introduction

THE global trend towards the implementation of (H)EVs is challenging from the perspective of energy supply and the use of materials with high fluctuation of prices in the international market such as Rare Earth Elements (REEs). Recycling of REEs has been proposed as an alternative for counteracting this situation. Furthermore, work has been carried out in the design of electrical machines with recycled materials [1], [2], [3]. However, there is a lack of tools allowing to determine the feasibility of the recycling of PMs in electrical machines. Hence, this article attempts to set the base for a methodology for evaluating of the recyclability of their PMs [4]. In this regard, two approaches might be adopted. One from the perspective of the disassembling process [5], [6]. The second one from the perspective of the energy consumption in the life cycle of the machine. The evaluation of the energy consumption of a machine used in (H)EVs may be done under any of the defined driving cycles [7]. Therefore, it is required to determine the efficiency of the machine at any given working point. In this sense, the methodology proposed here is validated with measurements performed to an outer rotor surface mounted PM machine of the hub type commercially available and used in both electrical scooters and small city cars.

Efficiency maps have shown to be useful at representing the performance of electrical machines in propulsion applications [8]. In addition, work has been carried out with efficiency maps as optimization tool [9]. Furthermore, the analysis of different machines under various driving cycles have been addressed in earlier studies [10]. However, the work presented here is aimed to validate a methodology for the evaluation of the recyclability criterion from an economic perspective (i.e. energy consumption).

Experimental results focused on the determination of efficiency of the machine are presented in Section II. In section III results of simulations are included, as well as, the elaboration of the efficiency maps. Section IV is devoted to the determination of the efficiency maps in a study case assuming the use of recycled magnets. The analysis of the results obtained are shown in section V. Lastly, conclusions are drawn and future work is proposed.

II. Experimental set-up

Measurements were performed on an outer rotor surface mounted PM which is generally used in electrical scooters or small city cars [11]. The set-up is shown in figure 1. A resistive load was connected to the machine operating as generator, and values of input and output power were measured. The results of efficiency at different values of torque and speed are illustrated in figure 2.

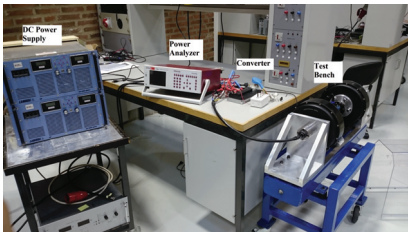

Fig. 1: Experimental set-up.

A. Disassembly

The disassembly of the machine was carried out in order to obtain the main dimensions for the elaboration of the 2D

Corresponding author: A Garcia Gonzalez. (email: agg@et.aau.dk). "A. Garcia Gonzalez, A. Kumar Jha, Z. Li, P. Upadhayay and P. Rasmussen contributed equally."

FEM model. Samples of the magnets were taken and analysed with the Physical Property Measurement System (PPMS) from Quantum Design®.

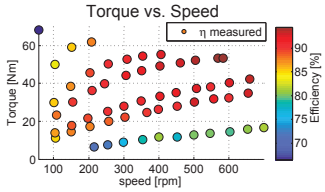

Fig. 2: Measured efficiency at different values of torque and speed.

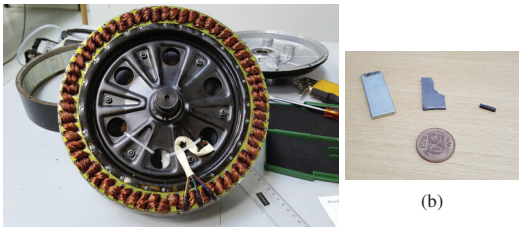

(a) (b)

Fig. 3: (a) Disassembly process, (b) Magnet samples.

B. Main dimensions

The main dimensions of the outer rotor machine analysed in this study are shown in table I.

TABLE I: Main machine dimensions.

Parameters	Value
Stack length L_{stack} [mm]	40
Maximum speed [rpm]	700
Air-gap length [mm]	0.6
Magnet axial length [mm]	40
Magnet thickness [mm]	3
Magnet width [mm]	14
Stator radius [mm]	126.5
Number of poles	56
Number of slots	63
Winding type: concentrated	

III. Elaboration of efficiency maps

Figure 4 illustrates the model implemented in 2D FEM. In addition to the dimensions in table I, the properties of the materials were required as inputs. The test performed to the magnet with PPMS yielded a value of remanence of approximately $B_r = 1.2$ T. On the other hand, the quality of the material of the stator laminations was unknown. Nevertheless, the properties of a standard SiFe lamination with similar thickness were modelled. Hence, the lamination M400-50 was selected. Simulations were run applying the measured current. The efficiency of the measured working points was estimated with the calculated no-load losses (i.e. stator and rotor iron losses and PM losses) and copper losses. The effect of harmonics induced by the modulation of the inverter were disregarded in the simulations. The results are shown in figure 5. Most of the results follow the trend of the measurements illustrated in figure 2.

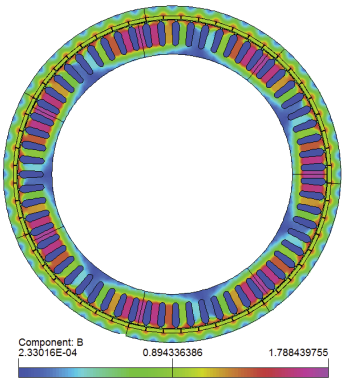

Fig. 4: Geometry modelled in FEM and magnetic flux density distribution at T=11.6 Nm and n=105 rpm.

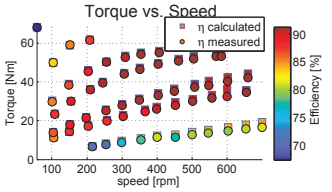

Fig. 5: Measured and calculated efficiency at different values of torque and speed.

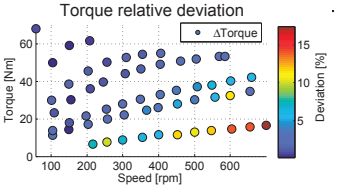

Fig. 6: Deviation in measured and calculated torque at different values of torque and speed.

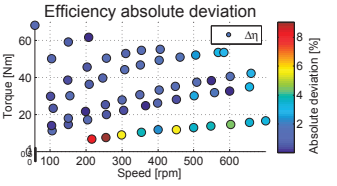

Fig. 7: Deviation in measured and calculated efficiency at different values of torque and speed.

Figure 6 shows the deviation in the calculation of the torque compared with measurements. The maximum deviation was

estimated of approximately 17 %. In addition, the deviation in the calculation of the efficiency is illustrated in figure 7, with a maximum value of approximately 9 %. Various factors might be the source of such differences. In the case of the torque, the quality of the lamination might influence the performance of the machine regarding torque production. The deviations in the efficiency calculations are due to the absence of the mechanical losses in the simulation results. In addition, simulations do not account for processes such as cutting, stacking, etc. that might diminish the quality of the laminations, thus increasing the losses. Additionally, errors in the measurements may influence the deviations between measured and simulated efficiencies. Further analysis in this regard is presented in section V.

After contrasting the simulated values with the measurements, the magnet flux linked with the stator windings Ψ_m was determined and the torque was obtained analytically with the expression:

$$T = \frac{3}{2}(\Psi_m \cdot I_q \cdot p) \tag{1}$$

Where I_q is the current applied in the *q-axis* and p is the pole-pairs number. This expression allows having torque values at currents that were not measured, enhancing the resolution for the elaboration of the efficiency maps. The copper losses p_{cu} were obtained with the DC resistance of the windings R_w and the measured current I_m as:

$$p_{cu} = 3 \cdot I_m^2 \cdot R_w \tag{2}$$

For obtaining the stator and rotor iron losses and PM losses at any speed, quadratic fitting was applied to the losses calculated with 2D FEM simulations. Consequently, the efficiency was determined at any working point of the machine. The resulting efficiency map is presented in figure 8. This efficiency map agrees with the efficiency map of a Surface Mounted PM machine, which values of efficiency are higher as the machine is at its highest performance. In addition, it shows the incremental behaviour of the iron losses with the speed, and the increment of the copper losses with the increment of the torque.

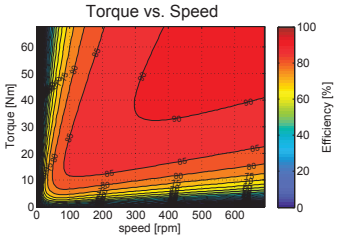

Fig. 8: Efficiency map of the original machine.

IV. Study Case

The main goal of DEMETER project [12] is the study of the recyclability and reuse of magnets in (H)EVs. Therefore, a study case was defined in order to verify the methodology followed so far. Magnets manufactured with recycled material are expected to have lower remanence [13]. Hence, the remanence adopted for this study case was assumed to be 20 % lower, that is, $B_r = 0.96$ T. In order to perform a fair comparison, some assumptions were adopted for the study case presented here:

- Same geometry as in figure 4 was analysed. That is, similar values of current were applied to a new set of simulations with PMs of lower remanence.
- For performing a valid comparison, same performance in terms of torque production was required. Consequently, the axial length of the machine was increased by 15 %, that is, the new stack length was $L_{stack} = 46$ mm.
- The thermal aspects of having higher copper losses were disregarded for the analysis.

The procedure described previously was followed for the elaboration of the efficiency maps for this study case. Figure 9, illustrates the efficiency maps resulting from the use of assumed recycled magnets. Here it is observed the reduction of the efficiency in the region at low speed and high torque, where the copper losses are dominant. In the region at high speed low torque, where the no-load losses are dominant, the variation is less noticeable.

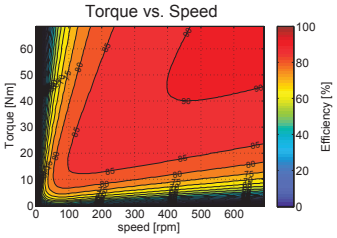

Fig. 9: Efficiency map of the machine for the study case.

A. Comparison of efficiency maps

Figure 10 shows the deviations between the efficiency map for the original machine and the efficiency map obtained for the study case. The differences are more noticeable in the regions at high torque and low speed. That is, where the copper losses are dominant due to the higher current. In contrast, in regions at low torque and high speed, the deviations are lower. In this region the iron losses are dominant due to the higher frequency. However, the reduction of the iron losses due to the reduction of the remanence of the PMs is compensated by the increment of the length of the machine.

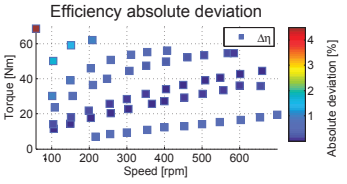

Fig. 10: Absolute error of efficiencies between efficiency map of original machine and machine with magnets of lower remanence.

V. Results Analysis

This section is intended to enhance the understanding of the results in the presence of deviations between measurements and calculations. Furthermore, the analyses reported in this section were carried out on the original machine for similar values of torque and speed as for measurements. Hence, a decay test was performed on the original machine. It consisted in running the machine solely by pulling the shaft and recording the back-emf waveforms in an oscilloscope. A time decaying back-emf wave-form was obtained, and the no-load losses p_{decay} (i.e. core losses, PM losses and mechanical losses) were obtained with the expression [14]:

$$p_{decay}(\omega_m) = -\omega_m J \frac{d\omega_m}{dt} \tag{3}$$

Where J is the inertia of the machine and ω_m is the mechanical angular speed. The inertia J was estimated with the main dimensions of the machine. The no-load losses as function of the speed of the machine were approximated by quadratic curve fitting. Figure 11 shows the decay test results, the calculated losses performed with 2D FEM and the measured no-load losses.

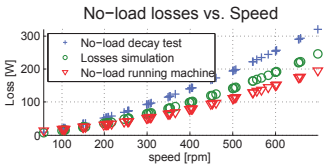

Fig. 11: Measured and calculated no-load losses in the original machine.

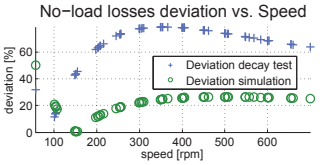

Fig. 12: Deviations in the no-load losses.

The deviations between measured and simulated results are shown in figure 12. The maximum deviation was estimated in approximately 50 %. The main source for this deviation would correspond to the portion of the mechanical and stray losses that are not included in the 2D FEM model. Additionally, the specific losses of the laminations in the actual machine remain unknown. Furthermore, as mentioned in section III the processing of the laminations (i.e. cutting, stacking, etc.) is not accounted in the simulations. Regarding the decay test results, figure 12 shows the largest deviations of approximately 79 %. The no-load losses p_0 with the machine running were determined with the following expression:

$$p_0 = P_m - P_o - p_{cu} \tag{4}$$

Where P_m is the input power measured with the power analyser and P_o is the output power obtained with the measurements of torque and speed in the torque transducer. Note that p_0 contains the mechanical losses, core losses and PM losses.

A. Effect of the calculation of J

In order to evaluate the sensitivity of the value of inertia J in the losses calculated with the decay test, J was modified by ± 10 %. The results are shown in figure 13.

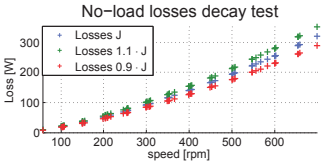

Fig. 13: Comparison of no-load losses with various values of inertia J.

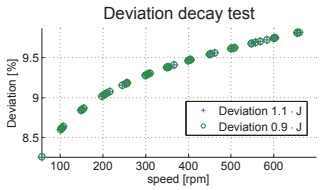

Fig. 14: Deviation of losses calculation with changing J.

As shown in figure 14 the maximum deviation was estimated in 10 %. In this work, the calculation of J was performed both analytically and with the help of CAD software. The relative error between the two methods was approximately 3 %. The inertia calculated analytically was $J_{ana} = 0.0899$ kg·m^2. With CAD software, this value was estimated in $J_{cad} = 0.0905$ kg·m^2. The maximum calculated deviation due to the variation of the value of J was estimated in 3 %.

B. Effect of the measurement of torque

During the test with load in the machine, oscillations in the reading of torque were observed. In addition, an offset value was present in the interface used to read the values of torque. Such offset was identified having a value of approximately 0.35 Nm. The goal in this section is to identify the behaviour of the measured losses accounting for such deviations of the torque measurements. Hence, expression 4 was evaluated for the calculation of the no-load losses, accounting for the torque offset, by subtracting its value from the measurements. The results after applying quadratic curve fitting to the data are shown in figure 15 together with the decay test results and the values obtained with simulations.

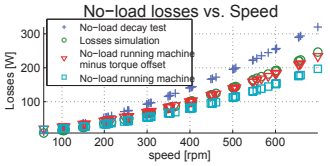

Fig. 15: No-load losses in the machine with torque offset.

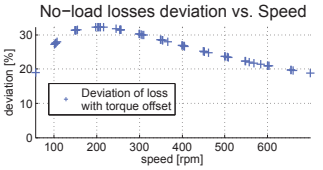

Fig. 16: Deviation in the no-load losses accounting for torque offset.

As it can be observed in figure 16, the subtraction of the torque offset from the measured values leads to the increment of the no-load losses. The maximum deviation between the decay test results and the measured values is of approximately 32 %. Which shows that the calibration of the torque transducer might have a significant impact in the estimation of the no-load losses as in equation 4. In addition, the losses calculated in 2D FEM are still close or even higher than the measured values. This might be the indication that in the original machine, an electrical lamination of lower specific losses was used. As future work, it would be interesting to determine the type of lamination that is being used by the manufacturer of this product.

VI. Conclusions

A reduction of efficiency when recycled magnets are used was quantified at 4.5%. This maximum value was obtained in the region at low speed and high torque in figure 10. Such deviation in the efficiency has its source in the increment of the stack length for obtaining the same torque as in the original machine. In addition, the increment of the resistance of the windings with increased stack length, had a significant impact in the copper losses. On the other hand, in the region at high speed and low torque the reduction in efficiency was estimated in 1%. This is consistent with having a reduced remanence of the magnets compensated with the increment of the stack length of the machine.

In general, a larger consumption of energy is expected if magnets manufactured with recycled materials and with lower remanence are used for electrical machines in (H)EVs. However, for future work it has been defined the study of the energy consumption of the machine analysed here under various driving cycles, including the European urban driving cycle ECE-15. Additionally, the prices of both energy and magnet materials will be evaluated for establishing a recycling index [15]. Furthermore, the methodology proposed here is expected to facilitate the comparison of diverse types of PM machines (e.g. surface mounted PM, inset PM, Halbach rotor, etc.) from an early design stage.

Acknowledgement

The research leading to the results presented in this article has been funded by the European Communitys Horizon 2020 Programme ([H2010/2014-2019]) under Grant Agreement no. 674973 (MSCA-ETN DEMETER). This publication reflects only the authors view, exempting the Community from any liability. Project website http://etn-demeter.eu/. Special thanks to professors Sylvie Hebert and Antoine Maignan for helping in the characterization of the magnets at the Laboratory of Cristallography and Material Sciences CRISMAT at ENSI-CAEN.

References

[1] M. Kimiabeigi, R. S. Sheridan, J. D. Widmer, A. Walton, M. Farr, B. Scholes, and I. R. Harris, "Production and application of hpms recycled bonded permanent magnets for a traction motor application," *IEEE Transactions on Industrial Electronics*, vol. 65, no. 5, pp. 3795–3804, May 2018.

[2] S. Högberg, J. Holbøll, N. Mijatovic, B. B. Jensen, and F. B. Bendixen, "Direct reuse of rare earth permanent magnets - coating integrity," *IEEE Transactions on Magnetics*, vol. 53, no. 4, pp. 1–9, April 2017.

[3] S. Högberg, F. B. Bendixen, N. Mijatovic, B. B. Jensen, and J. Holbøll, "Influence of demagnetization-temperature on magnetic performance of recycled nd-fe-b magnets," in *2015 IEEE International Electric Machines Drives Conference (IEMDC)*, May 2015, pp. 1242–1246.

[4] Y. Yang, A. Walton, R. Sheridan, K. Güth, R. Gauß, O. Gutfleisch, M. Buchert, B.-M. Steenari, T. Van Gerven, P. T. Jones, and K. Binnemans, "Ree recovery from end-of-life ndfeb permanent magnet scrap: A critical review," *Journal of Sustainable Metallurgy*, vol. 3, no. 1, pp. 122–149, Mar 2017. [Online]. Available: https://doi.org/10.1007/s40831-016-0090-4

[5] T. Elwert, D. Goldmann, F. Roemer, and S. Schwarz, "Recycling of ndfeb magnets from electric drive motors of (hybrid) electric vehicles," *Journal of Sustainable Metallurgy*, vol. 3, no. 1, pp. 108–121, Mar 2017. [Online]. Available: https://doi.org/10.1007/s40831-016-0085-1

[6] A. Kumar Jha, Z. Li, A. Garcia Gonzalez, P. Upadhayay, and P. Rasmussen, "Weighted index of recycling and energy (WIRE) cost for Motors in electric vehicles," in *SPEEDAM 2018, Accepted*, 2017.

[7] T. Barlow, "A reference book of driving cycles for use in the measurement of road vehicle emissions: Version 3," 2009. [Online]. Available: https://books.google.dk/books?id=jnowMwEACAAJ

[8] S. M. Lukic and A. Emado, "Modeling of electric machines for automotive applications using efficiency maps," in *Proceedings: Electrical Insulation Conference and Electrical Manufacturing and Coil Winding Technology Conference (Cat. No.03CH37480)*, Sept 2003, pp. 543–550.

[9] P. Lazari, J. Wang, and L. Chen, "A computationally efficient design technique for electric-vehicle traction machines," *IEEE Transactions on Industry Applications*, vol. 50, no. 5, pp. 3203–3213, Sept 2014.

[10] K. Kiyota, H. Sugimoto, and A. Chiba, "Comparing electric motors: An analysis using four standard driving schedules," *IEEE Industry Applications Magazine*, vol. 20, no. 4, pp. 12–20, July 2014.

[11] "Wuxi lingming electric drive technology co., ltd," Internet: http://www.lingmingmotor.com, 2015, [Nov. 22, 2017].

[12] "European training network for the design and recycling of rare-earth permanent magnets," Internet: http://etn-demeter.eu, 2015, [Nov. 22, 2017].

[13] R. Sheridan, A. Williams, I. Harris, and A. Walton, "Improved hddr processing route for production of anisotropic powder from sintered ndfeb type magnets," *Journal of Magnetism and Magnetic Materials*, vol. 350, pp. 114 – 118, 2014. [Online]. Available: http://www.sciencedirect.com/science/article/pii/S0304885313007014

[14] A. Fitzgerald, C. Kingsley, and S. Umans, "Parameter determination from no-load and block-rotor tests," in *Electric Machinery*, 6th ed. New York, US: McGraw-Hill, 2003, ch. 6.

[15] P. Upadhayay, A. Garcia Gonzalez, Z. Li, A. Kumar Jha, P. Rasmussen, A. Kedous-Lebouc, and J.-C. Mipo, "Evaluation of energy cost index for an electric vehicle motor over a particular drive cycle with recycled magnet concept," in *ICEM 2018, Submitted to*, 2018.

VII. BIOGRAPHIES

Adolfo Garcia Gonzalez received his M.Sc. degree in Electrical Engineering from KTH Royal Institute of Technology, Sweden, in 2015. He is currently working toward a Ph.D. degree at the Section of Electrical Machines of the Department of Energy Technology at Aalborg University. His research interests include modelling and design of electrical machines with 3D-Flux and non-traditional materials for traction applications.

Amit Kumar Jha received B.E degree (2008) in Electrical and Electronics Engineering from Birla Institute of Engineering, Mesra, India and M.Sc. degree (2012) in Electrical Power Engineering from Royal Institute of Technology, Stockholm, Sweden. He is currently working as Ph.D. researcher at G2Elab, Grenoble, France focusing on design of electrical motor with easy recycling for electric vehicles. Prior to PhD, he has worked in different companies like Bombardier Transportation AB, Vasteras, Sweden, Xylem water solutions, Stockholm, Sweden and Schneider Electric Pvt. Ltd, India. His fields of interest are design of electric motor and its drives for different motor applications and study system performance.

Ziwei Li received his M.Sc. degree in Electrical Engineering from KTH Royal Institute of Technology, Sweden, in 2015. He is currently working towards a Ph.D degree at the laboratory of G2Elab, Grenoble INP, Grenoble and Valeo - Equipements Electriques Moteur, Créteil, France. His research interests include modeling and optimization of radial flux electrical machines with rare earth magnets recycling concepts for electrical vehicle applications.

Pranshu Upadhayay was born in Jorhat, Assam, India in 1986. Following a B. Tech degree (2007) in Electrical Engineering from Nirma University, India, he received M. S. (Research) in Electrical Engineering (2015) from the Indian Institute of Technology Delhi, India. He is currently working towards his Ph.D. degree from G2Elab, Grenoble INP, Université Grenoble Alpes, and is also associated with Valeo - Equipements Electriques Moteur, Créteil, France. From 2007 to 2015 he was associated with multinational companies like Schneider Electric India Pvt. Ltd., and Crompton Greaves Ltd., at Mumbai, India. He has published 8 papers in International conference proceedings. His fields of interest include electrical machines and drives, design and FE analysis of special electrical machines, 3D flux claw-pole machines and rare earth magnet reuse and recycling concept in EV and HEV applications.

Peter Omand Rasmussen was born in Aarhus, Denmark, in 1971. He received the M.Sc.E.E. and Ph.D. degrees from Aalborg University, Aalborg, Denmark, in 1995 and 2001, respectively. In 1998, he became an Assistant Professor, and in 2002, he became an Associate Professor at Aalborg University. His research areas are the design and control of switched reluctance, permanent-magnet machines, and magnetic gears.

Publication P3

Weighted Index of Recycling and Energy (WIRE) Cost for Motors in Electric Vehicles

Amit Kumar Jha[1+], Ziwei Li[1,2+], Adolfo Garcia [3+], Pranshu Upadhayay [1,2+], Peter Omand Rasmussen[3], Afef Kedous-Lebouc[1] and Lauric Garbuio[1]
[1]Univ. Grenoble Alpes, CNRS, Grenoble INP G2Elab, 38000 Grenoble, France
[2]Valeo - Equipements Electriques Moteur, 2 rue Andr Boulle, 94000 Crteil, France
[3]Deaprtment of Energy Technology,Aalborg University, Pontopidanstrade 111, Aalborg East 9220
[+]These four authors contributed equally to this work
Email: Amit-kumar.jha@g2elab.grenoble-inp.fr

***Abstract*—With increasing demand of electric vehicles it is very important to recycle critical rare earth materials used in the permanent magnet motors such as Neodymium (Nd), Dysprosium (Dy) and Cobalt (Co) etc. To achieve easy recycling, focus of the motor design shall shift to design for recycling. The article presents a methodology (WIRE) to evaluate and benchmark the motor in terms of their recyclability. The method can be used to compare different motors. The method was used for evaluation of a commercial permanent magnet based HUB motor and the results are presented. A comparison between recyclability index of four different motors topology is also presented.**

***Index Terms*—Motor Recycling, Magnet Recycling, Motor Benchmarking**

I. Introduction

The demand for cleaner mode of urban transport is increasing and many countries like UK, France, Norway, Sweden etc have already announced the phasing out of diesel and petrol cars from their streets in couple of decades and likely more countries will join soon [1]. The sales of electric vehicle (EV) and hybrid electric vehicle (HEV) in recent years is growing every year and is projected to continue at higher rate in coming years [2]. At present, almost all automobile manufacturers are using permanent magnet (PM) motors to achieve high efficient vehicles [3]- [4]. The amount and quality of PM is critical for high performance motors. Therefore, to maintain the vehicle growth it is very important to have sufficient and sustainable supply of magnets. At present, Neodymium Iron Boron (NdFeB) magnets are the strongest magnets. The magnet contains critical rare earth materials like Nd and Dy. Due to limited availability of these materials it is very crucial to recycle them and use again in motors. In recent years, there has been some focus from industry and researchers on recycling of magnets. The projects like EREAN, RARE^3 etc are focusing on developing methods to recycle extracted magnets. The extraction of magnets from the existing electric motor design has been investigated in the project called MORE. The motor designs present today are not designed for recycling i.e. extraction of magnet is very difficult [3] & [5]. In Demeter (H2020) project one of the goals is to design motor for recycling. However, the challenge for the motor designers is to evaluate motors with respect to the recyclability and comparison of different designs. At present there is no tool to analyze the motors design for the recycling and benchmark them. In this article a method is presented to analyze and evaluate the recycling of the motors for EVs and HEVs. The method is divided in two parts. The first part evaluates recyclability of the motor considering standardization, assembly and disassembly of the motor. The second part evaluates the impact of the motor design on the performance of the motor considering energy consumption over the complete life cycle. In this article only first part is presented and discussed. The method was used to evaluate the recycling index of a commercial hub motor and the results are presented. The evaluation of four different motors designed for DEMETER project were carried out by using WIRE method. The comparison of scores are also presented and analysed.

II. Methodology

The first part of the WIRE methodology is to evaluate the ease of assembly/disassembly of electric motors. The evaluation process is divided in two parts - Standard and Cost. Each part has three categories Material, Assembly and Disassembly. Moreover, the evaluation of each material or process in each category is done in two parts. The first is **Score (S)** which depends on its relative scale in respective section. The second is **Importance (I)** which depends on material/process relative criticality in terms of recyclability of materials. The final score is the product of both i.e. **(SxI)**. The score for each activity is in the range of 1-5. For evaluation of WIRE it is recommended to have a group of 5-6 people from different fields, involved in design and manufacturing process of the motor. Figure 1 shows the evaluation sheet for the different materials of the motor for both the parts-standard and cost. Although, the evaluation largely depends on the mutual agreement of the group formed for evaluation i.e. standard and cost, certain guidelines are formed to evaluate different sections. Furthermore, the process/ materials in different sections are different depending on the criticality of the material/process. For example, the wires of sensor is important while assembling however, their importance is negligible while disassembly.

Scoring pattern	0-5	1 - Lowest score	5 - Highest score					
		1 - Lowest score	5 - Highest score	3 = neutral score				
Assumption	The motor developed is new and for the first time and manual disassembly with high volumes i.e. 50,00							
MOTOR ID	Hub motor for in-wheel application							
Component/ Parts		Standard			Cost			Recyclability SCORE
		S	I	SxI	S	I	SxI	
Materials								
- Stator								
	Lamination S	5	5	25	1	5	5	30
	Copper	5	5	25	2	1	2	27
- Rotor								0
	Steel R	5	5	25	1	4	4	29
	Magnets	5	4	20	5	1	5	25
-Shaft								0
	Shaft	4	5	20	1	2	2	22
-Endshileds								0
	Drive Side	2	5	10	1	2	2	12
	Non-Drive side	2	5	10	1	2	2	12
			34	135		17	22	157
	section score			79.41 %			25.88 %	

Fig. 1: Evaluation sheet of material for standardization and cost

A. *Definitions of WIRE sheet*

As mentioned earlier, the WIRE evaluation is relative and hence, the accuracy of the method largely depends on the definitions of different sections. Different process/materials has different significance in the final recycling of the motor. It is important to note that the scoring is relative and hence the tool is good for comparing two motors evaluated keeping same scaling in consideration. In the following section definitions of different terms used for the evaluation are given.

- **Standard** : The category focuses on the use of standard material/processes. The evaluation for Standard category is done with the view that use of standard parts/process will simplify and encourage the recycling. Furthermore, higher the number of standard component in the motor easier it will be for recycling and further improves the quality of the recycled output.
  1) Material
     - 'S' depends on the standardization of the material. The score is higher for material, which are easily available (off the shelf) and widely used. For example, random wound copper winding are more used and widely available then rectangular strand cable of certain dimension.
     - 'I' depends on materials recyclability. For example, NdFeB magnet with and without coating is easily available however, in terms of recyclability the magnet without coating will be easier for recycling and hence its index shall be higher.
  2) Assembly
     - 'S' depends on the process/activity standardization. While scoring it is also important to consider the tools used. More non-standard tools or process used in assembly shall lower the score. For example, if special heat treatment/ or other special environment is needed for assembly, process will be non-standard and thus the index shall be lower.
     - 'I' depends on the criticality of the step/process for recycling of the part. For example, if the assembly of the copper affects the recycling of the copper. Therefore, the index shall be high.
  3) Disassembly
     - 'S' depends on the process/activity standardization. While scoring it is also important to consider the tools used. More non-standard tools or process used in disassembly shall lower the index. For example, if some chemical is needed for extraction of certain component the score shall be lower for the process.
     - 'I' depends on the criticality of the step/process for recycling of the part. Same as assembly, if disassembly process of copper make recycling easier the index shall be high.
- **Cost** : The category focuses on the cost of material/processes and its impact on recycling. The evaluation for Cost category is done with the view that higher cost of any process will increase the overall recycling cost and hence, has negative impact on the recycling. On the other hand, higher material cost incentives the recycling of that particular material like magnets and encourages recycling.
  1) Material
     - 'S' depends on the cost of the material. Higher the material cost higher the score. The processing cost of the component varies over a wide range. Therefore, to keep the tool simple and to avoid processing cost variation of the component only material cost is considered. Moreover, the non-standard design or the impact of processing will be taken care while scoring standard category. For example, NdFeB magnet is roughly 10 times costlier than the laminations in the motor. Therefore, score of magnet will be higher than the laminations. The impact of different shapes of magnet should be considered while scoring standard material category.
     - 'I' depends on the impact of the material on recycling of the whole motor. For example, if the weight of the material is very low comparing to other materials, the material recovered will be very small. Therefore, the recovery in terms of economic value will be small, even with high price of the material.
  2) Assembly
     - 'S' depends on cost required to execute the assembly process/activity. Higher the assembly cost lower the score shall be as it impacts the recycling process negatively. For example, if there

TABLE I: Scoring of Material for Standard Category

Magnet Type	S
Rectangular small pieces with/ without coating sintered, Bonded Magnet	5
Sintered/bonded shape parallel/radially magnetized	4
Halbach bonded	3
Sintered or Bonded powder but magnetised in rotor	2
Sintered halbach multipole	1
Lamination Type	**S**
Silicone iron 0.35-0.6mm, Single solid rotor	5
Silicone steel modular type	4
Cobalt Steel	3
Amorphous, different shapes	2
SMC	1
Winding Type	**S**
Copper / aluminium strand circular	5
Copper rectangular standard, aluminium cast rotor	4
Copper rectangular/cricular non standard	3
Hollow circular copper wire	2
Any thing special	1

I	Magnet Type
5	Rectangular small pieces or powder without coating or binder
4	Sintered with coating
3	Sintered any shape with coating/glue
2	Bonded magnets
1	Bonded magnets with glue
I	**Lamination Type**
5	Any silicone iron lamination or solid rotor or Aluminum
4	Cobalt steel
3	Amorphous Steel
2	Soft Magnet Composites (SMC)
1	Any new special handling material
I	**Winding Type**
5	Copper any type
4	Aluminium wire/Cast aluminium /Copper rotor
2	Any new special handling material

is a need of special environment for assembly, it increases the complexity and hence cost.

- 'I' depends on the impact of cost of the process in recycling. For example, if a motor uses powder NdFeB magnet technology. The assembly cost is higher but this cost does not impact the recycling of the magnet at the end of life (EOL) of the motor. Therefore, the index shall be neutral.

3) Disassembly

- 'S' depends on cost required to execute the disassembly process/activity. Higher the disassembly cost lower the score shall be as it impacts the recycling process negatively. For example, if there is a need of special environment for disassembly, it increases the complexity and hence, cost which in turn discourages recyclability economically.
- 'I' depends on the impact of cost of the process in recycling. For example, the cost of disassembly of the magnet is very critical for the recycling of the magnet. Therefore, the index shall be high for that process.

B. Calculation of Recyclability Index

The final weighted recyclability index (R) is calculated using equation 1 and 2. The R_w is in the scale of 1-5 and using equation (2) is expressed in percent, R.

$$R_w = \frac{S_1 * I_1 + S_2 * I_2 + \cdots + S_n * I_n}{\sum I} \tag{1}$$

TABLE II: S of assembly/disassembly for Cost category

Assembly / Disassembly Cost	S
Easy assembly/disassembly without any tool	5
Easy assembly/disassembly with standard tools /process	4
Complex / Hard process with standard tools or more than one person required	3
Special pre/post treatment with special tools	2
New extra method to extract magnet from rotor	1

$$R = \frac{R_w * 100}{5} \tag{2}$$

C. General Guidelines for scoring

The section provides some general guidelines, which can be used to score different sections of WIRE sheet. It is important to note here that the scores are relative and can be varied on general consensus or when scenario changes. The authors decided the scores after discussing different scenarios.

1) Scoring of materials for Standard category: Table I shows the scoring of material and its importance for recyclability with respect to their standardization. The table shows the scores for main components of the motor like lamination, magnet and copper. The materials are scored based on the definition given in section II-A.

2) Assembly/Disassembly score for Cost: Table II gives the scoring guideline for assembly/disassembly in terms of cost. Simpler the process higher the score shall be.

3) Assembly/Disassembly of stator and rotor: The scoring guideline for individual components (stator, rotor, bearing etc)

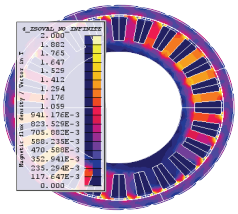

(a) Outer Rotor Motor (1)

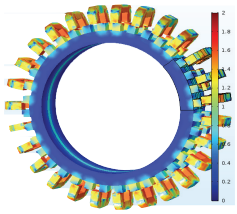

(b) 3D Flux Hybrid Motor (2)

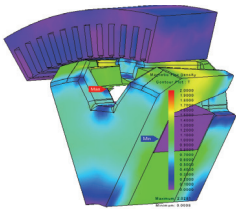

(c) Claw Pole Motor (3)

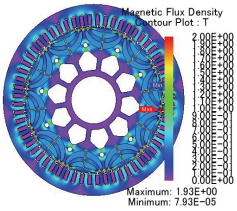

(d) Radial IPM Motor (4)

Fig. 2: Flux density distribution in different motors

TABLE III: Score of material cost in motor

Material Cost	S
Sintered Magnet	5
Bonded Magnet	4
SMC,Amorphous steel	3
Copper	2
Silicone Steel lamination	1

TABLE IV: Importance of Assembly/Disassembly process

Process	Standard Importance	Cost Importance
Assembly of stator lamination	3	3
Assembly of copper winding	3	3
Assembly of rotor lamination	3	3
Assembly of magnet and rotor	5	3
Assembly of sensor wires	1	3
Assembly of rotor and stator	3	3
Assembly of end shields	3	3
Assembly of shaft	3	3
Disassembly of end shields	3	3
Separation of rotor and stator	4	4
Disassembly of copper	3	4
Disassembly of stator	3	3
Disassembly of magnets from rotor	5	5
Disassembly of rotor	3	3

is shown in Table II. However, there is one more critical step in assembly/disassembly, which is separation of a rotor from a stator. The complexity of the process is even higher in PM motors. The ease of assembly / disassembly mainly depends on the force of extraction and its size. Therefore, to scale the process following method is used. Larger the volume and airgap flux density i.e. power of the motor, separation of rotor and stator will be difficult and hence, the score shall be lower. Mathematically it can be presented by equation 3. Figure 2 shows the flux density distribution in motor for 4 different topologies designed in framework of DEMETER project. Motor 3 has lowest flux density and hence, disassembly will be much easier compared to other motors.

$$\mathbf{S} \propto \frac{1}{V * B_{\delta}^{2}} \tag{3}$$

where, V is volume of the motor and B_{δ} is the airgap flux density.

4) Scoring 'I' of material for Cost category: The scoring of 'I' depends on the weight of the material in the motor. Higher the weight of the material higher will be the recovery of material from recycling. The proposed method to estimate that is as follows. Lets assume, the motor has W_c kg of Copper, W_s kg of Stator steel, W_r kg of rotor steel and W_m weight of Magnet and the weight (W_s) of stator steel is maximum. The I score for stator steel W_s is 5 and the rest is scaled in proportion to the W_s. The fraction numbers are rounded to nearest integer.

I for magnet is $\frac{W_m * 5}{W_s}$

I for copper is $\frac{W_c * 5}{W_s}$

Table III shows the relative score of material used in the motors.

5) 'I' of assembly/disassembly for Standard & Cost category: The criticality of each step during assembly and disassembly is shown in table IV. While indexing, the recycling of steel, copper and magnet was considered important and hence, the process affecting their recycling was index accordingly. If some step of assembly is very important for recycling of that material then it shall have high indexed. For example, assembly of magnet and rotor is very significant for extraction of magnet and hence, has high index.

III. WIRE EVALUATION FOR HUB MOTOR

The developed methodology was used for evaluating commercial permanent magnet based HUB motor. The motor was disassembled manually with standard tools and the process was observed keeping in mind the recycling of the parts. Figure 3 shows the different stages while disassembly of the motor. After complete disassembly of the motor the WIRE sheet, was filled by the authors. For simplicity many assembly/disassembly steps are clubbed together and score and importance were given. The scores of standard and cost of the WIRE evaluation is shown in figure 4. The final cost index is lower than the final standard index. The motor is a commercial motor and has used more standard parts and processes. The index for cost of the material is lower compared to assembly and disassembly. It is important to note here that the index is relative and in absolute terms cost of material can be higher than the assembly and disassembly of the motor. As mentioned earlier the method is developed to compare different motors recyclability. The final recycling index (R) of the motor is

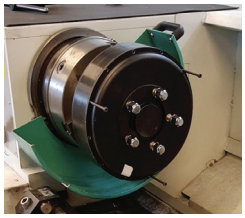

(a) Motor

(b) Motor without End-shields

(c) Stator

(d) Rotor

Fig. 3: HUB Motor Diassembly

68.5%. The low index was expected as motor is not designed for recycling.

IV. Comparison of Recyclability Index of four motors

Figure 4 shows the four different motors designed for (H)EVs with ease of recycling in the framework of DEMETER project. Motor 1 is an outer rotor topology motor with an ideal Halbach magnet manufactured using bonded magnet. Motor 2 is a 3D flux hybrid motor using modular amorphous steel stator core and the rotor has sintered magnet placed between rotor laminations. Motor 3 is a permanent magnet based claw pole motor topology designed for easy extraction of magnet for mild hybrid vehicle. Motor 4 is an interior PM(IPM) motor using thermoplastic type bonded magnets and can be magnetized inside a rotor core. The motors were evaluated using WIRE method to compare the recyclability index. Figure 6 presents the index of all 4 motors in standard and cost category for assembly, disassembly and material. It can be seen that motor 3 has highest score in assembly subcategory because the process for the claw pole is highly industrialized and the design change made for easy recycling is minor. On the other side motor 2 has lowest score because the 3D flux machine has U core laminations for stator which requires special process to assembly. Moreover, due to the magnets position and glue that used for magnet fixing, the rotor assembly is also more complicated than the rest. The disassembly of motor 1 has maximum score because of simple rotor structure and no glue is used for magnet assembly, whereas motor 2 has the lowest because to extract magnet special processing is required. The material used in all 4 motors are standard and hence, have similar scores. The material cost of motor 2 has the highest

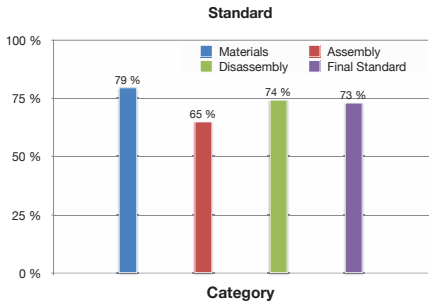

(a) Standard Distribution

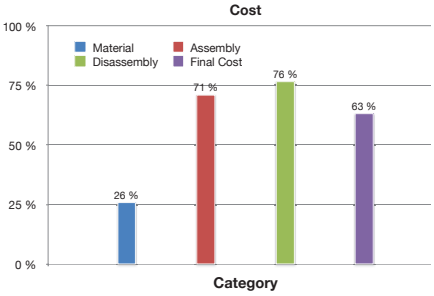

(b) Cost Distribution

Fig. 4: Distribution of Recycling index of the sample motor

score shows that the recovery of high valued material from motor 2 is maximum compared to others. For assembly and disassembly in terms of cost the trend is same for all the motors. Motor 1 has the highest score because of simple structure. Thus, the disassembly process does not need any special treatment of magnets before extraction. Whereas, some pretreatments are required for other motors to extract magnet, which contributes to lower indexes. The final recyclability index of four motors are 71%, 63%, 71% and 64% respectively

V. Conclusion and Discussion

The WIRE method is developed for indexing the recyclability (R) and energy impact of the motors. In this article recyclability part of the method is presented. The method is simple to use and can be modified as per the requirement. The methodology takes standardization and cost into consideration for determining the recyclability of the motor. The recycling of any motor depends on the materials used, assembly and disassembly. The evaluation is relative in nature and hence, will be effective in comparison of motors done keeping the scaling same. To make method evaluation objective, different scoring guidelines is also presented and can be modified if the evaluating team finds suitable. The motor designed for recycling should have higher standard components with easy assembly and disassembly process.

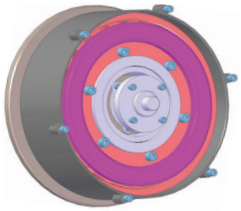

(a) Outer Rotor Motor (1)

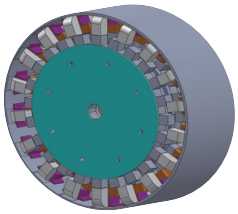

(b) 3D Flux Hybrid Motor (2)

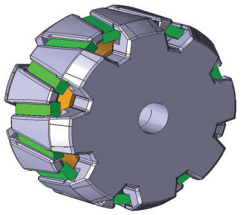

(c) Claw Pole Motor (3)

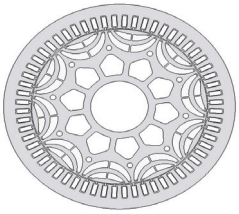

(d) Radial IPM Motor (4)

Fig. 5: Four Different Motors Designed in DEMETER project

The evaluation was done for a commercial hub motor and the scores are presented. Many processes in assembly/disassembly were clubbed together to keep the evaluation simple due to lack of certain information. The recycling index for the motor is 68.5%, which is low as motor is not designed for the recycling and the index can be improved by modifying small design changes.

The final recyclability index of four motors are 71%, 63%, 71% and 64% respectively. The scores obtained reflect that the method is able to distinguish the features of motor for easy recyclability. The WIRE score comparison of the 4 motors show that the recyclability increases with the high utilization of standard materials. It further improves if machine design is such that it can be assembled and disassembled using conventional process and tools. The use of glue for magnet assembly makes recovery of magnet from motor difficult and lowers the recyclability index. Furthermore, use of complicated motor structure also lowers the recyclability index. However, one has to keep in mind the method by its nature scores lower for new / innovative designs / method as can be seen in the case of motor 2. Therefore, the designers must strive to use conventional/ standard method of assembly and disassembly with magnet assembly without any glue to make motor easier for recycling.

ACKNOWLEDGMENT

The research leading to these results has received funding from European Communitys Horizon 2020 Programme ([H2010/2014-2019]) under Grant Agreement no. 674973 (MSCA-ETN DEMETER). This publication reflects only the authors view, exempting the Community from any liability. Project website http://etn-demeter.eu/

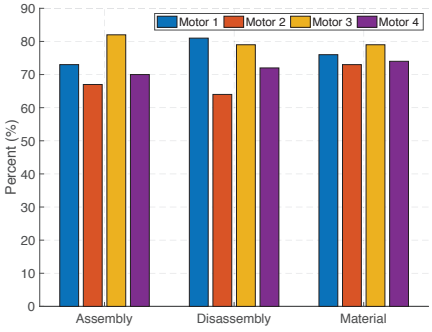

(a) Score of Standard category for 4 motors

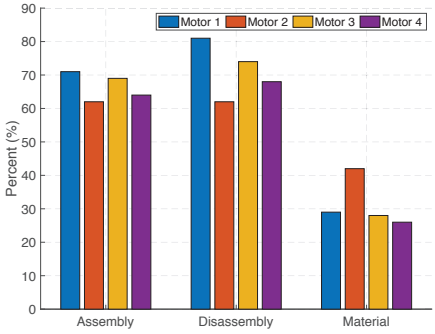

(b) Score of cost category for 4 motors

Fig. 6: WIRE evaluation scores for all four motors

REFERENCES

[1] Countries are announcing plans to phase out petrol and diesel cars. is yours on the list? [Online]. Available: https://www.weforum.org/agenda/2017/09/countries-are-announcing-plans-to-phase-out-petrol-and-diesel-cars-is-yours-on-the-list/

[2] Internaltion Energy Agency, Ed., *Global EV Outlook 2017*.

[3] T. Elwert, D. Goldmann, F. Rmer, M. Buchert, C. Merz, D. Schueler, and J. Sutter, "Current developments and challenges in the recycling of key components of (hybrid) electric vehicles," *Recycling*, vol. 1, no. 1, pp. 25–60, 2015. [Online]. Available: http://www.mdpi.com/2313-4321/1/1/25

[4] L. Kumar and S. Jain, "Electric propulsion system for electric vehicular technology: A review," *Renewable and Sustainable Energy Reviews*, vol. 29, no. Supplement C, pp. 924 – 940, 2014. [Online]. Available: http://www.sciencedirect.com/science/article/pii/S1364032113006734

[5] U. Bast, R. Blank, M. Buchert, T. Elwert, F. Finsterwalder, G. Hornig, T. Klier, S. Langkau, F. Marscheider-Weidemann, J.-O. Muller, C. Thurigen, F. Treffer, and T. Walter, "Recycling von komponenten und strategischen metallen aus elektrischen fahrantrieben," Aug-2014.

Publication P4

Evaluation of Energy Cost Index for an Electric Vehicle Motor over a particular Drive Cycle with Recycled Magnet Concept

Pranshu Upadhayay, Adolfo G. Garcia, Ziwei Li, Amit K. Jha, Peter O. Rasmussen, Afef Kedous-Lebouc, Jean-Claude Mipo

***Abstract* – Nowadays, in automotive applications, the electric vehicle (EV) motors generally utilize permanent magnet (PM) motors due to their various advantages like high torque density, high efficiency, compactness and ease of control. In this paper emphasis is given to the evaluation of energy cost index for an EV motor over a particular drive cycle during motors operational lifetime. Performance evaluation over the entire drive cycle, instead of at rated conditions, provides a better idea of the efficiency and energy consumption of an electric motor. Therefore, energy cost evaluation for the urban part of New European Driving Cycle (NEDC) i.e. ECE-15 is selected in this study and the energy cost index is evaluated for an EV motor for virgin and recycled magnets utilized in the machine. The comparison shows that utilizing recycled magnets can provide economical advantage over using virgin magnets albeit under certain assumptions.**

***Index Terms*—automotive, cost, driving cycle, electric motors, electric vehicles, energy, finite element analysis, permanent magnets, recycle, reuse.**

I. Introduction

THE electric and hybrid electric vehicles (HEV) are the new key developments in the automotive industry with the implementation of new regulations and norms in various countries around the world. Generally, the EV machines used in automotive applications are PM machines due to various advantages like high torque density, high efficiency, compactness and ease of control [1]. The PMs deployed in these EV motors are commonly rare earth (RE) magnets i.e. Neodymium Iron Boron (NdFeB) magnets. However, due to price fluctuations and supply-demand issues of RE materials utilized in NdFeB magnets, lot of research is being undertaken to reduce or utilize RE free magnets in PM machines. In recent years, numerous studies are being carried out in recycling of critical materials, and NdFeB magnets contain a few of these critical materials i.e. Neodymium (Nd) and Dysprosium (Dy) [2]. Due to the use of NdFeB magnets in PM machines, reuse and recycle of PMs in electric motors is being re-analyzed in some of the applications around the world [3]-[4]. Nevertheless, there are challenges in developing methodologies for reuse or recycle of magnets in electric motors due to varying motor topologies, technologies, material characteristics, proper disposal at end-of-life (EoL) and economic/environmental implications.

In this regard a methodology is being developed to analyze the recyclability of PM motors with two main aspects. First, recyclability of the motor considering standardization, assembly and disassembly of the motor and second, considering energy consumption by the electric motor during its complete lifetime with variation in permanent magnet compositions [5]-[6]. In this paper a commercial PM based HUB motor is used to evaluate the second part of the above methodology development. In Section II benchmarking of sample HUB motor is done by disassembly, experimentation and finite element (FE) analysis. Then in Section III efficiency map and energy consumption of sample HUB motor with virgin magnets for the urban part of NEDC drive cycle i.e. ECE-15 drive cycle [7] is evaluated. Similarly, machine performance and energy consumption with recycled magnets for the same ECE-15 drive cycle is evaluated in Section IV. Finally in Section V, comparison in energy consumption between virgin magnets and recycled magnets for sample HUB motor is done to obtain the energy cost index. Finally, conclusion is presented in the last section.

II. Benchmarking of Sample Electric Vehicle Motor

The sample EV motor is a commercial PM based HUB motor with outer rotor topology. The sample motor is utilized in high speed electric two wheeler or small compact low speed city cars. Fig. 1 shows the sample HUB motor. The DC bus voltage for the sample motor is 72 V, maximum speed of 700 rpm and output power upto 3.5 kW. The motor controller is a standard three-phase power electronic inverter

The research leading to these results has received funding from European Community's Horizon 2020 Programme ([H2020/2014-2019)] under Grant Agreement no. 674973 (MSCA-ETN DEMETER). This publication reflects only the author's view, exempting the Community from any liability. Project website: http://etn-demeter.eu/.

First four authors contributed equally to this work.

P. Upadhayay is with Valeo - Equipements Electriques Moteur, 2 rue André Boulle, 94000 Créteil, France & also with Univ. Grenoble Alpes, CNRS, Grenoble INP, G2Elab, 38000 Grenoble, France (e-mail: pranshulink@gmail.com).

A. G. Gonzalez is with the Department of Energy Technology, Aalborg University, Aalborg 9220, Denmark (e-mail: agg@et.aau.dk).

Ziwei Li is with Valeo - Equipements Electriques Moteur, 2 rue André Boulle, 94000 Créteil, France & also with Univ. Grenoble Alpes, CNRS, Grenoble INP, G2Elab, 38000 Grenoble, France (e-mail: ziwei.li@valeo.com).

A. K. Jha is with Univ. Grenoble Alpes, CNRS, Grenoble INP, G2Elab, 38000 Grenoble, France (e-mail: amit-kumar.jha@grenoble-inp.fr).

P. O. Rasmussen is with the Department of Energy Technology, Aalborg University, Aalborg 9220, Denmark (e-mail: por@et.aau.dk).

A. Kedous-Lebouc is with Univ. Grenoble Alpes, CNRS, Grenoble INP, G2Elab, 38000 Grenoble, France (e-mail: afef.lebouc@grenoble-inp.fr).

J. C. Mipo is with Valeo - Equipements Electriques Moteur, 2 rue André Boulle, 94000 Créteil, France (e-mail: jean-claude.mipo@valeo.com).

with hall sensor inputs used for position sensing.

Fig. 1. A commercial PM based HUB motor

A. *Experimental measurements*

The motor was assembled on a test bench with high precision torque transducer connected to the shaft. The input power measurements were recorded using an industrial grade power analyzer so as to limit the uncertainties in measurement. Fig. 2 shows the experimental test setup utilized for the measurements and performance evaluation.

Fig. 2. Experimental test setup for performance evaluation

Two machines were assembled back to back and a resistive load was connected to the machine which would operate as a generator and load the test machine. Different resistance values were used with a set of speed variations to get the torque, speed, voltage, output power and input power of the test machine. Fig. 3 depicts the experimental torque vs. speed with the corresponding efficiency values.

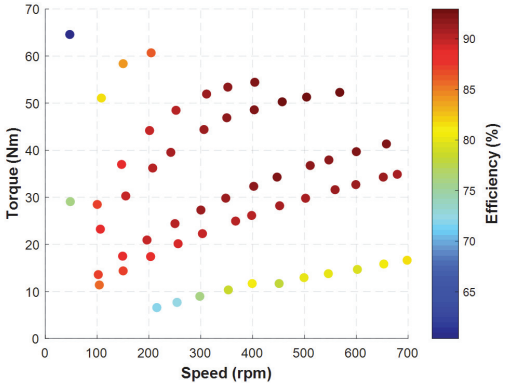

Fig. 3. Experimental torque vs. speed with corresponding efficiency values by virgin magnets

B. *Disassembly and dimensions*

The major dimensions, weight and materials were identified by disassembling the machine in step by step process. Fig. 4 shows the disassembled machine and the magnets. Table I depicts the main machine dimensions which would be utilized later on for 2-dimensional (2D) FE analysis so as to obtain simulated performance of the machine.

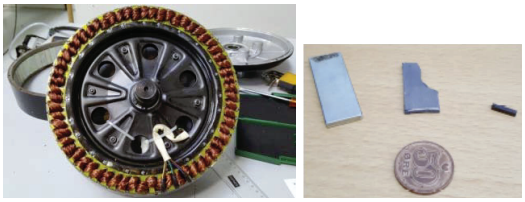

Fig. 4. Disassembled machine and permanent magnets

TABLE I
MAIN DIMENSIONS OF THE MACHINE

Parameters	Value
Stack length [mm]	40
Maximum speed [rpm]	700
Air-gap length [mm]	0.6
Magnet axial length [mm]	40
Magnet thickness [mm]	3
Magnet width [mm]	14
Stator outer diameter [mm]	253
Number of poles	56
Number of slots	63

The PMs were shaped in appropriate sizes so as to be analyzed for their magnetic properties. They were put to test in Magnetic Property Measurement System (MPMS®) from Quantum Design. It was observed that the magnetization (M) at 0 Oe applied field (H) of the magnet is around 130 emu/g which corresponds to around 1.2 T as remanence flux density (B_r) at temperature of 300 K i.e. approximately 27 °C.

C. *Finite element analysis & comparison with test results*

The machine was modeled in commercially available FE analysis software by using the dimensional details obtained earlier in Section II (B). The magnet properties were utilized from the MPMS measurements with 1.2 T as the B_r value. The stator lamination was a standard silicon iron soft magnetic material with loss of around 5 W/kg at 1.5 T, 50 Hz. Time-stepping 2D motion analysis was carried out to get the various performance parameters like back electromotive force (EMF), cogging torque, electromagnetic torque, iron losses, copper losses and winding voltages. Fig. 5 shows the 2D model along with the flux density plot at no-load by FE analysis.

The experimental winding current values were fed as an input in the FE analysis at various speed points to get the developed torque and losses of the machine. Finally the input power, output power, voltage and efficiency were evaluated by simulation results. In Fig. 6 it can be noticed that the comparison of simulated and experimental results for torque vs. speed with corresponding efficiency values of the machine.

It can be observed that the simulated and experimental results match fairly well and there is a maximum percentage error of 9% in torque and 5% in efficiency values.

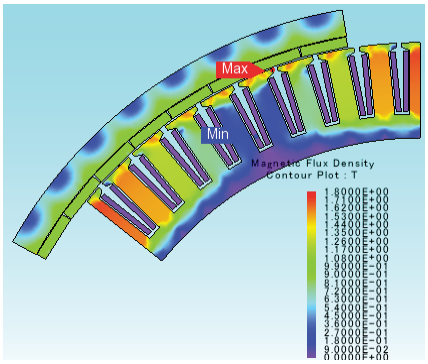

Fig. 5. Flux density plot of the sample HUB motor with virgin magnets

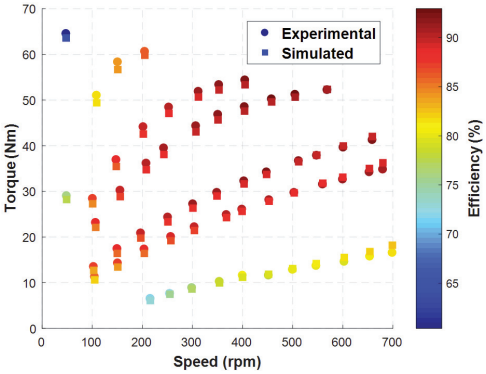

Fig. 6. Comparison of experimental & simulated torque vs. speed with corresponding efficiency values by virgin magnets

III. Efficiency Map and Energy Evaluation of the Sample HUB Motor with Virgin Magnets

Energy consumption for a reference drive cycle requires performance parameters of the machine for the complete torque vs. speed envelope. As a result, efficiency map of the motor needs to be evaluated so as to acquire the precise torque and efficiency points for the corresponding speed values in the reference drive cycle.

A. Methodology for energy consumption evaluation

A methodology has been developed to evaluate the energy consumed by the machine for a particular drive cycle. Various literatures depict the importance of evaluating the energy consumption of a machine for different drive cycles with diverse vehicle dynamics [8]-[17]. Fig. 7 shows the flow diagram of the developed methodology. In this, the machine performance is evaluated using FE analysis and utilizing the flux map of the machine, efficiency map is generated. Along with this, vehicle parameters like wheel radius, vehicle weight, rolling resistance, air density, drag coefficient and frontal area are used as input for deriving torque vs. time curve from speed vs. time of drive cycle. Now, these are used as input to the efficiency map and energy consumption for one cycle of the drive cycle is evaluated. Finally, total energy consumed in the lifetime of the machine is estimated by assuming that the motor operates for 2 hours daily for 10 years.

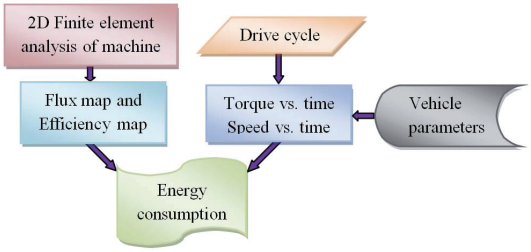

Fig. 7. Flow diagram for energy evaluation methodology

In this study it is assumed that the vehicle is a compact city car with the vehicle parameters as listed in Table II.

TABLE II
Vehicle Parameters

Parameters	Value
Vehicle weight [kg]	920
Density of air [kg/m^3]	1.225
Frontal area [m^2]	1.85
Drag coefficient	0.4
Coefficient of rolling resistance	0.01
Tyre radius [mm]	0.21

B. Efficiency map and energy consumption

The efficiency mapping of the machine is evaluated by utilizing the flux map with different values of direct axis current (I_d) and quadrature axis current (I_q). Similarly, iron loss mapping is also required for various values of machine flux induction and current levels. Therefore, by utilizing optimization algorithm, the efficiency mapping is obtained for the sample motor. Fig. 8 illustrates the efficiency map of the sample motor with virgin magnets.

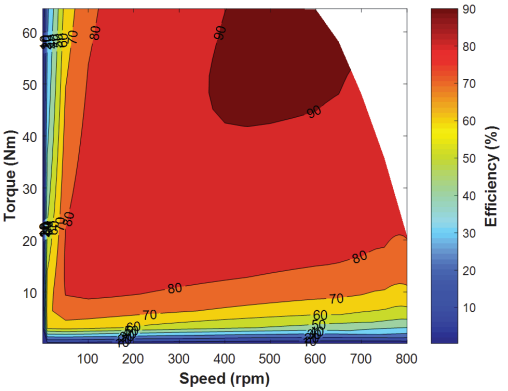

Fig. 8. Efficiency map of the sample HUB motor with virgin magnets

The drive cycle selected for this study is the urban part of the NEDC cycle i.e. ECE-15 [7]. Fig. 9 shows the speed vs. time profile of the ECE-15 drive cycle.

The instantaneous wheel torque can be derived by using

the following equation [8]-[17]:

$$T_w = \left(ma + mgC_r + \frac{1}{2}\rho_a C_d A_f v^2\right) r_w \quad (1)$$

where, T_w is wheel torque, m is mass of vehicle, a is acceleration, g is gravity, C_r is coefficient of rolling resistance, ρ_a is density of air, C_d is coefficient of drag, A_f is vehicle frontal area, v is velocity of vehicle and r_w is radius of the wheel. Hence, using Eq. (1), vehicle parameters as in Table II and ECE-15 drive cycle, the wheel torque vs. time profile can be obtained. Fig. 10 shows the wheel torque vs. time profile for the selected vehicle and ECE-15 drive cycle.

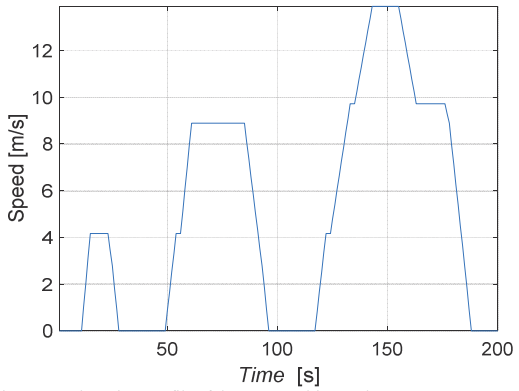

Fig. 9. Speed vs. time profile of the ECE-15 drive cycle

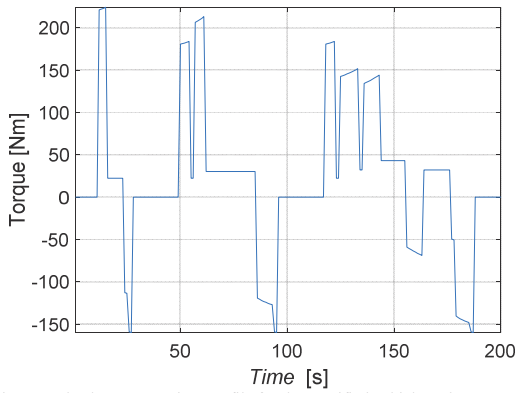

Fig. 10. Wheel torque vs. time profile for the specified vehicle and ECE-15

It can be observed that maximum torque required at wheel is around 220 Nm. The maximum motor torque which can be delivered is around 65 Nm. Hence, it is assumed that four motors would be used in the vehicle with direct drive configuration to achieve required wheel torque.

As per the flow diagram in Fig. 7, this torque vs. speed profile and efficiency map are employed together to get the energy consumed by one motor during the lifetime of 10 years with 2 hours of daily operation. The energy consumption can be calculated as:

$$E_c = \int_0^t E(t)dt \quad (2)$$

where, E_c is total energy consumed, $E(t)$ is energy input as function of time and t is time. The regenerative braking and negative torque values are assumed to be zero in the energy calculations. As a result, for the sample HUB motor with virgin magnets, the total energy consumed for the complete lifetime is 3071 kWh from Eq. (2). The harmonized electricity price for Europe region is considered as 0.22 €/kWh [18]. Therefore, the energy cost for one motor with virgin magnets is € 676 for the entire assumed lifetime. The weight of total magnet in the motor is 0.7 kg, and NdFeB material price considered is 45 €/kg [19], consequently the total magnet price is € 31.5 in one motor.

The study has utilized ECE-15 drive cycle, but the methodology can be used to evaluate any drive cycle like NEDC, Urban Dynamometer Driving Schedule (UDDS), Worldwide Harmonized Light Vehicles Test Procedure (WLTP), etc. and this is considered as future work.

IV. Machine Performance with Recycled Magnets

It has been observed for past many years that the rare earth material price fluctuates a lot due to regulatory factors, supply-demand issues, political and economical factors. It is for this reason recycling and reuse of rare earth materials from electronic components, computer hard drives and automotive components, have garnered a lot of interest [2]. Research is been carried out in recycling the PM scrap from various sources and fabricate recycled magnets by hydrogen decrepitation (HD) and hydrogenation, disproportionation, desorption, recombination (HDDR) [20]-[22].

In this study the magnetic property of the recycled magnet considered is around 0.96 T as B_r. This is as per reference [20], where the new magnet material has 1.36 T as B_r and the recycled magnet has 1.08 T as B_r, hence 20% reduction in the B_r. In this study the virgin magnet has 1.2 T as B_r, and taking 20% reduction for recycled magnet, the B_r evaluated is 0.96 T.

A. Performance characteristics

For the evaluation of machine performance with recycled magnets in the sample motor, the methodology utilized is similar to performance calculated with virgin magnets as in Section II (C). The sample motor's dimensional parameters are kept same as that with virgin magnets; only the magnet properties are altered with recycled magnet properties i.e. having 0.96 T as B_r and increased length of the motor to achieve same torque as obtained with virgin magnets. The length of stator, rotor and magnets is increased from 40mm to 46mm. Henceforth, 2D time-stepping FE analysis is carried out to get the performance characteristics like back EMF, cogging torque, electromagnetic torque, iron losses, copper losses and winding voltages. Performance has been evaluated with similar current values as used in test and simulations during the study with virgin magnets in Section II (C). Fig. 11 shows the simulated torque vs. speed with corresponding efficiency values by virgin and recycled magnets. It can be observed that torque values match fairly well for virgin and recycled magnets. But the efficiency at certain points has increased with recycled magnets due to cumulative decrease of total losses, as iron losses has reduced but copper losses has increased.

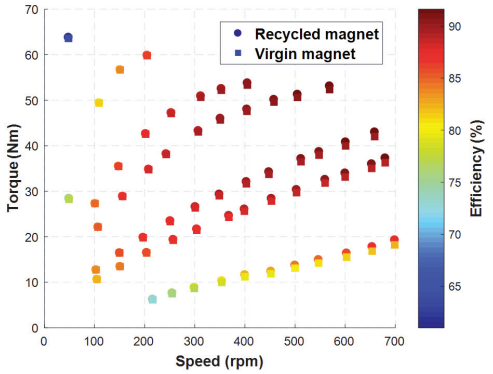

Fig. 11. Simulated torque vs. speed with corresponding efficiency values by virgin and recycled magnets

B. *Efficiency map and energy consumption*

The efficiency map and energy consumption of the sample motor with recycled magnets is evaluated similarly as done while using virgin magnets in Section III (B). By utilizing the flux map with different values of I_d and I_q and iron loss map for various values of machine flux induction and current levels, the efficiency map is generated for the motor with recycled magnets. Fig. 12 illustrates the efficiency map of the sample motor with recycled magnets.

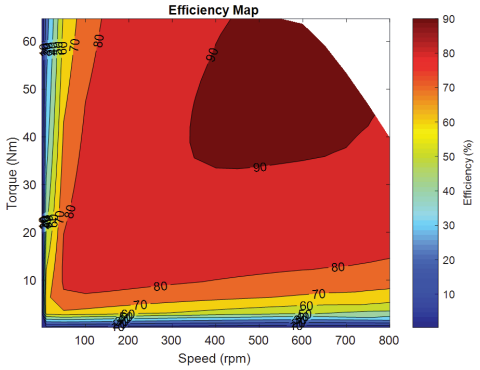

Fig. 12. Efficiency map of the sample HUB motor with recycled magnets

Hereafter employing the flow diagram in Fig. 7, torque vs. speed profile and efficiency map together can provide energy consumed by one motor during the lifetime of 10 years with 2 hours of daily operation with recycled magnets. Consequently, for sample motor with recycled magnets, total energy consumed for complete lifetime is calculated as 2995 kWh from Eq. (2). Similarly, assuming the harmonized electricity price for Europe region as 0.22 €/kWh [18], the energy cost for one motor with recycled magnets is € 659 for the assumed lifetime.

It is difficult to comment on the price of recycled magnets as it is subject to ongoing research studies. But as it is assumed to be prepared from scrap PMs the price is assumed to be lower compared to virgin PMs. Due to increased length the PM weight increases from 0.7 kg to 0.81 kg with recycled magnets. Therefore, assuming the price of recycled magnet material as half of virgin magnets i.e. 22.5 €/kg with certain estimates, the total PM price calculated would be € 18.23 since motor contains 0.81 kg of magnets.

V. Energy Cost Index and Comparison between Virgin and Recycled Magnets

Energy cost evaluation considering the machine performance on a particular drive cycle or duty cycle gives more insights than evaluating machine performance at rated loads. Since machine performance could be optimized for rated conditions but their operation may not be subjected to rated conditions during a specific duty cycle. Therefore, comparing machine performance at a particular drive cycle with different magnet scenarios would provide information about the importance of energy and magnet cost.

For this purpose, an index has been proposed to compare the energy cost in relation to magnet cost. The temperature for both the machines has been assumed the same. For instance, in this study energy consumption cost with virgin magnets is € 676 and magnet cost is € 31.5 for the sample motor. Considering this as the base scenario and naming it as Scenario 1 and/or Scenario base. The energy cost computed with recycled magnets is € 659 and magnet cost is € 18.23 for the sample motor; and naming it as Scenario 2. The energy cost index is defined as follows:

$$EC_i = \left(\frac{E_c(j)}{E_c(b)}\right).\left(\frac{Mag_c(j)}{Mag_c(b)}\right) \tag{3}$$

where, EC_i is the energy cost index, $E_c(j)$ is energy cost for Scenario j, $Mag_c(j)$ is magnet cost for Scenario j, $E_c(b)$ is energy cost for Scenario base and $Mag_c(b)$ is magnet cost for Scenario base. As a result, energy cost index for Scenario 2 as per Eq. (3) is evaluated as 0.564. From Fig. 13 it can been observed that the design with recycled magnets has low efficiency in low speed high torque region and high efficiency in high speed low torque region as compared to efficiencies with virgin magnets. However, the drive cycle has most of the points in high speed low torque region; hence energy consumption is low with recycled magnets for this drive cycle. Hence, it can be deduced that energy consumption depends on both drive cycle and machine design.

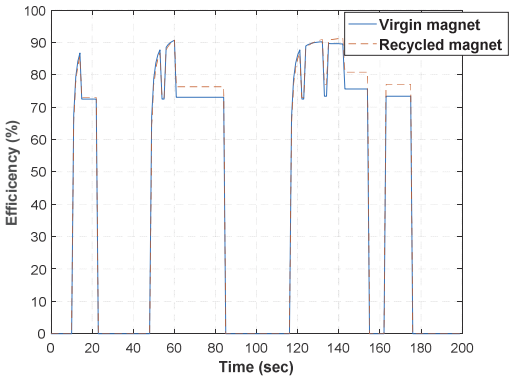

Fig. 13. Efficiency vs. time profile for virgin and recycled magnets

For analysis purpose, few more scenarios are assumed, for example, Scenario 3 where energy cost is € 676 (energy

cost for virgin magnets) and magnet cost is € 18.23 (magnet cost for recycled magnets) and Scenario 4 where energy cost is € 659 (energy cost for recycled magnets) and magnet cost is € 31.50 (magnet cost for virgin magnets). Table III represents the comparison of energy cost index for different scenarios, computed using Eq. (3).

TABLE III
COMPARISON OF ENERGY COST INDEX FOR DIFFERENT SCENARIOS

	Energy cost (€)	PM material price (€/kg)	Magnet cost (€)	Energy cost index
Scenario 1	676	45.0	31.50	1.000
Scenario 2	659	22.5	18.23	0.564
Scenario 3	676	22.5	18.23	0.579
Scenario 4	659	45.0	31.50	0.975
Scenario 5	700	37.6	30.46	1.000

Hence, it can be observed that the energy cost index for Scenario 3 is 0.579 and Scenario 4 is 0.975. This indicates that lower the energy cost index, better is the machine in economic aspects and is advantageous as compared to base scenario. Considering one more hypothetical scenario (Scenario 5), where the recycled magnet cost is approximately equal to virgin magnets i.e. € 30.46 and energy cost is € 700; the energy cost index computed is 1.000, as shown in Table III. This is equal to energy cost index of base scenario, indicating that even if the price of recycled magnet are similar to virgin magnet and have higher energy consumption, the economic impact is same. Other than the above cited advantages, with recycled magnets one can observe one more advantage which is that, they have low environmental impact as compared to virgin magnets. The mining of rare earth materials have negative repercussions in terms of environmental and human conditions. The preparation of recycled magnets has lower implications on human labour aspects as no mining is required. Additionally they have environmental benefits like reduction in air and water pollution. It can be argued that even for the preparation of recycled magnets a number of environmental hazards are possible like storage of hydrogen gas and its use in HD and HDDR process, and use of certain chemicals for separation of materials. But if both the circumstances are weighed together, the authors assume that mining would have higher negative impact than producing recycled magnets from scrap [23]. The authors recommend future studies and research into economic-environmental comparison between virgin and recycled magnet production and usage phase.

A general representation of the index is tabulated in Table IV, where energy cost index varies with the cost of virgin and recycled magnets. In this the E_c virgin magnet is € 676, E_c recycled magnet is € 659 and weight of virgin magnet is 0.7 kg and weight of recycled magnet is 0.81 kg. Hence, it can be observed that as the PM material price varies for virgin and recycled magnets the index varies accordingly. The greener the index it is better economically when compared to red coloured cells in Table IV. Similar, hypothesis can be generated with variable energy costs for different grades of magnets and the index would indicate the cases which are economically more advantageous.

TABLE IV
ENERGY COST INDEX WITH VARYING MAGNET COSTS

			VIRGIN MAGNETS					
	PM. mat. price(€/kg)		20	35	50	65	80	95
		PM. cost (€)	14.0	24.5	35.0	45.5	56.0	66.5
RECYCLED MAGNETS	5	4.05	0.282	0.161	0.113	0.087	0.071	0.059
	20	16.20	1.128	0.645	0.451	0.347	0.282	0.237
	35	28.35	1.974	1.128	0.790	0.607	0.494	0.416
	50	40.50	2.820	1.611	1.128	0.868	0.705	0.594
	65	52.65	3.666	2.095	1.466	1.128	0.917	0.772
	80	64.80	4.512	2.578	1.805	1.388	1.128	0.950
	95	76.95	5.358	3.062	2.143	1.649	1.340	1.128

VI. CONCLUSION

In this paper, the energy cost index evaluation methodology over ECE-15 drive cycle for an EV motor with PMs has been presented. The methodology is utilized to present different scenarios where virgin magnets and recycled magnets were employed and energy cost index was computed. It has been observed that the recycled magnets can provide better economical advantage than virgin magnets as it is assumed that the cost of recycled magnets would be lower than virgin magnets in this case study. Lower the energy cost index, the machine is better in terms of economic evaluation as compared to base scenario. The recycled magnets also provide benefits in terms of environmental aspects as they would be less polluting in their production than new magnet materials mined from various sources around the world. The methodology for energy cost index evaluation is a comparative tool and can be adjusted as per the individuals' needs and calculations. The scenarios can vary from motor design and different drive cycles, which can provide varied results and conclusions. Thus, generating an index for comparison provides reasonably good inspiration on using recycled magnets in electrical machines.

VII. ACKNOWLEDGMENT

The research leading to these results has received funding from European Community's Horizon 2020 Programme ([H2020/2014-2019)] under Grant Agreement no. 674973 (MSCA-ETN DEMETER). This publication reflects only the author's view, exempting the Community from any liability. Project website: http://etn-demeter.eu/.

Special thanks to Prof. Sylvie Hebert and Prof. Antoine Maignan for helping in the characterization of the magnets at CRISMAT lab of ENSICAEN.

VIII. REFERENCES

[1] T. Elwert, D. Goldmann, F. Romer, M. Buchert, C. Merz, D. Schueler, and J. Sutter, "Current developments and challenges in the recycling of key components of (hybrid) electric vehicles," *Recycling Journal*, vol. 1, no. 1, pp. 25– 60, October 2015.

[2] Y. Yang, A. Walton, R. Sheridan, K. Guth, R. Gauß, O. Gutfleisch, M. Buchert, B. M. Steenari, T. V. Gerven, P. T. Jones, and K. Binnemans, "REE recovery from end-of-life NdFeB permanent magnet scrap: A

critical review," *Journal of Sustainable Metallurgy*, vol. 3, no. 1, pp. 122–149, Mar 2017.
[3] M. Kimiabeigi, R. S. Sheridan, J. D. Widmer, A. Walton, M. Farr, B. Scholes, and I. R. Harris, "Production and Application of HPMS Recycled Bonded Permanent Magnets for a Traction Motor Application," *IEEE Trans. on Industrial Electronics*, vol. 65, no. 5, pp. 3795-3804, May 2018.
[4] U. Bast, R. Blank, M. Buchert, T. Elwert, F. Finsterwalder, G. Hornig, T. Klier, S. Langkau, F. Marscheider-Weidemann, J.-O. Muller, C. Thurigen, F. Treffer, and T. Walter, "Recycling von komponenten und strategischen metallen aus elektrischen fahrantrieben," MORE Project report, Aug 2014.
[5] A. K. Jha, Z. Li, A. Garcia, P. Upadhayay, P. O. Rasmussen, A. Kedous-Lebouc, and L. Garbuio, "Weighted index of recycling and energy (WIRE) cost for Motors in electric vehicles," accepted International *Symposium on Power Electronics, Electrical Drives, Automation and Motion (SPEEDAM)* 2018.
[6] A. G. Gonzalez, A. K. Jha, Z. Li, P. Upadhayay, and P. Rasmussen, "Validation of Efficiency Maps of an Outer Rotor Surface Mounted Permanent Magnet Machine for Evaluation of Recyclability of Magnets," accepted *INTERMAG 2018*.
[7] T. J. Barlow, S. Latham, I. S. McCrae, P. G. Boulter, *A reference book of driving cycles for use in the measurement of road vehicle emissions*, version. 3, United Kingdom: IHS, 2009, pp. 21.
[8] P. Lazari, J. Wang, and L. Chen, "A Computationally Efficient Design Technique for Electric-Vehicle Traction Machines," *IEEE Trans. on Industry Applications*, vol. 50, no. 5, pp. 3203-3213, Sep.-Oct. 2014.
[9] K. Kiyota, H. Sugimoto, and A. Chiba, "Comparing Electric Motors: An Analysis Using Four Standard Driving Schedules," *IEEE Industry Applications Magazine*, vol. 20, no. 4, pp. 12-20, July-Aug. 2014.
[10] Qi Li, Tao Fan, Ye Li, Z. Wang, X. Wen, and Jing Guo, "Optimization of external rotor surface permanent magnet machines based on efficiency map over a target driving cycle," *20th International Conference on Electrical Machines and Systems (ICEMS) 2017*, pp. 1-5, Aug. 2017.
[11] P. D. Walker, and H. M. Roser, "Energy consumption and cost analysis of hybrid electric powertrain configurations for two wheelers," *Applied Energy Journal*, vol. 146, pp. 279-287, May 2015.
[12] C. Krasopoulos, M. Beniakar, and A. G. Kladas, "Comparison of Three Different In-Wheel SMPM Motor Configurations Based on the Urban NEDC," *Materials Science Forum*, vol. 856, pp. 233-238, May 2016.
[13] Ganji B., Kouzani A. Z., Trinh H. M., "Drive Cycle Analysis of the Performance of Hybrid Electric Vehicles," In: Li K., Fei M., Jia L., Irwin G.W. (eds) *Life System Modeling and Intelligent Computing. Lecture Notes in Computer Science*, vol. 6328, pp. 434-444, Springer, Berlin, Heidelberg, 2010.
[14] J. O. Estima, and A. J. M. Cardoso, "Efficiency Analysis of Drive Train Topologies Applied to Electric/Hybrid Vehicles," *IEEE Trans. on Vehicular Technology*, vol. 61, no. 3, pp. 1021-1031, Mar. 2012.
[15] E. Carraro, M. Morandin, and N. Bianchi, "Traction PMASR Motor Optimization According to a Given Driving Cycle," *IEEE Trans. on Industry Applications*, vol. 52, no. 1, pp. 209-216, Jan.-Feb.. 2016.
[16] O. Karabasoglu, and J. Michalek, "Influence of driving patterns on life cycle cost and emissions of hybrid and plug-in electric vehicle powertrains," *Energy Policy Journal*, vol. 60, pp. 445-461, Sep. 2013.
[17] M. Novak, J. Novak, and Z. Novak, "Methodology for Efficiency Mapping of Permanent Magnet Synchronous Motors," *19th International Conference on Electrical Drives and Power Electronics (EDPE) 2017*, pp. 205-210, Oct. 2017.
[18] Electricity price statistics, http://ec.europa.eu/eurostat/statistics-explained/index.php/Electricity_price_statistics
[19] Alliance LLC, Commodity prices. http://www.allianceorg.com/magnetandmaterialcosts.html
[20] R .S. Sheridan, A. J. Williams, I. R. Harris, and A. Walton, "Improved HDDR processing route for production of anisotropic powder from sintered NdFeB type magnets," *Journal of Magnetism and Magnetic Materials*, vol. 350, pp. 114-118, Jan. 2014.
[21] R. S. Sheridan, R. Sillitoe, M. Zakotnik, I. R. Harris, and A. J. Williams, "Anisotropic powder from sintered NdFeB magnets by the HDDR processing route," *Journal of Magnetism and Magnetic Materials*, vol. 324, no. 1, pp. 63-67, Jan. 2012.
[22] M. Zakotnik, I. R. Harris, and A. J. Williams, "Multiple recycling of NdFeB-type sintered magnets," *Journal of Alloys and Compounds*, vol. 469, no. 1-2, pp. 314-321, Feb. 2009.
[23] H. Jin, P. Afiuny, S. Dove, G. Furlan, M. Zakotnik, Y. Yih, and J. W. Sutherland, "Life Cycle Assessment of Neodymium-Iron-Boron Magnet-to-Magnet Recycling for Electric Vehicle Motors," Environ. Sci. Technol. Journal, 52 (6), pp 3796–3802, 2018.

IX. BIOGRAPHIES

Pranshu Upadhayay was born in Jorhat, Assam, India in 1986. Following a B. Tech degree (2007) in Electrical Engineering from Nirma University, India, he received M. S. (Research) in Electrical Engineering (2015) from the Indian Institute of Technology Delhi, India. He is currently working towards his Ph.D. degree from G2Elab, Grenoble INP, Université Grenoble Alpes, and is also associated with Valeo - Equipements Electriques Moteur, Créteil, France.

From 2007 to 2015 he was associated with multinational companies like Schneider Electric India Pvt. Ltd., and Crompton Greaves Ltd., at Mumbai, India. He has published 8 papers in International conference proceedings. His fields of interest include electrical machines and drives, design & FE analysis of special electrical machines, 3D flux claw-pole machines and rare earth magnet reuse and recycling concept in EV and HEV applications.

Adolfo Garcia Gonzalez received his M.Sc. degree in Electrical Engineering from KTH Royal Institute of Technology, Sweden, in 2015. He is currently working toward a Ph.D. degree at the Section of Electrical Machines of the Department of Energy Technology at Aalborg University.

His research interests include modelling and design of electrical machines with 3D-Flux and non-traditional materials for traction applications.

Ziwei Li received his M.Sc. degree in Electrical Engineering from KTH Royal Institute of Technology, Sweden, in 2015. He is currently working towards a Ph.D degree at the laboratory of G2Elab, Grenoble INP, Grenoble and Valeo - Equipements Electriques Moteur, Créteil, France.

His research interests include modeling and optimization of radial flux electrical machines with rare earth magnets recycling concepts for electrical vehicle applications.

Amit Kumar Jha, received B.E degree (2008) in Electrical and Electronics Engineering from Birla Institute of Engineering, Mesra, India and M.Sc. degree (2012) in Electrical Power Engineering from Royal Institute of Technology, Stockholm, Sweden. He is currently working as Ph.D. researcher at G2Elab, Grenoble, France focusing on design of electrical motor with easy recycling for electric vehicles.

Prior to PhD, he has worked in different companies like Bombardier Transportation AB, Vasteras, Sweden, Xylem water solutions, Stockholm, Sweden and Schneider Electric Pvt. Ltd, India. His fields of interest are design of electric motor and its drives for different motor applications and study system performance.

Peter Omand Rasmussen was born in Aarhus, Denmark, in 1971. He received the M.Sc.E.E. and Ph.D. degrees from Aalborg University, Aalborg, Denmark, in 1995 and 2001, respectively.

In 1998, he became an Assistant Professor, and in 2002, he became an Associate Professor at Aalborg University. His research areas are the design and control of switched reluctance, permanent-magnet machines, and magnetic gears.

Afef Kedous-Lebouc has received her Electrical Engineering and Ph.D. degrees from Grenoble Institute of Technology (former Institut National Polytechnique de Grenoble) in 1982 and 1985. She is a Senior CNRS Researcher at Grenoble Electrical Engineering Laboratory G2Elab.

She managed its MADEA Team "Advanced Materials and electromagnetic devices" from 2004 to 2012. She is expert in magnetism, magnetic materials and application in electrical engineering devices. She managed more than 35 industrial projects and participated in many international research programs. She is expert within the International Electrotechnical Commission (IEC TC 68). She has more than 250 publications (80 international journals and 28 invited conferences). She has a large experience in PhD training (35 PhD, 30 already defended).

Jean-Claude Mipo received the Ph.D. degree in electrical engineering from the University "Pierre et Marie Curie", France. Since 1998, he has been with Valeo - Equipements Electriques Moteur, where he is currently Advanced Technical Manager.

Publication P5

Investigation of a Surface Mounted PM Machine Concept with 3D-Flux Paths, Modular Stator and Amorphous Material

Adolfo Garcia Gonzalez
Energy Technology Department
Aalborg University
Aalborg, Denmark
agg@et.aau.dk

Dong Wang
Energy Technology Department
Aalborg University
Aalborg, Denmark
dwa@et.aau.dk

Peter Omand Rasmussen
Energy Technology Department
Aalborg University
Aalborg, Denmark
por@et.aau.dk

***Abstract*—This paper deals with the design and investigation of a surface mounted machine concept targeted at the efficient recycling of rare-earth materials used in permanent magnets. The proposed machine has an outer rotor, single phase and a modular stator. In addition, the use of laminated iron based amorphous material is investigated. The implementation of this type of material in electrical machines is of interest due to their performance in terms of reduced losses when compared with standard electrical steel. However, the widespread use of amorphous materials is limited mainly due to their hardness and brittleness that make their processing (i.e. cutting and punching) a challenging task. Hence, an alternative for the use of such material is proposed in this paper, with the combination of both laminated C-shaped amorphous cores and a modular stator. 3D-FEM calculations of various parameters such as back-EMF, torque, inductance and losses, were validated with measurements performed on a demonstrator.**

***Index Terms*—amorphous materials, magnet losses, 3D-FEM, 3D-flux, modular stator, recyclability**

I. Introduction

The criticality of Rare Earth Elements (REEs) has increased awareness of the recycling of Permanent Magnet (PM) material in electrical machines [1]. Although there are methods available for recycling REEs, some of them are either high energy consuming or have a large environmental impact or may not be used at a large scale [2]. Therefore, developing new machine topologies with special focus on recycling of PM material have obtained special interest. The machine proposed in this work is an attempt to evaluate an alternative topology with non-traditional materials. The use of amorphous materials in electrical machines, have been studied on various types of machines [3] [4] [5] [6]. Furthermore, the use of laminated C-shaped amorphous cores has been investigated with both FEM simulations performed on a linear machine [7] and the experimental investigation of a claw pole transverse flux machine [4]. Regarding designs focused on recyclability of electrical machines, few work has been found [8]. Hence, the main goal of this paper is to propose an electrical machine design, aiming to the recyclability of the PMs, concurrently implementing amorphous material. In Section II both the definition of the concept and the description of the working principle are carried out. In Section III the assembly and the model built in 3D-FEM are explained. In Section IV the results of both calculations and measurements are presented and discussed. In Section V conclusions are drawn and future work is proposed.

II. Description of the Proposed Machine

A. Definition of the Concept

Ideally, having a machine with a large number of poles is of interest since it allows to improve the torque capability. However, an increased number of poles results in the increment of the iron losses in the stator, since these are proportional to the square of the frequency. Although the use of amorphous materials might be beneficial due to their intrinsic low value of specific losses, their magnetic properties might be degraded during their handling, cutting and punching. Hence, the use of laminated C-shaped amorphous cores [9] [10] is proposed as an alternative in order to restrict such degradation. As mentioned above, the use of this type of cores have been studied previously with both FEM simulations [7] and experimental results [4]. However, the machine proposed in this paper is based on the axial flux machine in Fig. 1 [11] [12] [13]. After few modifications applied to the stator core and the rotor in Fig. 2a, the geometry shown in Fig. 2b is obtained. That is, the axial air-gap has been modified in such fashion, that the result is a radial air-gap. Additionally, the stator core has been transformed to a C-shaped magnetic path, allowing the use of C-shaped cores and consequently, the use of laminated amorphous materials, as illustrated in Fig. 3. In order to simplify the manufacturing process, the remaining pieces (i.e. shaft, rotor back and end plates) of a HUB type, radial flux machine were re-used and a stator frame was built in order to house two laminated C-shaped cores of amorphous material. Fig. 4 shows the parts used for assembling the demonstrator.

B. Description of the Working Principle

The working principle is described in Fig. 5. When the permanent magnets on the rotor are aligned with the stator

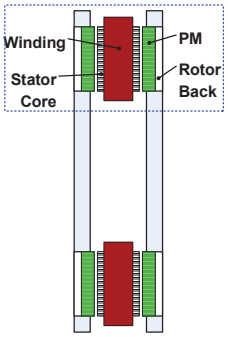

Fig. 1: Double sided internal salient pole stator and external twin rotor AFM.

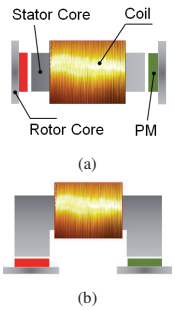

Fig. 2: Definition of the geometry of the machine proposed.

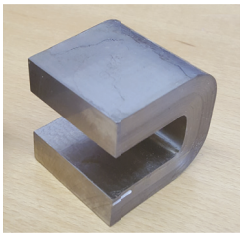

Fig. 3: C-shaped iron based laminated amorphous material 2605SA1 [9].

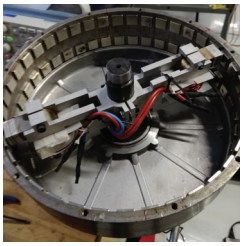

Fig. 4: Assembly of the demonstrator.

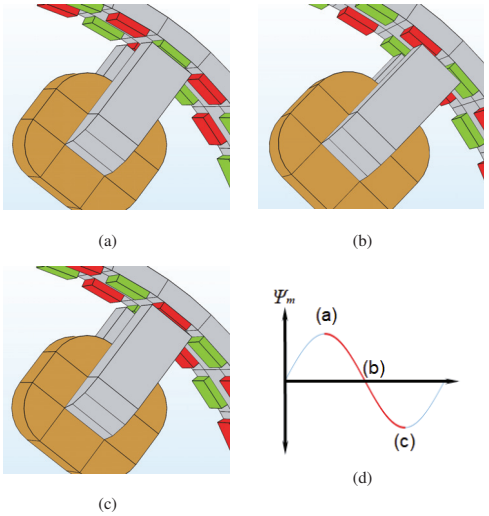

Fig. 5: Working principle.

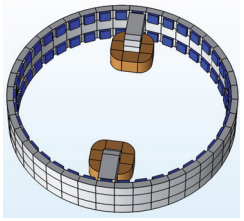

Fig. 6: 3D-FEM model geometry.

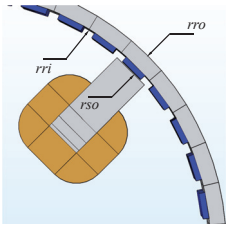

Fig. 7: Main dimensions of the demonstrator, *xy*-plane.

module as in Fig. 5a, the PM flux Ψ_m is maximum. If it is assumed that the rotor is travelling to the right for half a period, the position illustrated in Fig. 5b is reached. Hence, Ψ_m is equal to zero. Finally, when the rotor travels an additional half a period as in Fig. 5c, the PMs in the rotor are aligned with the stator modules but with opposite polarity. Therefore, a minimum is reached. The variation of Ψ_m with the displacement of the rotor is of sinusoidal nature as it is shown in Fig. 5d. Thus, the proposed machine may be driven simply as other PM machines with sinusoidal flux linkage/back-EMF.

III. Assembly and FEM Modelling

A. Main Dimensions

Once the dimensions of the active part of the machine were fixed, the construction of a 3D-FEM model was carried out. The main dimensions of the demonstrator are summarized in Table I. New magnets and iron based amorphous cores were obtained for building the new active part of the demonstrator. In addition, it was necessary to build a supporting frame for the stator modules and the windings. Fig. 6 shows the 3D-FEM modelled geometry where each one of the modules is included along with the PMs, in dark blue, mounted on the rotor cylinder. Additionally, Fig. 7 shows the definition of the main dimensions of the demonstrator. A detailed picture of the stator structure (i.e. coil, stator C-shaped core and supporting frame) is shown in Fig. 8. The test set-up is described in Fig. 9, and the machine was driven as a generator.

IV. Analysis of Results

A. Back-EMF

Fig. 10 shows the waveform of back-EMF measured and calculated at 100 rpm. Although the calculated back-EMF has a similar waveform when compared with measurements,

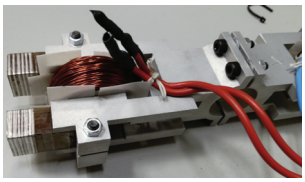

Fig. 8: Assembly of the coil and stator module to the supporting frame.

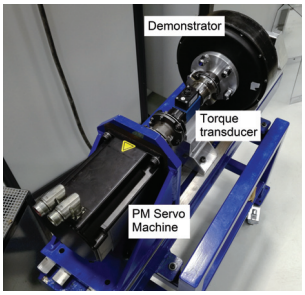

Fig. 9: Test bench used for experiment.

a deviation of approximately 11.8% was obtained. There are several factors that introduce uncertainties in the calculation of this parameter.

- The PMs were modelled in 3D-FEM with the curvature of the inner radius of the rotor rri. However, these are of rectangular shape.
- There might be deviations in the length of the air-gap during the assembly process.

Additional measurements of back-EMF at speeds of 200, 300, 400 and 500 rpm are reported in Fig. 11. The deviation between measured and calculated values remained at a value of approximately 12%.

TABLE I: Main dimensions of the demonstrator.

Dimension	**Value**
Rotor outer radius rro [mm]	139
Rotor inner radius rri [mm]	128
Stator outer radius rso [mm]	127.5
Stack Length [mm]	52
Air-gap length [mm]	0.5
PM thickness [mm]	3
PM width [mm]	15
PM length [mm]	15
PM remanence B_r [T]	1.37
Number of turns per coil	150
Pole pairs	20

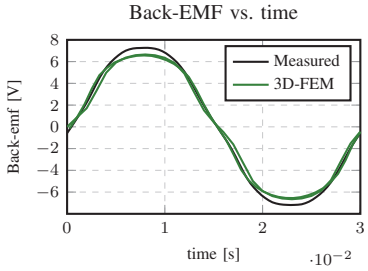

Fig. 10: Back-EMF measured and calculated at 100 rpm.

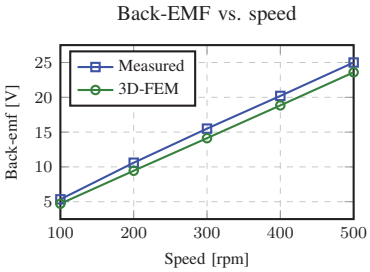

Fig. 11: Back-EMF measured and calculated at various speeds.

TABLE II: Inductance measured and calculated.

Inductance [mH]	
Measured	11.3
3D-FEM	10.3

B. Estimation of the Inductance

For calculating the inductance, the PMs on the rotor were modelled as air and a current applied to the windings. Then the inductance L_a was estimated as:

$$L_a = \frac{\lambda_a}{I_a} \tag{1}$$

Where λ_a is the flux linkage due to the applied current I_a. In contrast, the measurement of the inductance was performed with a Precision Magnetics Analyzer© equipment. The calculations yielded a deviation of 8.9%.The results are summarized in Table II.

C. Estimation of No-Load Losses

The no-load losses p_0 (i.e. bearings, stator iron, PM and rotor back losses) were measured with two different approaches:

- *Case 1:* The machine running at no-load. The product of torque and mechanical speed of the rotor corresponds to the total no-load losses of the machine. That is, $p_0 = T_0 \cdot \omega_{mech}$.
- *Case 2:* A spin down test was performed. The rotor was pulled to rotate and decaying waveform of back-EMF was recorded. The no-load losses were estimated by quadratic fitting of the expression $p_0 = J_m \cdot d\omega_{mech}/dt \cdot \omega_{mech}$. Where J_m is the moment of inertia of the machine.

The results are shown in Fig. 12 showing a good agreement. With *Case 1* as reference, the deviation of *Case 2* was estimated in a range of 9.7 to 19%. Such deviation might be result of the numerical approach that is required for its calculation, and the dependence on the accurate estimation of the inertia.

D. Segregation of the Losses

1) PM and Rotor Back Losses: Generally, PM losses due to slotting effect are insignificant. However, the study of these losses become relevant as a result of the changes of permeance

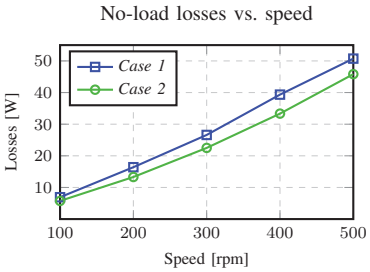

Fig. 12: No-load losses vs. speed.

TABLE III: Parameters used for calculation of losses.

Resistivity	**Value** [$\mu\Omega$/m]
Rotor back ρ_{fe}	0.1
PM ρ_{PM}	0.8

seen by the PMs due to the modular structure of the stator (i.e. large air openings between stator modules). In [14] and [15] analytical approximations are proposed. However, neither 2D-FEM nor analytical approaches yield reliable results since such models are appropriate when the length of the PMs is much larger than the thickness [16]. In order to validate the calculated values with the measurements, PM and rotor back losses were estimated with 3D-FEM simulations. The conductivity of the PMs was acquired from measurements performed to samples of sintered magnets of similar quality by the Physical Property Measurement System PPMS of Quantum Design® [17]. The variation of the resistivity with temperature is shown in Fig. 13. The conductivity of iron was assigned to the rotor back region. The values of conductivity implemented in the calculations are summarized in Table III.

2) Stator Iron Losses: The calculation of the iron losses in the stator modules was performed in order to validate the hypothesis of low iron losses in laminated amorphous materials exposed in Section I. The method proposed in [18] was followed. Therefore, a Fourier transformation of the waveform of the magnetic flux density at each finite element in the stator core region was applied to the radial, tangential and axial components of the magnetic flux density, $\hat{b}_r$, $\hat{b}_t$ and $\hat{b}_z$. The results are shown in Fig. 14 along with the calculated values of PM and rotor back losses.

As it was expected, the losses in the stator are significantly low, showing a linear behaviour and reaching a maximum value of approximately 1 W at 500 rpm. Thus, showing the convenience of the use of this type of material. Regarding the PM and rotor back losses, their increment is proportional to the square of the speed, confirming the significant slotting effect, due to the modular structure of the stator.

3) Bearing Losses: In order to perform the measurement of the bearing losses, it was necessary to extract the stator assembly (Fig. 8) (i.e. supporting frames, coils and stator modules) out of the demonstrator. Then, the machine was run

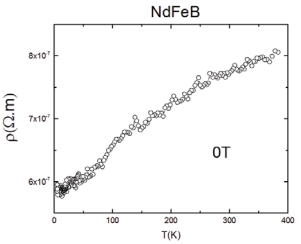

Fig. 13: PM resistivity vs. temperature [17].

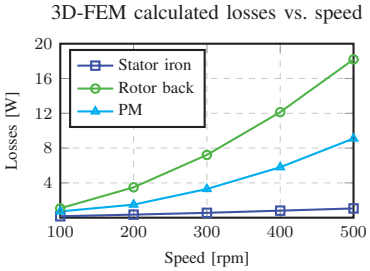

Fig. 14: 3D-FEM calculated losses vs. speed.

and measurements of torque and speed were registered. The bearing losses were estimated as the product of the measured torque and the rotational speed, that is, $p_{bear} = T_0' \cdot \omega_{mech}$. The measured bearing losses are illustrated in Fig. 15. Once the bearing losses were measured, it was possible to contrast both measured and calculated values of no-load losses p_0. The results are shown in Fig. 16, where the calculated values of no-load losses are the summation of the calculated PM, stator iron, rotor back losses and the measured bearing losses. On the other hand, the measured values of p_0 illustrated in Fig. 16 correspond to the values of *Case 1* calculated in Section IV-C.

A maximum deviation of approximately 10.7% was obtained at 500 rpm. The source of such deviation might be the uncertainties in the measurements (e.g. vibration, misalignment of the test set-up, etc.), which might result in the underestimation of the measured losses. Additionally, the uncertainty of the conductivity of the back iron, which material is unknown and as described in Section IV-A the air-gap uncertainties. The distribution of the current density in the PMs due to slotting effect is shown in Fig. 17.

E. Estimation of Torque

A resistive load R_{load} was connected to the terminals of the machine and measurements of torque, current, voltage and power factor were registered at 100, 200, 300, 400 and 500 rpm. In all cases, the resistive load was kept fixed. Fig. 18 shows the equivalent circuit of the test. The power factor at the load is approximately unity given the predominantly resistive nature of the load. Therefore, the current I_s and voltage V_s

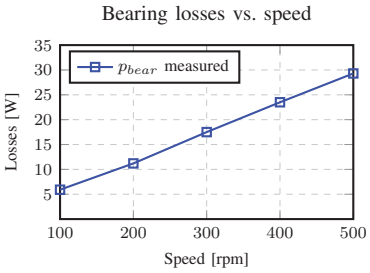

Fig. 15: Bearing losses vs. speed.

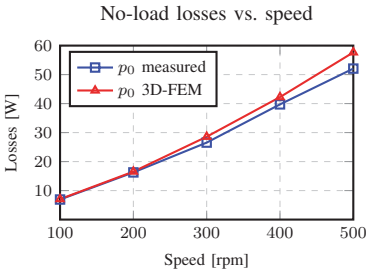

Fig. 16: No-load losses vs. speed.

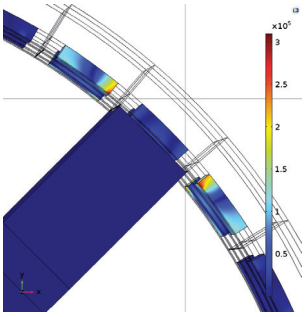

Fig. 17: PM current density at 100 rpm, t=4.6 ms.

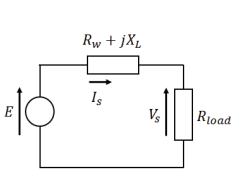

Fig. 18: Equivalent circuit of load test.

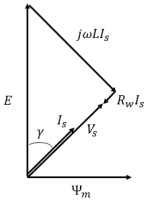

Fig. 19: Phasor diagram in generator mode.

are in phase, as shown in the phasor diagram in Fig. 19. In order to calculate the air-gap torque T_{em} both the amplitude and angle of I_s were required. The current as phasor may be estimated as:

$$\overline{I_s} = \frac{\overline{E}}{R_w + R_{load} + j\omega L} \tag{2}$$

Where $\overline{E}$ is the measured back-EMF, R_w and L are the measured winding resistance and inductance, respectively. Such currents were applied to the FEM models and the torque was calculated. Since the machine was operating as a generator, the measured shaft torque T_{shaft}, the air-gap torque T_{em} and the no-load losses p_0 follow the relation:

$$T_{shaft} = T_{em} + \frac{p_0}{\omega_{mech}} \tag{3}$$

The results are shown in Fig. 20. As it is observed, from measurements, the torque does not increase with the increment of the current I_s. Furthermore, its value starts reducing due to the variation of the load angle γ. The calculated torque follows a similar trend as the measured values. However, the large deviations (approx. 21.6%) might be caused by uncertainties in the measurements for the reasons exposed in Section IV-D3.

V. Conclusions and Future Work

A single phase PM surface mounted machine topology is proposed in which the use of amorphous material is investigated. The modular structure of the stator showed to be easily assembled and disassembled, which might be convenient when addressing the recyclability of the PMs. However, further evaluation of the recyclability potential is required. Additionally, various parameters such as back-EMF, inductance and losses were validated with measurements. Due to the modularity of the motor, it was possible to perform a segregation of the no-load losses in order to evaluate the rotor losses due to slotting effect. Furthermore, as PM losses are increasing with the square of the speed, a surface mounted rotor structure might not be convenient for a machine either running at higher speeds or with a higher pole count. Alternatives such as PM segmentation, and the use of bonded PMs are proposed as future work in the limitation of PM losses.

In addition to the rotor topology studied in this paper, the

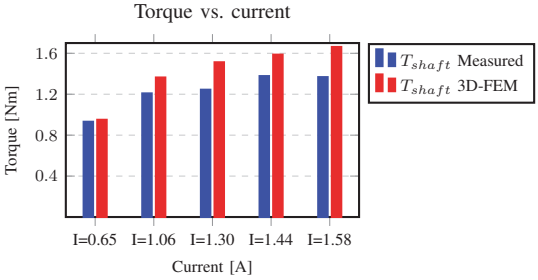

Fig. 20: Torque vs. current comparison.

geometry presented in Fig. 2b allows further modifications. Consequently, it would be possible to consider various rotor topologies (e.g. interior permanent magnet). Hence, the permanent magnets would be protected from the variation of the permeance of the air-gap, which might be beneficial in the reduction of the PM losses.

Unfortunately, the re-use of the parts of a larger motor introduced a large value of bearing losses, which results in a low value of efficiency for this demonstrator (approximately 30%). However, this might be improved by the construction of a complete 3-phase machine, adding stator modules to the structure, consequently improving the torque production. Finally, the concept was demonstrated to work and showed a fair agreement with the calculated values.

ACKNOWLEDGMENT

The research leading to the results presented in this article has been funded by the European Community's Horizon 2020 Programme ([H2010/2014-2019]) under Grant Agreement no. 674973 (MSCA-ETN DEMETER). This publication reflects only the authors view, exempting the Community from any liability. Project website http://etn-demeter.eu/.

REFERENCES

[1] T. Elwert, D. Goldmann, F. Roemer, and S. Schwarz, "Recycling of ndfeb magnets from electric drive motors of (hybrid) electric vehicles," *Journal of Sustainable Metallurgy*, vol. 3, no. 1, pp. 108–121, Mar 2017. [Online]. Available: https://doi.org/10.1007/s40831-016-0085-1

[2] Y. Yang, A. Walton, R. Sheridan, K. Güth, R. Gauß, O. Gutfleisch, M. Buchert, B.-M. Steenari, T. Van Gerven, P. T. Jones, and K. Binnemans, "Ree recovery from end-of-life ndfeb permanent magnet scrap: A critical review," *Journal of Sustainable Metallurgy*, vol. 3, no. 1, pp. 122–149, Mar 2017. [Online]. Available: https://doi.org/10.1007/s40831-016-0090-4

[3] Y. Enomoto, M. Ito, H. Koharagi, R. Masaki, S. Ohiwa, C. Ishihara, and M. Mita, "Evaluation of experimental permanent-magnet brushless motor utilizing new magnetic material for stator core teeth," *IEEE Transactions on Magnetics*, vol. 41, no. 11, pp. 4304–4308, Nov 2005.

[4] N. Dehlinger and M. R. Dubois, "Clawpole transverse flux machines with amorphous stator cores," in *2008 18th International Conference on Electrical Machines*, Sep. 2008, pp. 1–6.

[5] Z. Wang, Y. Enomoto, M. Ito, R. Masaki, S. Morinaga, H. Itabashi, and S. Tanigawa, "Development of a permanent magnet motor utilizing amorphous wound cores," *IEEE Transactions on Magnetics*, vol. 46, no. 2, pp. 570–573, Feb 2010.

[6] N. Ertugrul, R. Hasegawa, W. L. Soong, J. Gayler, S. Kloeden, and S. Kahourzade, "A novel tapered rotating electrical machine topology utilizing cut amorphous magnetic material," *IEEE Transactions on Magnetics*, vol. 51, no. 7, pp. 1–6, July 2015.

[7] J. Ou, Y. Liu, M. Schiefer, and M. Doppelbauer, "A novel pm-free high-speed linear machine with amorphous primary core," *IEEE Transactions on Magnetics*, vol. 53, no. 11, pp. 1–8, Nov 2017.

[8] M. Alatalo, S. T. Lundmark, and E. A. Grunditz, "Electric machine design for traction applications considering recycling aspects-review and new solution," in *IECON 2011 - 37th Annual Conference of the IEEE Industrial Electronics Society*, Nov 2011, pp. 1836–1841.

[9] L. Hitachi Metals America, "Amorphous and Nanocrystalline-POWERLITE C-Cores," [Online]: https://www.hitachimetals.com/ materials-products/amorphous-nanocrystalline/ powerlite-c-cores.php, October 2016, [Accessed]: Sept. 22, 2018.

[10] L. Advanced Technology & Materials Co., "Antaimo amorphous c-cores," [Online]: http://www.atmcn.com/Subsidiary/Metal/Products/ 3237.shtml, February 2018, [Accessed]: Sept. 22, 2018.

[11] J. F. Gieras, R. J. Wang, and M. J. Kamper, *Axial Flux Permanent Magnet Brushless Machines*. Dordrecht: Springer Netherlands, 2008.

[12] M. Aydin, S. Huang, and T. Lipo, "Axial flux permanent magnet disc machines: A review," *Conf. Record of SPEEDAM*, 01 2004.

[13] Y. Limited, "Yasa p400r series e-motor," [Online]: https://www.yasa.com/wp-content/uploads/2018/01/ YASA_P400_Product_Sheet.pdf, 2018, [Accessed]: Mar. 01, 2019.

[14] A. Bettayeb, R. Kaczmarek, and J.-C. Vannier, "Analytical estimation of rotor loss due to stator slotting of synchronous pm machines," *World Academy of Science, Engineering and Technology*, vol. 66, 2010.

[15] Z. X. Fang, Z. Q. Zhu, L. J. Wu, and Z. P. Xia, "Simple and accurate analytical estimation of slotting effect on magnet loss in fractional-slot surface-mounted pm machines," in *2012 XXth International Conference on Electrical Machines*, Sep. 2012, pp. 464–470.

[16] A. G. Gonzalez, J. Millinger, and J. Soulard, "Magnet losses in inverter-fed two-pole pm machines," in *2016 XXII International Conference on Electrical Machines (ICEM)*, Sept 2016, pp. 1854–1860.

[17] A. G. Gonzalez, A. K. Jha, Z. Li, P. Upadhayay, and P. Rasmussen, "Validation of efficiency maps of an outer rotor surface mounted permanent magnet machine for evaluation of recyclability of magnets," in *2018 IEEE International Magnetic Conference (INTERMAG)*, April 2018, pp. 1–6.

[18] H. Domeki, Y. Ishihara, C. Kaido, Y. Kawase, S. Kitamura, T. Shimomura, N. Takahashi, T. Yamada, and K. Yamazaki, "Investigation of benchmark model for estimating iron loss in rotating machine," *IEEE Transactions on Magnetics*, vol. 40, no. 2, pp. 794–797, March 2004.

ISSN (online): 2446-1636
ISBN (online): 978-87-7210-510-9 AALBORG UNIVERSITY PRESS